Institut für Erd- und Umweltwissenschaften
Mathematisch-Naturwissenschaftliche Fakultät
Universität Potsdam

Surface heat flow and lithospheric thermal structure of the northwestern Arabian Plate

Kumulative Dissertation

zur Erlangung des akademischen Grades
"doctor rerum naturalium"
(Dr. rer. nat.)
in der Wissenschaftsdisziplin "Geowissenschaften"

eingereicht an der
Mathematisch-Naturwissenschaftlichen Fakultät
der Universität Potsdam
von

Felina Schütz

Potsdam, September 2013

Betreuer:
Prof. Dr. Michael Weber (Universität Potsdam)

Gutachter:
Prof. Dr. Michael Weber (Universität Potsdam)
Prof. Dr. Gerhard Franz (Technischen Universität Berlin)
Prof. Dr. Roland Oberhänsli (Universität Potsdam)

Datum der Einreichung: 16. September 2013
Datum der Verteidigung: 19. Dezember 2013

Published online at the
Institutional Repository of the University of Potsdam:
URL http://opus.kobv.de/ubp/volltexte/2014/6962/
URN urn:nbn:de:kobv:517-opus-69622
http://nbn-resolving.de/urn:nbn:de:kobv:517-opus-69622

Selbständigkeitserklärung
Hiermit versichere ich, die vorliegende Arbeit selbständig und nur unter Verwendung der angegebenen Quellen und Hilfsmittel angefertigt zu haben.
Declaration of independent work
Hereby I declare that I have written this paper on my own, distinguished citations, and used no other than the named sources and aids.
Potsdam, im September 2013

The surface heat flow (q_S) is paramount for modeling the thermal structure of the lithosphere. Changes in the q_S over a distinct lithospheric unit are normally directly reflecting changes in the crustal composition and therewith the radiogenic heat budget (e.g., Rudnick et al., 1998; Förster and Förster, 2000; Mareschal and Jaupart, 2004; Perry et al., 2006; Hasterok and Chapman, 2011, and references therein) or, less usual, changes in the mantle heat flow (e.g., Pollack and Chapman, 1977). Knowledge of this physical property is therefore of great interest for both academic research and the energy industry.

The present study focuses on the q_S of central and southern Israel as part of the Sinai Microplate (SM). Having formed during Oligocene to Miocene rifting and break-up of the African and Arabian plates, the SM is characterized by a young and complex tectonic history. Resulting from the time thermal diffusion needs to pass through the lithosphere, on the order of several tens-of-millions of years (e.g., Fowler, 1990); q_S-values of the area reflect conditions of pre-Oligocene times. The thermal structure of the lithosphere beneath the SM in general, and south-central Israel in particular, has remained poorly understood.

To address this problem, the two parameters needed for the q_S determination were investigated. Temperature measurements were made at ten pre-existing oil and water exploration wells, and the thermal conductivity of 240 drill core and outcrop samples was measured in the lab. The thermal conductivity is the sensitive parameter in this determination. Lab measurements were performed on both, dry and water-saturated samples, which is labor- and time-consuming. Another possibility is the measurement of thermal conductivity in dry state and the conversion to a saturated value by using mean model approaches. The availability of a voluminous and diverse dataset of thermal conductivity values in this study allowed (1) in connection with the temperature gradient to calculate new reliable q_S values and to use them to model the thermal pattern of the crust in south-central Israel, prior to young tectonic events, and (2) in connection with comparable datasets, controlling the quality of different mean model approaches for indirect determination of bulk thermal conductivity (BTC) of rocks.

The reliability of numerically derived BTC values appears to vary between different mean models, and is also strongly dependent upon sample lithology. Yet, correction algorithms may significantly reduce the mismatch between measured and calculated conductivity values based on the different mean models. Furthermore, the dataset allowed the derivation of lithotype-specific conversion equations to calculate the water-saturated BTC directly from data of dry-measured BTC and porosity (e.g., well log derived porosity) with no use of any mean model and thus provide a suitable tool for fast analysis of large datasets.

The results of the study indicate that the q_S in the study area is significantly higher than previously

assumed. The new presented q_S values range between 50 and 62 mW m^{-2}. A weak trend of decreasing heat flow can be identified from the east to the west (55−50 mW m^{-2}), and an increase from the Dead Sea Basin to the south (55−62 mW m^{-2}). The observed range can be explained by variation in the composition (heat production) of the upper crust, accompanied by more systematic spatial changes in its thickness.

The new q_S data then can be used, in conjunction with petrophysical data and information on the structure and composition of the lithosphere, to adjust a model of the pre-Oligocene thermal state of the crust in south-central Israel. The 2-D steady-state temperature model was calculated along an E–W traverse based on the DESIRE seismic profile (Mechie et al., 2009). The model comprises the entire lithosphere down to the lithosphere–asthenosphere boundary (LAB) involving the most recent knowledge of the lithosphere in pre-Oligocene time, i.e., prior to the onset of rifting and plume-related lithospheric thermal perturbations. The adjustment of modeled and measured q_S allows conclusions about the pre-Oligocene LAB-depth. After the best fitting the most likely depth is 150 km which is consistent with estimations made in comparable regions of the Arabian Shield. It therefore comprises the first ever modelled pre-Oligocene LAB depth, and provides important clues on the thermal state of lithosphere before rifting. This, in turn, is vital for a better understanding of the (thermo)-dynamic processes associated with lithosphere extension and continental break-up.

Der Oberflächenwärmefluss (q_S) ist maßgeblich für die Modellierung der thermischen Struktur der Lithosphäre. Änderungen im q_S, innerhalb eines speziellen lithosphärischen Abschnitts, reflektieren direkt Änderungen in der krustalen Zusammensetzung und damit der radiogenen Wärmeproduktion (e.g., Rudnick et al., 1998; Förster und Förster, 2000; Mareschal und Jaupart, 2004; Perry et al., 2006; Hasterok und Chapman, 2011, und enthaltene Referenzen) oder aber, weniger häufig, Änderungen im Mantelwärmefluss (e.g., Pollack und Chapman, 1977). Die Kenntnis dieses physikalischen Parameters ist daher von großem Interesse, sowohl für die Forschung als auch für die Energiewirtschaft.

Die vorliegende Studie befasst sich mit dem q_S von Süd- und Zentralisrael als Teil der Sinai Mirkoplatte (SM), welche während des Riftings und Auseinanderbrechens der Afrikanischen und Arabischen Platte im Oligozän entstand und durch diese, sehr junge und komplexe tektonische Geschichte, geprägt ist. Die thermische Diffusion benötigt einige Zehner-Millionen Jahre (e.g., Fowler, 1990) um die Lithosphäre zu durchlaufen, q_S-Werte der Region reflektieren daher prä-oligozäne Bedingungen. Die thermische Struktur der Lithosphäre der SM generell, und insbesondere in Süd- und Zentralisrael, ist bis heute nur sehr wenig verstanden. Um dieses Problem anzugehen wurden, die für die q_S-Bestimmung benötigten Parameter, eingehend untersucht. An zehn ehemaligen Wasser- und Erdölexplorationsbohrungen wurden neue Temperaturmessungen durchgeführt, und die Wärmeleitfähigkeit von 240 Bohrkern- und Aufschlussproben wurde im Labor gemessen. Die Wärmeleitfähigkeit ist in der q_S-Bestimmung der sensitive Parameter. Die Labormessungen wurden sowohl an trockenen sowie an wasser-gesättigten Proben durchgeführt, was personal- und zeitaufwendig ist. Eine andere Möglichkeit ist die Messung der Wärmeleitfähigkeit im trockenen Zustand und das Konvertieren zu einem saturierten Wert unter der Verwendung von Mischungsgesetzen. Das Vorhandensein eines umfangreichen und sehr diversen Wärmeleitfähigkeit-Datensatzes ermöglicht (1) in Verbindung mit dem Temperaturgradienten die Berechnung von neuen zuverlässigen q_S-Werten sowie deren Verwendung zur Modellierung der thermischen Struktur der prä-oligozänen Kruste in Israel und (2) in Verbindung mit vergleichbaren Datensätzen, die vorhandenen Mischungsgesetzte zur indirekten Bestimmung der saturierten Gesamtwärmeleitfähigkeit (BTC) qualitativ zu überprüfen.

Die Zuverlässigkeit numerisch bestimmter BTC-Werte variiert für die verschiedenen Mischungsgesetze und ist darüber hinaus stark von der Lithologie der Proben abhängig. Mittels spezifischer Korrekturgleichungen können Abweichungen zwischen gemessenen und berechneten Werten jedoch erheblich reduziert werden. Die Datenanzahl und die statistische Analyse ermöglichte darüber hinaus die Ableitung von lithotypspezifischen Konvertierungsgleichungen, um die saturierte BTC anhand von trocken gemessenen BTC- und Porositätswerten (z.B. aus

Porositätslogs) zu berechnen. Dieser Ansatz führt, für alle Lithotypen, zu einer guten Reproduzierbarkeit gemessener Werte und ist daher eine nützliche Alternative, wann immer große Probenmengen behandelt werden.

Die Ergebnisse dieser Studie zeigen, dass der q_S im Untersuchungsgebiet signifikant höher ist, als bisher angenommen. Die q_S-Werte, die in dieser Studie für Südisrael bestimmt wurden, schwanken zwischen 50 und 62 mW m^{-2}. Ein schwacher Trend abnehmender Werte von Ost nach West (55−50 mW m^{-2}), und ein leichter Trend ansteigender Werte vom Toten Meer nach Süden (55−62 mW m^{-2}) können identifiziert werden. Diese beobachteten Schwankungen lassen sich mit Variationen in der krustalen Zusammensetzung (Wärmeproduktion) erklären, einhergehend mit regionalen Änderungen der Krustenmächtigkeit. Die neuen q_S-Daten können dann, im Zusammenhang mit petrophysikalischen Daten und Informationen über die Struktur und Zusammensetzung der Lithosphäre, verwendet werden um ein Model des prä-oligozänen thermischen Zustandes der Kruste Zentral- und Südisraels abzugleichen. Das stationäre 2-D Temperatur-Modell wurde entlang einer E−W Traverse, basierend auf dem seismischen DESIRE-Profil (Mechie et al., 2009), berechnet. Es reicht bis zur Lithosphären–Asthenosphären Grenze (LAB) und bezieht sich auf das aktuellste Wissen über die prä-oligozäne Lithosphäre, also vor dem Einsetzen von Rifting und plumebedingten thermischen Störungen. Durch den Abgleich zwischen gemessenen und modellierten q_S-Werten ist es möglich auf die prä-oligozäne LAB-Tiefe zurückzuschließen. Als wahrscheinlichste Tiefe ergeben sich 150 km, was konsistent ist mit LAB-Tiefen Abschätzungen aus vergleichbaren stabilen Regionen des Arabischen Schildes. Dies liefert wichtige Anhaltspunkte über den thermischen Zustand der Lithosphäre vor dem Einsetzen von Rifting in der Region und ist wiederum entscheidend für ein besseres Verständnis der (thermo-) dynamischen Prozesse in Assoziation mit Extension der Lithosphäre und dem kontinentalem Auseinanderbrechen.

TC, λ	Thermal conductivity
BTC	Bulk thermal conductivity
MTC	Matrix thermal conductivity
RHP, A	Radiogenic heat production
T	Temperature
q_s	Surface heat flow
Γ	Temperature gradient
DB	Divided-bar technique
OS	Optical scanning technique
DTS	Distributed Temperature Sensing
DST	Dead Sea Transform
DSB	Dead Sea Basin
AP	Arabian Plate
AS	Arabian Shield
APl	Arabian Platform
SM	Sinai Microplate
LB	Levantine Basin
SR	Suez Rift
LAB	Lithosphere–asthenosphere boundary
DESERT	Dead Sea Rift Transect
DESIRE	Dead Sea Integrated Research

I would like to gratefully and sincerely thank Dr. Andrea Förster and Dr. Hans-Jürgen Förster, who initiated and supervised this work. They guided me with the perfect mix of patience and pressure through the last years. Without them this work would not have been a success, I am especially thankful for the many fruitful sometimes even passionate discussions and for sharing their knowledge and ideas with me.

Furthermore, I like to thank Prof. Dr. Michael Weber, for supporting and reviewing this work. Dr. Ben Norden is thanked for accompany me to my first field trip and giving me a lot of assistance especially during the difficult first month. The field work would not have been possible without the technicians and their experience and serenity; therefore I like to thank Jörg Schrötter and Mathias Poser. Alex Reichardt and Ronny Giese are thanked for a nice and entertaining second field trip.

I like to thank Dr. Eyal Shalev and Hallel Lutzky, who supported the work with their knowledge of place. The Geological Survey of Israel is thanked for access to the drill core archives and for providing data. Dr. Gidi Steinitz supported my stays in Israel, gave important assistance and was always open for questions. Dr. Oded Navon, from the Hebrew University, is thanked for sharing his knowledge of xenoliths and providing some rare samples of those from the northern part of Israel. Furthermore, the work profited from comments and ideas of Prof. Zvi Ben-Avraham and Prof. Zvi-Garfunkel given during the DESIRE-workshops.

Lab-work was thoroughly supported by David Göhring and Alex Reichardt. My roommates Tom Schintgen, Dr. Gunther Baumann is thanked for the pleasant working atmosphere. This gratitude can be extended to the people in the A6 building in general, it has been a really nice working neighborhood. Furthermore, I like to thank Dr. Sven Fuchs for the very fruitful and nice cooperation and for always being helpful with comments and criticism. My gratitude is extended to my dear friends Dr. Christina von Nicolai and Dr. Inga Osbahr for many profound conversations.

My family, especially my husband Markus and my sons Henri and Jonah, is thanked for giving me a lot of support and freedom to focus on my work and especially for always being understanding and patient even in stressful times.
This work was funded by the Deutsche Forschungsgemeinschaft and by the GFZ German Research Centre for Geoscience.

1 Introduction

The thermal regime of the continental lithosphere depends on several parameters and its understanding is essential for the overall comprehension of a geodynamic setting, its development and history. The thickness of the different lithospheric layers, the composition and therewith the radiogenic heat production (RHP) and the basal heat flow are the main controlling parameters. The terrestrial heat flow directly reflects the interaction of all these factors. A good knowledge of the terrestrial heat flow is hence essential for understanding the lithospheric thermal pattern, and in turn allows conclusions about composition and structure of the lithosphere.

West of the Dead Sea Transform (DST), in central and southern Israel, the surface heat flow (q_S) is a matter of debate. Data published so far (Eckstein and Simmons, 1978; Shalev et al., 2012) show an anomalous large range 30−85 mW m^{-2}. The thermal conductivity (TC) of the rocks and the geothermal gradient are the two parameters which control the q_S. The large range of q_S values determined in a former study can be mainly attributed to insufficient knowledge about the thermal rock properties and the subsurface temperature distribution. A further parameter overprinting the crustal heat flow and producing this anomalous large range can be advective heat flow. Most likely the interplay of these different error sources produced the large range. In any case, the range cannot be explained with changes in crustal composition and structure and this study aimed to determine new reliable conductive q_S values for central and southern Israel.

Considerable effort was made to improve the knowledge of the thermal properties (TC, RHP) of the sedimentary rocks of central and southern Israel, discussed in chapter 2. The TC is the sensitive parameter in the q_S determination; changes in this parameter affect the final q_S to a greater extent than changes of the geothermal gradient. Extensive sampling of outcrops and drill cores was performed in the course of this study. The TC of different lithotypes was measured on dry and water-saturated samples. Furthermore, density and porosity were analyzed. The TC varies considerable between lithotypes and geological formations. Especially for sedimentary basins of very heterogeneous composition a careful consideration of this parameter is needed to get a proper evaluation of the conductive q_S. The TC is analyzed considering facies changes and accompanied changes in mineral assemblage, porosity and texture. The importance of the TC for the q_S determination can be shown by reevaluating an old heat-flow site and applying the newly determined TC-values. This leads to completely divergent mean q_S-values for the site (Eckstein and Simmons, 1978: 37 mW m^{-2}; Schütz et al., 2012: 57 mW m^{-2}). Further significance for quantifying the conductive q_S has the radiogenic heat produced in the sedimentary basin. The different lithotypes composing the sedimentary layer over the basement show a large range of RHP

depending on the genesis of the rocks and the source area. Clastic rocks generally show higher RHP values than carbonate rocks. Clay and shale are typically the sedimentary rocks with high amounts of radiogenic heat producing elements. The highest amounts, however, occur in K-rich evaporates and phosphate-rich sediments (Vila et al., 2010). To determine the radiogenic heat, produced in the sedimentary cover, gamma-ray logs from the study area were evaluated. The budget for each stratigraphic group and for the entire sedimentary section above the basement was calculated and amounts to ca. 4 mW m^{-2}, where the sedimentary veneer is thickest.

Chapter 3 is dealing with the indirect deduction of the bulk thermal conductivity (BTC) of sediments. Especially in sedimentary basins of very heterogeneous composition, like the one covering central and southern Israel, large amounts of TC data are needed to characterize the sedimentary setting. Here, efficient tools for TC computation are valuable to reduce the amount of work. The TC of a rock can be measured under dry and water-saturated conditions and it can be calculated if no direct measurements can be performed. The estimation of the BTC can base either on mineral content or matrix thermal conductivity (MTC) and the porosity of the rock. To calculate the TC different approaches exist based on different physical and empirical foundations. The fitting behavior of the approaches is highly diverse and often restricted to specific ranges in mineralogy or porosity of the rock. The most commonly used models for BTC calculation will be analyzed in this study. A dataset comprising 1147 single TC measurements, in the interval 1.0 to 6.5 W m^{-1} K^{-1}, of different lithotypes, is used for statistical analysis of the deviation between laboratory-measured and calculated BTC. The study indicates that the mismatch between laboratory-measured and calculated BTC can be quite high and strongly depends on the lithotype. Correction equations allow a significant improvement of the accuracy of BTC data calculated on the base of the different mean models and will be presented in this study. The amount of data and the statistical analysis allowed furthermore the derivation of lithotype-specific conversion equations to calculate the water-saturated BTC directly from data of dry-measured BTC and porosity (e.g., well log derived porosity) with no use of any mixing model. This approach leads to a good fit for all lithotypes and is a useful alternative, whenever huge amounts of samples have to be handled.

To shed light on the terrestrial heat flow new q_S determinations were made at ten borehole sites presented in chapter 4. Measurements of high-resolution continuous temperature logs in deep boreholes provide the opportunity to determine temperature gradients reflecting steady-state conditions. Temperature was recorded in the air- and water-filled intervals of ten boreholes, well spread over the study area. Considering that heat flow needs to be determined for both dry (air-filled) and water-filled borehole sections, dry and saturated measured TC values were applied. The newly determined q_S values were then used for adjusting a thermal model of the lithosphere.

Thermal modeling demands information about the structure and composition of the different lithospheric layers. The composition of the lithosphere can be studied in the field whenever outcrops exist. Especially the deeper parts of the crust are normally not exposed and need to be studied with geophysical methods or, if found, on the basis of xenoliths.

Information about the structure of the lithosphere derives mainly from seismic data, where velocity steps point to changes in composition (cf. also Appendix, A2). The lithosphere can be subdivided into the sedimentary veneer, the upper crystalline crust, the lower crust and the upper mantle. Gravity data can provide important additional information about layering in the lithosphere, where density differences are high. Especially the felsic upper crust, the mafic lower crust and the ultramafic mantle show significantly different densities.

The distinction of the different main layers building up the lithosphere is relatively clearly made. More challenging is the determination of composition changes within the layers. Information about the composition of the different layers of the sedimentary veneer and the upper crust derives from well logs and outcrops. Xenolith samples from the Qarnei-Hittin volcanic area in northern Israel, analyzed in this study, kindly provided by the Hebrew University in Jerusalem, deliver information about the composition of the lower crust and the upper mantle. This information in conjunction with the seismic and gravity data allows an estimation of the fraction of the different rock types composing the lithospheric layers.

After analyzing composition and structure, another critical point in geothermal modeling is the assignment of thermal parameters (TC, RHP) to the different geological units. The TC of the sedimentary basin rocks is analyzed in detail and therewith very well known. TC of upper crustal rocks from the area was measured in the studies of Förster et al. (2007) and Förster et al. (2010) and the values are assignable to this study area. Lower crustal xenoliths were analyzed concerning TC. Measurements of TC on these rocks have to be handled with care because of mineralogical changes and micro cracks related to overprinting (see Appendix, A3). The distribution of the radiogenic heat producing elements within the lithosphere is very heterogeneous. Typical upper mantle (lherzolite) and lower crustal (pyx-rich and plg-rich granulite) rocks generally comprise little amounts of radiogenic heat producing elements and hence have only a minor fraction on the bulk crustal heat flow. The main fraction of radiogenic heat is produced in the upper crystalline crust. The composition of the upper crystalline crust range from rhyolites, granites to gabbro and especially the granitic and granodioritic rocks contain large amounts of radioactive elements like U, Th and K. Information of the RHP of the different crustal layers derive from the study Förster et al. (2009) and from different studies (Beyth et al., 1994; Bogoch et al., 2002; Mushkin et al., 2003; Eyal et al., 2010) providing bulk rock chemistry data, giving the potential to calculate the RHP. For the thermal

modeling different lower boundary scenarios were adopted and crosschecked with the q_S values determined in the field (cf. also Appendix, A1). The impacts of slightly different upper crustal compositions, 10% more or less radiogenic, were tested. The results of the thermal modeling will be discussed in terms of lithosphere thickness prior to young thermal erosion processes, focal earthquake depth in the region and the formation of the DST.
The study was embedded in the Dead Sea Integrated Research (DESIRE) project, a multi-national interdisciplinary project led by the GFZ German Research Centre for Geoscience (GFZ-Potsdam).

1.1 Regional setting

Israel was, during long time of its history, located on a passive continental margin. Up to the Permian the region was part of the Gondwana continent and two major sedimentary series were deposited, separated by an unconformity. During the Mesozoic the platform subsided strongly and thick marine sediments were deposited. The Levantine Basin (LB), which occupies the eastern portion of the Mediterranean Sea and whose development started in late Triassic–early Jurassic times (Figure 1.1) (Garfunkel and Derin, 1984; Gardosh and Druckman, 2006), is remnant of the Tethys Ocean. Both transgressed and regressed over the area of southern Israel, which resulted in alternately deposition and erosion of sediments. The LB is bounded to the south and east by the continental slope of the Sinai Microplate (SM, also termed Sinai Subplate or Sinai Block; Salamon et al., 2003; Mahmoud et al., 2005) and to the west by the slope of the African Plate. The northern border is defined by the Cyprus Arc. The sediments over Israel deposited mainly in Jurassic and Cretaceous times. The phases of deposition and erosion were only temporarily interrupted by some magmatic events, like the Cretaceous igneous activity in Israel (Segev, 2000). In the study area the basement is covered by a sedimentary veneer of up to 7 km (Rybakov and Segev, 2004), dominated by carbonate rocks with interlayers of clastic rocks (Garfunkel, 1988).
The basement of the study area is part of the SM, which is a fragment of the Arabian Plate (AP) and hence underlay the same history starting in Neoproterozoic times (Salamon et al., 2003; Stern and Johnson, 2010). The SM formed when the African and Arabian Plate separated in Oligocene to Miocene times. The continental break-up started with the Red Sea rifting 30 Ma ago initiated by the Afar mantle plume followed by the development of the Suez Rift in early Miocene times and the DST activation 14–18 Ma ago (Freund et al., 1970; Bartov et al., 1980; Bohannon et al., 1989; Wilson et al., 2000; Sobolev et al., 2005). The AP is distinguished into the Arabian Shield (AS) and the Arabian Platform (APl). The lithosphere beneath Israel is part of the AS which only crops out in the southernmost part and is overlain by platform sediments towards the north. The outcrops of the

AS extend from southern Israel over Saudi Arabia to southern Yemen (Kröner et al., 1990). Basement outcrops in the southernmost part of Israel consist of politic-psammitic schists, orthogneisses, and plutonic rocks ranging from gabbro to granite (Kröner et al., 1990). The AS is known as the largest area of juvenile Neoproterozoic crust exposed worldwide (Stern and Kröner, 1993; Stern and Abdelsalam, 1998). The lithosphere beneath the APl is in general thicker (Hansen et al., 2007) and covered by sediments thickening towards the east to 10 km (Stern and Johnson, 2010). Outcrops of basement rocks are very rare, why composition of the lithosphere beneath the APl is relatively unknown.

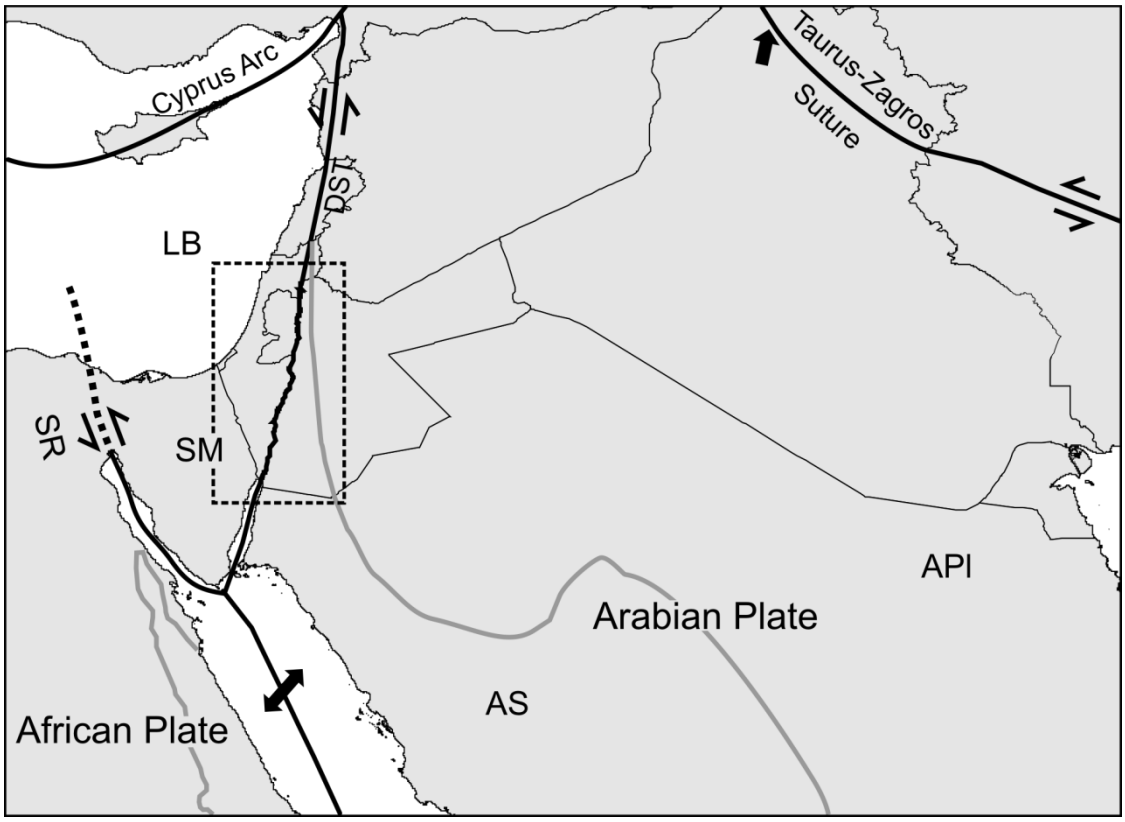

Figure 1.1: General map of the study area, dashed rectangle, and its immediate surroundings (modified from Mahmoud et al., 2005; Stern and Johnson, 2010; Johnson et al., 2011). AS – Arabian Shield, APl – Arabian Platform, , SM – Sinai Microplate, LB – Levantine Basin, DST – Dead Sea Transform, SR – Suez Rift.

1.2 Methods and database

1.2.1 Existing data in Israel

Numerous deep boreholes exist in southern and central Israel, partly drilled for oil and gas exploration and partly for water exploration. Oil exploration started in 1953 (Gill, 1992) and until today around 500 exploration and development wells have been drilled (Ministry of Energy and Water Resources: oil_and_gas_well_index). The Geological Survey of Israel owns a large digital database of the existing wells (509 oil/gas wells; 352 water wells) including coordinates, information of the lithostratigraphy and availability of core material. The data provided in this database were used in this study particularly to plan drillcore and outcrop sampling and temperature logging in the sedimentary basin. Due to data confidentiality the database is not enclosed here, however, an example of a database entry of one well is shown in the Appendix (A4). Gamma-ray logs were available for a number of wells, furthermore drill-stem-test-temperatures and for ten wells printed borehole reports. A printed borehole report containing a gamma-ray log is attached (see Appendix, A5). Drill cores of potential reservoir rocks were taken and archived by the Geological Survey of Israel. These cores are now available for research and constitute the base of sampling for this study.

TC-data of the sedimentary rocks building up the basin in southern and central Israel are scarce. Only one study treated this topic (Eckstein and Simmons, 1978). Eckstein and Simmons (1978) measured TCs of 180 drill core and loose sediment samples, most of which were limestone, sandstones, and siltstone. Drill core samples were measured with a divided bar apparatus and loose sediment samples using the needle probe. These techniques were described in detail by Birch (1950), Beck (1957) and Von Herzen and Maxwell (1959), respectively.

Eckstein and Simmons (1978) do not document the proceedings of the TC measurements in detail and present only data of measurements under dry conditions. Measurements of water-saturated TC are state-of-the-art due to the large impact of rock fluid on bulk TC. Hence the TC data are insufficient for a proper analysis of the q_s of central and southern Israel and the generation of new suitable TC data for this study was unavoidable.

1.2.1.1 Processing of existing data

The generation of new TC data required extensive sampling of the sedimentary rocks building up

the basin in southern and central Israel. In preparation of the drill core and outcrop sampling it was necessary to analyze the sedimentary succession covering the study area. Therefore lithostratigraphic reports (cf. Appendix, A4), available in the digital well database of the Geological Survey of Israel, were investigated and they constitute the base of lithostratigraphic cross sections of the area (see section 2.4). They were compiled using the software GeoDin-System 2.0. The lithostratigraphic reports give very detailed information on the lithological composition and thus had to be simplified to create more lucid lithostratigraphic-logs. This was achieved by geological interpretation; main lithologies were condensed into dominant lithological units and secondary components were neglected. For the lithostratigraphic cross sections only the deepest wells were considered, in total eleven wells (see Figure 2.3 and 2.4).

To quantify the fraction of heat of the q_S generated within the sedimentary veneer it is necessary to determine the radiogenic heat produced by the sediments themself. No data about the RHP of the sedimentary rocks in central and southern Israel exist so far. Gamma-ray logging performed by the mining industry is a suitable basis for determining the RHP of sedimentary rocks. Thus nine gamma-ray logs of the following wells: Hazerim 1, Halutza 2, Beersheva 1, EinOfarim 1, Palmahim 1, Peta Tiqva 2, Helez 34, Paran 28 (for location see Figure 2.1) were analyzed. Two of those were only available as printed version (cf. Appendix, A5); they were digitized using the software Plot Digitizer. The determination of the amount of radiogenic heat produced in the stratigraphic units base on the equation of Bücker and Rybach (1996). The gamma-ray log data (API units) were converted to RHP in μWm^{-3} (see section 2.5 and 2.6.3). The gamma-ray logs, 400 to 4400 m deep, cover stratigraphically the Jurassic, Cretaceous and in the Coastal Plain area, also the Pliocene (Late Cenozoic).
Mean values of the RHP were calculated for all stratigraphic units and used to calculate the heat budget over the crystalline basement. For stratigraphic units without gamma-ray coverage, mean values were calculated based on information of the lithological composition and RHP values from literature (see section 2.5). For the heat budget calculation the thicknesses of stratigraphic units was determined from the Helez Deep 1A well, which penetrates the whole sedimentary succession near the Mediterranean Sea, where the sediments are close to the maximum thickness occurring in Israel.

In order to get a first indication of the temperature conditions at depth in the sedimentary basin the temperature-depth distribution was calculated for five wells. Five deep wells reaching the top of basement were chosen. Calculation based on three heat-flow scenarios and the thermal rock properties determined in this study. To compare calculated temperature profiles with measured data,

drill-stem-test-temperatures available in the archive of the Geological Survey of Israel for a number of wells, were plotted for three of the five wells (see section 2.7.2, Figure 2.11): Zohar Deep 8, Hazerim 1, and Ramon 1. The data were raised between 1958 and 1975 by different mining companies: Naphta Israel Petroleum Corp. Ltd.; Oil Exp. (Inv) Ltd.; and Lapidoth Oil Prospectors Corp. Ltd., respectively.

In order to perform the temperature logging campaigns detailed information of the logged wells were required. Printed borehole reports were accessible, partly in Hebrew (cf. Appendix, A5). These borehole reports contain information on casing, log data for some wells (gamma-ray-, resistivity-, and sonic-logs and further hydraulic conductivity and salinity data), water table and lithostratigraphy.

1.2.2 Generation of new data

1.2.2.1 Drill core and outcrop sampling

In order to perform new TC and further porosity measurements samples of the sedimentary rocks of southern Israel were needed. Sampling in the archives of the Geological Survey of Israel was planned using the information existing in the digital well database. To characterize the thermal properties of the entire sedimentary succession, rock samples of all major stratigraphic units were requested. Where no drill cores were available outcrop samples were taken. Outcrop sampling was planned with the help of local Geologists, Eyal Shalev and Hallel Lutzky (Geological Survey of Israel). Map material is available online http://www.gsi.gov.il/maps.
Sixteen wells and eight outcrop locations were sampled (Figure 1.2). The maximum depth of samples taken from the drill cores was 3582 m. The samples cover stratigraphic formations from Precambrian to Eocene with most of the samples from the Jurassic and Cretaceous. All important lithologies composing the sedimentary veneer were sampled: limestone, sandstone, shale/claystone, siltstone, marlstone, dolomite, dolomitic limestone, igneous rocks, chalk, chert, gypsum, coal and anhydrite. In total 240 samples (see Appendix, A6) were taken and shipped to the GFZ-Potsdam for further analysis. A subdivision into lithotypes and geological formations based on 234 of the samples (56 outcrop and 178 drill core samples) is shown in Table 2.1. Samples with unclear stratigraphical or lithological assignment were not considered.

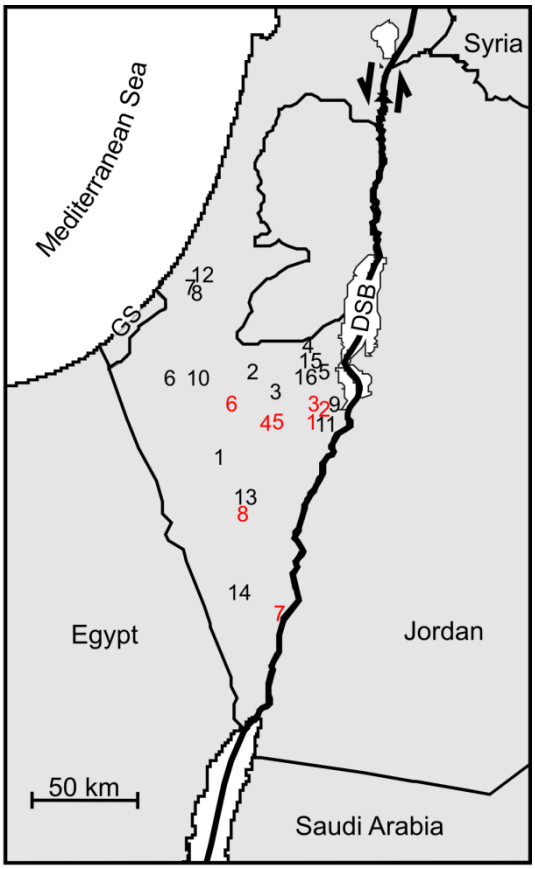

Figure 1.2: Study area with locations of sampled wells and outcrops. Black numbers mark the locations of sampled wells (see Table A6.1). Red numbers mark the locations of sampled outcrops (see Table A6.2). GS is Gaza Strip; DSB is Dead Sea Basin.

1.2.2.2 Thermal conductivity

The TC of the rock samples was measured at the GFZ-Potsdam, under dry and - for the larger part – water-saturated conditions using a TC Scanning (TCS) apparatus (Lippmann and Rauen, GbR). This apparatus is based on high-resolution optical scanning (Popov et al., 1999) (see section 2.4). For the measurements a plane surface is needed. The drill core samples, between 6 and 9 cm in diameter, were cut along the core axis and if necessary along the top/bottom surface. The outcrop samples were cut into blocks with at least 3 cm lateral length. The scanning lines were painted with black acryl lacquer. This is necessary to ensure that all surfaces have the same reflection- and absorption behavior.

1.2.2.2.1 Anisotropy and porosity

To characterize the anisotropy of the rock samples the TC was measured for the outcrop samples

parallel and perpendicular to layering or foliation, if present. TC of the drill core samples was measured on the top and bottom of the cores and parallel to the core axis either on the cut core surface or the core mantle surface (see Appendix, A6). The porosity of the rock samples was analyzed using the Archimedes method. To avoid clay swelling in clay-rich and shaly rocks saturation was carried out with isooctane instead of water (see section 2.5).

1.2.2.2.2 Thermal conductivity of lithotypes and geological formations

The complete TC data set is attached in the Appendix (A6). It contains for each sample the TC values (min, max, mean) of each scanning line and the resulting saturated mean TC value. Based on this database TC values were subdivided into lithologies and stratigraphic units (see Table 2.1). Certain ranges can be identified within and between lithologies. For seventeen different lithotypes mean TC values were determined (see Table 2.3). Especially clastic rocks, which show a remarkable range in TC values, were divided into several subtypes. Based on information of 30 wells the TC of 4 stratigraphic formations was determined as weighted mean of lithotype TCs and proportion of lithotype in % (Figure 2.8). Lithological changes in the respective stratigraphic units are therefore reflected in the resulting formation TC. This was done to understand facies-related trends in the formation TC and to evaluate the possibility of using formation TCs for the heat-flow determination (see section 2.6.2).

1.2.2.2.3 Indirect methods to determine thermal conductivity

There are various methods described in the literature to indirectly determine the TC using either data of the mineral composition, or other petrophysical properties and further the pore space and fluids. The most commonly applied methods are the empirical geometric-mean model (GM), the arithmetic-mean (AM) and harmonic-mean (HM) and less frequently the model of Hashin and Shtrikman (1962) and the effective-medium theory (see section 3.4.1). Which of the selected mixing models best describes the TC of sedimentary rocks is only insufficiently described in the literature.

The indirect determination of TC is also needed in this study. In order to analyze facies-related changes in the composition of sandstone samples and the related changes of TCs, TCs were determined indirectly based on mineralogy, porosity, and pore-filling. Furthermore the TC of lower crustal and upper mantle xenolith samples was calculated based on modal mineralogy and porosity. Choice of the best multi-component mixture model to describe the TC for this calculation was

solely based on sparse literature information. The large dataset of TCs produced in this study (Schütz et al., 2012) and further datasets of Fuchs and Förster (2010; 2013, unpublished results), Norden and Förster (2006), and Clauser (2007) allowed to conduct a validity study of the simple and usually used mixing models to better understand their accuracy and to furthermore improve the knowledge about the applicability of the models. To evaluate the reliability of the different mean models, the measured BTC was compared with the respective calculated BTC (see chapter 3).

1.2.2.3 Borehole temperature logging

In order to determine the geothermal gradient, required for the q_S determination, continuous precision temperature measurements are needed. Two temperature logging campaigns were carried out in central and southern Israel. The selection of potential boreholes based on the information accessible in the digital well database of the Geological Survey of Israel. Selecting suitable boreholes was time-consuming since a large number of boreholes had to be screened. Boreholes adequately deep (> 300 m), under thermal equilibrium, and penetrating the sufficiently sampled sedimentary units, were chosen for the temperature logging. Subsequent to the selection process dummy trips were performed in preparation of the temperature logging. Several of the originally chosen boreholes were not accessible, which additionally extended the selection process. Printed versions of borehole reports of the logged wells were available. Eleven wells were logged, however, one well showed disturbed conditions and was not considered for further analysis. The wells were logged during two campaigns, using two different logging systems. The analog, electric-line system was applied for the water-bearing parts of the borehole, whereas the Distributed Temperature Sensing (DTS) technology for the parts above the water table. The boreholes Paran 28, Notza 1, Ein Ofarim 1, Qiryat Gat 1, and Qetura 9 were logged with the conventional logging system and the boreholes Efeh 3, T.C. 1, Arad 1, Meishar 1, and Ashalim 2 with the DTS system (see section 4.5).

1.2.2.3.1 Analog, electric-line system

The analog, electric-line system was applied during the first logging campaign. It consists of a 28-mm-diameter sensor (max. temperature 80 °C, max. pressure 300 bar) and a 1,000-m-long cable (Vektor-Schlumberger-Kabel 1–10P 1/10’’). The system allows T-recordings to a precision of 0.01 °C, at a limiting accuracy of 0.1 °C. The recording interval was 0.1 m. The downward logging speed of 5.6 m min^{-1} was small enough to allow the measurement of the actual subsurface temperature without the need of subsequent deconvolutions of the records.

1.2.2.3.2 Distributed Temperature Sensing technology

Six wells with low water tables (> 260 m) were logged using the fiber-optic DTS technology during the second logging campaign. This technology is especially suited for a time-effective measurement of air-filled borehole sections (Förster et al., 1997; Wisian et al., 1998). The measurements were performed with the Sensa DTS 800 system, to which a 1,000-m-long optical sensor cable was attached. The DTS system allowed the online registration of a T-profile along the whole borehole section with an accuracy of 0.3 °C. The DTS processing mode was double ended. The total measuring time was at least two hours; the recording intervals lasted 1.4 min. Temperature data were obtained for every 1.02 m.

1.2.2.4 Heat-flow determination

The heat flow values were determined using the interval method and the Fourier equation (see section 4.5.3). For the interval method the geothermal gradient (Γ) and the TC of the selected intervals are needed. Temperature gradients were calculated on the basis of the temperature logs. The Interval TC results from the mean TC of the various lithologies and the percentage of each lithology making up the interval. Depth plots of the temperature gradient and the lithostratigraphy were produced with the software GeoDin-System 2.0 to determine suitable intervals (see Figure 4.5). To get reliable results a careful selection of the intervals for the heat-flow calulation is significant. Only the intervals, in which the change of temperature gradient could be explained by the TC, were used. In addition, preference was given to depth intervals with a relatively homogeneous lithology as indicated by the litho-log and the gradient plot. The interval heat-flow values were then used to average one mean q_S value for each of the ten wells. A detailed description of the heat-flow determination can be found in section 4.5.3.

1.2.2.5 Modeling

In order to understand the dependence of the heat flow on composition and structure of the crust and the thermal regime of the lithosphere in general a 2-D steady-state temperature model of the lithosphere was compiled. The structure of the lithosphere bases on the geological interpretation of an E–W section of the upper lithosphere derived from refraction/reflection seismic studies (Mechie et al., 2009). Additionally a second seismic section running NW–SE was used (DESERT seismic

profile; Weber et al., 2004; cf. Appendix, A2). Composition of the crustal units has been described by Förster et al. (2009) for Jordan and adapted for this study considering a homogenous crustal composition in the broader area. A temperature of 1300 °C was used as lower boundary condition which constitute the lithosphere–asthenosphere boundary (LAB). Since the position of the LAB is not surely known, different scenarios were tested (see section 4.6 and Appendix, A1). The position of the Moho is known from the seismic profiles but the lack of information of temperature and heat-flow excluded the Moho as lower boundary condition.

Thermal rock properties (TC, RHP) of the different modeling layers had to be assigned. TC of the sedimentary veneer is sufficiently known after Schütz et al. (2012). TC of the crystalline upper crustal layers correspond to those published by Förster et al. (2010). TC of the lower crust and upper mantle indirectly derive from xenolith samples. They were analyzed in terms of TC, which turned out problematic due to anomalously high porosities and variable degrees of overprinting of the xenoliths. Hence the TC values were calculated from modal mineralogy of the xenolith samples and corrected for in-situ conditions and assigned to the lower crustal and upper mantle layers of the model.

The RHP values for the sedimentary layers derive again from the study Schütz et al. (2012) and for the upper crystalline crust and the lower crust from the study Förster et al. (2010), crosschecked with further literature values. For the upper mantle values of Shaw et al. (2003) and Förster et al. (2010) were used.

The modeling considered conductive heat flow and is based on a numerical approach. The software MATLAB R2010b was used (section 4.6).

1.3 Overview of the manuscripts

Chapter	Publication/ Main goal	Journal/ Status
Chapter 2	Schütz, F., Norden, B., Förster, A., DESIRE Group Thermal properties of sediments in southern Israel: a comprehensive data set for heat flow and geothermal energy studies Main goal: Characterization of rock thermal conductivity of lithotypes scaled up for geological formations comprising the basin fill over southern Israel as basis for a better understanding of the thermal regime of the region.	Basin Research published
Chapter 3	Fuchs, S., Schütz, F., Förster, H.-J., Förster, A. Evaluation of common mixing models for calculating bulk thermal conductivity of sedimentary rocks: Correction charts and new conversion equations Main goal: The indirect determination of rock thermal conductivity with numerical models is useful when large datasets have to be handled. This study evaluates the quality of different common numerical models and offers alternative tools for bulk thermal conductivity determination. Contribution of F. Schütz: Interpretation of the data, discussion of the results	Geothermics published
Chapter 4	Schütz, F., Förster, H.-J., Förster, A. Surface heat flow and pre-Oligocene lithosphere thermal structure of the northern Sinai Microplate in Israel Main goal: The determination of new surface heat-flow values in the northern Sinai Microplate and the generation of a 2-D steady-state thermal model based on known lithosphere structure and composition.	Journal of Geodynamics under review

1.4 Author contributions

Chapter 2 Thermal properties of sediments in southern Israel: a comprehensive data set for heat flow and geothermal energy studies

I planned the research with the helpful advices of Andrea Förster and Ben Norden. I performed the sampling in the drill core archives of the Geological Survey of Israel and the outcrop sampling in the Negev. All the lab work was done by me with the help of laboratory assistances, Alexander Reichardt and David Göhring. I analyzed the data and wrote the manuscript with the help of Andrea Förster and Ben Norden.

Chapter 3 Evaluation of common mixing models for calculating bulk thermal conductivity of sedimentary rocks: correction charts and new conversion equations

The application of common mixing models was necessary during this study which raised the question of validity of the different models and therewith the idea of this paper. Planning and development of the research was done together with Sven Fuchs. Statistical analysis was done by Sven Fuchs and interpretation of the results by me. Together with Andrea Förster and Hans-Jürgen Förster we discussed and analyzed the outcomes and wrote the manuscript.

Chapter 4 Thermal conditions of the northern Sinai Microplate inferred from new surface heat-flow values and continuous borehole temperature logging in central and southern Israel

I planned the research together with Andrea Förster and Hans-Jürgen Förster. I did the temperature measurements in the Negev with the help of the technicians, Mathias Poser, Jörg Schrötter, Ronny Giese and Alexander Reichardt. The numerical modeling was done by me with the helpful advises of Ben Norden. I analyzed the data and wrote the Manuscript together with Andrea Förster and Hans-Jürgen Förster.

2 Thermal properties of sediments in southern Israel: a comprehensive data set for heat flow and geothermal energy studies

Felina Schütz, Ben Norden, Andrea Förster, DESIRE Group*

*Prof. Dr. M. Weber (GFZ-Potsdam), Prof. Dr. H.J. Götze (Univ. Kiel), Dr. S. Sobolev (GFZ-Potsdam) with Dr. G. Asch (GFZ-Potsdam), Dr. J. Klotz (GFZ-Potsdam), Dr. J. Mechie (GFZ-Potsdam), Dr. U. Meyer (BGR), Dr. O. Ritter (GFZ-Potsdam), Prof. Dr. G. Rümpker (Univ. Frankfurt/M.), Dr. H. Woith (GFZ-Potsdam), In collaboration with the Principal Investigators, Prof. Dr. Z. Ben-Avraham (Israel), Dr. K. Abu-Ayyash & Eng. J. Darwish (Jordan), Prof. Dr. R. El-Kelani (Palestine Territories)

Published in: Basin Research, 24, 357–376.

2.1 Abstract

To decipher the thermal structure of the sedimentary veneer in southern Israel, new values of thermal conductivity (TC) and porosity as well as of the radiogenic heat budget are provided.
TC is measured for lithotypes and scaled up for geological formations.
The new data are higher than most of the previously measured values, in particular for sandstones and siltstones, whose mean values are 5.0 and 2.9 W $m^{-1} K^{-1}$. Mean values of the most abundant lithotypes, which are dolomites and limestones, are on the order of 4.1 W $m^{-1} K^{-1}$ and 2.7 W $m^{-1}K^{-1}$, respectively. The total radiogenic heat production (RHP) of the sedimentary cover varies slightly over southern Israel, due to variable lithology and total sediment thickness, yielding a maximum heat flow on the order of 4 mWm^{-2}, where the sedimentary section is thickest (about 7 km). A temperature prognosis was made by calculating temperature profiles to the top of the crystalline basement at five well locations applying the new thermal-conductivity data set and three scenarios of q_S (50, 55, 60 mW m^{-2}). The calculated temperatures best match with measured drillstem-test temperatures by using heat-flow values close to the upper bound of range. Surface heat flow on the order of 55–60 mW m^{-2} is supported by a reevaluation of an existing temperature log and the application of TC from this study. The temperature prediction for southern Israel shows values of 100–120°C at 3500–4500 m depth, indicating a geothermal potential that can be used for heating as well as electricity production.

2.2 Introduction

Studies on the thermal structure of sedimentary settings imply first a delineation of the vertical temperature-depth relations, which can be extended to 2-D or 3-D thermal models. If temperature-depth profiles from borehole logging are abundant, the thermal structure of a sedimentary basin can be shown by a series of temperature maps, which are generated simply by interpolating the data. On the contrary, if temperature data are scarce the thermal structure can be numerically calculated based on a geological model. This approach allows an apprehension of temperature changes that may occur if the geological structure is complex and if rocks of different thermal properties are involved. However, to use this approach in a heat conduction domain, knowledge of the q_S and the thermal rock properties (thermal conductivity (TC), radiogenic heat production (RHP)) is essential. Likewise, data of the thermal rock properties are a prerequisite for the determination of the heat-flow density at borehole scale by combining the thermal properties with temperature data.

In this paper, the thermal properties of the sedimentary succession in southern Israel are investigated as part of the DESIRE project (http://www.gfz-potsdam.de) to form a basis on which an upcoming heat-flow study and thermal models will depend on. TC is measured of core and outcrop samples for different lithotypes and then scaled up to formation TC using information from well logs and litho-logs. RHP is determined for geological formations and scaled up for the entire sedimentary succession taking its lateral thickness change into account. Finally, the new data on thermal rock properties are used (I) exemplarily in conjunction with a temperature log (Eckstein and Simmons, 1978) to discuss the need for revising the q_S for southern Israel and (II) to provide geotherms for the sedimentary succession that can be used in exploration for geothermal energy.

2.3 Geological setting

Southern Israel, located at the western edge of the Arabo-Nubian Shield (ANS) is part of the southern Levantine Basin (Figure 2.1). The ANS was formed during the Pan-African Orogenic Cycle, about 1,000–530 Ma ago. The shield originated from the suturing of juvenile intra-oceanic arc terrains followed by magmatic thickening, giving rise to regional metamorphism and the generation of batholiths of predominantly granitic to granodioritic composition. Various structures of the ANS constitute fossil fragments of a Neoproterozoic Wilson cycle, representing opening and closure of an ocean basin that occurred between older crustal blocks of east and west Gondwanaland (Kröner et al., 1990; Stern, 1994). Volcanic and metamorphic rocks of late Precambrian age are exposed on outcrop only in the southernmost part of Israel, in the Timna Park, and the Eilat Complex.

From Cambrian to Paleogene times, the area was a stable platform owing to its position as a passive continental margin, and an extensive veneer of sediments was accumulated. The Levantine Basin has evolved through long and complicated processes which started in the late Triassic–early Jurassic times (Garfunkel and Derin, 1984; Ben-Avraham, 1989; Robertson et al., 1996). The platform history was interrupted by a period of faulting and magmatism related to shaping the Levant continental margin in the early Mesozoic, by intraplate magmatism in the early Cretaceous, and by mild folding and shearing in late Cretaceous to Miocene times (Garfunkel, 1988; and references therein).

During Miocene to Pliocene times, continental break up started with the extrusion of mafic volcanic rocks related to the opening of the Red Sea at about 30 Ma and the activity of the Afar mantle plume (Wilson et al., 2000). The Dead Sea Transform (DST) was activated 14–18 Ma ago after the initiation of rifting along the Red Sea and is attributed to lithosphere thinning owing to

asthenosphere upwelling, possibly involving a mantle-plume component (Camp and Roobol, 1992; Shaw et al., 2003; Krienitz et al., 2007; and references therein). Today the DST extends from the Red Sea spreading centre to the Zagros zone of plate convergence.

During the platform stage, several periods of major erosion interrupted the sediment deposition. The pre-Permian unconformity was the result of the 'Helez' uplift, which caused a substantial stack of Paleozoic sediments to be eroded. The Permian-Triassic disconformity, expressed by the hiatus of the lower part of the Triassic, separates the late Paleozoic Negev Group from the Triassic Ramon Group. The Triassic-Jurassic unconformity forms the boundary between the Ramon Group and the overlying Jurassic Arad Group (Hirsch, 2005a). The Jurassic paleotectonic setting is characterized by relative lows and highs, controlled by differential rates of subsidence. In the latest Jurassic and earliest Cretaceous times the area bordering the Eastern Mediterranean basin was affected by a phase of uplift and extensive erosion, therefore sediments of this age are missing (Gvirtzman and Garfunkel, 1998). During the Cretaceous, several regional events of erosion occurred resulting in unconformities which caused the separation of the Cretaceous into three stratigraphic groups: Kurnub, Judea and Mount Scopus Groups. With the beginning of the Alpidic faulting at the end of late Cretaceous, syntectonic deposition dominates until the end of the Paleogene. During late Oligocene regional uplift and erosion started contemporaneously with the opening of the Red Sea (Hirsch, 2005a).

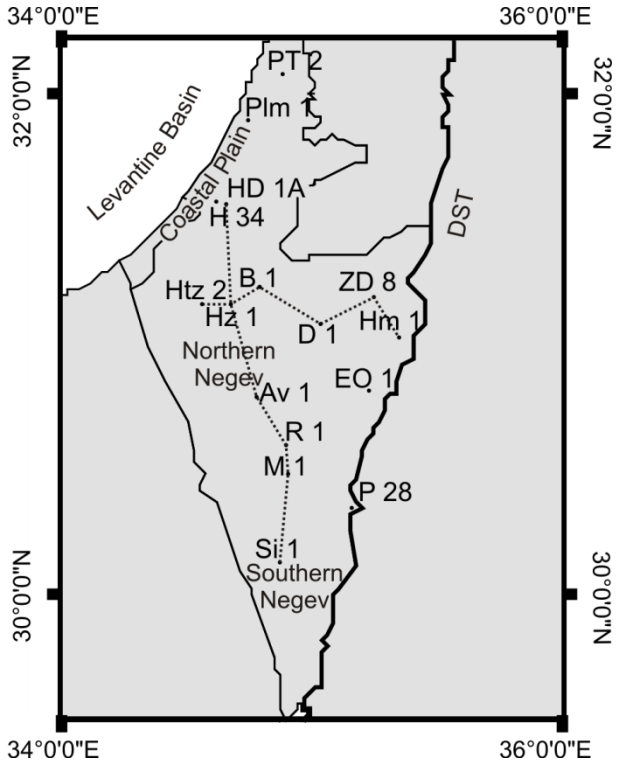

Figure 2.1: Study area with the location of the Dead Sea Transform (DST) and of boreholes reported in this study. Wells with analyzed gamma-ray logs: Hz 1-Hazerim 1, Htz 2-Halutza 2, B 1-Beersheva 1, EO 1-EinOfarim 1, Plm 1-

Palmahim 1, PT 2-Peta Tiqva 2, H 34-Helez 34, P 28-Paran 28. Well used for the heat budget calculation from gamma-ray logs: HD 1A-Helez Deep 1A. Well used for surface heat-flow calculation: D 1-Daya 1. Dotted lines show the position of the lithostratigraphic sections shown in Figure 2.3 and 4: Av 1-Avdat 1, R 1-Ramon 1, M 1-Meishar 1, Si 1-Sinaf 1, ZD 8-Zohar Deep 8 wells.

2.4 Stratigraphy and lithology

In the following, the Permian to Paleogene sedimentary succession is described stratigraphically (Figure 2.2) and lithologically (Figure 2.3, 2.4) from the oldest to youngest groups.

Sinaf Group:

The Precambrian Zenifim Formation, building up the Sinaf Group, consists of red to dark brown massive fine to coarse grained arkose. The arkose sequence is associated with extrusive igneous rocks (dolerite, rhyodacite and andesite) and it overlies the igneous basement (Weissbrod, 2005). In the Ramon 1 well (Figure 2.4) the formation is 2014 m thick which approximate the total thickness.

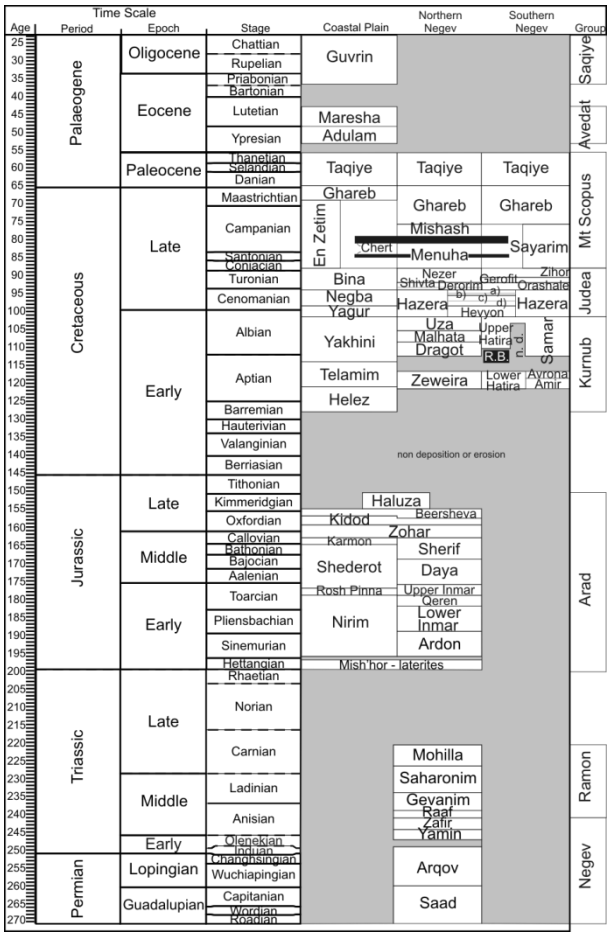

Figure 2.2: Chronostratigraphy of the Permian to Palaeogene in southern Israel (modified after Gvirtzman, 2004). R.B. is Ramon Basalt, n.d. is non deposition, a) Tamar, b) Avnon, c) En Yorqeam, d) Zafit.

Negev Group:

The Permian Sa'ad Formation overlaying the Precambrian Zenifim Formation forms the basis of the Negev Group. It is composed of fluviatile to deltaic sandstones. A few layers of limestone and dolomite interrupt the dominating fluviatile environment. The overlying Arqov Formation consists of alternating sandstone, shale and limestone. The Triassic Yamin Formation consists of dolomitic sandstone and limestone. The carbonate content in this formation varies largely across the Negev area. The overlying Zafir Formation is composed of calcareous and pyritic shales and sandy, glauconitic or dolomitic limestone (Weissbrod, 2005). The whole Negev Group is represented in the Zohar Deep 8 well (Figure 2.3).

Ramon Group:

The Triassic Ra'af Formation, making up the basis of the Ramon Group, is mainly composed of limestone and dolomite, rich in fossils, claystone and chalk.

The Gevanim Formation, overlying the Ra'af Formation, contains fluviatile sandstones, dark grey shale and limestone. The Saharonim Formation is a carbonate sequence with some shale, marlstone and evaporite intercalations. The Mohilla Formation at the top of the Ramon Group is mainly composed of dolomite and minor shale and gypsum (Benjamini et al., 2005). Towards the south the thickness of the Ramon increase to about 600 m (Ramon 1 well, Figure 2.4) farther south the Ramon Group is truncated by the base Cretaceous unconformity.

Arad Group:

The Mish'hor laterite constitutes the basis of the Jurassic Arad Group. The Mish'hor laterites are overlain by the Ardon Formation, which is composed of carbonates, shales and evaporates and thickens towards the Coastal Plain area to several hundred meters (Helez Deep 1A well, Figure 2.4). Fluviatile clastics characterize the overlying Inmar Formation. These are cross-bedded sandstones separated into two clastic units, the Lower and Upper Inmar intercalated by the marine Qeren Formation. The overlying Daya Formation contains carbonates and clastic rocks. Paralic clastic rocks and marlstone are typical for the Sherif Formation in southern Israel. These rocks are covered by a homogeneous sequence of limestones, shale and marlstone building up the Zohar Formation (Hirsch, 2005b). The Kidod Formation is predominantly composed of shale; its thickness increases progressively north-eastward. The Beersheva Formation and Haluza Formation consist primarily of limestone, dolomite, marlstone, shale and of subordinate sandstone. The Haluza Formation however is enriched in shale (Weinberger et al., 1991). In general, the Arad Group is of relatively homogeneous composition across southern Israel.

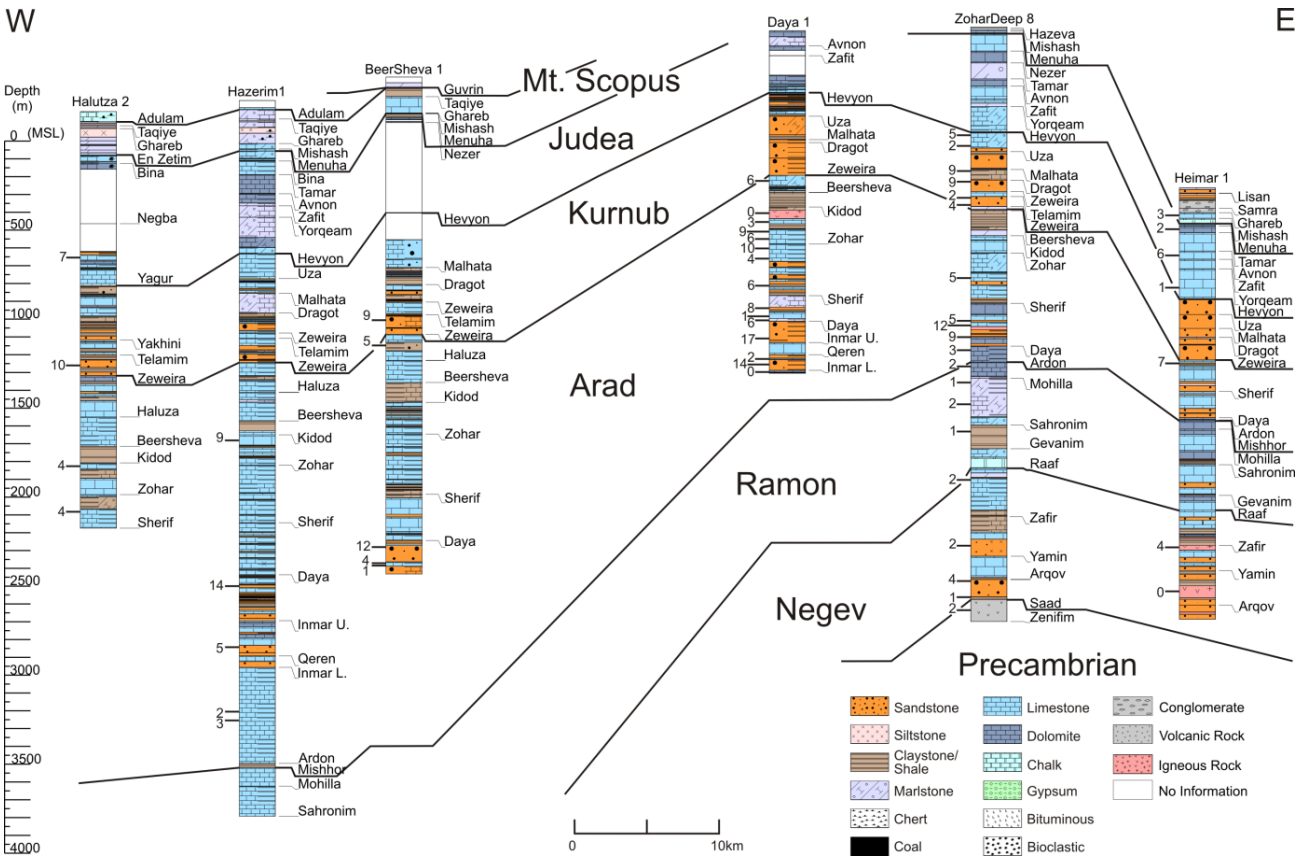

Figure 2.3: Lithostratigraphic E-W cross section of the Negev area based on boreholes shown in Figure 2.1. Numbers attached to columns indicate sampling depth for TC and porosity measurements on drill core and values of porosity (in %).

Kurnub Group:

The Kurnub Group, consisting mostly of terrestrial deposits and marine intercalations, includes all beds between the Jurassic marine Arad Group and the Middle Cretaceous marine Judea Group. In the southern part of the Negev, the Kurnub Group lies directly on the early Palaeozoic Nubian sandstone (Sinaf 1 well, Figure 2.4). The Jurassic here is completely eroded. The composition of the formations building up the Kurnub Group changes from the southern Negev to the central and northern Negev and to the Coastal Plain area; therefore different stratigraphic nomenclatures are used. The Amir, Avrona and Samar Formations occur only in the southernmost part of the Negev. They consist of quartzarenite, sandstone and siltstone. The Hatira Formation composed of very fine to coarse-grained and moderately to well-sorted quartzarenite, cross-bedded on a large scale and in minor amounts argillaceous sandstone, conglomerate and bioturbated siltstone, occurs only in the southern Negev. It is subdivided into the Lower and Upper Hatira Formation separated by the Ramon basalt. In the northern Negev, the Lower Cretaceous section is subdivided into the marine intercalations Zeweira, Dragot, Malhata and Uza. They consist of very fine to fine grained sandstone, siltstone and mudstone with limestone ledges, dolomite and marlstone (Lewy, 1990;

Weissbrod, 1993). The Helez and Telamin Formations occurring in the Coastal Plain area are overlain by the carbonatic Yakhini Formation. The Helez Formation is mainly composed of interbedded limestone and shale and minor amounts of sandstone and dolomite. In contrast, the Telamim Formation is mainly sandy-calcareous and exhibits some coral-stromatopora-rudist-reefs (Rosenfeld and Hirsch, 2005b).

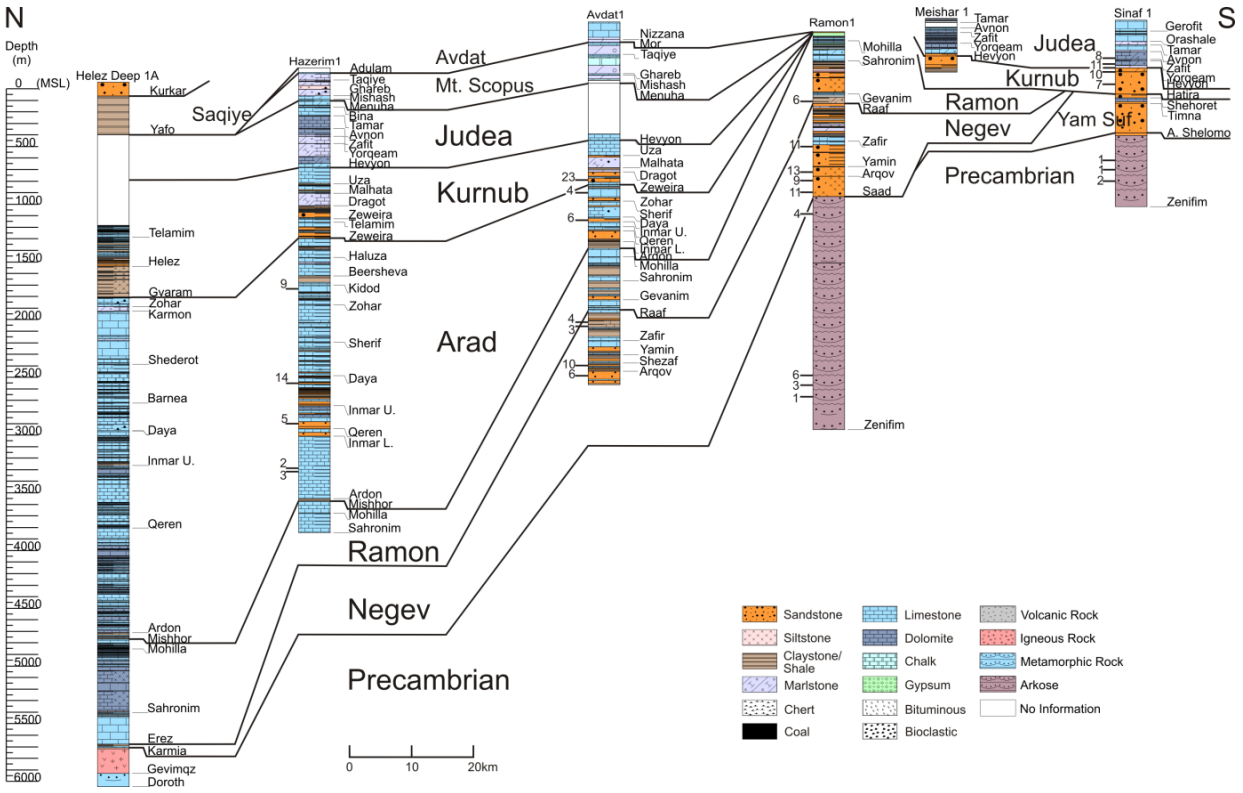

Figure 2.4: Lithostratigraphic N-S cross section of the Negev area based on boreholes shown in Figure 2.1. Numbers attached to columns indicate sampling depth for TC and porosity measurements on drill core and values of porosity (in %).

Judea Group:

The Judea Group is a rather homogeneous carbonate sequence due to the large thickness and good exposure over wide areas of Israel it is subdivided into several formations. The lowermost formation is the Hazera Formation, which is subdivided into five members: Hevyon, En Yorqeam, Zafit, Avnon and Tamar (Hazerim 1 well, Figure 2.3). Glauconitic-dolomite, sandy dolomite and dolomite build up the Hevyon Member in the basal parts merging upwards into sandstone with dolomite. In the uppermost beds chert nodules occur. The En Yorqeam Member is composed of fossiliferous marlstone, argillaceous limestone and dolomite. The overlying Zafit Member mostly consists of limestone interbedded with marlstone (Rosenfeld and Hirsch, 2005b). The Avnon

Member contains chalk, marlstone and nodular limestone and in the upper parts massive and bedded dolomite (Buchbinder et al., 2000). The Tamar Member forms a hard unit that consists of brown-yellow dolomite, dolomitic limestone and limestone alternating with marlstone.
In the Coastal Plain area, the Hazera Formation passes into the Yagur and Negba Formations. The Yagur Formation forms a sequence of dolomites at least 350 m thick, interbedded with limestone, sandstone, marlstone and chalk. The overlying Negba Formation can be subdivided into a lower member, comprising dolomite with marlstone intercalations and an upper member encompassing more marlstone interbedded with dolomite and limestone (Rosenfeld and Hirsch, 2005b).

In the southern Negev, the Hazera Formation is overlain by the Orashale, Gerofit and Zihor Formations (Sinaf 1 well, Figure 2.4). The Orashale Formation can be divided into a lower, mainly shaly member with numerous gypsum veins, a middle member containing limestone, argillaceous limestone, marlstone, shale and dolomite and an upper member composed of red and green shale, massive gypsum beds, glauconitic dolomite and sandstone. The Orashale Formation thins towards the north; north of the Ramon structure the upper part of the formation is missing. The Gerofit Formation is a sequence of massive well-bedded limestone and dolomite with oolites and fragmented fossils and minor amounts of shale and marlstone (Bartov et al., 1972, Rosenfeld and Hirsch, 2005b). Soft yellowish dolomite, marlstone, argillaceous and frequently fossiliferous limestone built up the overlying Zihor Formation in the south. In the north, the formation consists of chalky limestone and bioclastic limestone. The Derorim Formation overlying the Hazera in the northern Negev consists mainly of marlstone with some chalk and limestone. These rocks pass laterally into the limestones and calcarenites of the cliff-forming Shivta Formation (Braun and Hirsch, 1994). The Nezer Formation shows well-bedded hard limestone with quartz granules, crystals and chert concretions at the top of the formation. A few soft marlstone and chalk beds as well as dolomite beds occur. The equivalent of these three formations in the Coastal Plain area, the Bina Formation, is mainly composed of limestone. Only in the lower parts of the formation some dolomite and chert concretions occur (Rosenfeld and Hirsch, 2005b).

Mt. Scopus Group:
In the northern Negev, the mostly chalky and marly Mt. Scopus Group is subdivided into the Menuha, Mishash, Ghareb and Taqiye Formations (Beersheva 1 well, Figure 2.3). In the southern Negev, the Menuha and Mishash Formations are treated as one unit, the Say'yarim Formation. In the Coastal Plain area, the En Zetim Formation replaces the Menuha and Mishash Formations (Halutza 2 well, Figure 2.3) (Gvirtzman, 2004).

The Menuha Formation unconformably overlies the Judea Group. It consists of a marine, predominantly chalky sequence which is subdivided into two members. The lower one consists of limonitic chalk and the upper one of soft white chalk and marlstone, respectively. The transition to the Mishash Formation is characterized by the first occurrence of flint layers. The Mishash Formation is composed of calcareous, oolitic, phosphate layers alternating with phosphatic chalk, marlstone and limestone. The proportion of chert, as well as of phophorites increases upwards, reaching its maximum in a laminated chert member. The En Zetim Formation contains white chalk and marly chalk and is sometimes bituminous. The Say'yarim Formation in the southern Negev consists of alternating soft chalks and harder units of sandstone, shale, dolomite, limestone and chert. The Ghareb Formation overlying the Mishash, En Zetim or Say'yarim Formations occurs over most of the Negev. It encompasses limonitic marly chalk with pyrite and phosphate nodules and in some areas black oil-shale and bituminous marlstone (Rosenfeld and Hirsch, 2005b). The Taqiye Formation covers the Ghareb Formation. Its base is defined by the first occurrence of green shales. The shales gradually pass upwards into argillaceous chalks and chalky limestone (Bartov, 1972).

Avedat Group:
The Adulam Formation forms the basis of the Avedat Group and is composed of chalk and silicified chalk with thin chert horizons and chert nodules (Halutza 2 well, Figure 2.3). The overlying Maresha Formation contains globigerinid chalks (Rosenfeld and Hirsch, 2005a).

Saqiye Group:
The Saqiye Group is extensively developed in the Coastal Plain area but is missing in the southern Negev. It consists of the Bet Guvrin Formation composed of chalky marlstone and limestone (Hirsch, 2005c) and the Yafo Formation which is mainly made up of clay (Helez Deep 1A, Figure 2.4).

2.5 Analysis

Sediment samples for laboratory measurements were obtained in the drill core archive of the Geological Survey of Israel. Most samples pertain to the Jurassic and Cretaceous (Aptian to Turonian) section. Minor samples were obtained from Paleozoic to Triassic and Precambrian formations and from formations of Paleocene to late Eocene age. The lithostratigraphic information of 9 of the 16 sampled wells is shown in Figure 2.3 and 2.4. To overcome the lack of core samples

from the shallower formations, samples were also collected from outcrops, mostly from the Turonian to Paleocene section.

In total, 234 samples were obtained for TC and porosity measurements. With respect to rock type, 75 samples pertain to limestone, which also is the most frequent lithology in southern Israel, 46 samples pertain to sandstone, 32 samples to shale/claystone, 18 to siltstone, 16 to marlstone, 15 to dolomite, 14 to dolomitic limestone, 6 to igneous rocks, 5 to chalk, 3 to chert, 2 to gypsum, 1 to coal and to anhydrite, respectively.

TC was measured with the TC Scanning (TCS) apparatus (Lippmann and Rauen, GbR), which is based on high-resolution optical scanning (Popov et al., 1999). The error of determination is less than 3%. The samples were measured dry and, except for claystones, also water-saturated. The given water-saturated bulk thermal conductivity (BTC) values of claystone and shale were calculated using equation (2.1) and (2.2).

The effective porosity was quantified for all samples by the mass change between dry and water-saturated samples (Archimedes method). Because of clay swelling effects, these rocks were saturated with isooctane (density 0.69 g cm^{-3}) instead of water. In addition, porosity of selected shale samples was measured by Helium pycnometry.

In order to investigate the effect of mineral composition on measured BTC, the TC of the rock matrix was calculated for different lithotypes using the geometric mean model (Woodside and Messmer, 1961):

$$\lambda geo = \lambda m^{1-\phi} \cdot \lambda p^{\phi} \tag{2.1}$$

$$\lambda m = \left(\frac{\lambda sat}{\lambda p^{\phi}}\right)^{\frac{1}{1-\phi}} \tag{2.2}$$

where λgeo is the TC according to the geometric mean; λm is the TC of the rock matrix; λp is the TC of the pore fluid, ϕ is porosity, and λsat is the saturated BTC.

For sandstones, the matrix thermal conductivity (MTC) obtained from measurements was compared with respective values calculated from the major mineral constituents using the geometric, the arithmetic and the harmonic mean model (Voigt, 1928; Reuss, 1929; Horai and Simmons, 1969; Somerton, 1992). The arithmetic mean equation reproduced the measured values at best:

$$\lambda m_{ari} = \sum_{i=1}^{n} Vi \cdot \lambda i \tag{2.3}$$

$$\lambda sat_{ari} = (1-\phi) \cdot \lambda m_{ari} + \phi \cdot \lambda p \tag{2.4}$$

where λi is the TC, Vi is the volume fraction of the i-th mineral phase, λp is the TC of the pore fluid, and ϕ is porosity.

The modal mineralogy of sandstone samples was analyzed in thin sections by estimating the percentages of individual minerals.

TC was measured for lithotypes and then was upscaled to values for geologic formations by summing up the individual lithotype values multiplied by thickness. The proportions of lithotypes in each formation were obtained from lithological descriptions of cores available in the archives of the Geological Survey of Israel.

The radioactive heat generation in the sedimentary succession was determined from total gamma-ray logs, available from nine wells (Figure 2.1), using the equation of Bücker and Rybach (1996). The equation uses a linear relationship between natural total gamma-ray logs (GR) in API units and laboratory measured RHP A in μWm^{-3}.

$$A = 0.0158\,(\mathrm{GR[API]} - 0.8) \tag{2.5}$$

Heat production of stratigraphic units was calculated by averaging values over respective depth intervals. By multiplying the arithmetic mean with the thickness of the stratigraphic unit the heat flow produced in each unit was determined.

Surface heat flow q_S ($mW\,m^{-2}$) was recalculated for one borehole location (the Daya 1 well, Eckstein and Simmons, 1978, Figure 2.1) using the interval method (e.g., Powell et al., 1988) and the Fourier equation of heat conduction:

$$qs = -\lambda \frac{\partial T}{\partial z} \tag{2.6}$$

where λ is the TC (in $W\,m^{-1}\,K^{-1}$) and $\partial T/\partial z$ is the temperature gradient (in $°C\,km^{-1}$). The intervals for the calculation were selected from a depth plot of interval temperature gradients calculated from a continuous temperature log. The Daya 1 temperature log has a temperature recording interval of 10 m; hence the temperature gradients were calculated over 10-m depth intervals. No exponential smoothing was applied to the data. The log shows no signs of temperature perturbation due to fluid flow thus reflecting heat conduction conditions.

2.6 Results

2.6.1 Thermal conductivity of lithotypes

The water-saturated BTC differs considerably between and within lithotypes (major lithotypes are listed in Table 2.1) as indicated by the range and mean of values. Highest TC is observed for chert (5.1 W $m^{-1} K^{-1}$), sandstone (3.0–6.6 W $m^{-1} K^{-1}$), anhydrite (5.0 W $m^{-1} K^{-1}$) and dolomite (3.8–5.2 W $m^{-1} K^{-1}$), moderate values for siltstone (2.4–3.4 W $m^{-1} K^{-1}$), igneous rocks (2.3–3.2 W $m^{-1} K^{-1}$), dolomitic limestone (2.5–3.1 W $m^{-1} K^{-1}$), limestone (2.0–3.2 W $m^{-1} K^{-1}$), and marlstone (2.0–2.8 W $m^{-1} K^{-1}$), and lowest values for claystone/shale (1.6–2.2 W $m^{-1} K^{-1}$), chalk (1.2–2.0 W $m^{-1} K^{-1}$), gypsum (1.3 W $m^{-1} K^{-1}$) and coal (0.6 W $m^{-1} K^{-1}$), respectively.

While the variability of TC is small for claystone and moderate for siltstone and carbonates, it is particularly large for sandstone. The smaller range of values for limestones can be explained with a relatively homogeneous composition of this lithotype. In general, the limestone values vary due to different amounts of dolomite, sand or argillaceous rock components. The effect of different porosity (0.2–14.4%) is due to the low mean value of 6.0% less striking. The large diversity in saturated BTC observed for sandstones (3.2–6.6, mean 5.0 W $m^{-1} K^{-1}$, Table 2.1) is, to a large extent, an expression of both variable modal mineralogy of the samples causing MTC values of 4.2–7.8 W $m^{-1} K^{-1}$(Table 2.2) and variable porosity. The effect of sandstone porosity (3.7–23.0%) is larger than those of limestones indicated by a larger mean value (8.0%).

The sandstones can be classified either as quartzarenites and carbonatic sandstones or as argillaceous sandstones. The detrital component mainly consists of quartz and minor amounts of rock fragments and feldspar. Polycrystalline quartz and chert assemble the rock fragments. The grain-grain contacts of the lithics point to a magmatic origin. Calcite mainly constitutes the authigenic component. Dolomite, anhydrite, clay and gypsum are subordinate cement minerals, and quartz and iron oxide occur only sporadically.

For example, the Sinaf-1_04 and Sinaf-1_07 samples, relating to the Hatira Formation, (Table 2.2) are typical argillaceous sandstones with 31–37% authigenic clay and quartz and feldspar as detrital component. Both the saturated as well as the MTC are accordingly low.

Table 2.1: Range and mean λ value ($Wm^{-1}K^{-1}$) of the measured TC of water-saturated rocks from

Lithology		**Dolomite**				**Limestone**				**Dol Ls**				**Marlstone**			
Gr.	**Fm.**	range	m	n	Φ	range	m	n	Φ	range	m	n	Φ	range	m	n	Φ
Mt. Scop.																	
C.Plain/ N./S. Negev	Taqiye																
	Ghareb													*2.1–2.2*	*2.2*	*2*	*16*
N./S. Negev	Mishash		*4.9*	*1*	*3*												
	Menuha																
Judea																	
C. Plain/ N. Negev	Negba					2.3–2.6	2.4	2	8								
	Yagur	3.8–4.3	4	3	4	2.5–3.1	2.8	9	5	2.9-3.1	3.0	2	3		2.8	1	7
N. Negev	Nezer					*2.6–2.7*	*2.7*	*3*	*8*								
	Shivta					*2.8–3.1*	*2.9*	*3*		*2.8–3.1*	*2.9*	*3*	*3*				
N./S. Negev	Tamar		*4.6*	*1*	*1*	2.1–3.2	2.9	5	8		*2.9*	*1*	*1*	*2.0–2.6*	*2.4*	*3*	*5*
	Avnon					*3.0–3.1*	*3.0*	*2*	*8*	*3.0-3.1*	*3.1*	*2*	*6*		*2.3*	*1*	*8*
	Zafit	4.0–5.2	4.7	3	6									2.3–2.8	2.5	3	13
	En Yorq.													*2.3–2.4*	*2.3*	*2*	*9*
	Hevyon		*3.8*	*1*	*10*	2.0–3.2	2.6	3	10	*2.8–3.2*	*3.0*	*2*	*14*				
S. Negev	Zihor					*2.6–2.7*	*2.7*	*5*	*6*								
	Gerofit						*2.5*	*1*	*14*						*2.3*	*1*	*21*
	Orashale						*2.5*	*1*	*5*								
Kurnub																	
C. Plain/ N. Negev	Yakhini					2.1–2.9	2.5	5	8	2.5–2.8	2.6	3	3		2.6	1	9
	Telamin					2.6–2.8	2.7	2	4								
	Helez		3.7	1	5	2.1–3.2	2.8	7	7								
N. Negev	Uza		4.0	1	5		2.7	1	2								
	Malhata																
	Dragot																
	Zeweira																
S. Negev	U. Hatira		3.6	1	7												
	L. Hatira																
	Samar																
Arad																	
C. Plain/ N. Negev	Haluza																
	B.–Sheva					2.6–2.7	2.7	2	6								
	Kidod														2.3	1	4
	Zohar					2.2–2.6	2.4	10	5								
N. Negev	Sherif	3.7–4.1	3.9	3	6	2.3–2.9	2.5	4	3		3.2	1	10				
	Daya					2.3–3.2	2.7	6	3								
	U. Inmar																
	Qeren																
	L. Inmar																
	Ardon					2.6–2.8	2.7	3	2								
Ramon																	
N. Negev	Mohilla																
	Saharonim																
	Gevanim						2.7	1	1								
	Raaf																
Negev																	
N. Negev	Zafir														1.9	1	1
	Yamin																
	Arqov																
	Saad																
Sinaf	Zenifim																
mean		λ	4.1	Φ	5	λ	2.7	Φ	5.9	λ	3.0	Φ	6	λ	2.4	Φ	9

m marks the mean and n the number of measured samples. The mean porosity (Φ) is given in %. No values are

the Sinaf, Negev, Ramon, Arad, Kurnub, Judea and Mt. Scopus Groups subdivided into lithotypes.

Claystone				**Shale**				**Sandstone**				**Siltstone**				**Chalk**			
range	m	n	Φ	range	m	n	Φ	range	m	n	Φ	range	m	n	Φ	range	m	n	Φ
1.7–1.9	*1.8*	*5*	*20*	*1.7–2.2*	*2.0*	*5*	*19*												
																1.2–1.3	*1.3*	*2*	*15*
																1.8–2.0	*1.9*	*2*	*26*
																	2.1	*1*	*18*
	2.0	1	8																
	2.0	*1*	*12*		*2.0*	*1*	*13*												
				1.6–1.8	*1.7*	*4*	*5*												
	1.9	1	12																
1.6–1.9	1.7	3	7					4.3–4.8	4.6	2	4								
									4.2	1	6								
	1.7	1	9																
	2.1	1	9																
	2.1	1	9					5.1–5.7	5.4	2	6		2.4	1	4				
									5.1	2	6	3.2–3.4	3.3	2	7				
1.6–1.7	1.7	2	10																
									5.1	*1*	*15*								
													2.8	1	5				
	2.1	1	9																
1.9–2.2	2.1	2	6						4.8	1	23								
								4.4–4.6	4.5	3	7	2.4–2.7	2.6	4	10				
	1.9	1	6					3.7–6.2	5.2	4	4	2.6–3.1	2.8	4	7				
								4.3–6.6	5.4	5	9								
									5.1	1	5								
								3.2–5.1	4.4	4	9		2.9	1	2				
	1.9	1	3										3.2	1	3				
													3.4	1	2				
													2.7	1	1				
	2.1	1	10										2.7	1	3				
									5.9	1	11								
									4.9	1	13		3.4	1	10				
								4.6–6.6	6	7	5								
								2.3–3.3	3.0	11	4								
λ	1.9	Φ	9	λ	1.9	Φ	12	λ	4.9	Φ	8	λ	2.9	Φ	5	λ	1.8	Φ	20

available for the Avedat Group and Saqiye Group. Outcrop samples are in italics. Dol Ls-dolomitic limestone.

The carbonatic sandstone (Zohar-1_5 sample, Zeweira Formation) displays 67% detrital components consisting mainly of quartz (95%) and of minor amounts of rock fragments (5%). Calcite constitutes basically the authigenic component besides minor iron-oxide and clay. The MTC is higher (6.1 W $m^{-1} K^{-1}$) than in the first samples. Also the saturated BTC is comparable high (5.7 W $m^{-1} K^{-1}$) due to a low porosity. The second carbonatic sandstone sample (Hltza-2_03, Zeweira Formation) shows comparable properties.

Table 2.2: Measured (saturated λ_{sat} and matrix λm) and calculated (from modal mineralogy) thermal conductivity of sandstones.

			measured													calculated	
Stratigraphic		Sample	Depth	λ_{sat}	λm	ϕ	modal mineralogy (volume fraction, *Vi*):									λsat_{ari}	λm_{ari}
Group	Fm.		(m)	($Wm^{-1}K^{-1}$)		(%)	qtz	fsp	cal	dol	hem	anh	gp	sme	org. m.	($Wm^{-1}K^{-1}$)	
Kurnub	Hatira	Sinaf-1_04	447.7	3.5	4.2	10.3	0.47	0.22						0.31		4.3	4.7
	Hatira	Sinaf-1_07	494.6	4.2	4.8	6.5	0.53	0.10						0.37		4.7	5.0
	Zeweira	Zohar-1_05	954.7	5.7	6.1	4.0	0.67		0.23		0.05			0.05		6.4	6.6
	Zeweira	Hltza-2_03	1431.2	5.1	6.5	10.1	0.68	0.02	0.18		0.12					6.6	7.3
Arad	Inmar	Daya-1_20	1639.8	6.6	7.2	3.7	0.70			0.09		0.15	0.06			6.4	6.6
	Upper	Daya-1_23	1736.5	5.0	7.8	17.7	0.95		0.05							6.3	7.5
	Inmar	Daya-1_27	1876.3	4.9	7.8	17.9	0.95			0.05						6.3	7.6
	Lower	Daya-1_28	1905.6	4.5	6.4	14.5	0.90		0.05		0.01				0.04	6.2	7.2

Thermal conductivity of minerals (λi) used in the calculation of bulk and matrix λ (λsat_{ari}; λm_{ari}) : quartz 7.7 $Wm^{-1}K^{-1}$; feldspar 2.3 $Wm^{-1}K^{-1}$; calcite 3.6 $Wm^{-1}K^{-1}$; dolomite 4.7 $Wm^{-1}K^{-1}$; iron oxide (hematite) 11.3 $Wm^{-1}K^{-1}$, anhydrite 4.8 $Wm^{-1}K^{-1}$, gypsum 1.3 $Wm^{-1}K^{-1}$, smectite 1.9 $Wm^{-1}K^{-1}$, organic matter 0.3 $Wm^{-1}K^{-1}$ (Horai, 1971; Schön, 1996).

The Daya-1_20 sandstone sample (Upper Inmar Formation) displays the highest saturated BTC (6.6 W $m^{-1} K^{-1}$ at a porosity of 3.7%) as well as the highest MTC (7.2 W $m^{-1} K^{-1}$). The detrital component accounts for 70% of the rock matrix and is composed of quartz. The authigenic mineralogy is dominated by anhydrite; dolomite and gypsum are minor.

The pore filling minerals show a poikilitic texture (Figure 2.5a). Due to the presence of anhydrite and gypsum the sample can be characterized as evaporitic sandstone.

Typical quartzarenites are the Daya-1_23 (Upper Inmar Formation), Daya-1_27 and _28 samples (Lower Inmar Formation). In the Daya-1_28 sandstone sample the fine-grained detrital component makes up about 90% of the rock matrix. The major detrital component is quartz. Authigenic calcite can be identified, and black organic material is present along root channels. Although the quartz content is higher compared to the Daya-1_20 sample (Table 2.2), the saturated BTC and MTCs are lower. This can be explained by the presence of calcite cement, whose TC might be on the order of 3.6 $Wm^{-1}K^{-1}$ (Horai, 1971), and by the grain size of the detrital component, which here is smaller (Figure 2.5b) than in the Daya-1_20 sample. The Daya-1_27 sample comprises about 95% detrital component, basically consisting of quartz (85%) and minor amounts of rock fragment (15%). Due to the occurrence of polycrystalline quartz, the sample is classified as a quartzarenite. It has a calcite cementation and the highest porosity of all analyzed samples (17.9%), which results in a relatively

low saturated BTC (4.9 W m^{-1} K^{-1}) and a high MTC (7.8 W m^{-1} K^{-1}). The same applies to the fine-grained Daya-1_23 sandstone sample, which has a saturated BTC of 5.0 W m^{-1} K^{-1}, and a high MTC of 7.8 W m^{-1} K^{-1}. The detrital component of this sample consists of subrounded, moderately sorted quartz grains and lithics, probably from magmatic rocks. The authigenic component comprises two generations of cementation: first quartz overgrowth on the detrital grains and also as pore filling material and secondly calcite. In addition to the calcite matrix also idiomorphic calcite crystals appear. The detrital component covers 90% of the sample in which the lithics make up around 10%.

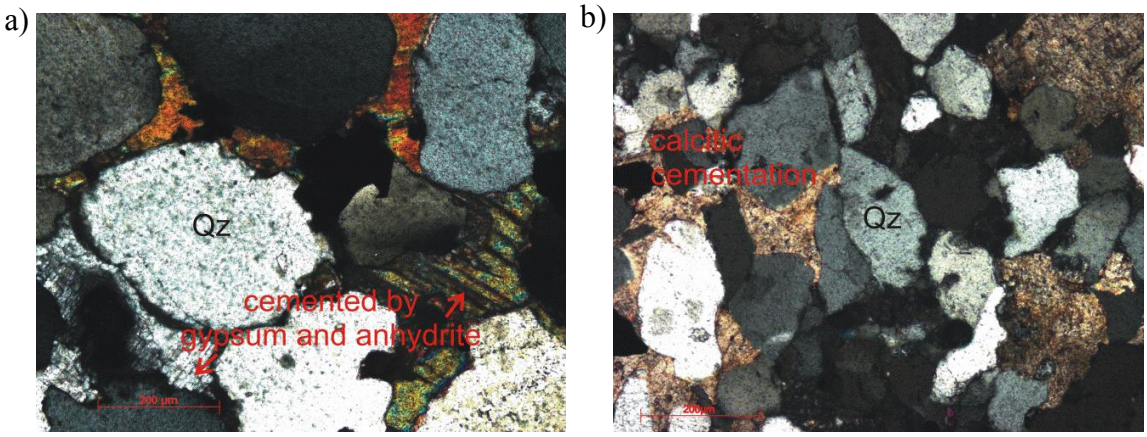

Figure 2.5: Thin section images of different sandstone types. (a) Sandstone with dolomite, anhydrite and gypsum cementation resulting in a TC of 6.6 $Wm^{-1}K^{-1}$; (b) sandstone with a calcareous cementation resulting in a TC of 4.6 $Wm^{-1}K^{-1}$.

To crosscheck the measured thermal conductivities, respective values were calculated based on the percentage of mineral constituents and porosity (Table 2.2, equation 2.3, 2.4). Comparison of measured and calculated saturated BTC shows a difference of 1.0 W m^{-1} K^{-1} on average with a range of 0.2–1.7 W m^{-1} K^{-1}. Comparison of the MTCs reveals a smaller range (0.2–0.8 W m^{-1} K^{-1}) with an average value of 0.5 W m^{-1} K^{-1}. The discrepancy is caused, on the one hand, by the determination of the percentage of mineral constituents and, on the other hand, by the choice of mineral TC from the literature. For example, there is large uncertainty in published quartz TC ranging from 6.5 to 13.0 W m^{-1} K^{-1} (Schön, 1996). MTC of 7.8 W m^{-1} K^{-1} measured on Daya-1_23 and Daya-1_27 sandstones, reflecting a multi-mineral assemblage including also minerals with a TC lower than quartz, suggests that the quartz value (7.7 W m^{-1} K^{-1}; Horai, 1971) used in the calculation is too low to reproduce the measured MTC.

In summary, the mean measured MTC of quartzarenite is, as expected, the highest (7.3 W m^{-1} K^{-1})

followed by the carbonatic sandstone value (6.3 W m^{-1} K^{-1}) and the argillaceous sandstone value (4.5 W m^{-1} K^{-1}). Figure 2.6 shows for two lithotypes the impact of pore fluid (air versus water) on the measured BTC. The increase of ratio with increasing porosity indicates that the type of pore fill does influence the BTC especially at porosity values >5%. The anisotropy between the TC measured parallel and perpendicular to bedding ($\lambda\parallel / \lambda\perp$) is in general nonexistent or small (<1.2). Most samples scatter around a ratio of 1.0.

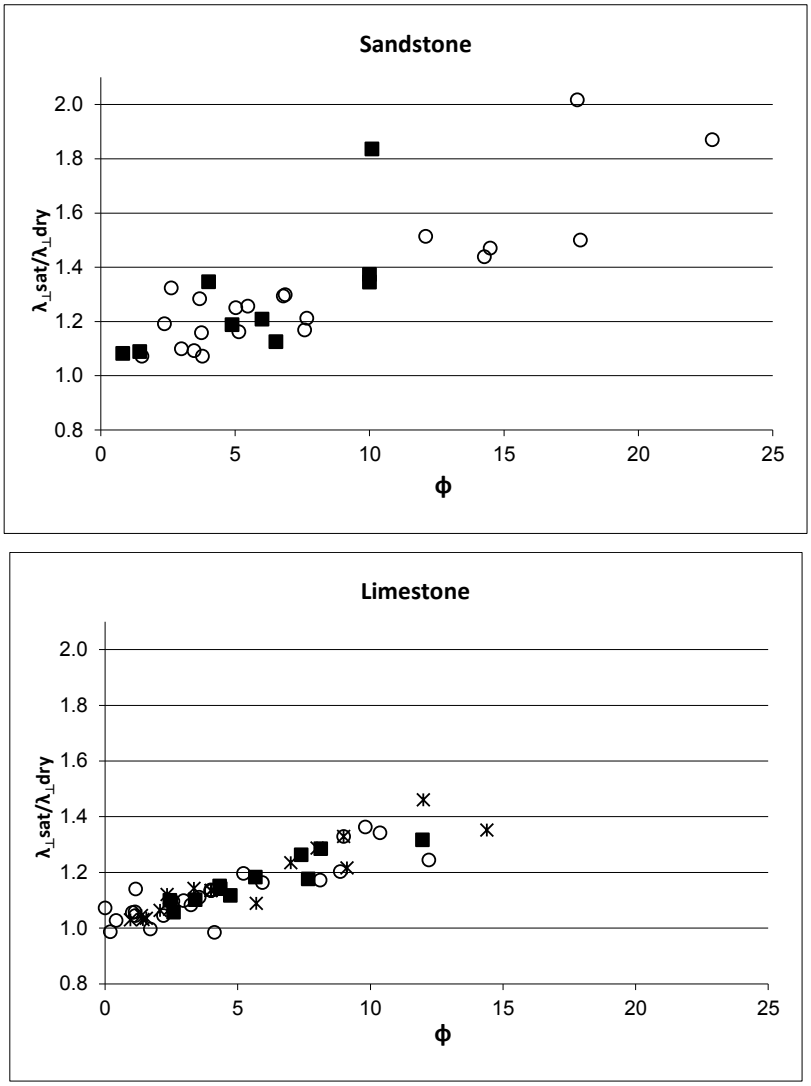

Figure 2.6: Ratio of water-saturated and dry measured TC cross plotted versus porosity (in %). (a) sandstone samples, (b) limestone samples. ○ Arad Group, ■ Kurnub Group, ✳ Judea Group.

2.6.2 Thermal conductivity of geological formations

The stratigraphic chart applied in this study for southern Israel is predominantly based upon chronostratigraphic and biostratigraphic information and to a minor extent upon the lithologic

composition of the different units. Consequently, it needed to be investigated whether mean formation thermal conductivities for southern Israel, determined from the sampled rock, would represent the subsurface geology and could be universally applied in geothermal studies. For this purpose, 30 well sections (Figure 2.7) were analyzed with respect to variable formation lithology resulting from facies changes that occur from the western to the eastern Negev as well as on a small regional scale. Figure 2.8 shows, exemplarily for four formations, the change across the area of individual lithotypes making up the formation together with the resulting formation TC. The latter was calculated as a weighted mean on the basis of lithotype TC (Table 2.3) according to:

$$\bar{x} = \frac{\sum_i^n t_i \cdot \lambda_i}{\sum_i^n t_i} \tag{2.7}$$

where λ is the TC of the lithotype and t is the proportion of lithotype in (%).

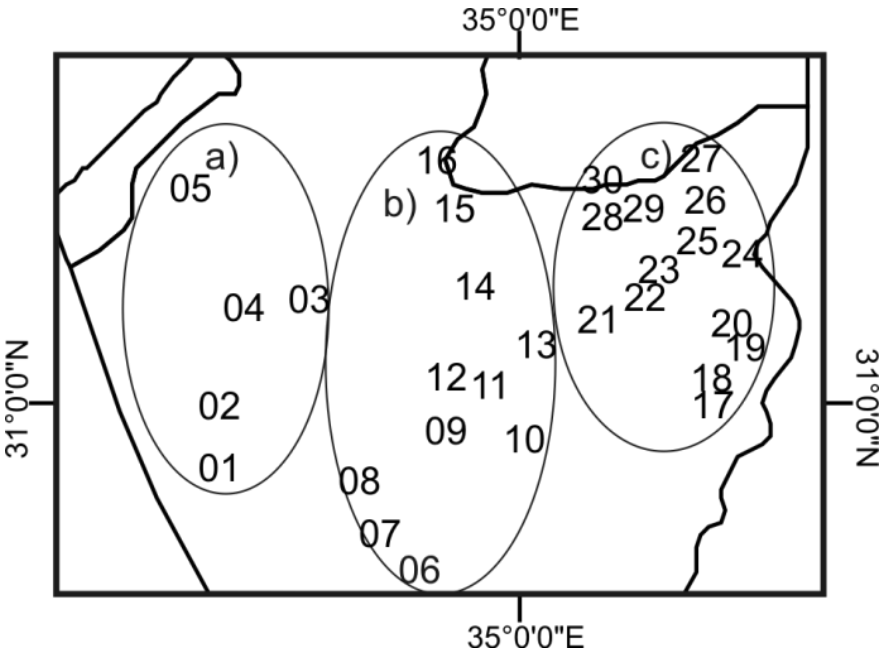

Figure 2.7: Wells from which lithostratigraphic information was used to characterize changes in composition and thickness of the stratigraphic formations across southern Israel. a) Western Negev, b) Central Negev, c) Eastern Negev. Numbers denote well IDs as used in Figure 2.8.

All four formations show a remarkable change in mean TC across the studied area. TC of the Ardon Formation (Arad Group), composed of limestone, dolomite and shale, has a range of 2.7–4.1 W m^{-1} K^{-1} (mean 3.2 W m^{-1} K^{-1}) and those of the Sherif Formation (Arad Group), mainly composed of limestone and shale, of 2.2–3.9 W m^{-1} K^{-1} (mean 2.9 W m^{-1} K^{-1}). For the latter, values are highest in sections partly comprised of sandstone. The Zeweira Formation (Kurnub Group), made up of

sandstone and shale, shows a TC of 2.8–5.3 W m^{-1} K^{-1} (mean 3.9 W m^{-1} K^{-1}) depending on the dominating rock type.

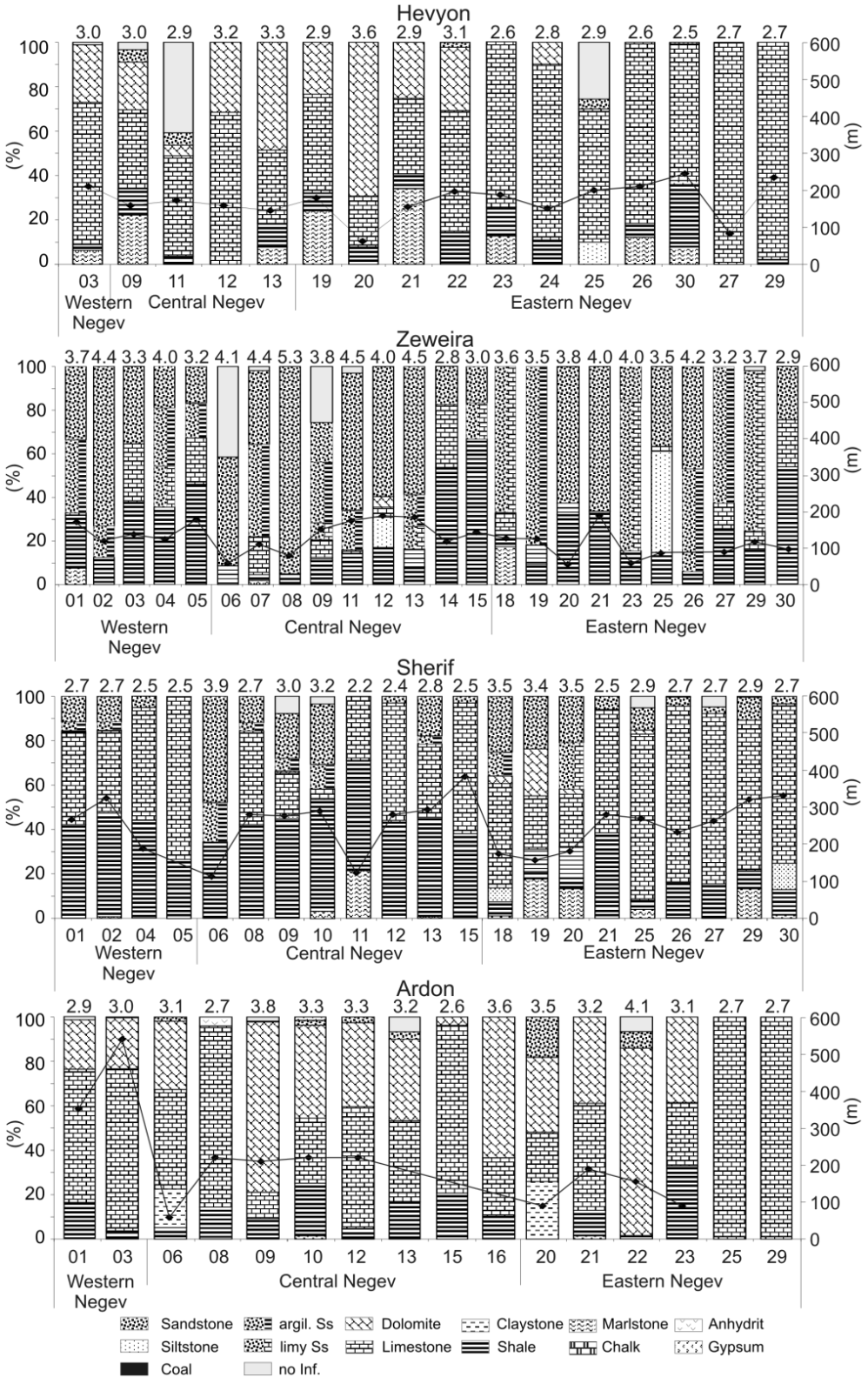

Figure 2.8: Changes in lithology (in %) between wells exemplarily shown for the Ardon, Zeweira, Sherif and Hevyon Formations in the northern Negev. Numbers below the bars are the well IDs as used in Figure 2.7. The curve plotted across the bars shows the changes in formation thickness (in m). Numbers above the bars indicate the TC ($Wm^{-1}K^{-1}$)

calculated from the percentages of the respective lithotypes in each well. argil. Ss-argillaceous Sandstone; limy Ss-limy Sandstone; no Inf.-no Information.

Table 2.3: The mean TC (m) of lithotypes determined in this study (saturated rocks) and as comparison determined by Eckstein and Simmons (1978, denoted with E & S).

λ this study			**λ E & S study**		
Lithology	**n**	**m ($Wm^{-1}K^{-1}$)**	**Lithology**	**n**	**m ($Wm^{-1}K^{-1}$)**
Dolomite	15	4.1	Dolomite	24	3.8
Limestone	75	2.7	Limestone	58	2.2
Dol Ls	14	3.0	Dol Ls	*18*	3.1
Marlstone	16	2.4	Limy Sh	*2*	1.3
Claystone	22	1.9	Shale	*4*	1.1
Shale	10	1.9	Marl and Chalk	4	1.8
Sandstone	16	5.6		*12*	1.3
carb. Ss	8	4.9	Ss and Siltstone	29	2.8
argil. Ss	11	3.6		*27*	2.2
Arkose	11	3.0			
Siltstone	18	2.9			
Chalk	5	1.8			
Gypsum	2	1.3			
Anhydrit	1	5.0			
Chert	3	5.1			
Coal	1	0.6			
Igneous	6	2.4			

Numbers in italics indicate measurements on cuttings. n is numbers of samples. Dol Ls-dolomitic limestone, Sh-shale, carb. Ss- carbonatic sandstone, argil. Ss-argillaceous sandstone, Igneous-igneous rock.

The Hevyon Formation (mostly carbonates, Judea Group) displays a TC of 2.5–3.6 W m^{-1} K^{-1} (mean 2.9 W m^{-1} K^{-1}). The values are highest where the dolomite dominates over limestone. Altogether a highly variable TC is observed within the formations indicating that the application of a regionally undifferentiated average formation TC would cause a false quantification of this parameter.

2.6.3 Radiogenic heat production and heat budget of the sedimentary veneer

To get an overall understanding of the q_S in a sedimentary basin and the temperature gradient, the amount of heat generated by the sediments themselves is an important component, which needs to be quantified. Especially clastic sediments can provide a substantial proportion of the q_S where sediment basins are deep.

The gamma logs used for heat-production calculation cover stratigraphically the Jurassic and Cretaceous and, in the Coastal Plain area, also the Pliocene (Cenozoic). Table 2.4 lists the results for stratigraphic formations observed at 9 well locations. It is obvious that the mean values do not

exceed 1.4 μW m^{-3} and that the majority of values is <1.0 μW m^{-3}. The lowest values are observed in carbonates as for example in the Shederot Formation (mostly argillaceous limestone) and the Yaqum Formation (limestone). Slightly higher is the value in formations of mixed lithology, as for example the Malhata Formation (sandstone, shale and limestone) or the Kidod Formation (shale and marlstone). The highest values pertain to formations composed of bituminous shales and phosphate-rich sediments (e.g., formations of the Mt. Scopus Group). Mean values calculated for the main stratigraphic groups show only small differences. The Saqyie and Mt. Scopus Formations display values of 0.9 μW m^{-3}, the Kurnub Formation of 0.7 μW m^{-3} and the Judea and Arad Formations of 0.5 μW m^{-3}, respectively.

The RHP of Table 2.4 then was used to calculate the heat budget (heat flow) for each stratigraphic group and finally for the entire sedimentary section above the crystalline basement. For stratigraphic units older than the Jurassic, for which no well logs were available, lithotype values from the literature (Vila et al., 2010 and references therein) were applied as follows: carbonates 0.4 μW m^{-3}, sandstone-wackestone 0.9 μW m^{-3}, and mudrocks 1.4 μW m^{-3}.

Table 2.4: RHP (range and mean value in µW m^{-3}) of stratigraphic formations from nine wells. The mean is

Well ID	PT 2		Plm 1		H 34		Htz 2	
Saqiye Gr.		**mean 0.9 µWm^{-3}**						
Yafo			0.6–1.7	1.3				
Afiq			0.4–1.5	1.1				
Mavqim			0.2–1.4	0.5				
B.–Guvrin			0.1–1.8	0.9				
Mt. Scopus Gr.		**mean 0.9 µWm^{-3}**						
Ghareb								
Mishash								
Menuha								
En Zetim							0.3–0.9	0.5
Judea Gr.		**mean 0.5 µWm^{-3}**						
Bina	0.1–0.5	0.3					0.2–0.4	0.3
Negba	0.0–1.6	0.4					0.2–0.7	0.3
Yagur	0.1–1.8	0.4			0.5–1.8	0.8	0.2–1.5	0.5
Talme-Yafe					0.7–1.2	0.9		
Zihor								
Nezer								
Shivta								
Gerofit								
Orashale								
Derorim								
Tamar								
Avnon								
Zafit								
Yorqeam								
Hevyon								
Kurnub Gr.		**mean 0.7 µWm^{-3}**						
Yakhini	0.0–1.3	0.4			0.7–1.0	0.8	0.2–1.4	0.7
Yaqum	0.4–0.9	0.5	0.1–1.9	0.6				
Uza								
Malhata								
Dragot								
Zeweira							0.4–1.2	0.8
Telamim	0.2–1.6	0.3	0.0–2.2	0.4	0.6–1.0	0.8	0.3–1.0	0.6
Zeweira								
Arad Gr.		**mean 0.5 µWm^{-3}**						
Haluza								
Beersheva			0.0–2.4	0.4				
Kidod			0.1–1.8	0.9				
Nir'am	0.2–1.0	0.4						
Zohar	0.1–0.6	0.3	0.1–1.7	0.3				
Karmon	0.4–1.0	0.8	0.2–1.4	0.4				
Shederot	0.2–1.2	0.3	0.2–0.8	0.3				

calculated by averaging values over respective depth intervals. For location of wells see Figure 2.1.

Hz 1		B 1		Daya 1		EO 15		Paran 28	
0.9–2.2	1.4							0.2–2.6	1.3
0.5–1.1	0.6	0.8–1.3	1.1					0.4–2.6	1.2
0.3–0.7	0.5	0.6–1.0	0.7					0.4–2.5	1.1
0.1–0.4	0.2								
								0.2–0.7	0.4
		0.0–0.9	0.3			0.2–1.0	0.3		
						0.1–1.3	0.2		
								0.2–1.4	0.4
								0.2–1.4	0.7
						0.3–1.5	0.6		
0.3–0.9	0.5	0.8–0.1	0.5			0.4–1.6	0.8		
0.2–0.9	0.5			0.2–0.4	0.3	0.1–1.6	0.4	0.4–1.6	1.0
0.2–0.9	0.4	2.0–0.2	0.6	0.2–0.4	0.3	0.3–1.3	0.6	0.4–1.1	0.5
0.3–0.8	0.6			0.2–0.5	0.3	0.3–1.0	0.5		
0.2–1.9	0.6			0.2–1.1	0.5	0.2–1.7	0.6		
0.2–1.5	0.6			0.2–1.7	0.8				
0.3–1.9	0.9			0.2–1.7	0.9				
0.3–1.5	0.6			0.4–1.5	0.9				
0.1–1.7	0.8			0.2–1.7	0.6				
0.4–1.1	0.7								
0.2–1.9	0.7								
0.2–1.4	0.6								
				0.2–0.8	0.4				
				0.3–1.0	0.8				
				0.3–0.8	0.4				

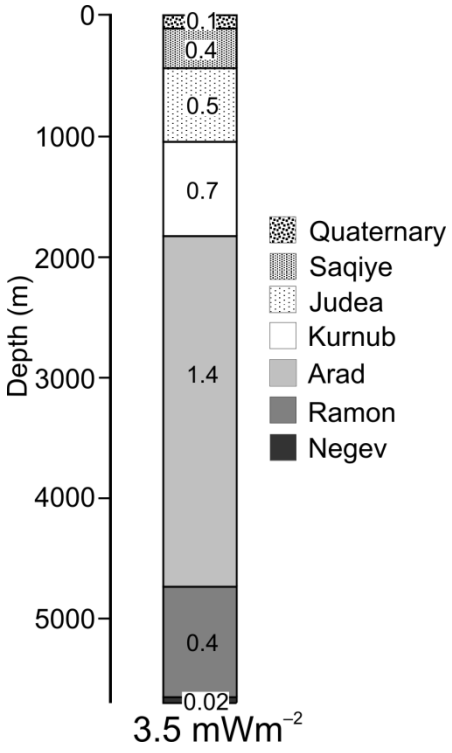

Figure 2.9: Generated heat (mW m^{-2}) of the stratigraphic groups contributes to q_S in the 5.8-km-thick sedimentary veneer of the Coastal Plain area. The thicknesses of stratigraphic groups are from the Helez Deep 1A well.

Figure 2.9 shows the results for the Helez Deep 1A well (Figure 2.1), which penetrates the whole sedimentary sequence down about 5800 m, which is close to the basement. The section generates a heat flow of 3.5 mW m^{-2}. However, it can be expected that the total heat production and hence the heat flow generated in the sediments varies slightly across southern Israel due to variable lithology and due to changes in total sediment thickness. For example, the sedimentary cover overlying the crystalline basement thins towards the outcrops of basement rocks in the northern Golf of Elat and the Timna area. To the north-west, the sedimentary cover thickens up to about 7 km (Rybakov and Segev, 2004) providing a maximum heat-flow component in the sediments of 4.2 mW m^{-2}, if geological data from the Helez Deep 1A well are extrapolated to the area.

2.7 Discussion

2.7.1 Implication for the determination of surface heat flow

As part of a reconnaissance heat-flow study conducted for Israel, TC of sedimentary rocks was measured with a divided bar apparatus on drill core samples and with a needle probe on cutting samples (Eckstein and Simmons, 1978). The data represent measurements under dry conditions only. If the Eckstein and Simmons data summarized for particular lithotypes (Table 2.3) are compared with the data of this study (also Table 2.3), it becomes obvious that the new data are higher than most previous values. This can be expected taking the different measuring conditions (dry versus saturated) into account. Only the values of dolomitic limestone are similar in the two data sets, probably because of the low porosity of this rock type and thus less difference between water-saturated and dry TC measurements. Some lithotype values in the two data sets are difficult to compare, because Eckstein and Simmons merged data of chalk and marlstone on the one hand and of sandstone and siltstone on the other hand to two single groups. However, the sandstone/siltstone group has values that are lower than the sandstone values determined in this study. They rather represent values typical for siltstone.

The effect that the application of the new TC data has on calculated heat-flow density is exemplarily shown for the Daya 1 well location (Figure 2.10) reported by Eckstein and Simmons (1978). Table 2.5 lists depth intervals, interval temperature gradients, major lithology and interval TC used in the previous study in addition to TC from this work. The new thermal-conductivity values were applied taking into consideration the location of water table. Thus thermal conductivities for dry rocks were assigned to intervals above the water table and values for saturated rocks (Table 2.3) below the water table, respectively.

The resulting new interval heat-flow values are generally higher than previous values. The increase is especially large in the interval 350–440 m, for which an unrealistically high value on the order of 84 mW m^{-2}, opposed to 53 mW m^{-2}, would result, if the interval is considered as a pure sandstone interval and the saturated TC value is applied. Another outlier of the trend is the small subinterval 360–370 m selected by Eckstein and Simmons, for which the interval heat flow remains low (46 mW m^{-2}) even after applying the new TC data for siltstone. We interpret the low temperature gradient as arbitrary being an artifact of the large temperature recording interval (10 m). In a refined new approach, we modified the selection of depth intervals for heat flow by better honoring the lithological changes in the lithostratigraphic section (Figure 2.10). Consequently, the three new intervals also honor better the temperature gradient pattern in the borehole. In addition, the new approach uses for each interval a TC that originates from the percentages of different sublithotypes making up the depth interval instead of using a single default lithotype TC (Table 2.5).

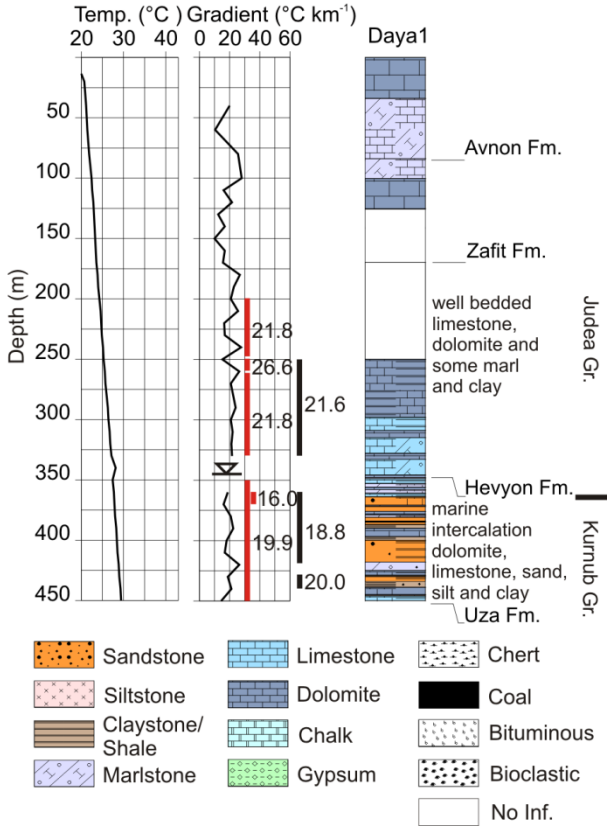

Figure 2.10: Heat flow determined in the Daya 1 well, based on a temperature log from Eckstein and Simmons (1978). Temperature and temperature gradient plots are shown together with a lithostratigraphic section. Blank intervals in the section indicate no information. Lines in gradient plots mark intervals of gradient calculation. Numbers attached are the calculated interval temperature gradients (°C km^{-1}). Black lines are the intervals used in this study; red lines mark the intervals used by Eckstein and Simmons (1978). Depth of water table (triangle) is shown.

The resulting heat-flow values again are consistently higher than the previous ones, varying from 52 to 62 mW m^{-2} (mean 57 mW m^{-2}). In addition, the values show less diversity than the previous interval values. The new mean heat flow is in contrast to the original mean value of 48 mW m^{-2} (Eckstein and Simmons, 1978) determined in the Daya 1 well. The new heat-flow value is even more in contrast to what is regarded by these authors as most reliable value for the site (about 37 mW m^{-2}).

Table 2.5: Geothermal data of the Daya 1 borehole.

Well Daya 1												
E and S study					**this study**		**new approach**					
Interval	**Γ**	**Lith.**	**λ**	**q**	**λ**	**q**	**Interval**	**Γ**	**Lith.**		**λ**	**q**
(m)	(°Ckm^{-1})		(Wm^{-1}K^{-1})	(mW m^{-2})	(Wm^{-1}K^{-1})	(mW m^{-2})	(m)	(°Ckm^{-1})		(%)	(Wm^{-1}K^{-1})	(mW m^{-2})
200–250	21.8	Ls	2.1	46.7	2.4	52.3	250–330	21.6	Dol	24.5	2.4	51.8
250–260	26.6	M	1.3	34.6	2.1	55.9			Dol Ls	12.0		
260–330	21.8	Ls	2.1	46.7	2.4	52.3			Ls	33.0		
350-440	19.9	Ss	2.7	52.9	4.2	83.6			Sh	22.7		
360–370	16.0	Si	2.2	34.9	2.9	46.4			M	7.8		
							360-410	18.8	argil. Ss	31.8	3.3	61.9
									carb. Ss	6.3		
									Dol	23.8		
									M	14.3		
									Cl	14.3		
									Ls	7.1		
									Coal	2.4		
							430-440	20.0	argil. Ss	50.0	2.9	58.0
									Cl	50.0		
											mean	**57.3 ± 4**

Results from Eckstein and Simmons (1978, E and S) are compared with results from this study using the same depth intervals and interval temperature gradients (Γ), but different TC (λ) and with data from a new approach using different depth intervals of gradient and heat-flow calculation together with a more detailed lithology for λ of the interval. Heat-flow density (q, in bold) is the mean value with 1σ-standard deviation. Abbreviated lithology Dol-Dolomite, Ls-Limestone, Sh-Shale, M-Marl, Cl-Clay and as in Table 2.4.

In general, a revisit of the q_S of southern Israel, reflecting crustal conductive heat flow, is desirable. Such a study, focused on an exclusion of hydrological perturbation of heat flow, could also investigate whether there is a regional trend of changes in q_S according to changes in crustal structure and composition.

2.7.2 Implication for the utilization of geothermal energy

The temperature and the hydraulic rock properties at depth are major parameters on which the type of utilization of geothermal energy depends. High porosity/permeability of geologic formations allow for a hydrothermal use of geothermal energy, whereas low porosity/permeability requires a

conditioning of the target rocks to enhance its hydraulic performance. These so-called Engineered or Enhanced Geothermal Systems (EGS) would allow, if successfully generated, a universal heat mining not only including tight sedimentary formations but also igneous or magmatic rocks beneath a sedimentary basin.

The porosity data measured in this study in conjunction with TC show for southern Israel individual sedimentary formations of high porosity but yet unknown temperature range. It is therefore desirable to delineate on a regional scale the temperature conditions at depth. The new data on thermal rock properties and qs presented in this study can be used to calculate temperature for depths beyond logging data and beyond temperature data available from drill-stem testing.

We followed this approach by calculating temperature (T) at depth (z) using the Fourier equation (2.6) as follows:

$$T_z = T_s + z\frac{q_s}{\lambda} \tag{2.8}$$

where T_s (°C) is the surface temperature, λ (W m^{-1} K^{-1}) the TC, and q_s (mW m^{-2}) the surface heat flow.

Considering the TC of stratigraphic formations, calculated by taking the proportion of different rock types into account, empirical temperature profiles are calculated for five well locations (shown in Figures 2.3 and 2.4), by summing the results of the incremental temperature calculations across individual layers of uniform conductivity:

$$T_z = T_s + \sum_i^n \left[(z_i \frac{q_s}{\lambda_i})\right] \tag{2.9}$$

Where T_s (°C) and q_s (mW m^{-2}) are the temperature and heat flow at the surface, z_i is the thickness of unit i and λ_i (W m^{-1} K^{-1}) is the TC of unit i. An annual average surface temperature of 20 °C and three different values of qS (50, 55, 60 mW m^{-2}) are used.

The temperature profiles are calculated to the top of basement (Figure 2.11). Four of the boreholes reach the basement between 1613 and 6093 m. The section of the 4019-m-deep Hazerim 1 well, which bottoms in the Ramon Group, is extended to the basement (at 4800 m depth) using the lithostratigraphic data from Gvirtzman (2004). In addition, temperatures from drill-stem tests obtained in the archives of the Geological Survey of Israel were plotted.

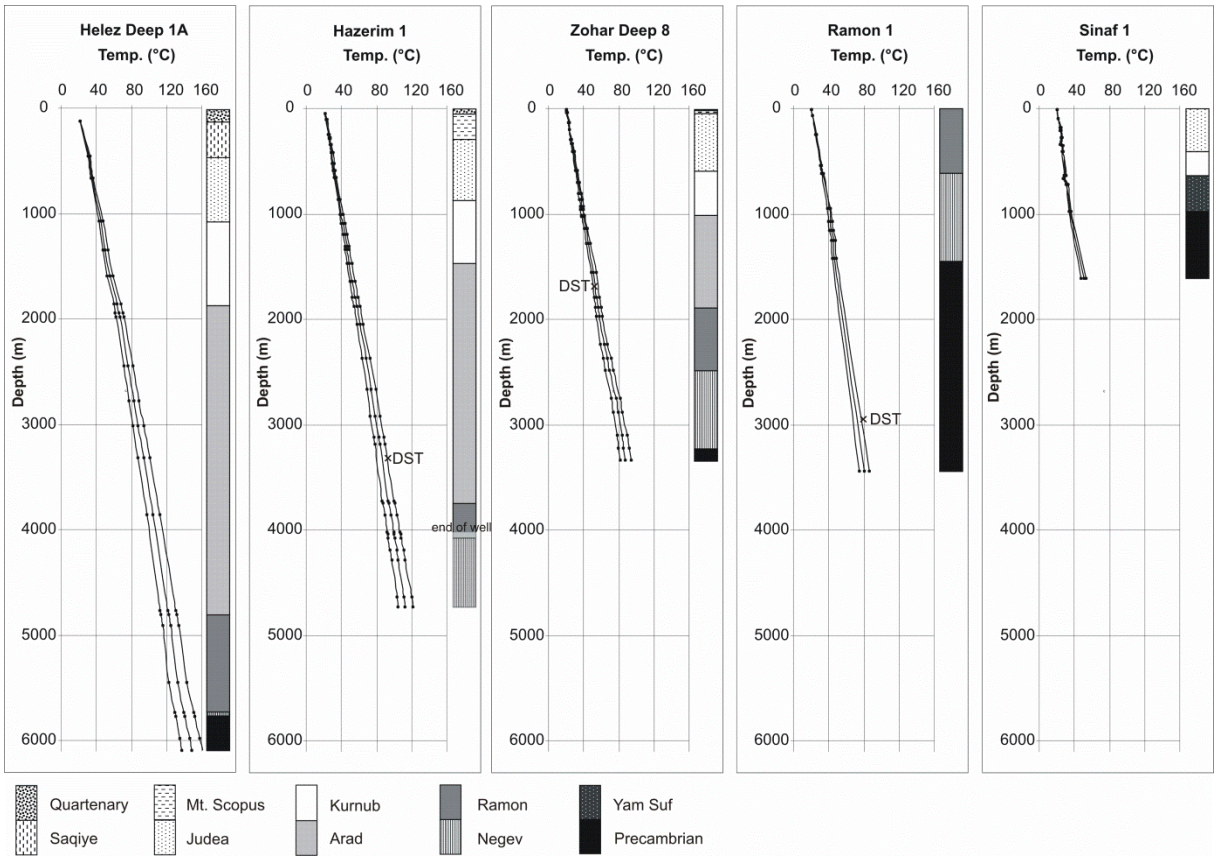

Figure 2.11: Geotherms calculated for three heat-flow scenarios (50, 55, 60 mW m^{-2}) for wells reaching the basement. For the location of the wells see Figure 2.1.

It is obvious that the geotherms based on the 55 and 60 mW m^{-2} best approximate the measured individual temperature drill-stem-test data. All logs show some gradient breaks due to different TC and thickness changes of individual geological formations. Therefore, different temperatures are prognosed at a fixed depth. For example, at 3 km, the 60 mW m^{-2} geotherm shows highest temperature (94 °C) at the Helez Deep 1A well location where the sedimentary cover above the basement is thickest, followed by the Hazerim 1 well (85 °C) and the Zohar Deep 8 well (87 °C). In the Ramon 1 well a temperature of 78 °C is predicted. In the deepest parts of the sedimentary basin, in the Coastal Plain area, temperatures at the top of the basement at about 6 km are 160 °C.

In summary, these first observations indicate temperatures in the sedimentary cover of between 100 °C and 120 °C at a depth of 3500–4500 m, if a q_S at the upper bound of range is considered. From this estimate it can be concluded that a production of electric power in the sedimentary section would be possible, but only in the deepest parts of the basin. Temperature predictions for areas where the sedimentary cover is thin and energy production is envisioned in basement units require knowledge of the TC of the igneous and metamorphic rocks and the anisotropy tensor of TC of these rocks. For a concluding evaluation of the geothermal potential in Israel further exploration

is needed targeted on petrophysical und hydrothermal properties of sediments and basement rocks as well as on the hydrological regime in aquifers that may overprint the thermal conditions by heat diffusion considered in this study.

2.8 Conclusions

TC and RHP are important thermal parameters in geothermal studies. This paper shows that the TC of the porous sediments of southern Israel strongly depends on whether it was measured on dry (air-filled pores) or water-saturated samples. The difference in values becomes higher the higher the rock porosity. In addition to porosity, TC is most sensitive to the mineral assemblage of a rock and in turn to facies changes in the sedimentary veneer. Thus, if no understanding is developed for depositional and diagenetic processes giving rise to the present-day characteristics of geological formations, an extrapolation of TC from one location to another seems conflicted with large errors.
Without sufficient measurements of TC, a proper evaluation of conductive q_S (equalized as terrestrial heat flow) in boreholes is hampered, even if the measured temperature log is of high quality and not afflicted by thermal perturbations due to fluid flow. On the other hand, careful interpretation of temperature logs and hence interval temperature gradients calculated from the log can assist in the evaluation of thermal properties in the sedimentary cover as the gradients reflect first order the lithology of a section.
The paper exemplarily showed in the case of the Daya 1 well, how different approaches and data affect the interpretation of an available temperature log for the determination of heat flow. The large range of suggested values (37 mW m^{-2}; Eckstein and Simmons, 1978 and 57 mW m^{-2}; this study) are of profound evidence for the need in investing in laboratory measurements of TC and in lithological characterization of the measured borehole section. As the RHP of the sedimentary cover in southern Israel, comprising mostly carbonates, is relatively low (max. 4 mW m^{-2}), the basement heat flow practically equals the q_S in the error range of determination.
The range of surface heat-flow values previously reported for southern Israel is broad (31–85 mW m^{-2}, Eckstein and Simmons, 1978) and can hardly be explained by variable thermal properties of the upper crust or by different geodynamic settings. It is assumed that part of this deviation is related to the aforementioned complexities in the determination of heat flow. However, the careful inspection of the logging results and the use of TC, honouring lithological changes in the section, allow for high-quality and thus reliable values of conductive heat flow.
Interestingly, the new q_S of 57 mW m^{-2} reported for the Daya 1 in this study is similar to the value determined in a cluster of five boreholes located farther east in southern Jordan (Förster et al.,

2007). Further heat-flow data need to substantiate whether this value is typical for southern Israel. The new data of TC constitute an important database for the modeling of the deep thermal field beyond the depth of measured temperature data. Together with data on hydraulic transport properties (effective porosity and permeability) the prognosed temperatures allow a delineation of the type of geothermal use. Calculated temperature profiles for southern Israel showed that hydrothermal resources maybe used where the sedimentary cover is thick. For the use of higher temperature the basement must be considered and therewith an EGS concept. Further studies on the values and the pattern of conductive heat flow across Israel can substantially add knowledge not only to lithosphere geothermics but also for the utilization of geothermal resources.

Acknowledgements:

We particularly wish to thank the Geological Survey of Israel (GSI) for granting permission for the use of core samples from its core library. We would like to thank Eyal Shalev (GSI) for intensive scientific discussions during this study. Hallel Lutzky (GSI) is thanked for logistic support and assistance in the field work. David Göring and Alexander Reichardt (GFZ-Potsdam) assisted with the laboratory work. FS was funded via a doctoral grant from the Deutsche Forschungsgemeinschaft in the framework of the DESIRE project. The paper profited from valuable remarks by J. Schön (Leoben) and an anonymous reviewer.

2.9 References

Bartov, J. (1972), Late Cretaceous and Tertiary stratigraphy and paleography of southern Israel, Isr. J. Earth Sci., 21, 69–97.

Ben-Avraham, Z. (1989), Multiple opening and closing of the Eastern Mediterranean and SouthChinaBasins, Tectonics, 8, 351–362.

Benjamini, C., Hirsch, F., and Y. Eshet (2005), The Triassic of Israel, in Geological Framework of the Levant, Volume II: The Levantine Basin and Israel edited by J.K. Hall, V.A., Krasheninnikov, F., Hirsch, C. Benjamini and A. Flexer, pp. 331–360, Historical Productions-Hall, Jerusalem.

Brigaud, F., Chapman, D. S., and S. Le Douaran (1990), Estimating thermal conductivity in sedimentary basins using lithological data and geophysical well logs, AAPG Bulletin, 74, 1459–1477.

Buchbinder, B., Benjamini, C., and S. Lipson-Benitah (2000), Sequence development of Late Cenomanian–Turonian carbonate ramps, platforms and basins in Israel, Cretaceous Research, 21, 813–843.

Bücker, C., and L. Rybach (1996), A simple method to determine heat production from gamma-ray logs, Marine and Petroleum Geology, 13, 373–377.

Camp, V. E., and M. J. Roobol (1992), Upwelling asthenosphere beneath western Arabia and its regional implications, J. Geophys. Res., 97, B11, 15,255–15,271.

Eckstein, Y., and G. Simmons (1978), Measurement and interpretation of terrestrial heat flow in Israel, Geothermics, 6, 117–142.

Förster, A., Förster, H.-J., Masarweh, R., Masri, A., and K. Tarawneh (2007), The surface heat flow of the Arabian Shield in Jordan, J. Asian Earth Sci., 30, 271–284.

Garfunkel, Z., and B. Derin (1984), Permian-early Mesozoic tectonism and continental margin formation in Israel and its implications for the history of the Eastern Mediterranean, Geological Society, London, Special Publications, 17, 187–200.

Garfunkel, Z. (1988), The pre-Quaternary geology of Israel, in The Zoogeography of Israel eidted by Y. Yom-Tov and E. Tchernov, Jungk Publishers, Dordrecht, 7–34.

Gvirtzman, Z. (2004), Chronostratigraphic table and subsidence curves of southern Israel, Isr. J. Earth Sci., 53, 47–61.

Gvirtzman, Z., and Z. Garfunkel (1998), The transformation of southern Israel from a swell to a basin: stratigraphic and geodynamic implications for intracontinental tectonics, Earth Planet. Sci. Lett., 163, 275–290.

Hirsch, F. (2005a), Introduction to the stratigraphy of Israel, in Geological Framework of the Levant, Volume II: The Levantine Basin and Israel edited by J. K. Hall, V. A. Krasheninnikov, F. Hirsch, C. Benjamini and A. Flexer, pp. 269–283, Historical Productions-Hall, Jerusalem.

Hirsch, F. (2005b), The Jurassic of Israel, in Geological Framework of the Levant, Volume II: The Levantine Basin and Israel edited by J. K. Hall, V. A. Krasheninnikov, F. Hirsch, C. Benjamini and A. Flexer, pp. 361–393, Historical Productions-Hall, Jerusalem.

Hirsch, F. (2005c), The Oligocene–Pliocene of Israel, in Geological Framework of the Levant, Volume II: The Levantine Basin and Israel edited by J. K. Hall, V. A. Krasheninnikov, F. Hirsch, C. Benjamini and A. Flexer, pp. 459–488, Historical Productions-Hall, Jerusalem.

Horai, K. (1971), Thermal Conductivity of Rock-Forming Minerals, J. Geophys. Res., 76, B5, 1278–1308.

Horai, K., and G. Simmons (1969), Thermal conductivity of rock-forming minerals, Earth Planet. Sci. Lett., 6, 359–368.

Krienitz, M.-S., Haase, K. M., Mezger, K., and M. A. Shaikh-Mashail (2007), Magma genesis and mantle dynamics at the Harrat Ash Shamah volcanic field (southern Syria), J. Petrol., 48, 1513–1542.

Kröner, A., Eyal, M., and Y. Eyal (1990), Early Pan-African evolution of the basement around Elat, Israel, and the Sinai Peninsula revealed by single-zircon evaporation dating, and implications for crustal accretion rates, Geology, 18, 545–548.

Lewy, Z. (1990), Transgressions, regressions and relative sea level changes on the Cretaceous shelf of Israel and adjacent countries. A critical evaluation of Cretaceous global sea level correlations, Paleoceanography, 5, 619–637.

Popov, Y. A., Pribnow, D. F. C., Sass, J. H., Williams, C. F., and H. Burkhardt (1999), Characterization of rock thermal conductivity by high-resolution optical scanning, Geothermics, 28, 253–276.

Powell, W. G., Chapman, D. S., Balling, N., and A. E. Beck (1988), Continental heat flow density, in Handbook of Terrestrial Heat-Flow Density Determination edited by R. Haenel, L. Rybach and L. Stegena, pp.167–222, Kluwer, Dordrecht.

Reuss, A. (1929), Berechnung der Fließgrenze von Mischkristallen auf Grund der Plastizitätsbedingung für Einkristalle, Z. Angew. Math. Mech. 9, 49–58.

Robertson, A. H. F., Dixon, J. E., Brown, S., Collins, A., Morris, A., Pickett, E., Sharp, I., and T. Ustaömer (1996), Alternative tectonic models for the Late Palaeozoic-Early Tertiary development of Tethys in the Eastern Mediterranean region, Geological Society, London, Special Publications, 105, 239–263.

Rosenfeld, A., and F. Hirsch (2005a), The Paleocene–Eocene of Israel, in Geological Framework of the Levant, Volume II: The Levantine Basin and Israel edited by J. K. Hall, V. A. Krasheninnikov, F. Hirsch, C. Benjamini and A. Flexer, pp. 437–458, Historical Productions-Hall, Jerusalem.

Rosenfeld, A., and F. Hirsch (2005b), The Cretaceous of Israel, in Geological Framework of the Levant, Volume II: The Levantine Basin and Israel edited by J. K. Hall, V. A. Krasheninnikov, F. Hirsch, C. Benjamini and A. Flexer, pp. 393–437, Historical Productions-Hall, Jerusalem.

Rybakov, M., and A. Segev (2004), Top of the crystalline basement in the Levant, Geochem. Geophys. Geosyst., 5, 1–8.

Shaw, J. E., Baker, J. A., Menzies, M. A., Thirlwall, M. F., and K. M. Ibrahim (2003), Petrogenesis of the largest intraplate volcanic field on the Arabian plate (Jordan): a mixed lithosphere–asthenosphere source activated by lithosphere extension, J. Petrol., 44, 1657–1679.

Schön, J. H. (1996), Physical properties of rocks: fundamentals and principles of petrophysics, in Handbook of Geophysical Exploration eidted by K. Helbig and S. Teitel, pp. 323–373, Section 8, Thermal Properties of Rocks, Oxford, United Kingdom, Pergamon, 18.

Somerton, W. H. (1992), Thermal properties and temperature related behavior of rock/fluid systems, Developments in Petroleum Sciences, 37, Elsevier, Amsterdam.

Stern, J. R. (1994), Arc Assembly and Continental Collision in the Neoproterozoic East African Orogen: Implications for the Consolidation of Gondwanaland, Annu. Rev. Earth Planet. Sci., 22, 319–351.

Vila, M., Fernández, M., and I. Jiménez-Munt (2010), Radiogenic heat production variability of some common lithological groups and its significance to lithospheric thermal modelling, Tectonophysics, 490, 152–164.

Voigt, W. (1928), Lehrbuch der Kristallphysik. Teubner, Leipzig.

Weinberger, G., Rosenthal, E., and A. Flexer (1991), The subsurface geology of Central and Northern Negev with possible implications on the regional ground water flow pattern, J. Afr. Earth. Sci., 14, 155–172.

Weissbrod, T. (1994), Lithology and stratigraphy of the Lower Cretaceous formations in the southern Negev (Elat region), Isr. Geol. Surv., Current Res., 8, 62–64.

Weissbrod, T. (2005), The Paleozoic in Israel and Environs, in Geological Framework of the Levant, Volume II: The Levantine Basin and Israel edited by J. K. Hall, V. A. Krasheninnikov, F. Hirsch, C. Benjamini and A. Flexer, pp. 283–316, Historical Productions-Hall, Jerusalem.

Wilson, M., Shimron, A. E., Rosenbaum, J. M., and J. Preston (2000), Early Cretaceous magmatism of Mount Hermon, Northern Israel, Contrib. Mineral. Petrol., 139, 54–67.

Woodside, W., and J. Messmer (1961), Thermal conductivity of porous media. I Unconsolidated sands, J. Appl. Phys., 32, 1699–1706.

3 Evaluation of common mixing models for calculating bulk thermal conductivity of sedimentary rocks: Correction charts and new conversion equations

Sven Fuchs, Felina Schütz, Hans-Jürgen Förster, Andrea Förster

Published in: Geothermics, 47, 40–52.

3.1 Abstract

Different numerical models can be deployed to calculate the matrix thermal conductivity of a rock from the bulk thermal conductivity (BTC), if the effective porosity of the rock is known. Vice versa, using these parameters, the BTC can be determined for saturation fluids of different thermal conductivity (TC). In this paper, the goodness-of-fit between measured and calculated BTC values of sedimentary rocks has been evaluated for two-component (rock matrix and pores) models that are used widely in geothermics: arithmetic mean, geometric mean, harmonic mean, Hashin and Shtrikman mean, and effective-medium theory mean. The examined set of samples consisted of 1147 TC data in the interval 1.0 to 6.5 W m^{-1} K^{-1}. The quality of fit was studied separately for the influence of lithotype (sandstone, mudstone, limestone, dolomite), saturation fluid (water and isooctane), and rock anisotropy (parallel and perpendicular to bedding). From the studied models, the geometric mean displays the best, however not satisfying correspondence between calculated and measured BTC. To improve the fit of all models, respective correction equations are calculated. The "corrected" geometric mean provides the most satisfying results and constitutes a universally applicable model for sedimentary rocks. In addition, the application of the herein presented correction equations allows a significant improvement of the accuracy of existing BTC data calculated on the basis of the other mean models. Finally, lithotype-specific conversion equations are provided permitting a calculation of the water-saturated BTC from data of dry-measured BTC and porosity (e.g., well log derived porosity) with no use of any mixing model. For all studied lithotypes, these correction and conversion equations usually reproduce the BTC with an uncertainty < 10%.

3.2 Introduction

In geothermal studies, the rock thermal conductivity (TC) constitutes an important parameter. It is essential for the determination of the heat flow from the Earth's interior and is indispensable in any thermal modeling. In sedimentary-basin research, large databases of TC are required to characterize the major lithotypes making up the different geological formations and hence entire sedimentary sections. The amount of data needed to characterize fully a sedimentary setting thereby depends on the geological history and associated facies changes and may be large.

The most reliable TC values originate from direct laboratory measurements. If core samples are not available, indirect methods are used to calculate TC from petrophysical properties, including porosity, a parameter provided through well logging (e.g., Goss and Combs, 1976; Balling et al.,

1981; Hartmann et al., 2005; Goutorbe et al., 2006). Another indirect approach of TC determination uses the abundance and composition of the rock-forming minerals and the porosity as a multi-component system (e.g., Brailsford and Major, 1964; Brigaud et al., 1990; Demongodin et al., 1991, Vasseur et al., 1995). All these indirect methods have their shortcomings and restrictions.

Various laboratory methods for the measurement of TC are available comprising steady-state techniques (e.g., divided bar technique, needle probe) and transient techniques (e.g., line-source methods, ring-source methods, optical scanning). Comprehensive reviews on these techniques are provided by Kappelmeyer and Haenel (1974), Beck (1988), Blackwell and Steele (1989), and Somerton (1992). The less time-consuming optical scanning technique (OS) is, since introduced in the 1990s by Y. Popov, recently the most frequently used method to measure TC for large sample sets. This method was applied successfully to crystalline rocks (e.g., Popov et al., 1999; He et al., 2008) as well as to sedimentary rocks (e.g., Popov et al., 1995, 2003, 2010, 2011; Mottaghy et al., 2005; Hartmann et al., 2005, 2008; Norden and Förster, 2006; Clauser, 2006; Homoth et al., 2008; Majorowicz et al., 2008; Orilski et al., 2010; Fuchs and Förster, 2010; Liu et al., 2011; Schütz et al., 2012). It involved the measurement of TC under ambient temperature and pressure, which is in contrast to the other widely used method, the divided-bar technique (DB). This method obtains TC applying uniaxial pressure. Measurements under pressure have the advantage that micro cracks that may have originated from decompression and cooling as result of borehole drilling or rapid uplift, will get closed. The presence of micro cracks would cause underestimation of TC compared to an intact sample, whereby the rate of underestimation strongly depends on the type of saturation (air or water). Schärli and Rybach (1984) showed that because of micro cracks, the difference between dry and water-saturated TC in granitic rocks may be as high as 30%. For saturated metamorphic rocks (gneiss and amphibolite), the comparison of TC obtained by the DB and OS methods resulted in small discrepancies (AME < 3%), although an axial load of 4 to 6 MPa was applied in the DB approach (Popov et al., 1999). An analog study for sedimentary rocks is missing. However, despite this circumstance we are confident that the approach of this paper, which is entirely based on OS results, is scientifically sound.

To perform the laboratory work economically, i.e., studying large sample numbers in affordable time, measurements are usually performed in dry state, with air as the pore-saturating medium. Additional effort then is needed to convert these TCs to values typical for e.g., aquifers with water as the pore-filling fluid or hydrocarbon reservoirs, in which the rock contains either water, oil, or gas, or a mixture of those. The calculation of the rock TC for different saturation fluids then requires the use of mixing models.

In general, those multi-component mixture models to describe the TC of a rock can be grouped in

(1) well-defined physical (often referred as structural or theoretical) models and in (2) purely empirical or semi-empirical approaches. A third group of models is based on numerical simulations. Physical models may have a wider applicability (depending on the degree of simplification to obtain a solution), but their usability is often limited by the inclusion of empirically determined parameters, compositional variations, or structural aspects (e.g., Sugawara and Yoshizawa, 1961; Zimmerman, 1989; Schopper, 1991; Popov et al., 2003). Empirical models have the drawback that they are strictly valid for the particular rock suite being used for model development. Extensive overviews of TC models are provided by Tinga et al. (1973) and Progelhof et al. (1976) (for two-component mixtures) as well as by Abdulagatova et al. (2009).

Rather simple models, easily and comfortably applied, are based on a two-phase system of the rock comprising the solid mineral matrix and the pore space. Thus, if porosity and bulk thermal conductivity (BTC) of a sample are measured, a matrix thermal conductivity (MTC) can be inferred for the sample and in turn a BTC for another pore fluid with different TC calculated.

This paper provides a validity study of simple and usually used mixing models for a two-phase rock system involving (1) the layered medium model (series and parallel model corresponding to the arithmetic and harmonic means and the mean of both), (2) an empirical model not relying on any physical theory (the geometric mean), (3) the Hashin and Shtrikman mean, the upper and lower bounds of which provide tighter constraints than the arithmetic and harmonic means, and (4) the effective medium mean (based on the effective-medium theory). The selection of these models builds on results of Clauser (2009), who discussed the performance of these mixing models for a fixed MTC and a variable porosity, however without validating the results with measured laboratory TC.

It was examined, which of the selected mixing models best describes the TC of sedimentary rocks. The evaluation considers three different aspects: (1) lithotype, (2) pore content (air, water, or other saturating fluids), and (3) anisotropy. The statistical analysis of the deviations between laboratory-measured and calculated BTC data comprises 1147 single values obtained from 717 samples of sandstone, mudstone, limestone, and dolomite. As a result of this statistical analysis, the paper provides correction equations that yield an improved fit for some of the examined models. Finally, we present conversion equations that permit calculation of the water-saturated BTC from the dry-measured BTC for the case that porosity is known, e.g., from petrophysical well logging. This approach has the advantage that a BTC could be inferred for a different saturating fluid without application of any mixing model.

3.3 Previous comparison studies

A verification of the different mathematical models, considering a solid and a pore volume, by comparison with real data has not yet been comprehensively performed. Most studies comparing between measured and calculated BTC values encompassed crystalline rocks.

Robertson and Peck (1974) compared BTC calculated from eleven theoretical mean models with TC values measured on 61 olivine-bearing basalt samples. None of the models showed a good agreement over the large range of porosity that the samples possessed (2–97%). The study showed on the one hand that a correction factor must be applied to the computed values to reduce the calculation error and on the other hand that the geometric-mean model belongs to those few approaches yielding the best, although unsatisfying, match. Horai (1991) reevaluated the data from Robertson and Peck (1974) and concluded that the mismatch in modeled and measured data is caused by errors introduced by the use of data from different measurement techniques.

More recently, Pribnow (1994) examined the four most widely used models (geometric mean, arithmetic mean, harmonic mean, and the Hashin and Shtrikman mean) for 85 water-saturated amphibolite and gneiss samples using the DB technique (Birch, 1950) and the line-source approach (Lewis et al., 1993). The geometric mean model, together with the mean of the arithmetic and harmonic mean models, provided the best fit.

Analog studies of the evaluated mean models focusing on sedimentary rocks are rare. Woodside and Messmer (1961b) used six sandstone samples to validate the geometric mean model for consolidated rocks and recognized a good agreement between predicted and measured BTC. Hutt and Berg (1968) analyzed several mean models (arithmetic mean, harmonic mean, geometric mean, Bruggeman, Maxwell, Rayleigh, Archie) for 28 sandstone samples. They compared the calculated BTC (using the TC of minerals for calculating the MTC) with values measured with a needle probe. The harmonic mean showed a good fit, whereas the arithmetic and geometric mean model overestimated the measured data. Buntebarth and Schopper (1998) explored various models for a suite of eleven sedimentary-rock samples saturated with different fluids (TC measurements with a needle probe). In their study, the application of the harmonic and arithmetic mean models resulted in a better fit relative to the geometric mean model. Clauser (2006) compared TC data of various sedimentary lithotypes with theoretical model curves and graphically identified the closest approximation of measured (using the OS technique) and calculated values for the geometric-mean model, except for limy sandstones. Several authors (e.g., Zimmerman, 1989; Revil, 2000; Carson et al., 2005) used the database of Woodside and Messmer (1961b) to test their own models for consolidated and unconsolidated rock. However, the number of data available for comparison was

small and not comparable to the data set deployed in this study.

3.4 Methods applied

3.4.1 Models of two-phase systems

Calculation of the BTC (λ_b) of a two-component rock system involves the MTC (λ_m), the effective porosity (ϕ), and the TC of the pore content (λ_p).

Geometric mean

The empirical geometric-mean model (GM), which went back to Lichtenecker (1924) and was evaluated first by Woodside and Messmer (1961a, 1961b) for consolidated sandstones and unconsolidated sands, represents the most usual approach. The empirical formula provides a relatively simple mathematical expression to calculate the BTC of a porous rock.

GM: $$\lambda_b = \lambda_m^{1-\phi} \cdot \lambda_p^{\phi} \tag{3.1}$$

Arithmetic and Harmonic Mean

Other frequently applied approaches comprise the arithmetic-mean (AM) and harmonic-mean (HM) models, which both are based on a sheet model representing a layered structure of phases, where the heat flow passes either parallel (AM) or perpendicular (HM) with respect to the plane boundaries. The two models are independent of the pore structure and constitute special cases (boundaries) of Wiener's mixing law (Wiener, 1912), which applies to both isotropic and anisotropic mixtures. The models were introduced by Voigt (1928) and Reuss (1929) to define the upper and lower TC boundaries.

AM: $$\lambda_b = (1-\phi) \cdot \lambda_m + \phi \cdot \lambda_p \tag{3.2}$$

HM: $$\lambda_b = \frac{1}{\frac{(1-\phi)}{\lambda_m} - \frac{\phi}{\lambda_p}} \tag{3.3}$$

Hashin and Shtrikman mean

The model of Hashin and Shtrikman (1962) (also referred as Maxwell-Eucken equations) is based on the theory of Maxwell (1892) and was extended by the work of Eucken (1940). It also uses upper (λ_{HS}^{U} ; represents fluid-filled, spherical pores) and lower (λ_{HS}^{L} ; represents grains suspended in a fluid) boundaries to calculate the TC of a two-phase system. The Hashin-and-Shtrikman bounds provide more restrictive narrower upper (Eq. (3.5)) and lower bounds (Eq. (3.7)) for isotropic mixtures, yet independent of the pore structure (Zimmerman, 1989). The mean of both bounds is often used as best approximation of rock BTC.

$$\lambda_b = \frac{1}{2}(\lambda_{HS}^U + \lambda_{HS}^L) \tag{3.4}$$

$$\lambda_{HS}^U = \lambda_m + \frac{\phi}{\frac{1}{\lambda_p - \lambda_m} + \frac{1-\phi}{3\lambda_m}} \tag{3.5}$$

$$\lambda_{HS}^L = \lambda_p + \frac{1-\phi}{\frac{1}{\lambda_m - \lambda_p} + \frac{\phi}{3\lambda_p}} \tag{3.6}$$

Solving Eq. (3.5) for λ_m produces a quadratic equation requiring the quadratic formula for the solution, which leads to two results but only one produces the real value (Eq. (3.8)).

$$\lambda_m = \frac{1}{2}(\lambda_{m\,HS}^{\ U} + \lambda_{m\,HS}^{\ L}) \tag{3.7}$$

$$\lambda_{m\,HS}^{\ U} = \frac{b + \sqrt{(b)^2 + 4 \cdot ac}}{2a} \tag{3.8}$$

$a = 2(\phi - 1)$; $\quad b = \lambda_{HS}^U(2+\phi) - \lambda_p(1+2\phi)$; $\quad c = \lambda_{HS}^U \lambda_p(1-\phi)$

$$\lambda_{m\,HS}^{\ L} = \frac{\lambda_p^2(2\phi) - \lambda_{HS}^L \cdot \lambda_p(3-\phi)}{\lambda_{HS}^L \cdot \phi + \lambda_p \cdot (2\phi - 3)}) \tag{3.9}$$

Effective-Medium theory mean

To infer the TC for homogenous (isotropic) rocks, Bruggeman (1935) put forward the effective-medium theory (often referred as self-consistent medium approximation), which also uses the Lichtenecker (1924) formula. The effective-medium theory assumes different spherical inclusions embedded in a conducting host medium where all phases were mutually dispersed. This approach was further developed by Hanai (1960) and Sen et al. (1981) to the Bruggeman-Hanai-Sen equation for two-component systems. In this differential effective-medium theory the host phase percolates for the full range of fractions and the inclusions (second phase) may or may not conduct.

The effective-medium theory model is applicable to the determination of the TC of a multiphase system. Clauser (2009) transformed this equation to calculate the BTC for a two-component system (Eq. (3.10)) consisting of pore fluid and rock matrix:

$$\lambda_b = \frac{1}{4}\left\{\begin{array}{l} 3\phi(\lambda_p - \lambda_m) + 2\lambda_m - \lambda_p + \\ \sqrt{9\phi^2\lambda_m^2 + 18\phi\lambda_m\lambda_p - 18\phi^2\lambda_m\lambda_p - 12\phi\lambda_m^2 + \lambda_p^2 - 6\phi\lambda_p^2 + 4\lambda_m\lambda_p + 9\phi^2\lambda_p^2 + 4\lambda_m^2} \end{array}\right\} \tag{3.10}$$

Equation (3.10) can be transposed to get MTC on its own (Eq. (3.11)):

$$\lambda_{\mathrm{m}} = \frac{\lambda_b\left(-2\cdot\lambda_b + 3\cdot\phi\cdot\lambda_p - \lambda_p\right)}{\lambda_b\left(3\phi - 2\right) - \lambda_p} \tag{3.11}$$

3.4.2 Anisotropy of thermal conductivity

The anisotropy of TC is a property that relates to the structure and texture of a rock, such as crystal anisotropy of the individual rock-forming minerals, intrinsic or structural anisotropy related to the shape of the grains and their textural arrangement, orientation and geometry of cracks, the spatial fracture distribution and other defects (Schön, 1996). For the quantification of anisotropy, TC is usually measured parallel ($\lambda_{\parallel}$) and perpendicular ($\lambda_{\perp}$) to bedding or schistosity. The anisotropy ratio (A) then is defined as:

$$A = \frac{\lambda_{\parallel}}{\lambda_{\perp}} \tag{3.12}$$

3.4.3 Methods of error calculation

To evaluate the reliability of the different mean models applied, the measured BTC is compared with the respective calculated BTC.

For an individual sample, the deviation (E, in %) between calculated (λ_{cal}) and measured (λ_{mea}) TC is expressed as:

$$\mathrm{E} = 100\cdot\frac{\left|\lambda_{cal} - \lambda_{mea}\right|}{\lambda_{mea}} \tag{3.13}$$

For evaluating the different mean-model approaches, the arithmetic mean error (AME) was used to compare the calculated and the measured BTC:

$$\mathrm{AME} = \frac{1}{n}\sum_{i=1}^{n} E_i \tag{3.14}$$

where n is the number of samples in each lithotype group.

In the following, the error is noted as the AME complemented by the respective 1σ standard deviation (SD). The AME can be expressed also as root mean square error (RMSE), which is a good measure of model accuracy, having the form:

$$\mathrm{RMSE} = \sqrt{\frac{\sum_{i=1}^{n} E_i^2}{n}} \tag{3.15}$$

The fit between predicted and measured data is statistically evaluated by regression analysis and the analysis of variances. The critical significance level α (mostly the statistical benchmark of 0.05), the observed significance level p, and the F-value constitute the key parameters for comparison (see section 5.1).

3.5 The database

In total, 1147 TC measurements performed on 717 samples were evaluated. The database comprises four data sets from different sedimentary basins: (a) Mesozoic platform sediments of the northern Sinai Microplate in Israel (81 drill core samples; Schütz et al., 2012), (b) the eastern part of the North German Basin (339 drill core samples of the Mesozoic; Fuchs and Förster, 2010, 2013 (unpublished results); 129 drill core samples of the Permo-Carboniferous; Norden and Förster, 2006); and (c) the South German Scarplands and the Molasse Basin (168 drill core and outcrop samples; Clauser et al., 2007). The studied samples encompass the following lithotypes: 137 limestone samples, 63 dolomite samples, 409 sandstone samples, and 108 mudstone (claystone + siltstone) samples. The TC data from these lithological subsets were scrutinized with respect to statistical distribution, and outliers (> 2σ SD) were omitted in additional analysis.

All these TC data have in common that they were obtained with the Thermal Conductivity Scanning (TCS) apparatus (Lippmann and Rauen, GbR Schaufling, Germany), which is based on the high-resolution OS method (Popov et al., 1999) The sample size correlated with the drill core diameter, which varied between 5 and 10 cm. Sample thickness was variable, but exceeded the required minimal length of scanning lines of 4 cm. Measurements were performed on a flat sample surface displaying a roughness of < 1 mm. The error of determination was less than 3%.

All samples were measured under ambient pressure and temperature, both dry (oven-dried at 60 °C) and water-saturated using distilled water. Determination of the anisotropy ratio of macroscopically isotropic samples involved TC measurement on the top/bottom of the cylindrical core and along the vertical core axis. For optically anisotropic samples, this ratio was calculated by measuring TC parallel and perpendicular to bedding (see section 3.2). The effective porosity was quantified by the mass change between dry and water-saturated samples (Archimedes method). Because of clay-swelling effects, mudstones and argillaceous sandstones were saturated with isooctane (density: 0.698 x 10^3 kg m^{-3}; Budavari, 1989) instead of water to determine their porosity. TC values of

0.025 W m^{-1} K^{-1} for air (Gröber et al., 1955), 0.095 W m^{-1} K^{-1} for isooctane (Watanabe, 2003), and 0.604 W m^{-1} K^{-1} (Lemmon et al., 2005) for distilled water were used in the calculations.

Figure 3.1 provides a compilation of measured BTC and effective porosity for the four lithotypes. The rocks covered a large range in effective porosity, from almost zero to about 30%. The carbonate rocks are usually less porous relative to the clastic rocks. Eighty percent of the entire data population of carbonates fall in the porosity range 1–13%, in contrast to 3–28% encompassed by the clastic rocks.

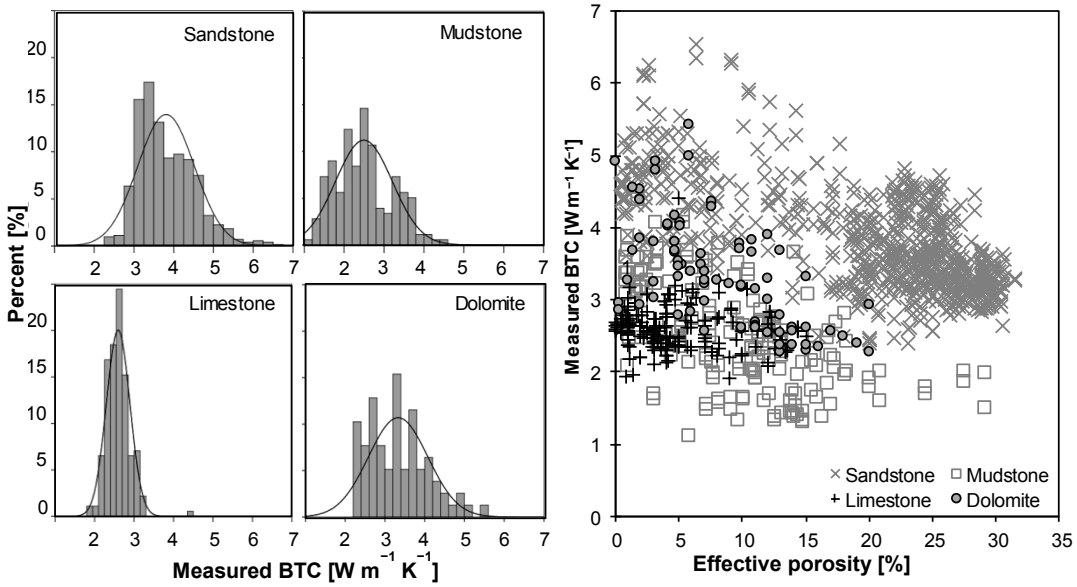

Figure 3.1: Effective porosity and measured BTC (both water and isooctane-saturated) of the clastic and carbonate samples from this study.

As to the measured BTC, the sample suite spans the interval between 1.0 and 6.5 W m^{-1} K^{-1}. The larger variability in TC observed for sandstone (3.8 ± 0.7 W m^{-1} K^{-1}), mudstone (2.5 ± 0.7 W m^{-1} K^{-1}), and dolomite (3.3 ± 0.7 W m^{-1} K^{-1}) relative to limestone (2.6 ± 0.3 W m^{-1} K^{-1}) is a reflection of their greater heterogeneity in terms of modal mineralogy.

3.6 Results

The matrix thermal conductivity was calculated from measured dry and saturated values for arithmetic, harmonic, and geometric means using Eqs. (3.1), (3.2) and (3.3) transposed to λ_m. Eqs. (3.7) and (3.11) were applied for the Hashin-Shtrikman and the effective medium means, respectively. Water-saturated BTC for the various mixing models were subsequently calculated from Eqs. (3.1) – (3.4) and (3.10). The BTC results are shown as scatter plots for the six models (Figure 3.2). Figure 3.3 illustrates the influence of different saturation fluids (water and isooctane)

on BTC.

3.6.1 General model fit

A regression analysis was performed to ascertain the model with the highest coefficient of determination (R^2). The results show that most of the evaluated mixing models predict the measured BTC unsatisfactorily. The highest value of R^2 is related to the geometric mean ($R^2 = 0.62$, $F \sim 1348$). Significantly poorer fits are observed for the arithmetic mean ($R^2 = 0.37$, $F \sim 600$), followed by the effective medium mean ($R^2 < 0.24$, $F \sim 321$) and Hashin and Shtrikman mean ($R^2 = 0.23$, $F \sim 298$). The harmonic mean ($R^2 < 0.01$, $F = 1.56$) as well as the mean of arithmetic and harmonic mean ($R^2 = 0.01$, $F = 9.01$) show even lower coefficients of determination. If the value obtained for F is equal to or larger than the critical F-value, then the null hypothesis (H_0: $\mu_1 = \mu_2$) is rejected, and the result is significant at the chosen level of probability ($\alpha = 0.05$). This critical value is assumed to be F_{crit} (1/1017) = 3.85.

Figure 3.2 shows the comparison between measured and calculated BTC for the different models. The arithmetic mean (Figure 3.2a) tends to underestimate BTC in particular for clastic sediments (AME 33 ± 20%), but yields an acceptable fit for carbonate samples (deviation 11 ± 20%). The majority of BTC values calculated with the harmonic mean are negative (96%) and hence do not plot in the diagram (Figure 3.2b). Given that the harmonic mean consistently shows abnormal values and with respect to the insignificant regression relation it is excluded from further discussion. This poor match also holds for the mean of arithmetic and harmonic means (Figure 3.2c). The geometric mean (Figure 3.2d) shows a reasonably good fit for both carbonate (AME 6 ± 10%) and clastic (AME 5 ± 17%) rocks. It tends to slightly overestimate BTC, but 80% of the samples show deviations ≤ 20%.

The Hashin and Shtrikman mean (Figure 3.2e) shows an acceptable fit for carbonate (AME 19 ± 13%), but a poor fit for clastic rocks (AME 51 ± 18%). Its overall distribution pattern largely corresponds to those of the arithmetic and effective medium means (Figure 3.2f). Because these three models provided virtually the same goodness of fit (ANOVA, Tukey's HSD, $\alpha = 0.05$, $n = 1019$), the effective medium mean could be eliminated from further analysis.

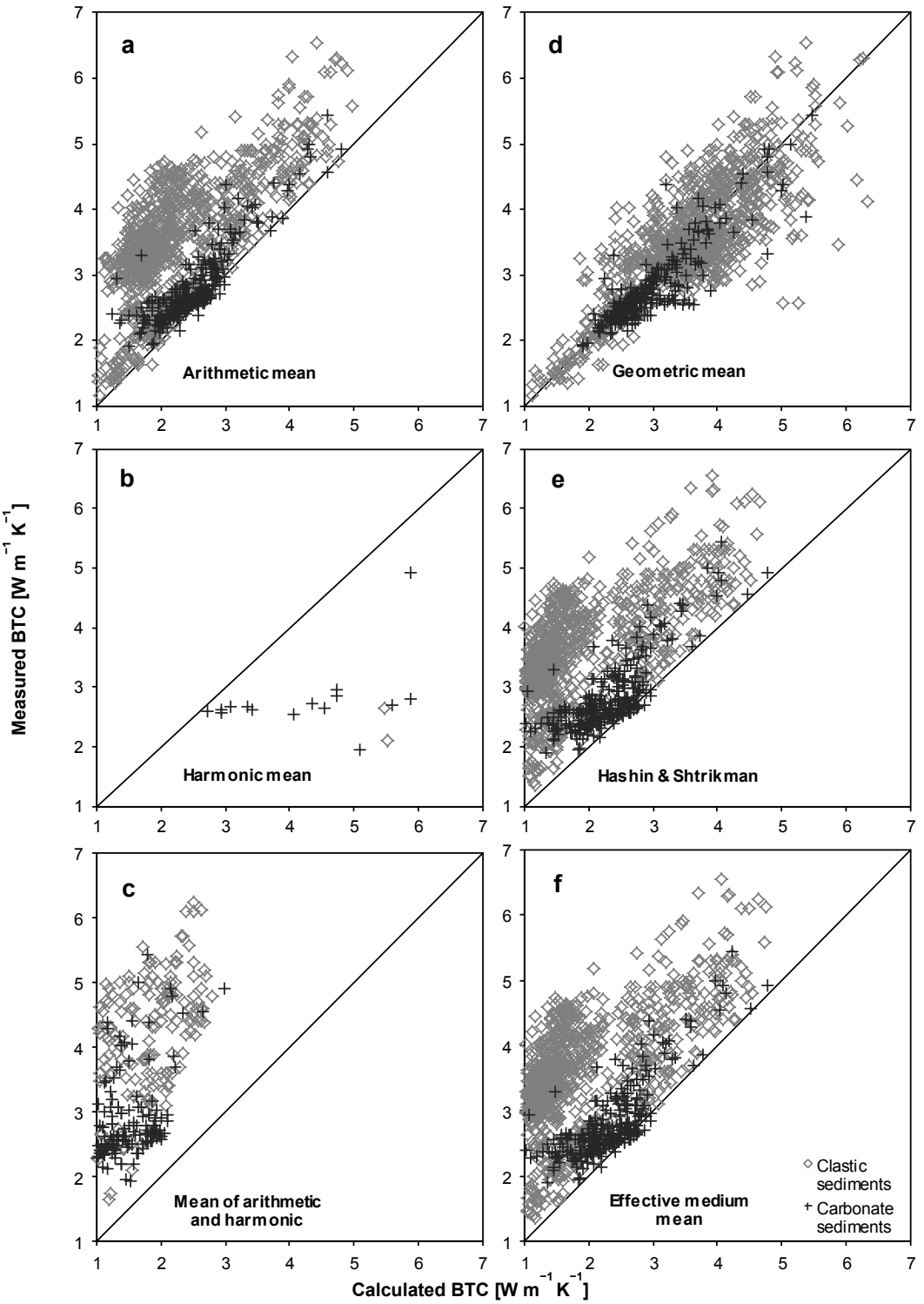

Figure 3.2: Scatter plots of measured vs. calculated water-saturated BTC for clastic (n = 885) and carbonate sediments (n = 262).

3.6.2 Anisotropy of thermal conductivity

The vast majority of rock samples possess anisotropy ratios between 0.8 and 1.2 (Figure 3.3). Whereas the carbonate rocks and most sandstone samples are largely isotropic (mean anisotropy ratio = 1.01 ± 0.05 and 0.97 ± 0.08, respectively), many mudstone samples are anisotropic, exposing a mean anisotropy ratio of 1.11 ± 0.19.

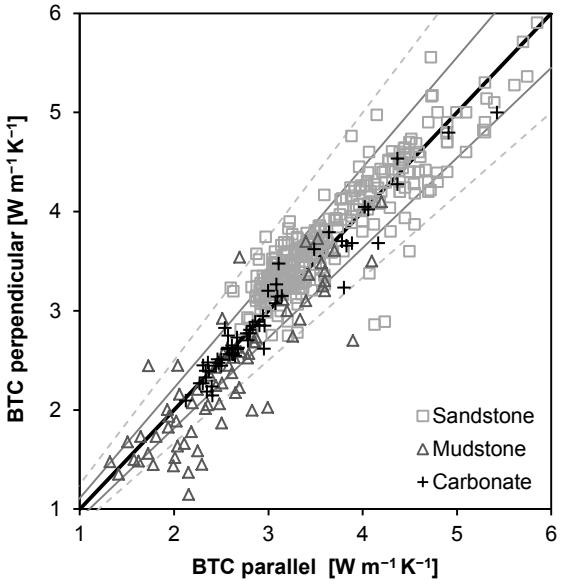

Figure 3.3: Scatter plot of measured water-saturated BTC parallel and perpendicular. See text for explanation.

Rock samples showing an anisotropy > 5% (n = 424) are evaluated in terms of a possible impact that anisotropy has on the mixing model that should be selected for calculation. A paired T-test was made to compare the average deviations of the predicted BTC with the BTC measured parallel and perpendicular to bedding.

Because the arithmetic-mean model is based on a sheet model with the heat flowing parallel to the components, it seemed reasonable to assume that this model will better fit the BTC parallel than perpendicular to bedding (harmonic mean) as well as those models that refer to isotropic media (the geometric and the Hashin and Shtrikman means). However, the expectations are not met. For data referring to measurements parallel to bedding, the arithmetic mean model provides the same poor fit as for data related to measurements performed in the opposite direction (paired T-test, n = 128, α = 0.01, p = 0.425). As to the geometric and Hashin and Shtrikman means, the results are in line with the theoretical background that the goodness of fit is basically the same for isotropic or anisotropic rocks.

3.6.3 Saturating fluid

The correlation between measured and calculated BTC of samples saturated with water or isooctane is displayed in Figure 3.4.

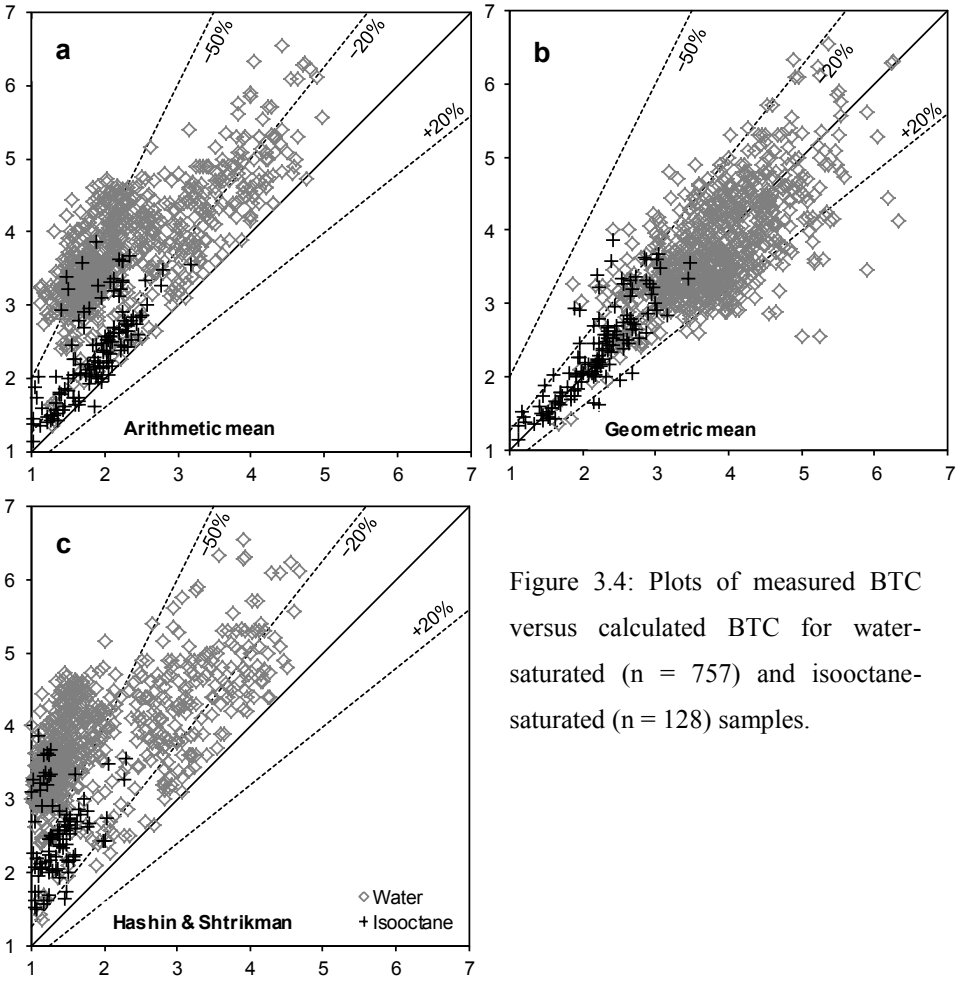

Figure 3.4: Plots of measured BTC versus calculated BTC for water-saturated (n = 757) and isooctane-saturated (n = 128) samples.

For the range for where measured TC values are available, the goodness of fit for samples saturated with isooctane is basically the same as for samples saturated with water. Accordingly, both the arithmetic and Hashin and Shtrikman means seriously underestimate BTC also for samples saturated with isooctane. For this saturation fluid, the geometric mean again shows the best fit (AME 6 ± 6%).

3.6.4 Impact of lithotype

Figure 3.5 shows the model-based relations between measured and calculated BTC for the different lithotype groups.

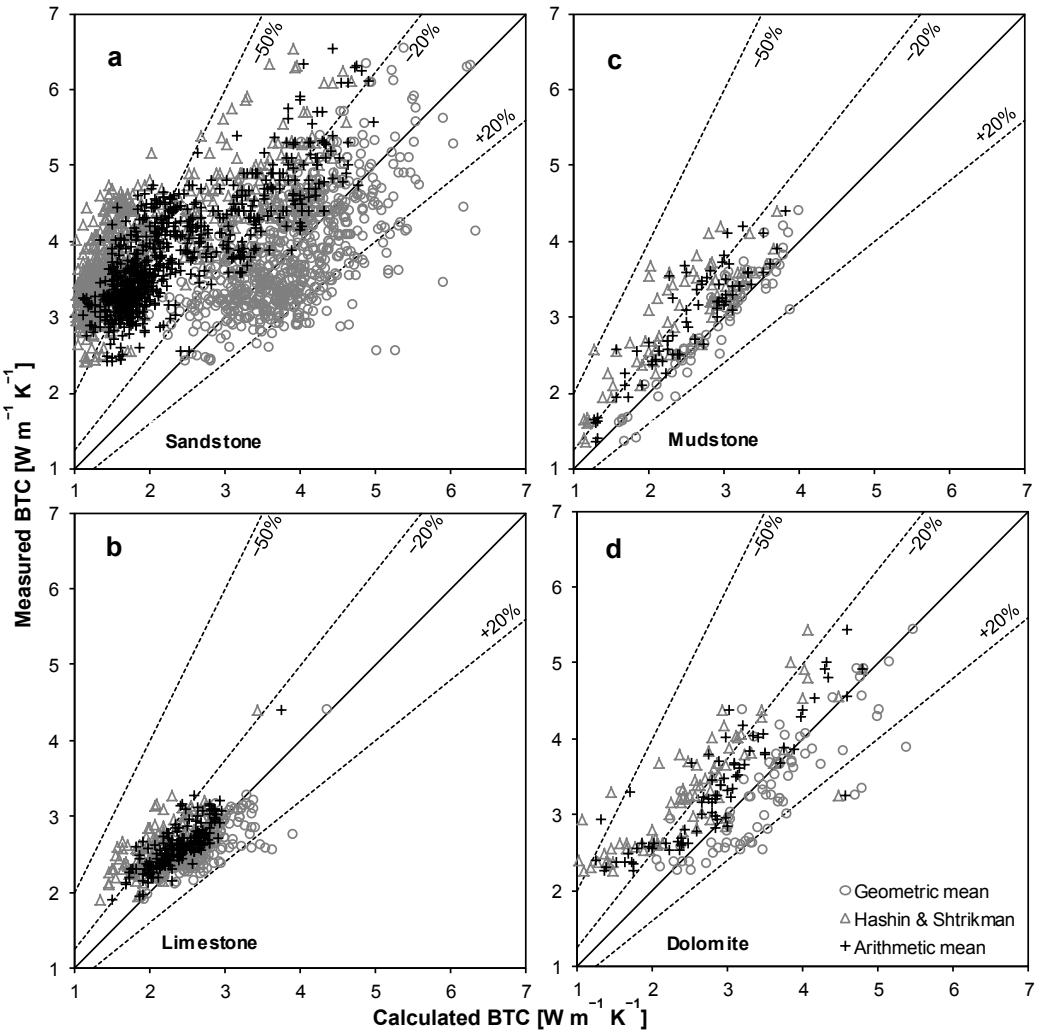

Figure 3.5: Calculated BTC (water-saturated) based on different mixing models compared to measured BTC for different lithotypes.

For sandstones (Figure 3.5a), only the geometric mean shows an acceptable fit (AME 13 ± 11%), whereas the arithmetic and the Hashin and Shtrikman means strongly underestimate the BTC (AME 41 ± 14% and 53 ± 16%, resp.). For limestones (Figure 3.5b), the fit for the geometric and the arithmetic means is reasonably good (AME 6 ± 5% and 8 ± 6%) and still acceptable for the Hashin and Shtrikman mean (AME 12 ± 9%). For mudstones (Figure 3.5c), the geometric mean is the only approach resulting in a good fit. Both the arithmetic (AME 14 ± 9%) and the Hashin and Shtrikman means (AME 20 ± 12%) again underestimate the BTC, but less significantly. For dolomite (Figure 3.5d), none of the models gave rise to a fit evaluated as good. An acceptable fit was obtained upon

utilization of the geometric and arithmetic means (AME 12 ± 11% and 16 ± 12%, resp.).

3.7 Discussion

3.7.1 General model fit, anisotropy, and saturating fluid

The various mixing models evaluated in this study approximate measured BTC data in different, however mostly unsatisfying quality. Only the geometric mean consistently shows a good fit, with the bulk of calculated data deviating less than ± 20% from measured BTC (Figure 3.5). Considering the entire sample suite, the deviation averages between 11% (geometric mean) to 31% (arithmetic mean) and 42% (Hashin and Shtrikman mean). Only examining the lithotype, the deviation varies between 5.7% and 13% (geometric mean), 7.6% and 40% (arithmetic mean), and 12% and 53% (Hashin and Shtrikman mean). These results are in line with observations reported by Pribnow (1994) and Buntebarth and Schopper (1998). The latter authors rated the geometric mean model as best solution for situations, in which no additional criterion (e.g., an empirical alpha-value describing the pore structure of the rock) is considered.

Calculation of BTC with the harmonic mean (Eq. (3.3)) results in abnormal values (Figure 3.2). More than 96% of the calculated BTC values are negative. This misfit, which was already recognized, for instance, by Beck and Beck (1965), Robertson and Peck (1974), and Pribnow (1994), can be attributed to the equation for calculating the MTC which allows the denominator to get zero or negative. Especially high porosities almost inevitably cause a negative denominator. Hence, this model is unfeasible and, with it, also the mean of the harmonic and arithmetic mean.

The goodness-of-fit and the effective porosity are antipathetically related also for the other models. This observation is linked with the mathematical formalisms of BTC calculation, causing greater uncertainties with increasing porosity.

For rocks with anisotropies > 5%, the arithmetic-mean model did not show the expected correlation with the direction of measurement, (i.e., the fit between measured and calculated TC should be better for data acquired parallel to bedding). The observations made in this study are just in opposition to this expectation and may question the physical concept of this model. This criticism is in line with earlier observations (e.g., Zimmerman, 1989) and implies that a body (rock) consisting of alternating slabs of matrix and pore space is physically unrealistic, at least for clastic sediments. The arithmetic-mean model, however, may apply for fractured aquifers in carbonate rocks in the situation of a layered fracture pattern. Moreover, because the bulk of our samples is only weakly anisotropic, the results of this study strictly apply only to rocks with anisotropies ≤20%. More strongly anisotropic rocks may fit the arithmetic-mean model better.

The use of isooctane (Figure 3.4) has no statistically discernible impact on the quality of fit for either model (independent t-test, $\alpha = 0.05$, $p > 0.1$). The lower TC of isooctane compared to water and, hence, the much smaller ratio between the TC of saturating fluid and air (factor ~ 3 for isooctane compared to factor ~ 24 for water) does not result in larger deviations between measured and predicted BTC, as one might expect. This observation is in contradiction to results of Buntebarth and Schopper (1998), who showed that the type of saturating fluid had a strong influence on the fitting of the geometric mean. These authors identified an acceptable fit for the geometric mean only for sandstone samples that were water-saturated ($n = 11$). More work is needed to explain this discrepancy.

The re-calculation of isooctane-saturated BTC to water-saturated BTC is afflicted with several uncertainties. Therefore, saturation with water should be preferred to isooctane saturation in determining BTC. The use of isooctane or other alkanes, such as n-heptane utilized by Woodside and Messmer (1961b) and Zimmerman (1989), is an expedient alternative only for determining the porosity of argillaceous rocks.

In the special situation of handling BTC measured with different saturation fluids (air, water, n-heptane), we recommend averaging the respective matrix values. This recommendation is rooted in the observation of a significant difference in MTC calculated from dry-measured BTC (lower by 5.2%) compared to the matrix value calculated from isooctane-saturated BTC (paired t-test, $n = 127$, $\alpha = 0.05$, $p < 0.000$). A difference also is observed, but with an opposite trend, between MTC calculated from dry-measured BTC (higher by 4.9%) compared to the matrix value calculated from water-saturated BTC (paired t-test, $n = 1019$, $\alpha = 0.05$, $p < 0.000$).

3.7.2 Correction charts

The only mixing model that generally reproduces the measured BTC satisfactorily is the geometric mean, but the data scatter is still large. The other mean models examined in this paper produce TC data often significantly deviating from measured values. The question arises whether it is possible to calculate correction charts that permit reduction of the deviation and the scatter of the different mean models. In order to verify this idea, the relations between absolute deviation (in W m^{-1} K^{-1}) and porosity for the different lithotypes and mean models (Figure 3.6a-d) are investigated. For this purpose, the data set is subdivided into porosity (%) classes: 0−3; 3−6; 6−10; 10−15; 15−20; 20−25; 25−30; 30−35 (Figure 3.6e-h).

The mean deviation within each porosity class is the input parameter for the regression analyzes. The statistical treatment resulted in linear or logarithmic trend lines and respective equations, which in turn provided the correction values for every mean model and lithotype. For statistical reason, the initial data set was randomized into two groups. The first group (85% of data) is the regression set, from which the equations were derived; the second group (15% of data) is the testing set, from which the fitting parameters were calculated. The inversion of the curves shown in Figure 3.6e-h gives the correction value (in W m^{-1} K^{-1}) for sandstone, mudstone, limestone, and dolomite, calculated by the arithmetic or geometric means.

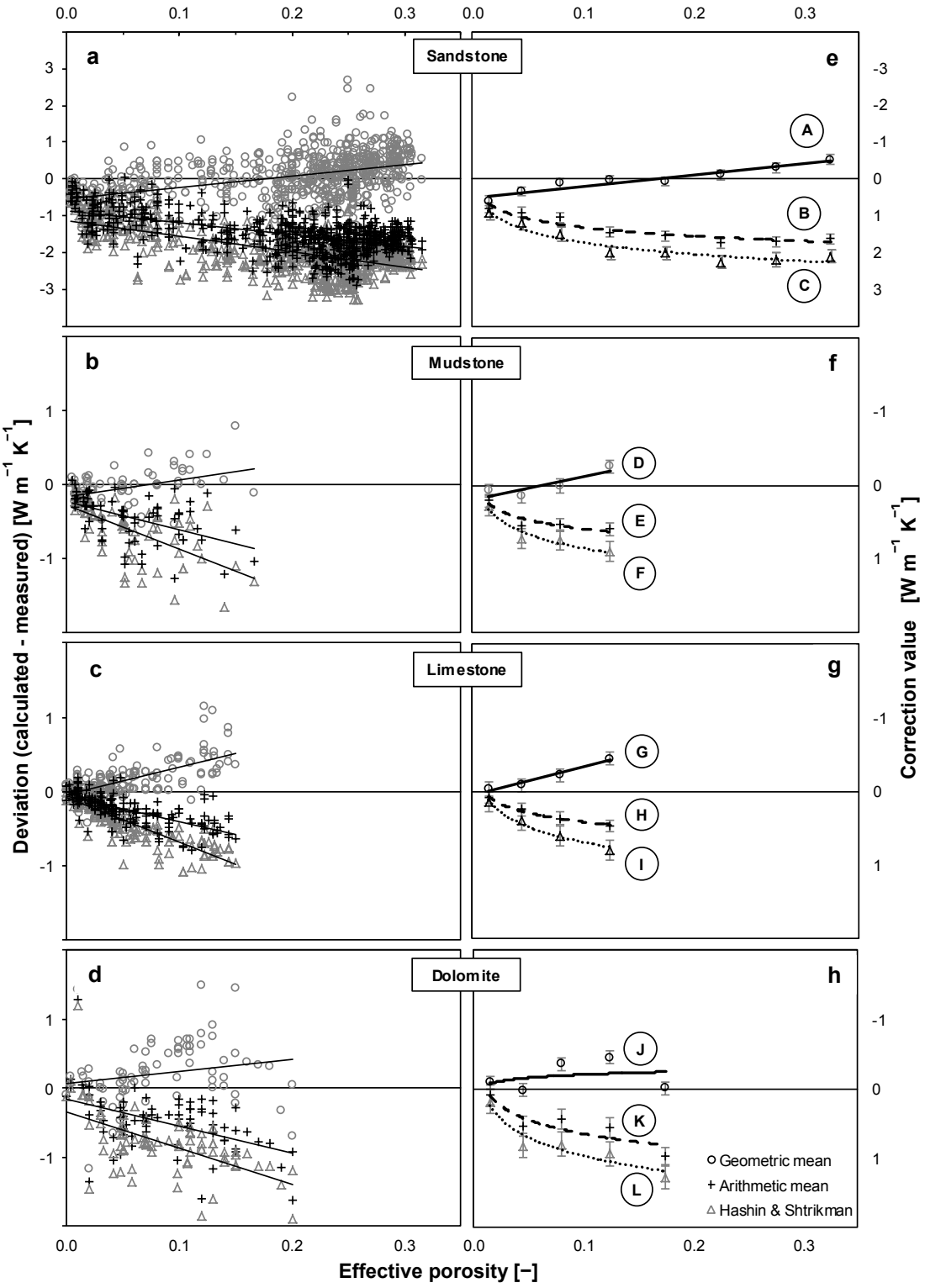

Figure 3.6: Variations between calculated and measured BTC values (a, b, c, d) and derived correction values (e, f, g, h) for different lithotypes and mixing models, respectively. Regression coefficients and RMS values for A-L are listed in Table 3.1.

Table 3.1 is a compilation of the computed regression parameters for the various lithotypes and mean models.

Table 3.1
Coefficients of determination for correction charts shown in Fig. 6 (right panel).

	Mean Model[1]	Regression Parameter[2]			
		Type	b_o	b_1	R^2
			Sandstone		
A	GM	linear	0.504	-3.039	0.927
B	AM	ln	2.091	0.340	0.887
C	H&S	ln	2.779	0.461	0.922
			Mudstone		
D	GM	linear	0.208	-3.261	0.757
E	AM	ln	1.003	0.179	0.871
F	H&S	ln	1.502	0.282	0.941
			Limestone		
G	GM	linear	0.059	-3.833	0.967
H	AM	ln	0.820	0.178	0.986
I	H&S	ln	1.378	0.301	0.976
			Dolomite		
J	GM	linear	-0.104	-1.648	0.436
K	AM	ln	1.329	0.293	0.781
L	H&S	ln	1.869	0.388	0.909

[1] GM: Geometric mean; AM: Arithmetic mean; H&S: Hashin & Shtrikman.
[2] b_0 and b_1 are constants for regression model. Linear (linear) equation is $y = b_1 x + b_0$, logarithm equation (ln) is $y = b_1 \ln(x) + b_0$, where y ist the calculated correction value and x is the given porosity value.

The correlation coefficients for the different groups scatter between 0.76 and 0.99, indicating a remarkably good degree of tracking. The only lithotype, for which the linear regression did not result in a satisfying improvement of the fit, is dolomite, with a quite poor correlation coefficient of 0.43 for the geometric mean. The possible reason for this unsatisfying result is the fact that in our suite of dolomite rocks, the number of samples and the TC deviations in each porosity class are highly variable and, consequently, the calculated averages of deviation display larger uncertainties.
The impact of implementing these correction coefficients in the calculation of BTC is shown in Figure 3.7a and b, separately for every model and lithotype. The application of the correction results in noticeable improvements of the fits for all mean models, on average reducing the deviations for the Hashin and Shtrikman equation by 70%, for the arithmetic mean by 59%, and for the geometric mean by another 15%. This improvement is exemplarily shown for the arithmetic mean used for BTC calculation of sandstone samples (Figure 3.7c), exposing a smaller mean deviation and variance. In order to improve the applicability of the correction chart, mean deviations were converted to user-friendly correction values (Figure 3.8). Those porosity-dependent correction values either have to be added to or subtracted from (depending on the algebraic sign) the original mixing-model results.

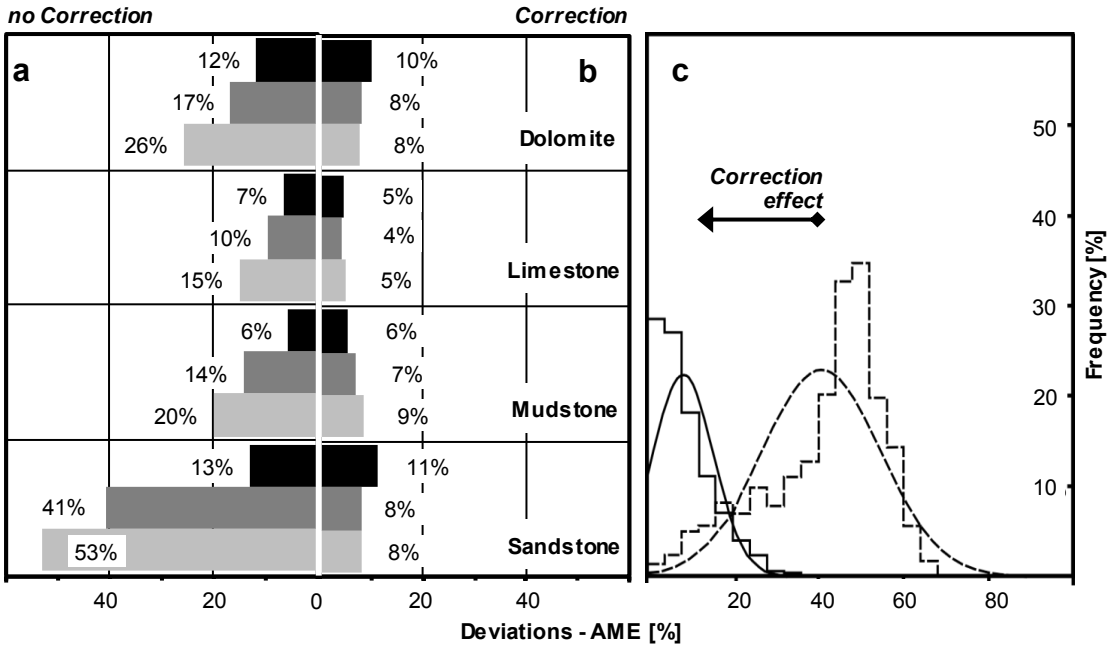

Figure 3.7**:** Left: Comparison of corrected (b) (Figure 3.6 and Table 3.1) and uncorrected (a) calculations. Black bar: geometric mean; dark grey bar: arithmetic mean; light grey bar: Hashin and Shtrikman mean. Right: Distribution of percent errors (c) for corrected (solid line) and uncorrected (dashed line) values for sandstones calculated with the arithmetic mean.

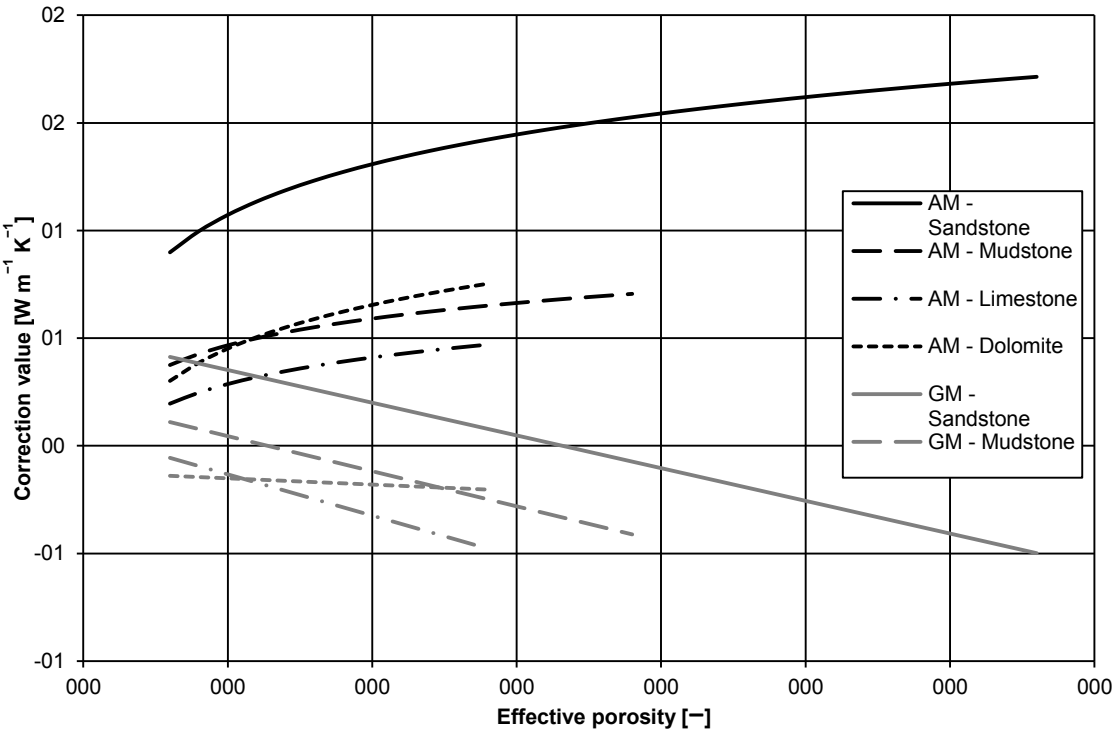

Figure 3.8: Correction values for BTC calculation from dry measurements for sedimentary rocks. Arithmetic mean (AM): black lines, geometric mean (GM): grey lines.

3.7.3 Conversion equations

The unsatisfying fitting behavior of most mean models and the necessity of applying correction charts encouraged us to examine our data set in whether is it possible to set up an equation that permits estimation of the water-saturated BTC directly from dry-measured BTC data and known porosity values.

For this goal, the data set was tested using a multiple regression analysis. The fitting result of this type of analysis is shown in Figure 3.9. For statistical reasons, the initial data set was randomized into two groups of 85% (regression set) and 15% (testing set). The plot of measured versus predicted BTC shows a good fit for both the regression and the testing sets, with a deviation of 10 ± 8% (AME) for the testing set.

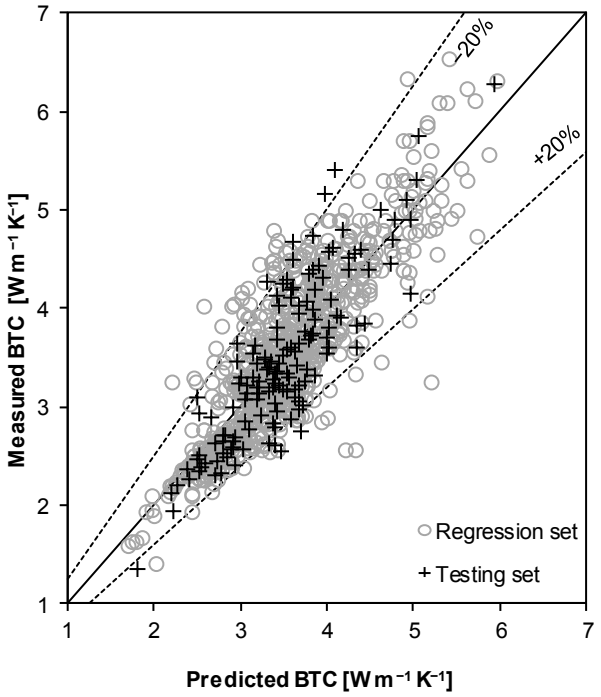

Figure 3.9: Scatter plot of predicted (conversion equation based on multiple regression analyzes) vs. measured water-saturated BTC.

The coefficients of determination resulting from the multiple regression analysis are listed in Table 3.2 for the entire sample set and, additionally, for the various lithotypes. All listed equations display an AME equal or less than 10%. If the lithotype is sufficiently well known, we recommend application of the equations elaborated for mudstone, limestone, and dolomite instead of the one based on the entire set of samples, because the specific equations exhibit significantly lower AMEs (ANOVA, Tukey's HSD, $\alpha = 0.05$).

Table 3.2
Results of multiple regression analyses of dry and saturated-measured TC and effective porosity, respectively.

Samples	Regression Parameter			R^2	ANOVA			AME
	b_0	b_1	b_2		F	n	p	
All	-0.406	7.417	1.216	0.726	1348.0	740/130	<0.001	10.2 ± 7.8 %
Sandstone	1.579	2.244	0.817	0.667	581.4	494/87	<0.001	8.7 ± 7.2 %
Mudstone	-0.696	8.446	1.290	0.895	243.9	51/8	<0.001	8.3 ± 7.7 %
Limestone	0.272	3.961	0.914	0.758	243.2	134/23	<0.001	4.8 ± 4.3 %
Dolomite	0.631	2.527	0.890	0.779	119.6	60/10	<0.001	6.5 ± 9.0 %

b_0, b_1 and b_2 are constants for the multiple regression model. Equation is $y = b_1 x + b_2 z + b_0$, where y ist the calculated bulk thermal conductivity, x is the given porosity value and z is the dry thermal conductivity.
R^2 = coefficient of determination, F = F-value, n = number of samples (first value: regression set, second value: testing set), p = observed significance level, AME = arithmetic mean error ± 1 standard deviation for testing group.

Table 3.3 finally compares the errors after applying correction charts to the various mean models with the errors resulting from utilizing the new conversion equations. Considering all samples, the implementation of correction charts resulted in the smallest error for the arithmetic mean. If lithotypes are concerned, the fit of all these approaches is good for every mixing model, except for the geometric mean applied to sandstone. This misfit is a consequence of the high porosity of the sandstone samples (19.8 ± 8.8%), combined with the mathematical structure of the geometric mean.

Table 3.3
BTC mean errors as from correction equations and direct conversion equations.

Samples	Correction Equations			Conversion Equations
	AM	GM	H&S	
All	7.4 ± 6.9 %	9.5 ± 9.5 %	7.6 ± 7.0 %	10.2 ± 7.8 %
Sandstone	8.3 ± 7.2 %	11 ± 10.2 %	8.4 ± 7.2 %	8.7 ± 7.2 %
Mudstone	7.1 ± 7.3 %	5.7 ± 4.9 %	8.5 ± 9.1 %	8.3 ± 7.7 %
Limestone	3.9 ± 3.7 %	4.6 ± 4.5 %	4.4 ± 4.0 %	4.8 ± 4.3 %
Dolomite	8.0 ± 7.4 %	10.0 ± 9.5 %	7.6 ± 7.1 %	6.5 ± 9.0 %

GM: Geometric mean; AM: Arithmetic mean; H&S: Hashin & Shtrikman.

For all lithotypes, both the correction equations for the mean models and the conversion equations yield to uncertainties in the BTC ranging between 5% and 10% (AME). These uncertainties are significantly better than those arising from application of the mean models without correction (range of AME 11–42%).

3.8 Conclusions

In both, the general geothermal characterization of sedimentary basins, including the assessment of geothermal reservoirs, as well as the modeling of other potential resources, for exapmle oil and gas, the implementation of large numbers of BTC data is required. In the light of the time-extensive effort necessary to determine water-saturated TC for such large sample sets, methods are requested to reduce the work load. The mean models for BTC of two-phase rocks presented and evaluated in this study constitute efficient tools to transfer air-saturated BTC to water-saturated BTC, if porosity is known from independent sources (e.g., derived from standard well logs). If a correction equation (see section 6.2) is applied to the mean model result, the errors in water-saturated BTC can be reduced to 4−11%, depending on lithotype. In turn, the application of model-independent conversion equations (reported in section 3.6.3) allows a general reduction of the error to < 10%. This accuracy is sufficient for many industrial as well as specific scientific applications.

The more sophisticated physical rock models, that are advanced effective-medium theory models, require knowledge of additional rock parameters that are not readily available. Acquisition of such additional parameters (for instance, distribution and size of grains and pores) is labor-intensive and requires special analytical equipment. Therefore, such models are suitable for basic research, but are unlikely to be routinely used in exploration studies.

It remains to be investigated whether the TC measuring technique, on which the data evaluated in this study are based and which do not apply pressure to the sample, eventually underestimates the measured TC, and whether these effects are statistically relevant to alter the equations and correction charts developed in this study. In addition, laboratory studies are required to eliminate the ambiguity in pressure dependency of TC in the range < 10 MPa. This would also shed light on the reasoning of the small deviation between DB and OS values recognized by Popov et al. (1999), implying a pressure dependency of TC that is much smaller than reported by other authors (e.g., Somerton et al., 1963; Walsh and Decker, 1966; Hurtig and Brugger, 1970; Buntebarth, 1991; Kukkonen et al., 1999). Unless those ambiguities are overcome, we consider our results as universal for application for isotropic to weakly anisotropic sedimentary rocks.

Acknowledgements

The authors would like to thank Ilmo T. Kukkonen and one further anonymous reviewer who helped to considerably improve the paper with their constructive feedback. We are deeply in debt to Daniel F. Merriam for his valuable comments.

3.9 References

Abdulagatova, Z. Z., Abdulagatov, I. M., and S. N. Emirov (2009), Effect of temperature and pressure on the thermal conductivity of sandstone, Int. J. Rock Mech. Min. Sci., 46, 6, 1055−1071.

Balling, N., Kristiansen, J., Breiner, N., Poulsen, K. D., Rasmusen, R., and S. Saxov (1981), Geothermal measurements and subsurface temperature modelling in Denmark, Geologiske Skrifter, Department of Geology Aarhus University 16, 172 pp.

Beck, A. E. (1988), Methods for determining thermal conductivity and thermal diffusivity, in Handbook of terrestrial heat-flow density determination, edited by Haenel et al., pp. 87−124, Dordrecht, Netherlands, Kluwer Academic Publishers.

Beck, J. M., and A. E. Beck (1965), Computing Thermal Conductivities of Rocks from Chips and Conventional Specimens, J. Geophys. Res., 70, 20, 5227−5239.

Birch, F. (1950), Flow of heat in the Front Range, Colorado. Bulletin of the Geological Society America 61, 567−630.

Blackwell, D. D., and J. L. Steele (1989), Thermal conductivity of sedimentary rocks: measurement and significance, in Thermal history of sedimentary basins, methods and case histories, pp. 13−35, edited by Naeser, N.D. and T.H. McCulloh, Springer.

Brailsford, A. D., and K. G. Major (1964), The thermal conductivity of aggregates of several phases, including porous material, Br. J. Appl. Phys., 15, 313–319.

Brigaud, F., Chapman, D. S., and S. Le Douran (1990), Estimating thermal conductivity in sedimentary basins using lithological data and geophysical well logs, AAPG Bulletin, 74, 1459−1477.

Bruggeman, D. A. G. (1935), Berechnung verschiedener Konstanten von heterogenen Substanzen – I. Dielektrizitätskonstanten und Leitfähigkeiten der Mischkörper aus isotropen Substanzen, Annalen der Physik, 24, 5, 636–679.

Budavari, S. (1989), The Merck Index - Encyclopedia of Chemicals, Drugs and Biologicals. Rahway, NJ: Merck and Co., Inc., 817 pp.

Buntebarth, G. (1991), Thermal properties of KTB Oberpfalz VB core samples at elevated temperature and pressure, Scientific Drilling 2, 73−80.

Buntebarth, G., and J. R. Schopper (1998), Experimental and theoretical investigations on the influence of fluids, solids and interactions between them on thermal properties of porous rocks, Phys. Chem. Earth., 23, 9−10, 1141−1146.

Carson, J. K., Lovatt, S. J., Tanner, D. J., and A. C. Cleland (2005), Thermal conductivity bounds

for isotropic, porous materials, Int. J. Heat Mass Transfer, 48, 11, 2150−2158.

Clauser, C. (2006), Geothermal Energy, in Advanced Materials and Technologies edited by K. Heinloth, pp. 541, Landolt-Börnstein, Group VIII, Vol. 3, Energy Technologies, Subvol. C: Renewable Energies, Springer Verlag, Heidelberg-Berlin.

Clauser, C. (2009), Heat transport processes in the earth's crust, Surv. Geophys., 30, 3, 163–191.

Clauser, C., Hartmann, A., Koch, A., Mottaghy, D., Pechnig, R., and V. Rath (2007), Erstellung statistisch abgesicherter thermischer und hydraulischer Gesteinseigenschaften für den flachen und tiefen Untergrund in Deutschland, Phase 1 – Westliche Molasse und nördlich angrenzendes Süddeutsches Schichtstufenland, Final report for BMU-Project FKZ 0329985, RWTH Aachen, http://137.226.107.10/aw/cms/website/zielgruppen/gge/research_gge/geothermik/~vfa/Erstellung_statistisch_abgesicherter_thermischer/, last accessed: 09.07.2012.

Demongodin, L., Pinoteau, B., Vasseur, G., and R. Gable (1991), Thermal conductivity and well logs: a case study in the Paris Basin, Geophys. J. Int., 105, 3, 675–691.

Eucken, A. (1940), Allgemeine Gesetzmäßigkeiten für das Wärmeleitvermögen verschiedener Stoffarten und Aggregatzustände, Forschung auf dem Gebiete des Ingenieurwesens, Ausgabe A, 11 (1), pp. 6–20.

Fuchs, S., and A. Förster (2010), Rock thermal conductivity of Mesozoic geothermal aquifers in the Northeast German Basin, Chemie der Erde, 70 (Supplement 3), 13−22.

Goss, R. D., and J. Combs (1976), Thermal conductivity measurement and prediction from geophysical well log parameters with borehole application, Dallas, Institute for Geosciences, University of Texas at Dallas, 1019–1027.

Goutorbe, B., Lucazeau, F., and A. Bonneville (2006), Using neural networks to predict thermal conductivity from geophysical well logs, Geophys. J. Int., 166 (1), 115−125.

Gröber, H., Erk, S., and U. Grigull (1955), Die Grundgesetze der Wärmeübertragung, 2rd ed., Springer, Berlin, Wien, Heidelberg, 465 pp.

Hanai, T. (1968), Electrical properties of emulstons, in Emulsion science, edited by P. Sherman, New York, Academic Press, pp. 354−477.

Hartmann, A., Rath, V., and C. Clauser (2005), Thermal conductivity from core and well log data, Int. J. Rock Mech. Min. Sci., 42, 7−8, 1042–1055.

Hartmann, A., Pechnig, R., and C. Clauser (2008), Petrophysical analysis of regional-scale thermal properties for improved simulations of geothermal installations and basin-scale heat and fluid flow, Int. J. Earth Sci., 97, 2, 421–433.

Hashin, Z., and S. Shtrikman (1962), A variational approach to the theory of the effective magnetic permeability of multiphase materials, J. Appl. Phys., 33, 10, 3125–3131.

He, L., Hu, S., Huang, S., Yang, W., Wang, J., Yuan, Y., and S., Yang (2008), Heat flow study at the Chinese Continental Scientific Drilling site: borehole temperature, thermal conductivity, and radiogenic heat production, J. Geophys. Res., 113 (B02404), doi:10.1029/2007JB004958.

Homuth, S., Sass, I., Hamm, K., and S. Rumohr (2008), In-Situ-Messungen zur Bestimmung geothermischer Untergrundkennwerte, Grundwasser 13, 4, 241–251.

Horai, K.-I. (1991), Thermal conductivity of Hawaiian basalt: a new interpretation of Robertson and Peck's data, J. Geophys. Res., 96, 3, 4125–4132.

Hurtig, E., and H. Brugger (1970), Wärmeleitfähigkeitsmessung unter einaxialem Druck, Tectonophysics, 10, 67−77.

Hutt, J. R., and J. W. Berg (1968), Thermal and electrical conductivities of sandstone rocks and ocean sediments, Geophysics, 33, 3, 489−500.

Kappelmeyer, O., and R. Haenel (1974), Geothermics with special reference to application, Gebrüder Borntraeger Berlin, Geopublication Associates, Geoexploration Monographs, Series 1, No. 4., 238 pp.

Kukkonen, I. T., Jokinen, J., and U. Seipold (1999), Temperature and pressure dependencies of thermal transport properties of rocks: implications for uncertainties in thermal lithosphere models and new laboratory measurements of high-grade rocks in the Central Fennoscandian Shield, Surveys in Geophysics 20, 1, 33−59.

Lemmon, E. W., McLinden, M. O., and D. G. Friend (2005), Thermophysical properties of fluid systems, in NIST Chemistry WebBook, NIST Standard Reference Database, edited by Linstrom, P. J., Mallard, W. G., pp. 20899, Number 69, National Institute of Standards and Technology, Gaithersburg MD, http://webbook.nist.gov.

Lewis, T., Villinger, H., and E. Davis (1993), Thermal conductivity measurement of rock fragments using a pulsed needle probe, Can. J. Earth Sci., 30, 3, 480–485.

Lichtenecker, K. (1924), Der elektrische Leitungswiderstand künstlicher und natürlicher Aggregate, Physikalische Zeitschrift 25 (8), pp. 169−181, 193−204, 226−233.

Liu, S., Feng, C., Wang, L, and L. Cheng (2011), Measurement and analysis of thermal conductivity of rocks in the Tarim Basin, Northwest China, Acta Geologica Sinica - English Edition, 85, 3, 598−609.

Majorowicz, J., Šafanda, J., and Torun-1 Working Group (2008), Heat flow variation with depth in Poland: evidence from equilibrium temperature logs in 2.9-km-deep well Torun-1, Int. J. Earth Sci., 97, 2, 307−315.

Maxwell, J. C. (1892), A treatise on electricity and magnetism, Clarendon Press 1, 3rd ed., 440, Oxford, UK, 425 p.

Mottaghy, D., Schellschmidt, R., Popov, Y. A., Clauser, C., Kukkonen, I. T., Nover, G., Milanovsky, S., and R. A. Romushkevich (2005), New heat flow data from the immediate vicinity of the Kola super-deep borehole: Vertical variation in heat flow confirmed and attributed to advection, Tectonophysics, 401, 1−2, 119−142.

Norden, B., and A. Förster (2006), Thermal conductivity and radiogenic heat production of sedimentary and magmatic rocks in the Northeast German Basin, AAPG Bulletin 90, 6, 939−962.

Orilski, J., Schellschmidt, R., and T. Wonik (2010), Temperaturverlauf und Wärmeleitfähigkeit im Untergrund der Bohrung Groß Buchholz GT1 in Hannover. Extended Abstract, Geothermiekongress 2010. 17.–19.11.2010, Karlsruhe, 10 p.

Popov, Y. A., Pevzner, L. A., Rumushkevich, R. A., Korostelev, V. M., and M. G. Vorob'jev (1995), Thermophysical and geothermal sections obtained from Kolvinskaya well logging data, Physics of the solid Earth, English Translation, 30, 9, 778–789.

Popov, Y. A., Pribnow, D. F. C., Sass, J. H., Williams, C. F., and H. Burkhardt (1999), Characterization of rock thermal conductivity by high-resolution optical scanning, Geothermics, 28, 2, 253–276.

Popov, Y. A., Tertychnyi, V., Romushkevich, R., Korobkov, D., and J. Pohl (2003), Interrelations between thermal conductivity and other physical properties of rocks: Experimental data, Pure Appl. Geophys., 160, 5, 1137–1161.

Popov, Y. A., Miklashevskiy, D., Romushkevich, R., Novikov, S., Parshin, A., and S. Safonov (2010), Proceedings World Geothermal Congress 2010, Bali, Indonesia, 25−29 April 2010, 9 p.

Popov, Y. A., Romushkevich, R., Korobkov, D., Mayr, S., Bayuk, I., Burkhardt, H., and H. Wilhelm (2011), Thermal properties of rocks of the borehole Yaxcopoil-1 (Impact Crater Chicxulub, Mexico), Geophys. J. Int., 184, 2, 729–745.

Pribnow, D. F. C. (1994), Ein Vergleich von Bestimmungsmethoden der Wärmeleitfähigkeit unter Berücksichtigung von Gesteinsgefügen und Anisotropie. VDI Fortschrittsberichte Reihe 19 (75), VDI-Verlag, Düsseldorf, Germany, 111 p.

Progelhof, R. C., Throne, J. L., and R. R. Ruetsch (1976), Methods for predicting the thermal conductivity of composite systems: a review, Polymer Engineering & Science 16, 9, 615−625.

Reuss, A. (1929), Berechnung der Fließgrenze von Mischkristallen auf Grund von Plastizitätsbedingung für Einkristalle,. Zeitschrift für Angewandte Mathematik und Mechanik, 9, 49–58.

Revil, A. (2000), Thermal conductivity of unconsolidated sediments with geophysical applications, J. Geophys. Res., 105, B7, 16749−16768.

Robertson, E. C., and D. L. Peck (1974), Thermal conductivity of vesicular basalt from Hawaii, J. Geophys. Res., 79, 32, 4875−4888.

Schärli, U., and L. Rybach (1984), On the thermal conductivity of low-porosity crystalline rocks, Tectonophysics, 103, 307−313.

Schön, J.-H. (1996), Physical properties of rocks, fundamentals and principles of petrophysics, in Handbook of Geophysical Exploration: Seismic Exploration, Vol. 18, edited by Treitel, S. and Helbig, K., Oxford, UK, Pergamon, 583 p.

Schopper, J. R. (1991), An amendment to Gassmann's theory. Proceedings of the 14th SPWLA European Formation Evaluation Symposium, December 9-11, London, England.

Schütz, F., Norden, B., Förster, A., and DESIRE Group (2012), Thermal properties of sediments in southern Israel: a comprehensive data set for heat flow and geothermal energy studies, Basin Research, 24, 357–376.

Sen, P. N., Scala, C., and M. H. Cohen (1981), A self-similar model for sedimentary rocks with application to the dielectric constant of fused glass beads, Geophysics, 46 (5), 781−795.

Somerton, W. H. (1992), Thermal properties and temperature-related behavior of rock/fluid systems, Amsterdam, Elsevier Science Publishers B.V., 257 p.

Somerton, W. H., Ward, S. H., and M. S. King (1963), Physical Properties of Mohole Test Site Basalt, J. Geophys. Res., 68, 3, 849−856.

Sugawara, A., and Y. Yoshizawa (1961), An investigation on the thermal conductivity of porous materials and its application to porous rock, Aust. J. Phys., 14, 4, 469−480.

Tinga, W. R., Voss, W. A. G., and D. F. Blossey (1973), Generalized approach to multiphase dielectric mixture theory, J. Appl. Phys., 44, 9, 3897−3902.

Vasseur, G., Brigaud, F., and L. Demongodin (1995), Thermal conductivity estimation in sedimentary basins, Tectonophysics, 244, 1−3, pp. 167−174.

Voigt, W. (1928), Lehrbuch der Kristallphysik, Teubner, Leipzig, 978 p.

Walsh, J. B., and E. R., Decker (1966), Effect of pressure and saturating fluid on the thermal conductivity of compact rock, J. Geophys. Res., 71, 12, 3053−3061.

Watanabe, H. (2003), Thermal conductivity and thermal diffusivity of sixteen isomers of alkanes: CnH2n+2 (n = 6 to 8), J. Chem. Eng. Data, 48, 1, 124–136.

Wiener, O. H. (1912), Die Theorie des Mischkörpers für das Feld der stationären Strömung, Erste Abhandlung: Die Mittelwertsätze für Kraft, Polarisation und Energie. Abhandlungen der mathematisch-physischen Klasse der Königlich-Sächsischen Gesellschaft der Wissenschaften 32, 6, 507–604.

Woodside, W., and J. Messmer (1961a), Thermal conductivity of porous media. I. Unconsolidated

Sands, J. Appl. Phys., 32, 9, 1688–1699.

Woodside, W., and J. Messmer (1961b), Thermal conductivity of porous media. II. Consolidated Rocks, J. Appl. Phys., 32, 9, 1699–1706.

Zimmerman, R. W. (1989), Thermal conductivity of fluid-saturated rocks, Journal of Petroleum Science and Engineering, 3, 3, 219–227.

4 Thermal conditions of the central Sinai Microplate inferred from new surface heat-flow values and continuous borehole temperature logging in central and southern Israel

Felina Schütz, Hans-Jürgen Förster, Andrea Förster

Submitted to: Journal of Geodynamics

4.1 Abstract

This paper reports ten new surface heat-flow density (q_S) values for central and southern Israel (central Sinai Microplate), whose crystalline crust and lithosphere formed as part of the Neoproterozoic Arabian-Nubian Shield. Heat flow was calculated in Mesozoic sediments using the classical approach of heat-flow determination by implementing in the analysis high-precision continuous temperature logs obtained in air- and/or water-filled boreholes. Thermal conductivity (TC) measured for a large suite of rock samples of lithotypes making up the sequence was assigned to temperature gradients in intervals for which the lithology was known. The heat-flow values obtained for different depth intervals in a borehole as well as the average values for the individual borehole locations cover a narrow range, attesting heat-conduction conditions. A steady-state thermal model along an E–W crustal cross section through the area shows that the observed systematic spatial distribution of the q_S values, which range between 50 and 62 mW m^{-2}, can primarily be explained to variations in the thickness of the upper crust and in the ratio between sedimentary and crystalline rocks therein. Given the lapse time of thermal heat transfer through the lithosphere, the q_S data monitor the crustal thermal conditions prior to rift- and plume-related lithospheric thermal perturbations that have started in the larger area ca. 30 Ma ago. Observed and modeled q_S display the best fit for a pre-Oligocene lithosphere–asthenosphere boundary (LAB) at ~150 km, which would be at the upper end of LAB depths determined from stable areas of the Arabian Shield (150–120 km) not affected by the young, deep-seated thermal processes that have caused a further uprise of the LAB. Our data imply or predicts that the surface heat flow of the Sinai Microplate generally tends to decrease along N–S and W–E traverses, from ~45–50 mW m^{-2} to ~55–60 mW m^{-2}. Surface heat flows on the order of 55–60 mW m^{-2} may be common in the northern Arabian Shield, where it exhibits typical lithosphere structure and composition and is unaffected by young heating processes, compared to values of ≤ 45 mW m^{-2} recently determined in the southern Arabian Plate for the Arabian Platform.

4.2 Introduction

Knowledge of the thermal regime of a lithosphere unit is required to understand its geodynamic setting and the tectonic processes involved in its formation (Pollack, 1982; Nyblade and Pollack, 1993; Jaupart and Mareschal, 1999). The conductive surface heat flow (q_S) (also termed terrestrial heat flow) provides insight into the steady-state thermal situation of an area for time scales of tens of millions of years. Its variation across a distinct lithosphere unit is usually related to changes in

crustal composition and therewith associated variations in the radiogenic heat budget (e.g. Rudnick et al., 1998; Förster and Förster, 2000; Mareschal and Jaupart, 2004; Perry et al., 2006; Hasterok and Chapman, 2011, and references therein) or by variations in mantle heat flow (e.g. Pollack and Chapman, 1977).

Methodically, there are different ways to determine the continental q_S. The classic approach is to measure a continuous borehole temperature (T) log and process it in terms of temperature gradients (Powell et al., 1988). In a thermally undisturbed borehole, these gradients can be determined at low levels of inaccuracy over intervals of centimeters to tens of meters. On the contrary, there are studies that use single T-readings determined in one borehole or, to enlarge the spatial data coverage, in a cluster of boreholes. Those single T-readings are obtained during petrophysical well-logging (bottom-hole temperatures) or during well testing (drillstem-test temperatures). The single T-data approach causes a larger uncertainty in the q_S value (Deming et al., 1990) as the temperature gradient is usually determined over a large depth interval.

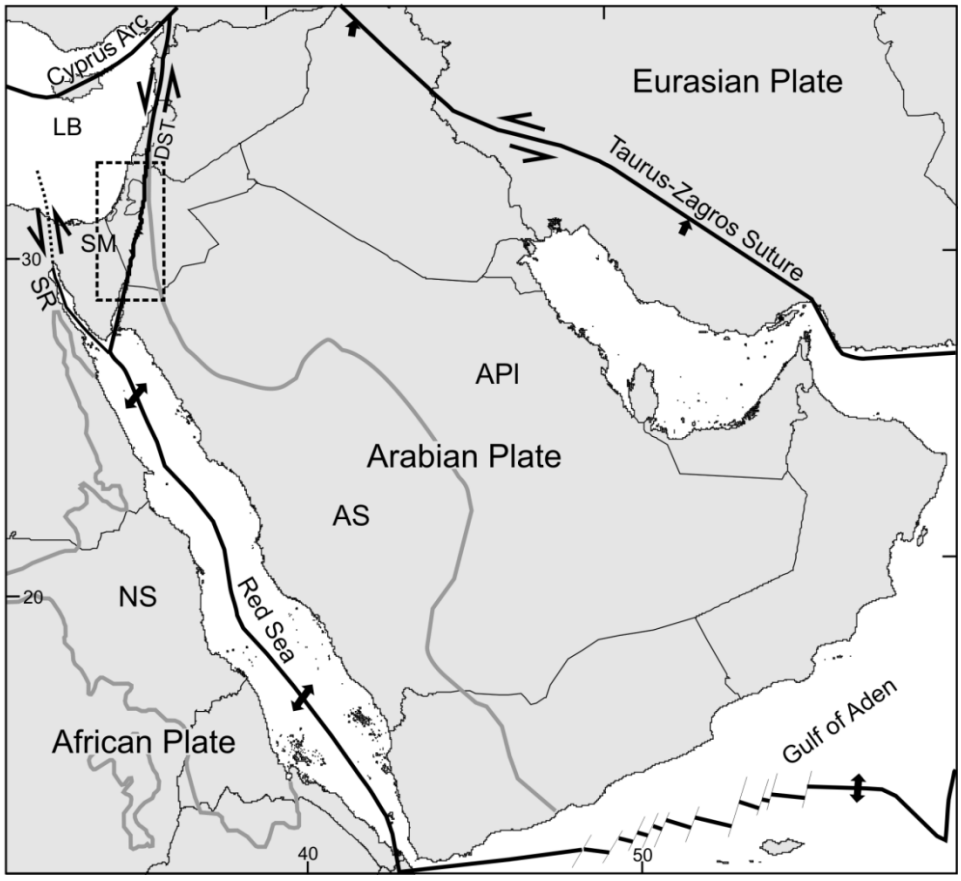

Figure 4.1: General map of the Arabian Plate and its immediate surroundings (modified from Mahmoud et al., 2005; Stern and Johnson, 2010; Johnson et al., 2011). AS – Arabian Shield, APl – Arabian Platform, NS – Nubian Shield, SM – Sinai Microplate, LB – Levantine Basin, DST – Dead Sea Transform, SR – Suez Rift. Dashed line encloses the study area.

In this paper, we present and discuss new q_S values for the central Sinai Microplate (SM; also termed Sinai Block or Sinai Subplate) in central and southern Israel (Figure 4.1), determined by the classic approach using continuous T-logs. These values, interpreted as representing the terrestrial heat flow, are discussed in comparison to heat-flow data previously obtained by Eckstein and Simmons (1978) using the same approach, and to data recently determined for entire Israel that are mostly based on the single-T-data approach (Shalev et al., 2013). In contrast to these former studies, our focus was not to consider and statistically examine all T-data available for a discrete area, but rather to perform an in-depth study for a selection of boreholes accessible for precision T-logging, for which detailed lithostratigraphic descriptions were available. With the inclusion of borehole intervals above the water table and comparison of heat-flow values obtained there with those of the water-filled portions of the same borehole, it was assured that the q_S values represent the heat-conduction conditions in the subsurface, i.e., were not perturbed by hydrogeologic processes. The lack of core samples in all studied boreholes did not permit to directly obtain laboratory-measured rock thermal-conductivity (TC) of the studied sedimentary section. This drawback could be largely compensated by the circumstance that an extensive database of TC measured on core material from neighboring boreholes or from outcrops for the respective lithotypes typical for the study area was at disposal (Schütz et al., 2012). The assignment of lithotype-specific TC to T-gradient intervals allowed a fine-tuned determination of interval heat-flow values that ultimately gave rise to modest-error average heat-flow values for each individual borehole site.

The new q_S values are envisioned to improve the knowledge about spatial patterns in terrestrial heat flow across the area of central and southern Israel. For an elucidation of the effects of variable crustal properties, e.g. structure and composition, on q_S, a steady-state thermal model along an E–W cross section was generated, in the direction in which former studies implied large and unsystematic fluctuations of q_S over short distances.

Considering that the diffusion rate of heat pulses through the lithosphere is on the order of several tens-of-millions of years (e.g. Fowler, 1990), the q_S values reported here largely reflect the thermal conditions prior to the onset of young lithospheric heating, which has started at ~30 Ma ago with the initiation of the Red Sea rifting farther south (Bohannon et al., 1989) and which has caused the separation of the African Plate from the Arabian Plate (AP) and the Nubian Shield from the Arabian Shield (AS) (see Figure 4.1). Since then, deep-rooted magmatic processes linked with rifting and plume generation caused lithosphere thinning and upwelling of the asthenospheric mantle (Camp and Roobol, 1992; Shaw et al., 2003; Krienitz et al., 2007; Chang and Van der Lee, 2011; Hansen et al., 2012). As manifested by T-data recorded in xenoliths entrained in young alkali basalts (cf. Al-Mishwat and Nasir, 2004; Kaliwoda et al., 2007), these processes resulted in a substantial increase

of the temperature in the upper mantle and, likely, already in the lower portions of the crust, but have not yet caused an increase of the heat flow at the surface.

The SM was part of the AP until about 15 Ma ago, when it got separated by the onset of the Dead Sea Transform (DST) (see Figure 4.1). Consequently, the q_S data presented here also support a more substantiated knowledge on the terrestrial heat-flow pattern of the AP, which is not yet well constrained and a matter of controversial discussion. Existing q_S data are unevenly distributed across the plate, with fairly new values only determined for its marginal portions (Oman and Yemen: Lucazeau et al., 2008; Rolandone et al., 2013; Jordan: Galanis et al., 1986; Förster et al., 2007; southern Saudi Arabia: Gettings, 1982; Gettings and Showail, 1982).

4.3 Geological background

Israel is located on the SM, which extends from the Gulf of Suez in the south along the DST in the east to the Levantine Basin (LB) in the west (Figure 4.1). The boundaries towards the north and northwest are poorly defined (Mascle et al., 2000), but the northern border may correspond to the active collision/subduction boundary along the Cyprus Arc (Mahmoud et al., 2005). In the early Miocene, the SM was separated from the African Plate via the Gulf of Suez and from the AP via the DST. The DST was activated 14–18 Ma ago (Freund et al., 1970; Bartov et al., 1980), connecting the zone of oceanic spreading in the Red Sea with the Zagros–Taurus collision zone. Along the DST, left-lateral strike slip of 105 km is accommodated (Freund et al., 1970), with a slip rate of ~4.4 mm a^{-1} (Mahmoud et al., 2005).

The crystalline crust in Israel formed as part of the Arabian-Nubian Shield (ANS). The shield rocks only outcrop in southernmost Israel and are overlain by sediments farther north. These sediments reflect a Triassic-Cretaceous passive margin deposition and show an increase in thickness to the northwest and a change of composition from clastic to carbonatic (Garfunkel and Derin, 1984; Laws and Wilson, 1997).

The ANS formed basically during the Pan-African orogenic cycle lasting from 870−550 Ma (Stern, 1994; Stein and Goldstein, 1996; Stern and Johnson, 2010). A recent study of Morag et al. (2012) implied an earlier onset (marked by island-arc activity at about 1.0 Ga ago) as well as a termination of this orogenic cycle about 580 Ma ago. In some parts of SW Arabia and Yemen, small tracts of older (Archean) crust are also preserved (Stern and Johnson, 2010).

The “Supercontinent Cycle” started with rifting and the breakup of Rodinia (870−800 Ma). The production of juvenile crust is associated with the formation of the Mozambique ocean (800−690 Ma) which closed when East and West Gondwana collided (630−600 Ma) (Stern and

Johnson, 2010). The final post-orogenic stage started at ~600 Ma and ended in early Cambrian times at ~530 Ma, characterized by crustal and lithospheric reworking and orogenic collapse. The assembly of amalgamated juvenile magmatic arcs, post-amalgamation of sedimentary and volcanic basins and magmatic intrusions/extrusions generated a multifaceted suite of igneous and sedimentary rocks that form the bulk of the crust in Israel (Segev, 1987; Weissbrod, 2005). Subsequently, stabilization and cooling of the northern ANS was accompanied by subsidence towards the north and the beginning of the platform stage at early Cambrian times (Segev, 2005). The area was a stable platform owing to its position as a passive continental margin until Paleogene times, and an extensive veneer of carbonate and clastic sediments had accumulated. In southern Israel and adjacent areas, sedimentation was accompanied by several short-lived minor episodes of Mesozoic intra-plate magmatic activity associated with the evolution of the Eastern Mediterranean Neotethyan passive continental margin (Wilson et al., 2000). The most widespread phase of igneous activity, accompanied by considerable basement uplift and erosion, occurred during the late Jurassic and early Cretaceous.

The lithosphere of the AS (which was part of the ANS until ~30 Ma ago) differs in terms of composition and history from the Arabian Platform (APl) (cf. Figure 4.1). The crust of the APl lacks Cryogenian and Ediacaran rocks (700−543 Ma) (Stern and Johnson, 2010) and is up to several-km thicker than that of the AS (Hansen et al., 2007). The AS hosts several large Cenozoic basalt fields, the emplacement of which is connected with the origin of the Afro-Arabian rift system (Stern and Johnson, 2010; Nasir and Stern, 2011). Thus, although mostly covered by variably thick sedimentary sequences, central and southern Israel was formerly part of the northern AS.

4.4 Background on surface heat flow in Israel

Heat flow in the study area was first evaluated by Eckstein and Simmons (1978) as part of a reconnaissance geothermal exploration of Israel by performing temperature logging in abandoned oil wells and idle water wells (cf. Figure 4.2a). Different groups of values were delineated according to the different heat-transfer processes interpreted from the data. The q_S values notably not affected by hydrogeological effects and interpreted as representing a “regional” heat flow show relatively low values ranging from 31 to 47 mW m^{-2}. In contrast, higher values (57–85 mW m^{-2}) were attributed to local, deep thermal anomalies without a specification of their origin. All these values, although attributed to conductive heat flow, display a remarkable variation over short distances (31−84 mW m^{-2}). It remained unknown whether this large range in value bears a large uncertainty due to the methodology used. A disadvantage of the early study certainly was that it had

to rely on a limited number of TC values determined for general lithotypes that may not fully comply with the observed lithology-dependent T-gradient variations observed in the boreholes. In addition, TC values represent dry rock. For porous rocks, those values are generally lower than the TC of water-saturated rocks (Schütz et al., 2012; Fuchs et al., 2013). Thus, a consideration of the real in- situ TC for the water-filled part of a borehole section would likely alter the heat-flow value.

The most recent publication of q_S values for Israel reports data based on bottom-hole temperatures (BHTs) and drill-stem-test-temperatures (DSTs), complemented by some temperature logs (Shalev et al., 2013). With respect to rock TC, the study has practically the same limitations (see Schütz et al., 2012) as inherent in former studies in the area. The borehole locations, from which T data were used to calculate heat flow, are shown on a colored map (Figure 4.2b), with the disadvantage that the color coding of heat flow (in 5 mW m^{-2} steps) is not in accordance to the mapped pattern. Unfortunately, the individual heat-flow values are not reported in table form with all the data used in the determination. However, for the study area of this paper, the map displays a similarly wide range of values as shown by previous work (40–55 mW m^{-2} with local anomalies of 60–80 mW m^{-2}) (cf. section 3).

Other heat-flow studies in Israel pertain to measurements in lake and marine environments along the DST, yielding mean q_S values of 29 mW m^{-2} for the Dead Sea Basin (DSB) and 67 mW m^{-2} for the Gulf of Eilat (Ben-Avraham et al., 1978). The latter value is in the range of offshore data (64–93 mW m^{-2}; Ben-Avraham and Von Herzen, 1987) interpreted as being affected by heating of the crust due to continental rifting.

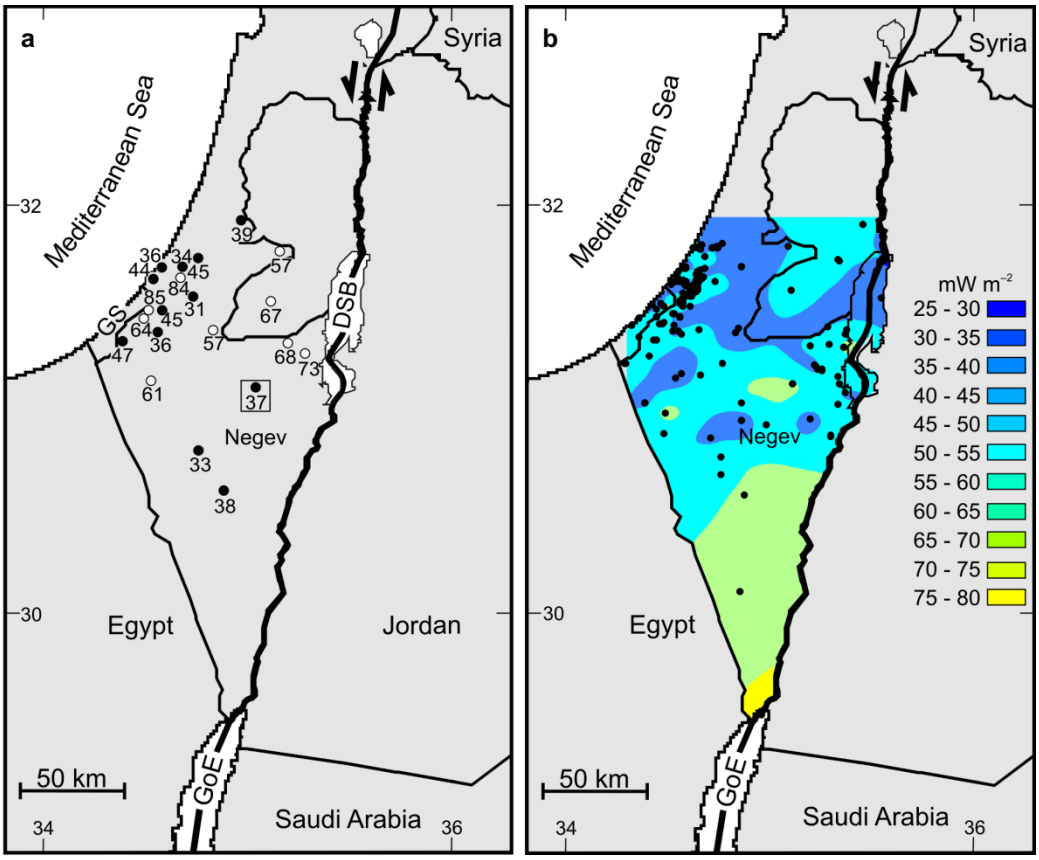

Figure 4.2: (a) Surface heat-flow data (in mW m^{-2}) of Eckstein and Simmons (1978) plotting within and immediately adjacent to the area studied in this paper. Filled circle = unaffected by hydrologic processes indicating regional heat flow; open circles = unaffected by hydrologic processes indicating locations with deep thermal anomalies. Location framed by rectangle is the Daya 1 borehole, which was re-interpreted by Schütz et al. (2012) (see Figure 4.3). GoE is Gulf of Eilat; DSB is Dead Sea Basin. (b) Detail of a surface heat-flow map provided by Shalev et al. (2012). Dots mark the locations of boreholes, from which temperature data were used for interpolation.

4.5 New surface heat-flow values

4.5.1 Borehole temperature logs

To faithfully decipher the relationship between terrestrial heat flow and lithosphere properties, high-quality q_S values are indispensable. In the best situation, a continuous precision temperature log is obtained in the borehole, and TC is measured on the recovered drill core (e.g., Blackwell and Steele, 1989; Deming et al., 1990). Ideally, the boreholes are several hundred meters to kilometers deep, under thermal equilibrium, and conductive heat flow predominates over large depth intervals. Given these requirements we selected ten boreholes in the area between the Mediterranean Sea in the west and the DST in the east (Figure 4.3).

The boreholes, in which new T-logs were measured, were originally drilled for oil or water exploration. The drilling process was completed between 1980 and 2006, thus having allowed the

boreholes to fully recover from thermal perturbations caused by drilling and drill-mud circulation. All boreholes are cased so that intra-borehole fluid flow was inhibited. The T-logs and details on T-logging are provided in Appendix A.

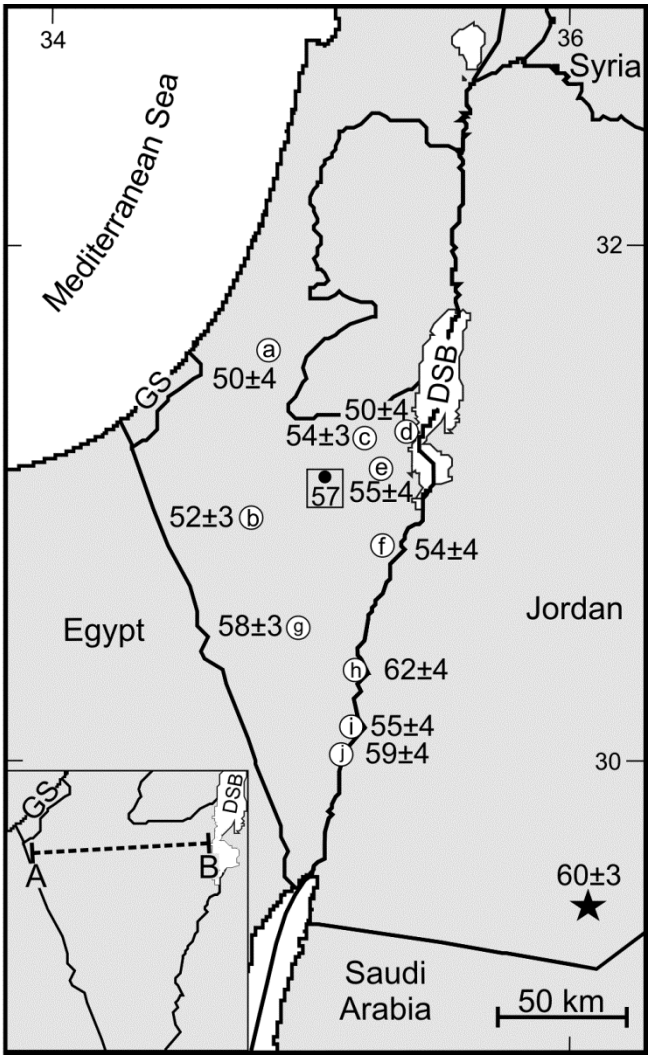

Figure 4.3: Surface heat-flow values (in mW m^{-2} with mean absolute error) from this study. Letters in circles refer to the name of wells and the thermal data shown in Table 4.1. The rectangle marks the Daya 1 borehole, for which revision of the original data of Eckstein & Simmons (1987) yielded a q_S average of 57 mW m^{-2} (Schütz et al., 2012), which exceeds the originally determined value by 20 mW m^{-2} (cf. Figure 4.2a) and is fully in line with the q_S values reported in this study. The dashed line in the inset map marks the trace of the DESIRE seismic profile (A–B) along which lithosphere thermal modeling was performed (cf. Figures 4.4–4.5). The star approximates the location of the heat-flow borehole cluster studied by Förster et al. (2007).

4.5.2 Rock thermal conductivity

As practiced in previous heat-flow studies in Israel, the lack of core samples from the T-logged boreholes required an assignment of TC measured on samples from nearby wells or outcrops. We

used the TC data measured on core and rock samples from 16 boreholes in the vicinity of our heat-flow sites as well as from five outcrop locations. The measurements were performed as part of a preceding study (Schütz et al., 2012) and covered all major sedimentary formations and lithotypes of the study area.

Samples were measured both dry and water-saturated using the optical-scanning apparatus (Lippmann and Rauen, GbR Schaufling, Germany) (Popov et al., 1999), considering that the T-data for heat-flow determination are from both dry (air-filled) and water-filled borehole sections. Details on the lithotype TC and how TC was assigned to borehole heat-flow intervals (Table 4.1) are provided in Appendix B.

4.5.3 Heat-flow determination

Surface heat flow was calculated by using the interval method and the Fourier equation of heat conduction:

$$qs = -\lambda \cdot \frac{\partial T}{\partial z} \tag{4.1}$$

where λ is the TC (W m^{-1} K^{-1}) and $\partial T/\partial z$ is the T-gradient (°C km^{-1}) for the interval. Possible sources of error were considered after Powell et al. (1988). A standard deviation (σ) is provided for each interval T-gradient. The standard error (SE) for the interval T-gradient was determined using the following equation:

$$SE = \frac{\sigma}{\sqrt{N-1}} \tag{4.2}$$

where σ is standard deviation and n marks the number of temperature gradient values in the interval. The error of interval TC was estimated to be 10 % (σ_λ). The absolute error (α_i) of the interval heat-flow value results from the uncertainties of interval T-gradient and TC:

$$\alpha_i = \sqrt{(\partial T/\partial z \cdot \sigma_\lambda)^2 + (\lambda \cdot SE)^2} \tag{4.3}$$

The mean heat-flow value for a borehole site is given with a mean absolute error, which is calculated using the following error propagation formula based on the geometric mean:

$$\alpha = qs/n\sqrt{(\alpha_i/qs_i)^2 + (\alpha_{in}/qs_{in})^2} \quad (4.4)$$

where n is the number of individual interval heat-flow values and α_i the corresponding absolute error. A critical evaluation of the T-profiles was made to decipher temperature perturbations due to fluid movement. Some localized temperature perturbations were indeed recognized, but are not omnipresent in formations known to be aquifers. Thus, in the selection of intervals for heat-flow calulation only those borehole intervals were considered, in which the change of T-gradient could be unequivocally related to variations in TC. Preference was given to depth intervals that display a relatively homogeneous lithology indicated by the litho-log and the T-gradient plot, to keep the uncertainty in interval TC determination low. A detailed description of the heat-flow determination in each borehole is elaborated in Appendix C.

The mean values of q_S determined for each of the ten borehole sites are in the range of 50–62 mW m^{-2} (Table 4.1). The values expose mean absolute errors between <5 and 7 mW m^{-2}. Three clusters of values can be distinguished. Cluster 1 includes four heat-flow sites immediately south and west of the DSB, with values in the range of 50–55 mW m^{-2} (Figure 4.3). Cluster 2 comprises two heat-flow sites located some 50 km west of cluster 1, with q_S of 50 resp. 52 mW m^{-2}. This pattern may imply a weak trend of decrease in heat flow from the east (near the DST) to the west (near the Mediterranean cost). Cluster 3 comprises four heat-flow sites in southern Israel, with slightly higher q_S than the values farther north (55–62 mW m^{-2} compared to 50–55 mW m^{-2}; cf. Figure 4.3).

Table 4.1: Thermal data for 10 borehole locations.

Site		Interval (m)	Well cond.	Interval T-gradient ∂T/∂z (°Ckm^{-1})	SE	σ (°Ckm^{-1})	Interval λ λ (Wm^{-1}K^{-1})	σ_λ	Interval qs_i qs_i (mW m^{-2})	α_i	qs mean qs (mW m^{-2})	α
a	Qiryat	130–228	w	17.1	0.3	2.8	3.0	0.3	51.3	5.8	49.7	3.9
	Gat 1	355–405	w	28.3	0.3	2.1	1.7	0.2	48.1	5.1		
b	Ashalim 2	73–141	a	14.7	0.2	1.3	3.7	0.4	54.4	5.8	51.8	2.8
		141–225	a	15.7	0.2	2.2	3.3	0.3	51.8	5.8		
		288–316	a	16.3	0.2	0.8	3.0	0.3	48.9	5.1		
		360–400	w	17.4	0.2	1.0	3.0	0.3	52.2	5.5		
c	Arad 1	84–140	a	24.3	0.2	1.6	2.2	0.2	53.6	5.6	53.5	3.2
		188–251	a	15.5	0.1	0.8	3.4	0.3	52.5	5.4		
		262–330	a	22.6	0.2	1.5	2.4	0.2	54.3	5.6		
d	Efeh 3	50–160	a	18.8	0.2	1.6	2.7	0.3	50.8	5.3	50.1	3.7
		171–220	a	14.1	0.1	0.7	3.5	0.4	49.4	5.1		
								0.0				
e	T.C. 1	170–225	a	24.0	0.1	1.1	2.4	0.2	57.6	5.9	55.1	4.1
		250–276	a	14.2	0.2	1.0	3.7	0.4	52.5	5.8		
f	Ein	169–265	w	15.9	0.0	0.2	3.4	0.3	54.1	5.4	54.3	3.9
	Ofarim 1	304–330	w	20.2	0.1	0.4	2.7	0.3	54.5	5.5		
g	Meishar 1	100–157	a	17.7	0.2	1.4	3.4	0.3	60.2	6.4	58.3	2.6
		185–211	a	17.1	0.4	1.8	3.6	0.4	61.7	7.9		
		222–250	a	19.8	0.2	1.2	3.0	0.3	59.4	6.4		
		263–300	a	23.7	0.1	0.8	2.5	0.3	59.3	6.0		
		325–423	a	14.3	0.1	1.2	3.8	0.4	54.3	5.6		
		446–467	a	29.0	0.2	1.1	1.9	0.2	55.1	5.7		
h	Paran 28	80–139	w	24.9	0.5	3.8	2.2	0.2	54.7	6.7	62.1	4.0
		139–222	w	26.6	0.2	1.7	2.6	0.3	69.2	7.2		
		222–405	w	27.1	0.2	2.3	2.3	0.2	63.3	6.5		
i	Notza 1	160–250	w	18.4	0.2	1.7	3.0	0.3	55.2	5.8	55.2	3.6
		350–423	w	34.0	0.5	4.3	1.7	0.2	57.8	6.5		
		555–625	w	17.0	0.3	2.7	3.1	0.3	52.7	6.3		
j	Qetura 9	100–130	w	28.8	0.3	1.5	2.1	0.2	60.5	6.4	59.0	3.9
		150–220	w	24.5	0.6	4.7	2.4	0.2	58.8	7.7		
		316–363	w	14.1	0.1	0.7	4.1	0.4	57.8	5.9		

Well cond. - well condition, a - air- or w - water-filled, λ - interval TC, qs_i - interval surface heat flow, qs - surface heat flow, SE - standard error, σ - standard deviation, σ_λ - standard deviation of TC , α_i - absolute interval error, α - absolute error

4.6 Crustal thermal modeling

To investigate the dependence of q_S on properties of the crust (e.g., thickness, internal structure, composition) and thus to elucidate whether trends in q_S can be caused by these crustal properties, a 2-D steady-state temperature model was calculated along an E–W traverse described in section 4.6.1. The modeling considered conductive heat flow and is based on a numerical approach to solve the following equation:

$$qs = qd + \int A(z)\partial z = \lambda d\left[\frac{\partial T}{\partial z}\right]_d + \int A(z)\partial z \qquad (4.5)$$

where q_S is the surface heat flow and q_d (in mW m^{-2}), λ_d (in W m^{-1} K^{-1}), and $(\partial T/\partial z)_d$ (in °C km^{-1}) are the heat flow, the TC, and the thermal gradient, respectively, at a certain depth (d). $\int A(z)\partial z$ is the integral of the radiogenic heat production (in µW m^{-3}) from the surface to the depth (d). The MATLAB R2010b software was used to solve the equation, applying the finite-element method.

The lower thermal boundary of the model is the temperature at the lithosphere–asthenosphere boundary (LAB), which is assumed to be 1300 °C (Turcotte and Schubert, 2002). The upper thermal-boundary condition is the annual surface temperature, which is 19.5 °C in the Negev and 20.0 °C in the Gaza strip. Both to the east and to the west, the model is extended by 30 km, to minimize random effects. At the side boundaries, heat-flow density is set to zero, thus excluding any horizontal heat transfer.

Modeling was performed for two LAB depths (150 km and 120 km), which were kept constant across the modeled transect. They reflect the likely maximum and minimum pre-Oligocene lithosphere thicknesses beneath the AP and, thus, central and southern Israel. In regions of Arabia, not influenced by post-Oligocene geodynamic and magmatic processes, Hansen et al. (2007) determined the LAB in the transition zone between the AS and the APl at 150 km stepwise decreasing to 120 km towards the shield. Steady-state geotherms calculated for the APl in Oman also implied a LAB depth of 150 km (Rolandone et al., 2013). Such a range in thickness is in accordance with estimates made by Artemieva and Mooney (2001) for Neoproterozoic lithosphere in general (140 ± 40 km).

In the modeling, rock TC is handled as temperature- and pressure-corrected values. Temperature correction for sedimentary rocks was done applying the equation of Somerton (1992). For igneous and metamorphic rocks, temperature-correction equations experimentally determined for granite,

gneiss, mafic granulite, and peridotite were used (Seipold, 2001). Pressure correction of TC for crustal rocks was performed using the formalism elaborated by Seipold (2001):

$$\lambda = \lambda_0 \cdot (1 + \alpha \cdot p) \qquad (4.6)$$

where λ_0 is temperature-corrected TC (W m^{-1} K^{-1}), α is the rock-specific pressure coefficient (% kbar^{-1}), and p is pressure (kbar). Pressure determination considered a mean crustal density of $3.0 \cdot 10^3$ kg m^{-3} as implied by the gravity data of Götze et al. (2007). Furthermore, it was assumed that density increases by $0.015 \cdot 10^3$ kg m^{-3} down to a lithostatic pressure of $4 \cdot 10^2$ MPa and by $0.001 \cdot 10^3$ kg m^{-3} further down to $15 \cdot 10^2$ MPa (Schön, 1983).

4.6.1 Conceptual model

4.6.1.1 Structure

The structure of the model is based on the geological interpretation of an E−W section of the upper lithosphere studied by refraction/reflection seismic soundings (Mechie et al., 2009). This section was given preference over a SE−NW oriented, geologically quasi-identical crustal section farther to the south (Weber et al., 2004) as it resolves more finely the crystalline crust, especially the lower crust (cf. Figure 4.1). The E−W section is in total 235 km long and crosses the DST at the latitude of the Lisan Peninsula of the DSB. Our thermal model considered only the western part of this traverse, extending from the western edge of the DSB to the south of the Gaza Strip (cf. Figure 4.3). The first three layers of the model encompass sedimentary units distinguished by different P-wave velocities (2.8, 3.8−4.2 and 5.1−5.4 km s^{-1}, resp.). The top of the fourth layer equals the top of Pan-African crystalline basement. The upper crust is divided into two layers with P-wave velocities of 5.8−6.1 and 6.4−6.5 km s^{-1}, respectively, implying a more silicic upper part and a less silicic lower part. The lower crust is separated into two layers with P-wave velocities of 6.8 resp. 7.2 km s^{-1}, again indicating a certain inhomogeneity in composition as corroborated by the relatively large variation in composition and modal mineralogy of lower-crustal xenoliths entrained in basalts from Israel (Esperança and Garfunkel, 1986; Mittlefehldt, 1986).

The crust thins from the east towards the west from about 35 to 25 km and shows a minimum value underneath the Gaza Strip of 21 km (Mechie et al., 2013). The upper crystalline crust is ~18 km thick in the proximity of the DST, but only ~13 km in the most west. In the same direction, the

lower crust thins from between 14−15 km to about 6 km. The sedimentary cover is relatively thin (~3 km) just west of the DST and thickens to values of ~6 km close to the Gaza Strip. The westward thinning of the crust prolongs offshore of Israel towards the Mediterranean LB (Netzeband et al., 2006, and references therein).

4.6.1.2 Composition of the lithosphere

The sedimentary rocks overlying the crystalline basement in Israel encompass various stratigraphic groups and rock types (Bartov et al., 1972; Weissbrod, 2005, Schütz et al., 2012). The very thin upper model layer 1 (Figure 4.4b) correlates with the Mt. Scopus Group (Senonian) and younger sediments, consisting mainly of marl and chalk (Table 4.2). Layer 2 comprises the Cretaceous Kurnub Group (mostly clastic sediments) and the Judea Group (mostly carbonates). The third layer contains the Jurassic Arad Group (mostly carbonates), the Triassic Ramon Group (carbonates and clastic rocks), and the Triassic to Paleozoic Negev Group (mostly clastic sediments).

The model layer 4 represents the two uppermost crystalline crustal layers distinguished in the seismic velocity model (cf. Figure 4.4a). On outcrop west and east of the DST, these rocks encompass a rich variety of types, ranging from felsic alkali-feldspar granites to mafic gabbros and diorites and their extrusive and metamorphic equivalents (Beyth et al., 1994; Mushkin et al., 2003; Eyal et al., 2010). The fractions of the different rock types reported in Table 4.2 correspond to those used by Förster et al. (2010, their Table 1) for modeling the thermal state of the lithosphere in adjacent southern Jordan.

Xenolith data from Israel (Navon et al., 2007) and adjacent Jordan and Syria (Al-Mishwat and Nasir, 2004; Krienitz and Haase, 2011) correspondingly indicate that the lower crust of the northern AS is mainly composed of plagioclase-rich (concentrated in the upper part = layer 5) and pyroxene-rich mafic granulites, which likely predominate in the lower part and make up model layer 6. Moreover, xenoliths from the Qarnei-Hittin volcano (N Israel) document the additional occurrence of garnet-bearing granulites, likely forming the lowermost part of the crust near to the Moho (cf. Navon et al., 2007). Ignoring this probably volumetrically subordinate type in our model is justified, because its thermal properties are virtually the same as those of the two major varieties of granulites.

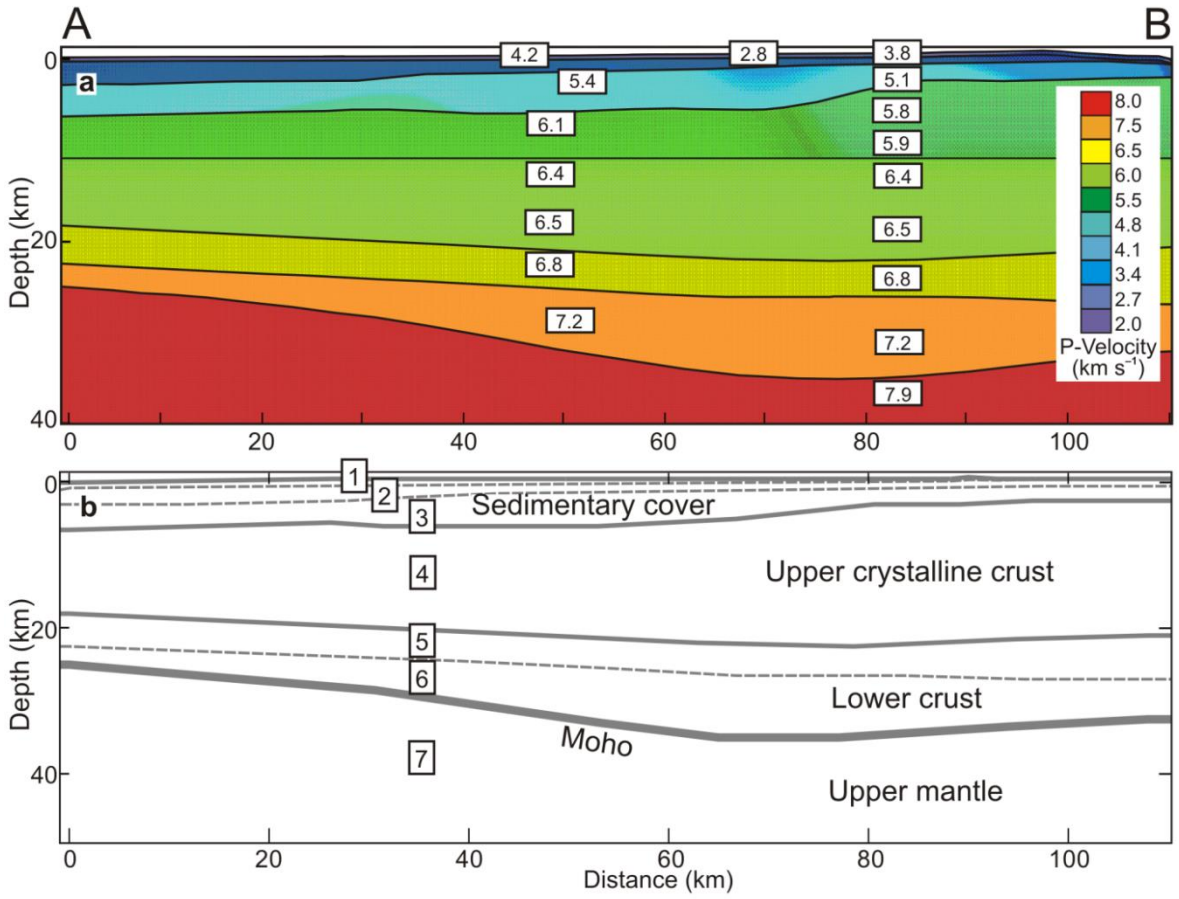

Figure 4.4: (a) Lithosphere structure and P-wave velocities along the DESIRE seismic profile (Mechie et al., 2009) (cf. Figure 4.3). (b) Geological interpretation. The numbering of the lithosphere units refers to the conceptual model for thermal modeling explained in detail in section 4.6.1 (cf. Table 4.2).

Our model is in line with recent geophysical studies implying a thinned continental crust also offshore of Israel in the LB (Netzeband et al., 2006; Gardosh and Druckman, 2006). These results questioned the existence of oceanic crust beneath the Mediterranean as favored by other authors (Ginzburg and Ben-Avraham, 1987; Segev, 2002; Ben-Avraham et al., 2002). Irrespective of having formed or not in the LB, oceanic crust is unlikely to constitute the base of crust in the modeled section.

Direct information on the composition of the lithospheric mantle beneath northern Arabia, coming from xenoliths from Jordan and Syria, indicate peridotites (spinel lherzolite) as dominant rock type, accompanied by pyroxenites (Nasir, 1992; Nasir and Safarjalani, 2000; Navon et al., 2007; Nasir and Rollinson, 2009). Pyroxenites remained unconsidered in the modeling, since these rocks differ only insignificantly in thermal properties from the overwhelming peridotites.

Additionally to this (base) compositional model, two other models were calculated, aimed at examining the sensitivity of parameter variation on the thermal result. Since the upper crystalline crust exerts by far the major control on q_S, owing to being the major source of radiogenic heat

production, parameter variation was limited to layer 4. These additional models considered that this layer could easily be 10% more felsic or more mafic than predicted by the base model data listed in Table 4.2 (cf. section 4.5.2).

Table 4.2: Composition and petrophysical parameters of the lithosphere

Unit	Rock type	Layer		λ	A	ρ
		No.	%	($Wm^{-1}K^{-1}$)	(μWm^{-3})	(10^3 kgm^{-3})
Sedimentary cover	Marl/chalk	1	100	2.1	0.7	2.4
	Clastic/ carbonatic	2	100	2.8	0.6	2.6
	Clastic/ carbonatic	3	100	2.8	0.5	2.6
Upper crystalline crust	Metamorphic rocks	4	17.0	2.79	1.19	2.71
	Rhyolite/rhyodacite	4	6.0	2.63	2.52	2.63
	Afs granite/syenogranite	4	6.0	2.93	3.55	2.58
	Monzogranite	4	17.0	2.60	1.47	2.61
	Granodiorite/qtz monzonite	4	32.0	2.30	1.73	2.69
	Qtz monzodiorite	4	11.0	2.17	0.95	2.77
	Monzogabbro	4	11.0	2.04	0.73	2.83
		mean		2.45	1.55	2.69
Lower crust	Plg-rich granulite	5	100	3.5	0.06	3.0
	Pyx-rich granulite	6	100	3.1	0.03	3.0
Upper mantle	Spinel lherzolite	7	100	4.2	0.02	3.36

For layer numbering see Figure 4.6b, λ - thermal conductivity, A - radiogenic heat production, d - density, Afs - alkali feldspar, Qtz - quartz, Plg - plagioclase, Pyx - pyroxene.

4.6.1.3 Thermal properties of the lithosphere

Data from Schütz et al. (2012) were used to calculate average TC values for model sedimentary layers 1–3 (Table 4.2). The values range from 2.1 to 2.8 W m^{-1} K^{-1}. The TC estimates for upper crustal rocks (layer 4) correspond to those published by Förster et al. (2010), who measured a broad spectrum of igneous and metamorphic rocks outcropping in southern and western Jordan. Average TC values of these rocks were between 2.0 and 2.9 W m^{-1} K^{-1} (cf. Table 4.2).

Own attempts to measure in the laboratory the TC of lower crustal rocks on xenolith samples failed for mainly two reasons. First, xenoliths collected from Jordan, Syria, and Israel are generally cracked, thus displaying anomalously high porosities. Second, they experienced variable degrees of overprinting which resulted in the partial destabilization of alteration-prone primary minerals. Alternatively, TC values for xenoliths were calculated from modal mineralogy corrected for in-situ conditions, i.e., reconstructing the mineralogy at the P-T conditions of the pre-Oligocene lower crust. This approach resulted in an average TC of 3.5 W m^{-1} K^{-1} for plagioclase-rich granulite (layer 5) and of 3.0 W m^{-1} K^{-1} for pyroxene-rich granulite (layer 6). The TC of the lithospheric

mantle (4.2 W m^{-1} K^{-1}) considered lab-measured data for spinel lherzolite reported by Kukkonen and Peltonen (1999) and Tommasi et al. (2001).

Heat production of the rocks assigned to the three model sedimentary units was determined from gamma logs and inferred from literature values (Vila et al., 2010; Schütz et al., 2012), averaging to ~0.6 μW m^{-3} (Table 4.2). Data on heat production of the upper crystalline crust and the lower crust are those determined by Förster et al. (2010) for rocks exposed in Jordan, slightly verified by data related to studies on corresponding rock types outcropping in Israel (Beyth et al., 1994; Bogoch et al., 2002; Mushkin et al., 2003; Eyal et al., 2010). Values applied in the model range from 0.03 (lower crust) to 3.1 μW m^{-3} (alkalifeldspar granites in the uppermost crust). The heat production for the upper mantle was committed to 0.02 μW m^{-3}, considering abundant spinel-lherzolite xenolith data from northern Arabia, whose values varied only in a narrow range between 0.01 and 0.04 μW m^{-3} (Shaw et al., 2003; Förster et al., 2010).

4.6.2 Results

Considering the thermal properties listed in Table 4.2, modeling yielded the following results. **Scenario 1 (LAB at 150 km):** The modeled q_S pattern perfectly reproduces the measured q_S values between profile km 30 and 110, for which data control is provided (Figure 4.5a). Given the uncertainties in q_S, the measured data are also matched, if the upper crust would be either about 10% more or less radiogenic than reported in Table 4.2. Such small spatial variations, implying that percentages of the rock types differ from those used in our calculations, are certainly within the realm of possibility and do not interfere with the geophysical data for this crustal segment. The match between modeled and measured q_S by using a homogeneous LAB depth across the model domain attributes the changes in q_S entirely to variations in continental crust properties. In accordance to what is recorded in the measured values, the calculated q_S values possess a small decrease from the east (~55 mW m^{-2}) to the west (~52 mW m^{-2}). Considering the uncertainties in the measured q_S data, the corresponding heat flow at the Moho would amount to 27−24 ± 2 mW m^{-2}.

Scenario 2 (LAB at 120 km): The modeled q_S values (56−58 mW m^{-2}) slightly overestimate the measured values (Figure 4.5b). The measured q_S would be satisfied only if the upper crystalline crust has a 10% or lower radiogenic heat production, i.e., a more mafic upper crust than suggested in the base model (cf. Table 4.2).

Although this “less silicic” subcase of scenario 2 would also provide a reasonable match with the

measured q_S, two circumstances exist that enforce us to favor a pre-Oligocene LAB at 150 km beneath this part of the former AS. First, LAB depths as deep as 160 km have been determined in those areas of the AS east of the DST, which remained unaffected by the young thermal processes and, therefore, may reflect the pre-Oligocene LAB signature (e.g., Mohsen et al., 2006). Second, in the immediate vicinity of the DST, the 120-km-LAB thermal model implies a pre-Oligocene Moho temperature as high as 710 °C, exceeding those suggested for the 150 km scenario by roughly 70 °C (cf. Figure 4.5c). Such a high Moho temperature (710 °C) prior to any lithospheric heating in the area would be in apparent conflict with the occurrence of earthquake activity with the present-day focal depth distribution patterns (cf. section 4.7.1), inasmuch as the young geodynamic and magmatic processes have increased the recent lower crustal temperatures even further.(e.g. Sobolev et al., 2005).

Figure 4.5c shows those isotherms down to 50 km depth that relate to the best-fit subcase of scenario 1. Accordingly, Moho temperatures are implied to decrease from about 635 °C near the DST to 550 °C at profile km 30. In the same direction, the temperature at the base of the upper crust is suggested to decrease from 520 °C to 460 °C, respectively. All these temperature estimates remain virtually unaffected, if making the upper crust a little more or less radiogenic as discussed above.

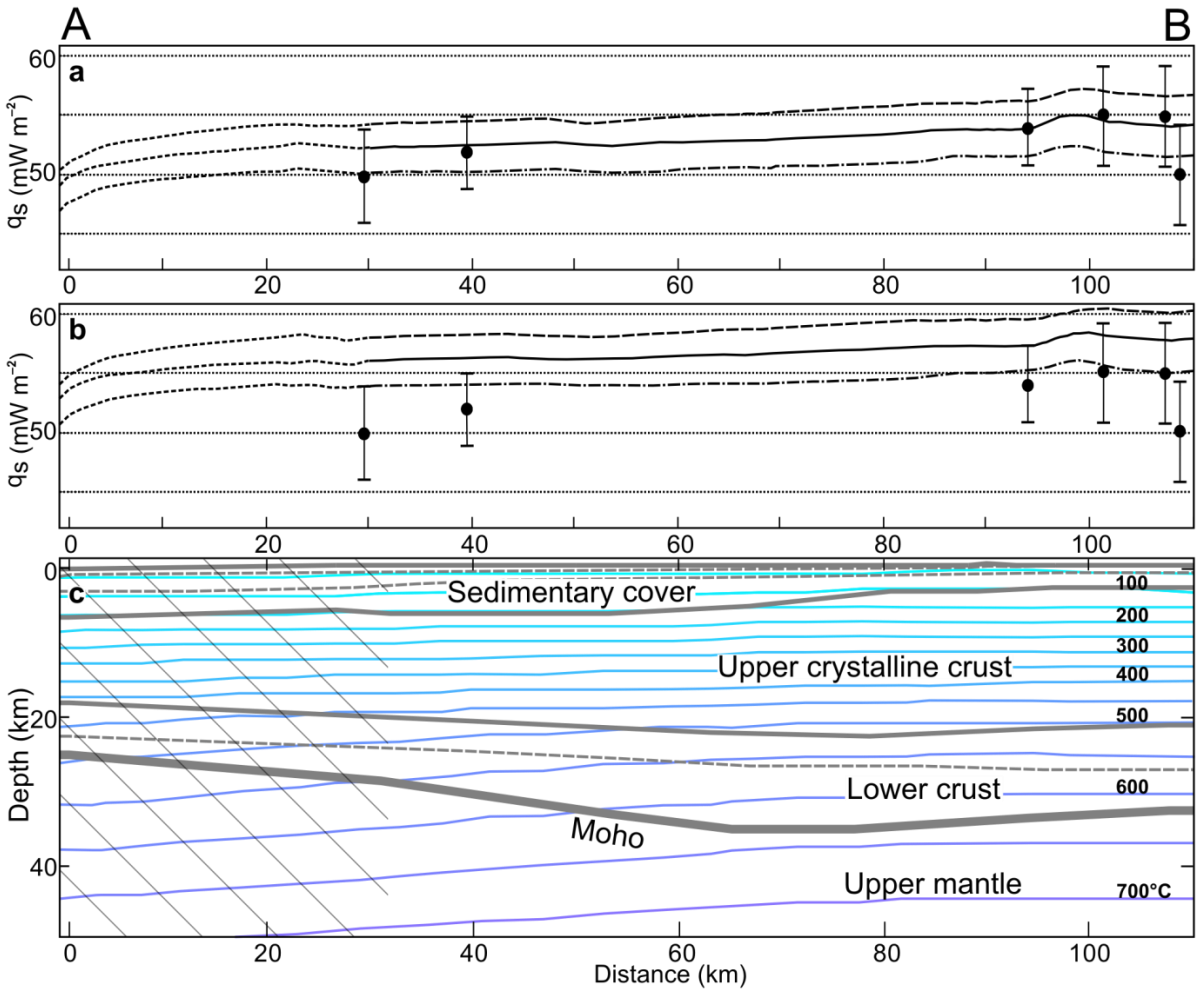

Figure 4.5: Modeled surface heat-flow (q_S) patterns along the DESIRE seismic profile shown in Figure 4.3. The dots with the mean absolute error bars refer to the q_S values determined for the six sites closest to the profile (cf. Figure 4.3). Modeling was conducted for pre-Oligocene LAB depths of 150 km (**a**) and 120 km (**b**). Full lines represent the modeled q_S patterns obtained with the thermal parameters listed in Table 4.2. Dashed and dashed-dotted lines mark the patterns modeled for an upper crystalline crust 10% richer resp. poorer in radiogenic heat production (A) relative to the A data in Table 4.2. Dotted portions of lines indicate the section of the profile, for which there is no q_S control (kilometers 0–30). (**c**) Modeled isotherms for a LAB depth of 150 km using the thermal rock properties shown in Table 4.2. Shaded is the portion of the profile with no measured surface heat flow.

4.7 Discussion

4.7.1 The surface heat flow of the Sinai Microplate

Determination of the new heat-flow data presented in this study is largely inconsistent with the procedure applied in former work in the study area. The differences center in the processing of the T-logs and in the fine-tuned assignment of TC for dry and saturated rocks to the respective borehole intervals above and below the water table.

Our heat-flow values appear to vary systematically and do not show the less systematic pattern characterizing the earlier studies, with values as low as 30 mW m^{-2} and as high as 80 mW m^{-2}. The q_S values presented in this paper for central and southern Israel (Figure 4.3) display a range (50−62 mW m^{-2}, Figure 4.3) that is considerably narrower than the range observed for the area in previous studies of Eckstein and Simmons (1978; Figure 4.2a) and Shalev et al. (2013; Figure 4.2b). Notably, not a single value falls in the range of heat flow (40–45 mW m^{-2}) emphasized by both collectives of authors as being the typical regional heat flow onshore Israel.

Apart from regional trends, individual comparisons of values from adjacent boreholes show that the high values, interpreted as heat flow due to deep thermal anomalies (Eckstein and Simmons, 1978), are not recognized by our data. For example, values on the order of 67–73 mW m^{-2} in the area southwest of the DSB compete with 50–55 mW m^{-2} (this study). Also different are the values for the Negev area: 33–38 mW m^{-2} (Eckstein and Simmons, 1978) compared to 52–58 mW m^{-2} (this study). For the q_S values in the Arava Valley (55–62 mW m^{-2}), there is no equivalent of measured boreholes neither by Eckstein and Simmons (1978) nor by Shalev et al. (2013). Notably, the heat-flow map of Shalev et al. (2013) implies for this area essentially larger values on the order of 70–75 mW m^{-2} (see Figure 4.2b).

Our q_S values in the range of 50 and 62 mW m^{-2} are consistent with the results of a steady-state thermal model, in which the most recent knowledge on the structure, composition and thermal properties of the crust and pre-Oligocene lithosphere thickness was implemented. Accordingly, the observed range in q_S could easily be explained by variation in the composition (heat production) of the upper crust and the geophysically well-constrained and more systematic spatial changes in its thickness. This part of the lithosphere is certainly not compositionally homogeneous over the entire study area as treated in our models. On a small scale, in areas of a relatively thinner upper crystalline crust containing a larger proportion of less-radiogenic material, q_S may be eventually as low as 45 mW m^{-2}. Conversely, in regions of thick crystalline crust, a comparatively larger amount of more-radiogenic material would cause the q_S to exceed 60 mW m^{-2}.

The weak trend of q_S to decrease from the east to the west from ~54 mW m^{-2} to ~50 mW m^{-2} along the modeled transect (cf. Figure 4.3) is likely caused by the general thinning of the magmatic and metamorphic upper crust, associated with an increase of the ratio sedimentary rocks/crystalline rocks. From the east to the west, the upper crust generates increasingly less heat, thus causing a reduction of the q_S values. Our modeling predicts for the coast of the Mediterranean Sea q_S of about 45 mW m^{-2} for thinned continental crust.

The minor q_S increase from the north (~55 mW m^{-2} just south of the DSB) to the south (~59 mW m^{-2} just north of the outcropping shield rocks) may be simply the effect of the increase of the volume

of more-radiogenic crystalline rocks at the expense of the less-radiogenic sedimentary veneer (e.g., Gvirtzman, 2003) at a fairly constant total thickness of the upper crust. Moreover, at geologically favorable conditions, conductive heat flow may be locally on the order of 60−65 mW m^{-2}. No conclusive evidence has yet provided that heat flow onshore southern Israel is instationary, i.e., is increased in response to a young regional thermal pulse associated with the opening of the Gulf of Eilat (Shalev et. al., 2013). There are insufficient and well-constrained q_S data available in the region south of our heat-flow clusters to strengthen such a hypothesis.

Our 2-D-temperature predictions are in line with recent estimates on the earthquake focal depths in the area of the DSB. Accordingly, epicenters of $M_L \geq 2.5$ earthquakes clustering at depths of 8−10 km and 12−16 km, i.e., are concentrated in the upper crystalline crust (Shamir, 2006; ten Brink et al., 2006; Bräuer et al., 2012), but are also observed at 20−25 km depth (Aldersons et al., 2003; Shamir, 2006). For mantle peridotite, the transition from seismic to aseismic behavior occurs at ~600°C (McKenzie et al., 2005; Boettcher et al., 2007), which is lower than the minimum Moho-temperature of 635°C determined in this study for the DSB area. Our temperature model explains the absence of mantle-induced earthquakes on the territory of Israel (Aldersons et al., 2003; Shamir, 2006).

Although the depth of the brittle-ductile transition in the area can only be roughly estimated, owing to insufficient knowledge on the rheological properties of the various rocks forming the crust, the LAB at 120 km steady-state thermal model shows temperatures of 540–620 °C between 20 and 25 km depth around the DST that appear to be too elevated as to allow the generation of micro-earthquakes in the lower crust. This circumstance supports our preference for a Pre-Oligocene LAB depth of about 150 km in this part of the AS.

Eventually, microseismicity down to depths of 31 km in parts of Israel (Bräuer et al., 2012) may be explained in a different way. Keir et al. (2009) investigated lower crustal earthquakes in the East African rift system and claimed deep magmatic processes related to the rift development as a possible explanation. Indeed, present-day lithosphere thickness of about 60−80 km (Mohsen et al., 2006) indicating an erosion of the lithosphere by 90−70 km over short time can be explained by a thermo-chemical plume (Sobolev et al., 2011), in turn triggering earthquake activity at great depth. Conclusively, present-day microseismic activities in the lower crust of Israel could not be taken as argument in opposition to the thermal model elaborated here.

Varying assumptions on the magnitude of regional q_S and related temperature fields has triggered different assumptions on the deep processes giving rise to the development of the DST and DSB. Al-Zoubi and ten Brink (2002) postulated that the insignificant Moho uprise beneath the DST is induced by a strike-parallel ductile flow in the lower crust at q_S values of 45−53 mW m^{-2}. In

contrast, Petrunin and Sobolev (2006, 2008) required q_S values as high as 55–60 mW m^{-2} to explain the formation of the pull-apart DSB by thermo-mechanical modeling. These values are in line with the results from this study and corroborate the measured q_S east of the DST, in Jordan (Förster et al., 2010).

The results of this study strictly apply only to the central part of the Sinai Microplate. Inferences on the thermal state of its northern (Lebanon, eastern Syria) and southern parts (Sinai Peninsula) are afflicted with serious problems involving the paucity or even lack of q_S data and insufficient knowledge on the structure and composition of the crust. Available seismic data (Hofstetter et al. 1991) may suggest that both the bulk and upper crust in the northern Sinai Microplate is relatively thinner, and the ratio of sedimentary to crystalline upper crust is higher. For those areas, the thermal properties from our study predict heat flow values on the order of 45–50 mW m^{-2}, which broadly coincide with the pattern displayed in the heat-flow map of Shalev et al. (2013) for northern Israel. Similarly, the heat flow in Sinai, where the Pan-African Shield is largely outcropping, is inferred being on the order of 55–60 mW m^{-2} in areas of average upper-crustal composition outside of regions of crustal thinning towards the Mediterranean.

4.7.2 The surface heat flow of the Arabian Plate

Although presently being part of the central SM, the q_S data measured for central and southern Israel also add another glimpse to the still insufficient knowledge on the heat-flow pattern of the AS that received its major pre-Oligocene shape in Neoproterozoic to Cambrian times.

The heat-flow values obtained from the westernmost cluster in central Israel near the Mediterranean Sea do not typify the AS. Instead, these low values of ~50 mW m^{-2} relate to a sedimentary-rock covered shield segment of thinned crust (<30 km), in comparison to “undisturbed” AS crustal thicknesses of 32–39 km (e.g. Stern and Johnson, 2010). This statement holds even more to the predictions made for the northern Sinai Microplate, where the crust is still more thin.

Heat-flow values on the order of ~55 mW m^{-2} and ~59 mW m^{-2} obtained for east-central Israel and southern Israel near the DST, respectively, refer to lithosphere segments that are largely representative for the AS even covered with a thin sedimentary veneer. The q_S values in southern Israel correspond with data recently determined immediately east of the DST in southern Jordan, in an area of equivalent spatial proximity to the exposed shield rocks (Förster et al., 2007). These values, averaging to 60 ± 3 mW m^{-2}, originated as in this study from high-precision temperature logging to depths up to 950 m, in conjunction with systematic rock sampling and laboratory

measurements of TC for the major Paleozoic formations forming the borehole-penetrated sedimentary succession. In conclusion, heat flows ranging between 55 and 60 mW m^{-2} may be commonplace rather than atypical for the northern AS. Certainly, surface heat flow may be locally substantially lower or higher if measured in areas of voluminous mafic or felsic rocks with less or more than average radiogenic heat production (cf. Förster and Förster, 2000).

Whether this range is also a reliable estimate for the entire AS needs to be investigated, but appears not unrealistic. Substantially lower q_S values reported for the western AS in Saudi Arabia outside of the Red Sea rift (36–45 mW m^{-2}; Gettings, 1982; Gettings and Showail, 1982) are likely attributed to poor raw data and, thus, have to be questioned. The most serious problems encountered in this data are the use of (a) small depth intervals for the determination of interval temperature gradients and (b) shallow boreholes (usually ≤ 70 m deep), in which abnormally low temperature gradients were recorded (cf. Förster et al., 2007).

Heat-flow values in the middle and upper 50s would be consistent with the q_S patterns established in provinces of the same, i.e., Neoproterozoic age (Nyblade and Pollack, 1993; Rudnick et al., 1998). Considering the thermal properties listed in Table 4.2, a lower q_S of 45 mW m^{-2} (the value postulated by most previous workers as representative for the AS) would require that the upper crust of the AS is entirely composed of intermediate and mafic rocks of low heat production (i.e., 50% granodiorite and 50% diorite/gabbro), a scenario contrasting with the geophysical data and the variability of Pan-African igneous rocks exposed in surface outcrops. Alternatively, a q_S of 45 mW m^{-2} would coincide with a Moho heat flow as low as 13 mW m^{-2}. As already emphasized by Förster et al. (2010), such magnitudes of surface and mantle heat flows refer to terranes of thick lithosphere (>200 km) commonly characterizing Archean and Paleoproterozoic cratons (Artemieva and Mooney, 2001), but is irreconcilable with the pre-Oligocene thickness and composition of the lithosphere of the AS.

Heat-flow calculations recently performed in the APl onshore and offshore east Yemen and Oman yielded consistently low values of ≤ 45 mW m^{-2} (Lucazeau et al., 2008; Rolandone et al., 2013). These observations imply that the q_S on the APl (southeastern part of the AP) is lower than on the shield, assuming that q_S values clustering around 55 mW m^{-2} as reported here are reasonably good estimates not only for the northern AS, but for the AS in general. The rationale behind this difference is not yet sufficiently well understood. One explanation involves a different lithospheric composition between shield and platform (Stern and Johnson, 2010). These authors identified a thinner and more buoyant lithosphere beneath the AS and a denser one beneath the APl with a more complex structure and more felsic composition. Nasir and Stern (2011) studied lower crustal and upper mantle xenoliths from Oman and compared their compositions with those of much more

abundant and well-studied xenoliths of the shield areas on the western side of the AP (Nasir and Rollinson, 2009). They report that the Omani xenoliths are more MgO-rich, possess tholeiitic affinity, and contain spinel instead of garnet and hydrous minerals.

However, distinct compositions of the lower crust and upper mantle alone could not account for the suggested differences in qs between the western and eastern AP. They must be accompanied by compositional differences of the upper crust, where the largest heat fraction is generated. However, the upper crystalline crust of eastern Arabia is mostly buried by Phanerozoic formations, with outcrops being restricted to small, scattered locations in Oman. Here, Rolandone et al. (2013) analyzed 22 samples of exposed upper crustal crystalline basement and indeed determined a surprisingly low mean heat production of 0.7 $\mu W\ m^{-3}$ (compared to 1.55 $\mu W\ m^{-3}$ in our model; cf. Table 4.2), which can partly explain the differences in heat flow between the eastern and western part of the AP. Other than that, the lithosphere of eastern Arabia is thicker (> 40 km; cf. compilation by Stern and Johnson, 2010), increasing as a sudden step at the shield–platform boundary. Hence, deviations in the thermal structure of the AS and the APl are not only related to different compositions, but also to structural changes in the lithosphere.

Acknowledgements:

We wish to thank the Geological Survey of Israel (GSI), particularly H. Lutzky and E. Shalev, for logistic support and assistance during the field work. M. Poser, J. Schrötter, R. Giese and A. Reichardt (GFZ-Potsdam) are acknowledged for performing the temperature logging. O. Navon (Hebrew University, Jerusalem) kindly provided lower crustal and mantle xenoliths from Qarnei-Hittin volcano for laboratory analysis. Z. Garfunkel and Z. Ben-Avraham offered thought-provoking discussions on the heat-flow patterns of the study area. Constructive comments of two anonymous reviewers helped to improve the paper. F. S. was funded via a doctoral grant from the Deutsche Forschungsgemeinschaft in the framework of the DESIRE project.

4.8 References

Aldersons, F., Ben-Avraham, Z., Hofstetter, A., Kissling, E. and T. Al-Yazjeen (2003), Lower-crustal strength under the Dead Sea basin from local earthquake data and rheological modeling, Earth Planet. Sci. Lett., 214, 129–142.

Al-Mishwat, A. T., and S. J. Nasir (2004), Composition of the lower crust of the Arabian Plate: a xenolith perspective, Lithos, 72, 45–72.

Al-Zoubi, A., and U. ten Brink (2002), Lower crustal flow and the role of shear in basin subsidence: an example from the Dead Sea basin, Earth Planet. Sci. Lett., 199, 67–79.

Artemieva, I. M., and Mooney, W. D. (2001), The thermal thickness and evolution of Precambrian lithosphere: A global study, J. Geophys. Res., 106, B8, 16,387–16,414.

Bartov, J., Eyal, Y., Garfunkel, Z., and G. Steinitz (1972), Late Cretaceous and Tertiary stratigraphy and paleography of southern Israel, Isr. J. Earth Sci., 21, 69–97.

Bartov, Y., Steinitz, G., Eyal, M., and Y. Eyal (1980), Sinistral movement along the Gulf of Aqaba – its age and relation to the opening of the Red Sea, Nature, 285, 220–221.

Beach, R. D. W., Jones, F. W., and J. A. Majorowicz (1986), Heat Flow and Heat Generation Estimates for the Churchill Basement of the Western Canadian Basin in Alberta, Canada, Geothermics, 16, 1, 1–16.

Ben-Avraham, Z., Hänel, R. and H., Villinger (1978) Heat flow through the Dead Sea Rift, Mar. Geol., 28, 253–269.

Ben-Avraham, Z., and R. Von Herzen (1987), Heat Flow and Continental Breakup: The Gulf of Elat (Aqaba), J. Geophys. Res., 92, B2, 1407–1416.

Ben-Avraham, Z., Ginzburg, A., Makris, J., and L., Eppelbaum (2002), Crustal structure of the Levant Basin, eastern Mediterranean, Tectonophysics, 346, 23–43.

Beyth, M., Stern, R., Altherr, R., and A. Kröner (1994), The Late Precambrian Timna igneous complex, Southern Israel: Evidence for comagmatic-type sanukitoid monzodiorite and alkali granite magma, Lithos, 31, 103–124.

Blackwell, D. D., and J. L. Steele (1989), Thermal conductivity of sedimentary rocks: Measurement and significance, in Thermal History of Sedimentary Basins, edited by N.D. Naeser and T.H. McCulloh, Springer-Verlag, pp.13−36.

Boettcher, M. S., Hirth, G., and B. Evans (2007), Olivine friction at the base of oceanic seismogenic zones, J. Geophys. Res., 112, B01205, doi:10.1029/2006JB004301.

Bohannon, R. G., Naeser, C. W., Schmidt, D. L., and R. A. Zimmermann (1989), The timing of uplift, volcanism, and rifting peripheral to the Red Sea: a case for passive rifting? J. Geophys.

Res., B 94, 1683–1701.

Bogoch, R., Avigad, D., and T. Weissbrod (2002), Geochemistry of the quartz diorite–granite association, Roded area, southern Israel, J. Afr. Eart. Sci., 35, 51–60.

Bräuer, B., Asch, G., Hofstetter, R., Haberland, C., Jaser, D., El-Kelani, R., and M. Weber (2012), Microseimicity distribution in the southern Dead Sea area and its implications on the structure of the basin, Geophys. J. Int. Geophys. J. Int., 188, 3, 873–878.

Camp, V. E., and M. J. Roobol (1992), Upwelling asthenosphere beneath western Arabia and its regional implications, J. Geophys. Res., 97, 15,255–15,271.

Chang, S.-J., and S. Van der Lee (2011), Mantle plumes and associated flow beneath Arabia and East Africa, Earth Planet. Sci. Lett., 302, 448–454.

Deming, D., Nunn, J. A., Jones, S., and D. S. Chapman (1990), Some problems in thermal history studies, in Applications of Thermal Maturity Studies to Energy Exploration: RMS-SEPM, edited by V.F. Nuccio et al., pp. 61−80, Denver, Colorado, USA.

Eckstein, Y., and G. Simmons (1978), Measurement and interpretation of terrestrial heat flow in Israel, Geothermics, 6, 117–142.

Esperança, S., and Z. Garfunkel (1986), Ultramafic xenoliths from the Mt. Carmel area (Karem Maharal Volcano), Israel, Lithos, 19, 43–49.

Eyal, M., Litvinovsky, B., Jahn, B. M., Zanvilevich, A., and Y. Katzir (2010), Origin and evolution of post-collisional magmatism: Coeval Neoproterozoic calc-alkaline and alkaline suites of the Sinai Peninsula, Chemical Geology, 269, 153–179.

Förster, A. and H.-J. Förster (2000), Crustal composition and mantle heat flow: Implications from surface heat flow and radiogenic heat production in the Variscan Erzgebirge (Germany), J. Geophys. Res., 105, B12, 27,917–27,938.

Förster, A., Schrötter, J., Merriam, D. F., and D. D. Blackwell (1997), Application of optical-fiber temperature logging – An example in a sedimentary environment, Geophysics, 62, 4, 1107–1113.

Förster, A., Förster, H.-J., Masarweh, R., Masri, A., Tarawneh, K., and Desert Group (2007), The surface heat flow of the Arabian Shield in Jordan, J. Asian Earth Sci., 30, 271–284.

Förster, H.-J., Förster, A., Oberhänsli, R., and D. Stromeyer (2010), Lithospheric composition and thermal structure of the Arabian Shield in Jordan, Tectonophysics, 481, 29–37.

Fowler, C. M. R. (1990), The Solid Earth. An Introduction to Global Geophysics, Cambridge University Press, Cambridge, 418 pp.

Freund, R., Garfunkel, Z., Zak, I., Goldberg, M., Weissbrod, T., and B. Derin (1970), The shear along the Dead Sea rift, Philosophical Transaction of the Royal Society of London, Series

A267, 107–130.

Galanis, S. P., Sass, J. H., Munroe, R. J., and M. Abu-Ajamieh (1986), Heat flow at Zerqa Ma'in and Zara and a geothermal reconnaissance of Jordan, US Geological Survey, Open File Report, 86–63, Menlo Park.

Gardosh, M., and Y. Druckmann (2006), Stratigraphy and tectonic evolution of the Levantine Basin, offshore Israel. in Tectonic Development of the Eastern Mediterranean Region, edited by A. Robertson, Geological Society Special Publication, 260, 201–227.

Gettings, M. E. (1982), Heat-flow measurements at shot points along the 1978 Saudi Arabian seismic deep-refraction line, part II: discussion and interpretation, Open File Report USGS-OF-02–39, Saudi Arabia Deputy Minister for Mineral Resources, Jiddah.

Gettings, M. E., and A., Showail (1982), Heat-flow measurements at shot points along the 1978 Saudi Arabian deep-refraction line, part I: results of measurements. Open File Report USGS-OF-02–39, Saudi Arabia Deputy Minister for Mineral Resources, Jiddah.

Ginzburg, A., and Z. Ben-Avraham (1987), The deep structure of the central and southern Levant continental margin, Ann. Tecton., 1, 105–115.

Götze, H.-J., El-Kelani, R., Schmidt, S., Rybakov, M., Hassouneh, M., Förster, H.-J., and J. Ebbing (2007), Integrated 3D density modelling and segmentation of the Dead Sea Transform, Int. J. Earth Sci. Geol. Rundsch., 96, 289–302.

Gvirtzman, Z. (2003), Chronostratigraphic table and subsidence curves of southern Israel, Isr. J. Earth Sci., 53, 47–61.

Hansen, S. E., Nyblade, A. A., and M. H. Benoit (2012), Mantle structure beneath Africa and Arabia from adaptively parameterized P-wave tomography: Implications for the origin of Cenozoic Afro-Arabian tectonism, Earth Planet. Sci. Lett., 319–320, 23–34.

Hansen, S. E., Rodgers, A. J., Schwartz, S.Y., and A. M. S. Al-Amri (2007), Imaging ruptured lithosphere beneath the Red Sea and Arabian Peninsula. Earth Planet. Sci. Lett., 259, 256–265.

Hasterok, D., and D. S. Chapman, (2011), Heat production and geotherms for the continental lithosphere, Earth Planet. Sci. Lett., 307, 1−2, 59−70.

Jaupart, C., and J. C. Mareschal (1999), The thermal structure and thickness of continental roots, Lithos, 48, 94–114.

Johnson, P. R., Andresen, A., Collins, A. S., Fowler, A. R., Fritz, H., Ghebreab, W. Kusky, T., and R. J. Stern (2011), Late Cryogenian–Ediacaran history of the Arabian–Nubian Shield: A review of depositional, plutonic, structural, and tectonic events in the closing stages of the northern East African Orogen, J. Afr. Earth. Sci.,61 ,167–232.

Kaliwoda, M., Altherr, R., and H.-P. Meyer (2007), Composition and thermal evolution of the lithospheric mantle beneath the Harrat Uwayrid, eastern flank of the Red Sea rift (Saudi Arabia), Lithos, 99, 105–120.

Keir, D., Bastow, I. D., Whaler, K. A., Daly, E., Cornwell, D.G., Hautot, S., 2009. Lower crustal earthquakes near the Ethiopian rift induced by magmatic processes. Geochemistry Geophysics Geosystems, 10, 6, Q0AB02.

Krienitz, M.-S., and K. M. Haase (2011), The evolution of the Arabian lower crust and lithospheric mantle – Geochemical constraints from southern Syrian mafic and ultramafic xenoliths, Chem. Geol., 280, 271−283.

Krienitz, M.-S., Haase, K. M., Mezger, K. and M. A. Shaikh-Mashail (2007), Magma genesis and mantle dynamics at the Harrat Ash Shamah volcanic field (southern Syria), J. Petrol., 48, 1513−1542.

Kukkonen, I. T., and P. Peltonen (1999), Xenolith-controlled geotherm for the central Fennoscandian Shield: implications for lithosphere–asthenosphere relations, Tectonophysics, 304, 301–315.

Laws, E. D., and M. Wilson (1997), Tectonics and magmatism associated with Mesozoic passive continental margin development in the Middle East, J. Geol. Soc. London, 154, 459–464.

Lucazeau, F., Leroy, S., Bonneville, A., Goutorbe, B., Rolandone, F., D'Acremont, E., Watremez, L., Düsünur, D., Tuchais, P., Huchon, P., Bellahsen, N., and K. Al-Toubi (2008), Persistent thermal activity at the Eastern Gulf of Aden after continental break-up, Nature Geoscience, 1, 854–858.

Mahmoud, S., Reilinger, R., McClusky, S., Vernant, P., and A. Tealeb (2005), GPS evidence for northward motion of the Sinai Block: Implications for E. Mediterranean tectonics, Earth Planet. Sci. Lett., 238, 217–224.

Mareschal, J. C., and C. Jaupart (2004), Variations of surface heat flow and lithospheric thermal structure beneath the North American craton, Earth Planet. Sci. Lett., 233, 65−77.

Mascle, J., Benkhelil, J., Bellaiche, G., Zitter, T., Woodside, J., Loncke, L. and Prismed II Scientific Party (2000), Marine geologic evidence for a Levantine–Sinai plate, a new piece of the Mediterranean puzzle, Geology, 28, 779–782.

McKenzie, D., Jackson, J., and K. Priestley (2005), Thermal structure of oceanic and continental lithosphere, Earth Planet. Sci. Lett., 233, 337– 349.

Mechie, J., Abu-Ayyash, K., Ben-Avraham, Z., El-Kelani, R., Qabbani, I., Weber, M., and DESIRE Group (2009) Crustal structure of the southern Dead Sea basin derived from project DESIRE wide-angle seismic data, Geophys. J. Int., 178, 1, 457–478.

Mittlefehldt, D. W. (1986), Petrology of high pressure clinopyroxenite series xenoliths, Mount Carmel, Israel, Contrib. Mineral. Petrol., 94, 245–252.

Morag, N., Avigad, D., Gerdes, A, and Y. Harlavan (2012), 1000–580 Ma crustal evolution in the northern Arabian-Nubian Shield revealed by U–Pb–Hf of detrital zircons from late Neoproterozoic sediments (Elat area, Israel), Precambrian Res.,208–211, 197–212.

Mohsen, A., Kind, R., Sobolev, S. V., Weber, M., and DESERT Group (2006), Thickness of the lithosphere east of the Dead Sea Transform, Geophys. J. Int., 167, 845–852.

Mushkin, A., Navon, O., Halicz, L., Hartmann, G., and M. Stein (2003), The Petrogenesis of A-type Magmas from the Amram Massif, Southern Israel, J. Petrol, 44, 815–832.M

Nasir, S. (1992), The lithosphere beneath the northwestern part of the Arabian plate (Jordan): evidence from xenoliths and geophysics, Tectonophysics, 201, 357–370.

Nasir, S., and H. Rollinson (2009), The nature of the subcontinental lithospheric mantle beneath the Arabian Shield: Mantle xenoliths from southern Syria, Precambrian Res., 172, 323–333.

Nasir, S., and A. Safarjalani (2000), Lithospheric petrology beneath the northern part of the Arabian plate in Syria: evidence from xenoliths in basalts, J. Afr. Earth Sci., 30, 149–168.

Nasir, S., and R. Stern (2011), Lithospheric petrology of the eastern Arabian Plate: Constraints from Al-Ashkhara (Oman) xenoliths, Lithos, 132–133, 98–112.

Navon, O., Gazit, O., Halicz, L., Don, A., Garfunkel, Z., and M. Stein (2007), The composition and evolution of the crust beneath Israel: Inferences from xenoliths and granites, Final Report ES-46–2006, Israel, Earth Science Research Administration.

Netzeband, G. L., Gohl, K., Hübscher, C. P., Ben-Avraham, Z., Dehghani, G. A., Gajewski, D., and P. Liersch (2006), The Levantine Basin – crustal structure and origin, Tectonophysics, 418, 167–188.

Nyblade, A. A., and H. N. Pollack (1993), A Global Analysis of Heat Flow From Precambrian Terrains: Implications for the Thermal Structure of Archean and Proterozoic Lithosphere, J. Geophys. Res., 98, B7, 12,207–12,218.

Perry, H. K. C., Jaupart, C., Mareschal, J.-C., and G. Bienfait (2006), Crustal heat production in the Superior Province, Canadian Shield, and in North America inferred from heat flow data, J. Geophys. Res., 111, B04401.

Petrunin, A., and S. Sobolev (2006), What controls thickness of sediments and lithospheric deformation at a pull-apart basin? Geology, 34, 389–392.

Petrunin, A., and S. Sobolev (2008), Three-dimensional numerical models of the evolution of pull-apart basins, Phys. Earth Planet. Inter., 171, 387–399.

Pollack, H. N., and D. S., Chapman (1977), Mantle heat flow, Earth Planet. Sci. Lett., 34, 174−184.

Pollack, H. N. (1982), The heat flow from the continents, Annu. Rev. Earth Planet. Sci., 10, 459−482.

Popov, Y. A., Pribnow, D. F. C., Sass, J. H., Williams C. F., and H. Burkhardt (1999), Characterization of rock thermal conductivity by high-resolution optical scanning, Geothermics, 28, 253–276.

Rolandone, F., Lucazeau, F., Leroy, S., Mareschal, J.-C., Jorand, R., Goutorbe, B., and H. Bouquerel (2013), New heat flow measurements in Oman and the thermal state of the Arabian shield and platform, Tectonophysics, 589, 77–89.

Rudnick, R. L., McDonough, W. F., and R. J. O'Connell (1998), Thermal structure, thickness and composition of continental lithosphere, Chem. Geol., 145, 395–411.

Schön, J. H. (1983), Petrophysik, Physikalische Eigenschaften von Gesteinen und Mineralen, Ferdinand Enke Verlag, Stuttgart.

Schütz, F., Norden, B., Förster, A., and DESIRE Group (2012), Thermal properties of sediments in southern Israel: a comprehensive data set for heat flow and geothermal energy studies, Basin Research, 24, 357–376.

Segev, A. (1987), The age of the latest Precambrian volcanism in southern Israel, northeast Sinai and southwest Jordan - a reevaluation, Precambrian Res., 36, 277–285.ION.

Segev, A. (2002), Flood basalts, continental breakup and the dispersal of Gondwana: evidence for periodic migration of upwelling mantle flows (plumes), EGU Stephan Mueller Special Publication Series, 2, 171–191.

Segev, A. (2005), Phanerozoic magmatic activity associated with vertical motions in Israel and adjacent countries, in Geological Framework of the Levant: Volume II: Levantine Basin and Israel, edited by V. A. Krasheninnikov et al., Historical Productions-Hall, Jerusalem, 553–577.

Seipold, U. (2001), Der Wärmetransport in kristallinen Gesteinen unter den Bedingungen der kontinentalen Kruste, Techn. Ber. STR 01/13, GeoForschungsZentrum Potsdam, 92.

Shalev, E., Lyakhovsky, V., Weinstein, Y., and Z. Ben-Avraham (2012), The thermal structure of Israel and the Dead Sea Fault, Tectonophysics, 602, 69–77.

Shaw, J. E., Baker, J. A., Menzies, M. A., Thirlwall, M. F., and K. M. Ibrahim (2003), Petrogenesis of the Largest Intraplate Volcanic Field on the Arabian Plate (Jordan): a Mixed Lithosphere-Asthenosphere Source Activated by Lithospheric Extension, J. Petrol., 44 (9), 1657–1679.LAS

Sobolev, S. V., Petrunin, A., Garfunkel, Z., Babeyko, A. Y., and DESERT Group (2005), Thermo mechanical model of the Dead Sea Transform, Earth Planet. Sci. Lett., 238, 78–95.

Sobolev, S. V., Sobolev, A. V., Kuzmin, D. V., Krivolutskaya, N. A., Petrunin, A. G., Arndt, N. T., Radko, V. A. and Y. R. Vasiliev (2011), Linking mantle plumes, large igneous provinces and environmental catastrophes, Nature, 477(7364), 312−316.

Somerton, W. H. (1992), Thermal properties and temperature related behavior of rock/fluid systems, Developments in Petroleum Sciences, 37, Elsevier, Amsterdam.

Stein, M., and S. Goldstein (1996), From plume head to continental lithosphere in the Arabian Nubian shield, Nature, 382, 773–778.

Stern, R. J. (1994), Arc Assembly and Continental Collision in the Neoproterozoic East African Orogen: Implications for the Consolidation of Gondwanaland, Annu. Rev. Earth Planet. Sci., 22, 319–351.

Stern, R. J., and P. Johnson (2010), Continental lithosphere of the Arabian Plate: A geologic, petrologic, and geophysical synthesis, Earth Sci. Rev., 101, 29–67.

Tommasi, A., Gibert, B., Seipold, U., and D. Mainprice (2001), Anisotropy of thermal diffusivity in the upper mantle, Nature, 411, 783−786.

Turcotte, D. L., and G. Schubert (2002) Geodynamics, Cambridge Univ. Press, Cambridge, UK, pp. 5.

Vila, M., Fernández, M., and I. Jiménez-Munt (2010), Radiogenic heat production variability of some common lithological groups and its significance to lithospheric thermal modelling, Tectonophysics, 490, 152–164.

Weber, M., et al. (2004), The crustal structure of the Dead Sea Transform, Geophys. J. Int., 156, 655–681.

Weissbrod, T. (2005), The Paleozoic in Israel and Environs, in Geological Framework of the Levant, in Geological Framework of the Levant: Volume II: Levantine Basin and Israel, edited by V. A. Krasheninnikov et al., Historical Productions-Hall, Jerusalem, 283–316.

Wilson, M., Shimron, A.E., Rosenbaum, J.M., and J. Preston (2000), Early Cretaceous magmatism of Mount Hermon, Northern Israel, Contrib. Mineral. Petrol., 139, 54–67.

Wisian, K. W., Blackwell, D. D., Bellani, S., Henfling, J. A., Normann, R. A., Lysne, P. C., Förster, A., and J. Schrötter (1998), Field comparison of conventional and new technology temperature logging systems, Geothermics, 27, 2, 131–141

Appendix A: Details on borehole temperature logging

In boreholes, where the water table was at depth <150 m, an analog, electric-line system was deployed, which consisted of a 28-mm-diameter sensor (max. temperature 80 °C, max. pressure 300 bar) and a 1000-m-long cable (Vektor-Schlumberger-Kabel 1–10P 1/10''). The system allows T-recordings to a precision of 0.01 °C, at a limiting accuracy of 0.1 °C. The recording interval was 0.1 m, compared to the intervals measured by Eckstein and Simmons (1978), which were 2.5 and 10 m respectively. The downward logging speed of 5.6 m min^{-1} was sufficient that the actual subsurface temperature could be recorded in water without a need to deconvolve the records afterwards. The records from the air-filled parts of the wells were discarded from these logging runs due to the inappropriate logging speed used for air.

Six wells with water tables on the order of several hundred meters deep were logged using the fibre-optic Distributed Temperature Sensing technology (DTS). This technology is especially suited for a time-effective measurement of air-filled borehole sections (Förster et al., 1997; Wisian et al., 1998). The measurements were performed with the Sensa DTS 800 system, to which a 1000-m-long optical sensor cable was attached. The DTS system allowed the online registration of a T-profile along the whole borehole section with an accuracy of 0.3 °C. The DTS processing mode was double ended. The total measuring time was at least two hours; the recording intervals lasted 1.4 min. Temperature data were obtained for every 1.02 m.

All T-data, independent of the logging system used, were smoothed by a 10-m-running average. A T-gradient then was determined by calculating a simple average for each recording interval. Temperature readings at depths < 50 m were omitted to exclude annual climate effects.

Appendix B: Thermal conductivity

Thermal conductivity for each individual heat-flow interval (Table 4.1) was determined on the basis of lithotype TC values. Values for dry and saturated rocks are provided for each lithotype (Table B.1) and used in dependence on the borehole conditions (air-filled part or water-filled part of the borehole), under which heat flow was determined.

Table B.1.: Mean thermal conductivity of lithotypes (Schütz et al., 2012)

Lithology	λ_{dry} ($Wm^{-1}K^{-1}$)	λ_{sat} ($Wm^{-1}K^{-1}$)
Dolomite	3.5	4.1
Limestone	2.3	2.7
Dolomitic ls	2.5	3.0
Marlstone	1.8	2.4
Claystone	1.4	1.9
Shale	1.3	1.9
Sandstone	4.3	5.6
Carbonatic ss	3.8	4.9
Argillaceous ss	2.8	3.6
Siltstone	2.5	2.9
Chalk	1.0	1.8
Gypsum	1.1	1.3
Chert	5.1	5.1
Conglomerate	-	3.2*

λ_{dry} - mesaured air-saturated, λ_{sat} - measured water-saturated, ls - limestone, ss - sandstone, * after Beach et al. (1986).

Appendix C: Determination of surface heat flow

In the following, the procedure of the heat-flow calculation is briefly described for each of the ten boreholes. The respective data are compiled in Table 4.1. The composition of the different heat-flow intervals in terms of lithotypes is provided in Table B.2. Based on these compositions and the lithotype TC an average TC was calculated, which together with the average T-gradient of the interval yield the interval heat-flow value.

Table B.2: Lithological composition of the intervals chosen for heat-flow calculation.

Well	Interval (m)	Lithological composition (%)												
		Dol	Ls	Dol ls	M	Cl	Sh	Ss	Car. Ss	Arg. Ss	Ch	Gyp	Chert	Congl.
Qiryat Gat 1	130–228				10						45		25	20
	355–405				40							60		
Ashalim 2	73–141	80						20						
	141–225	80		20										
	288–316	75			25									
	360–400	25	30	35		10								
Arad 1	84–140				65							20	15	
	188–251	75	5	10					10					
	262–330		40	55	5									
Efeh 3	50–160		20	70									10	
	171–220	100												
T.C. 1	170–225	10	60	30										
	250–276	90											10	
Ein Ofarim 1	169–265	60	15		20		5							
	304–330		70	10	20									
Meishar 1	100–157	90		10										
	185–211	80		5				15						
	222–250	50		50										
	263–300		50	30	5	5		10						
	325–423						5	70		25				
	446–467					85		15						
Paran 28	80–139		30								65		5	
	139–222		10		10						60		20	
	222–405		60		25							15		
Notza 1	160–250	50	20									30		
	350–423		5			55						40		
	555–625	25	30		20			10				15		
Qetura 9	100–130		20		30		15				20	15		
	150–220		40		30	30								
	316–363								35	65				

Dol - dolomite, Ls - limestone, Dol ls - dolomitic limestone, M - marlstone,Cl - clay, Sh - shale, Ss - sandstone, Car. Ss - carbonatic sandstone, Arg. Ss - argillicaeous sandstone, Si - siltstone, Ch - chalk, Gyp - gypsum, Congl - conglomerat

The T-logs obtained in the boreholes are shown in Figure C.1 and the T-gradient plots for these boreholes together with detailed lithostratigraphic descriptions in Figure C.2, respectively.

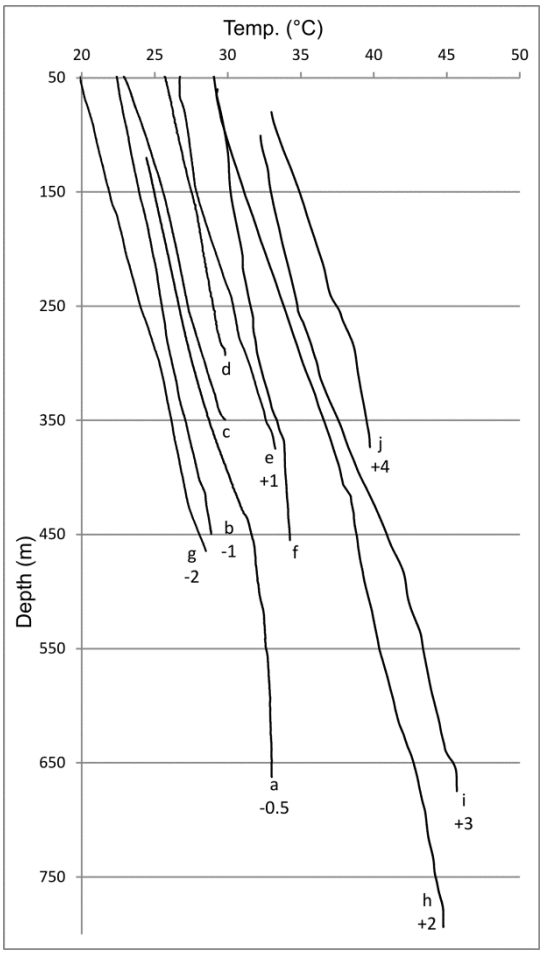

Figure C.1. Temperature-depth curves for the boreholes listed in Table 4.1. Offset of temperatures (in °C) from origin is given behind log ID.

In the *Qiryat Gat 1* well, T was recorded below the water table. The T-log shows some remarkable breaks in the T-gradient. A sudden increase in T at 425 m is followed by a very low T-gradient for the remainder of the section (Figure C.1, Figure C.2). The low gradient cannot be explained by any lithology and associated TC. We interpret the thermal pattern as an effect of fluid flow in the lower part of the section. Two depth intervals in the supposedly conductive part of the profile are selected for the heat-flow determination. These intervals (125–250 m and 350–400 m depth) show remarkably homogeneous T-gradients (Figure C.2). The upper interval, composed of mainly chalk and cherts, has a mean T-gradient of 17.1 °C km^{-1}; the lower interval, composed of gypsum and marl has a gradient of 28.3 °C km^{-1}. The resulting heat-flow values (51 and 48 mW m^{-2}, Table 4.1) are on the same order attesting heat conduction in the shallow subsurface above the thermally perturbed part of the borehole section.

In the *Ashalim 2* well, interval heat flow was determined below and above the water table (at 315 m). The four intervals selected show mean T-gradients in the range of 14.7–17.4 °C km^{-1}, resulting in interval heat flow between 49 to 54 mW m^{-2} (Table 4.1). Part of this scatter relates to

uncertainties in the assignment of interval TC, which in turn is linked with difficulties in estimating the fractions of sandy dolomite, dolomitic limestone or limy dolomite in the carbonate intervals. Heat flow in the air-filled part of the borehole is the same as in the water-filled section.

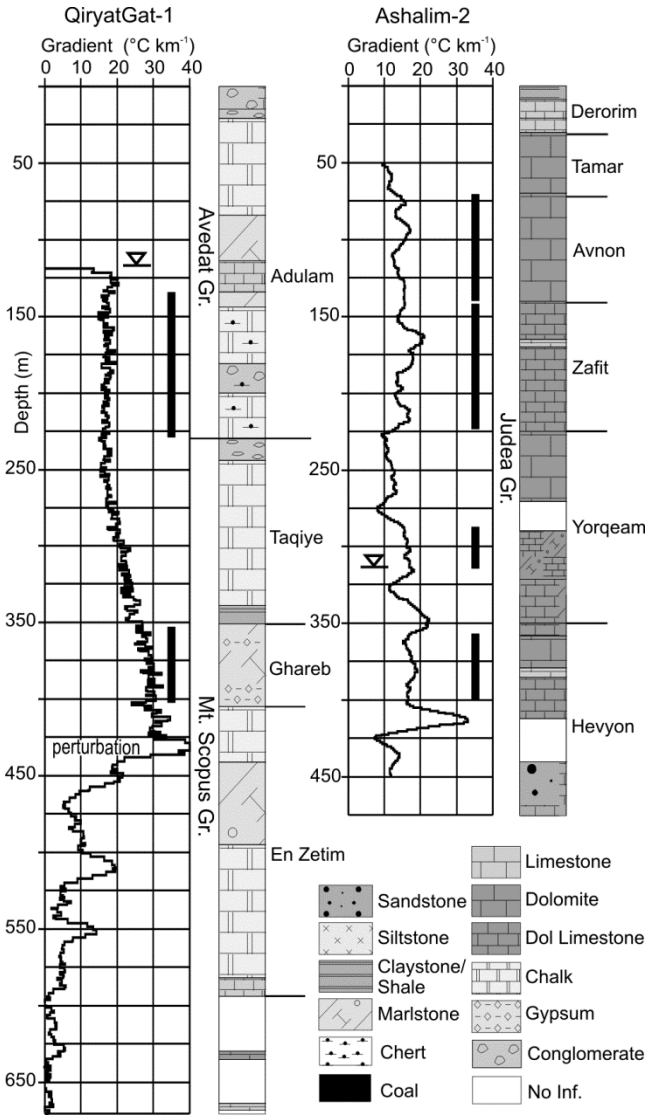

Figure C.2. T-gradients, determined for recording intervals, plotted versus depth. Also given are the lithology and stratigraphy. Blank intervals in the lithostratigraphic section are intervals of no information. Black vertical lines mark the intervals for which heat flow is determined. Triangle denotes the water table. Dol Limestone is dolomitic limestone, and K. Gr. is Kurnub Group. For location of wells see Figure 4.3.

In the *Arad 1* well, T-logging was performed above the water table (at 360 m). Three intervals were selected for heat-flow determination. The T-gradients show a range of 15.5–24.3 °C km^{-1}. The lowest value is from an interval of dolomitic composition and the largest value from an interval of marls with some gypsum (Table B.2), both of low TC. Interval heat flow ranges from 53 to 54 mW m^{-2} (Table 4.1).

In the *Efeh 3* well, T-logging was predominantly conducted in the air-filled borehole section, above the water table at 260 m. Two intervals were selected for heat-flow determination. The T-gradients of these intervals yield 18.8 °C km^{-1} and 13.9 °C km^{-1}. The gradient difference is a reflection of changes in lithology and hence changes in TC. The interval heat flow is 51 and 49 mW m^{-2} (Table 4.1).

In the *T.C. 1* well, heat flow also is determined in the air-filled portion of the well above the water table at 355 m depth. The mean T-gradients of the two intervals selected are 14.2 and 24.0 °C km^{-1}, again reflecting differences in lithology and therewith changes in TC. The lower gradient refers to dolomites, the higher gradient reflects an interlayering of limestone, chalk and marl (Table B.2). The interval heat-flow values are 53 and 58 mW m^{-2}.

In the *Ein Ofarim 15* well, the T-log was obtained in the water-filled part of the borehole. The log

shows several breaks in the temperature gradient with a major break at about 370 m (Figure C.1). Below this depth the temperature gradient is very low and needs to be associated with regional fluid flow. The log is problematic for heat-flow determination, and it was hoped that at least some intervals above the perturbed section were in the heat conduction domain. The best interval is at depth of 169–225 m (Figure C.2), covering the lithologically homogeneous Tamar and Avnon Formations. A second choice interval (304–330 m) is in the Yorqeam Formation. The two intervals show a slightly different lithological composition (Table B.2) and hence different T-gradients (15.9 and 20.2 °C km^{-1}). The upper interval, composed mainly of dolomite, has a heat-flow value of 54 mW m^{-2}, the lower interval, composed of limestone with minor dolomitic limestone and marl, a value of 55 mW m^{-2}, respectively (Table 4.1). As these heat-flow values are in line with those obtained in the air-filled portions of other boreholes, we feel confident that they are not affected by heat advection in aquifers.

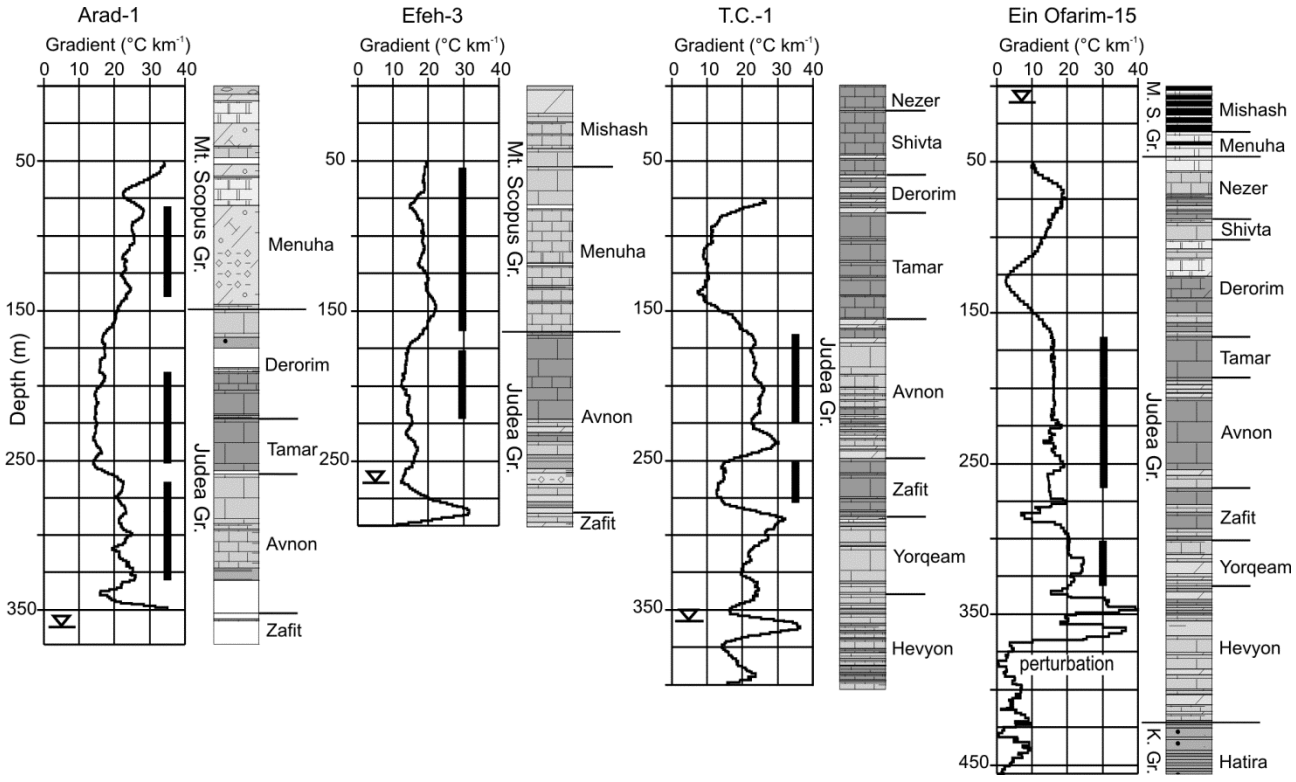

Figure C.2: continued.

In the *Meishar 1* well, heat flow was determined in six intervals of the air-filled part of the borehole. The interval T-gradients range from 14.3 to 29.0 °C km^{-1} in dependence on lithology. The lowest gradient is observed in the upper Hatira Formation, composed of argillaceous sandstone and quartzarenite (Table B.2), where TC is highest. The highest T-gradient is observed in the lower Hatira Formation consisting of shale of low TC. The interval heat-flow values range from 54 to 62 mW m^{-2} (Table 4.1).

In the *Paran 28* well, logging was performed below the water table occurring at 70 m depth. The T-log shows some local perturbation at about 420 m (Figure C.1). Three intervals were selected for heat-flow determination, all above the section in which fluid perturbations may play some role (Figure C.2). All intervals represent different geological formations of variable lithology (Table B.2). The average T-gradients of the intervals are in the range of 24.9–27.1 °C km^{-1}. The interval heat-flow values are between 55 and 69 mW m^{-2} (Table 4.1).

In the *Notza 1* well, T-logging was performed below the water table (below 130 m). The log shows breaks in the T-gradient that may be associated with fluid thermal perturbations (Figure C.1). The best-choice interval for the heat-flow determination is an interval of homogeneous lithology between 160–250 m depth (Figure C.2). In this interval the T- gradient is 18.4 °C km^{-1} and the heat flow 55.2 mW m^{-2}, respectively. The other two intervals (350–423 m and 555–625 m) show more lithological diversity, but provide heat-flow values on the same order (Table 4.1).

In the *Qetura 9* well, a T-log was recorded below the water table located at 85 m. It shows some breaks in the T-gradient at about 250–280 m depth (Figure C.1) related to fluid perturbations. Three intervals are selected for heat-flow determination (Figure C.2). Interval T-gradients range from 14.1 to 28.8 °C km^{-1}, reflecting well the different lithologies (Table B.2). The lowest TC (and hence the highest T-gradient) is in the argillaceous Orashale Formation; the highest TC (lowest gradient) in the Samal Formation, composed of shaly sandstone and quartzarenite. The resulting interval heat-flow values range from 58 to 61 mW m^{-2}. Heat flow being on the same order above and below the local thermal perturbation is indicative for heat conduction over large parts of the borehole section.

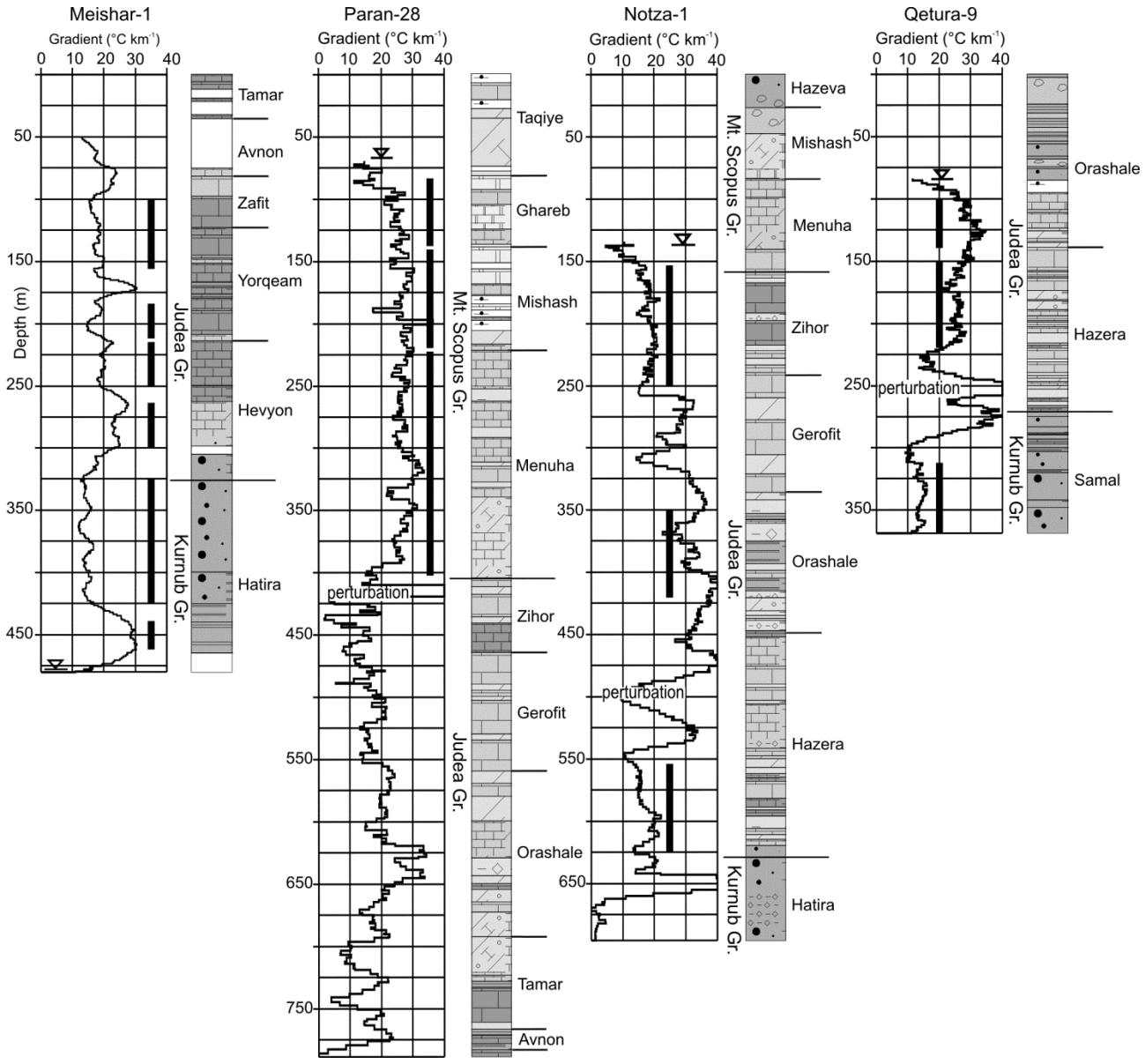

Figure C.2: continued.

5 Conclusions

The thermal properties (TC, RHP) of the sediments covering central and southern Israel were so far only barely known. With the first part of this study (chapter 2) huge progress is made in understanding TC variances in connection with porosity within the sedimentary basin, depending on lithotype and facies changes. It turned out that the TC is highly sensitive to facies changes in the sedimentary basin. Determined TCs of the same formations differ considerable with the depositional environment. Especially for sandstones it can be shown that facies related trends are not restricted to formation TC but also strongly affect TCs of lithotypes (cf. section 2.6.1; Table 2.2). An extrapolation of TC from one location to another seems conflicted with large errors. A detailed examination of depositional and diagenetic processes of geological formations hence is indispensable and the determination of average formation TCs has to be critically examined (section 2.6.2).

The TC values determined for dry and water-saturated samples are overall higher than values published until now (Eckstein and Simmons, 1978). Especially for clastic rocks, the values differ considerable from former published values (cf. Table 2.3). The influence of the pore-filling was so far neglected in studies about TC of the sedimentary rocks of central and southern Israel. Particularly for the rock samples with high porosities, it can be shown that the deviations between measurements on dry samples and on water-saturated samples are distinct and cannot be disregarded. Moreover, this study provides data for a very detailed subdivision of lithotypes (mean values for 17 lithotypes, cf. Table 2.3).

Second thermal parameter is the RHP. The amount of heat generated by the sediments themselves is an important component in the thermal characterization of a sedimentary basin. Especially clastic sediments can have high RHP values. To quantify this parameter gamma-ray logs from the area were analyzed and the RHP of the important stratigraphic formations were determined (cf. Table 2.4). Based on this dataset the heat budget for each stratigraphic group and finally for the whole sedimentary section down to the basement were calculated. Where the sedimentary veneer is thickest (7 km) an amount of ca. 4 mW m^{-2} is produced by the sediments (section 2.6.3). This is comparably low owing to the dominance of carbonates in the sedimentary basin.

The reevaluation of a heat-flow site studied by Eckstein and Simmons (1978) shows the importance of the TC in order to determine the q_S. A diverse approach, considering more carefully the lithological changes in the borehole, and the combined gradient changes leads, in connection with the higher TC values, to higher q_S values (cf. Table 2.5). The improved approach also results in a much smaller range of q_S values for the different intervals (51.8–61.9 mW m^{-2}, mean 57.3 ±

4 mW m^{-2}) compared to the former study (34.6–52.9 mW m^{-2}, mean 37 mW m^{-2}) and, therewith, seems to better reflect undisturbed crustal heat flow (section 2.7.1).
With the new TC values a database exists which enables to model the deep thermal field. The new data were used to calculate temperature at depth beyond logging data. Considering the utilization of geothermal resources the prognosed temperature showed that hydrothermal resources may be used where the sedimentary cover is thick. For higher temperatures the basement must be considered (cf. section, 2.7.2; Figure 2.11).

The fist part of this study clearly highlights that a sufficient knowledge of the TC is indispensable for the determination of reliable q_S values and moreover for understanding the thermal regime of a sedimentary basin. Different theoretical approaches for calculating the BTC based on MTC and porosity can lead to significantly different results. The most commonly used models were tested in the second part (chapter 3) of this study: the geometric, arithmetic and harmonic mean, the Hashin and Shtrikman mean and the effective-medium theory mean. The different mixing models were applied on a large dataset of BTC measured on dry rocks to calculate the water-saturated BTC using the porosity. The calculated values were then compared with the measured water-saturated BTC (cf. section 3.6.1; Figure 3.2) and a statistical analysis of the deviations was performed. The deviation between laboratory measured and calculated BTC is highly different for the various mixing models and the different lithotypes (cf. section 3.7.1; Figure 3.6). The database comprises sandstone, limestone, dolomite and mudstone. For characterizing a sediment basin, huge amounts of samples are required. To measure them dry and water-saturated is somehow time-consuming. The evaluation of the different approaches to calculate the water-saturated values based on dry measured values and porosity improves the knowledge of the applicability of the different mixing models. Some of the mixing models achieve for none of the lithotypes a good fit, like the harmonic mean and the effective medium mean. Others show a variable fitting behavior for the different lithotypes, like the arithmetic mean and the Hashin and Shtrikman mean. The geometric mean shows basically a good fitting behavior. Nevertheless, also the geometric mean does not satisfy for all lithotypes. Correction equations are developed to reduce the mismatch between measured and calculated BTC for the three most common models; the geometric, arithmetric and Hashin and Shtrikman mean (cf. section 3.7.2; Table 3.1). Furthermore, equations were set up to directly calculate water-saturated BTC from dry-measured BTC data and known porosity (e.g., well log porosity) for the four studied lithotypes and one general equation considering all lithotypes (section 3.7.3). This equation achieves a good fit for all lithotypes and is a useful alternative to reduce the workload of studies dealing with the thermal characterization of a sedimentary basin and handling huge amounts of

samples and saves the appliance of correction equations to one of the mean models.

The thermal regime of the lithosphere beneath Israel was studied in detail in the last part of the study (chapter 4). The main parameter in understanding the lithospheric thermal regime is the q_S, which was determined at ten well locations, well spread over central and southern Israel. The thermal parameters of the sediments composing the basin, studied in detail in chapter 2, were the critical quantity for this determination. With this knowledge it was possible to determine new reliable q_S values. The resulting q_S values were overall higher than former published values and spread over a relatively small range, 50–62 mW m^{-2} compared to 30−85 mW m^{-2} reported in the studies of Eckstein and Simmons (1978) and Shalev et al. (2012) (cf. Figure 4.2 and 4.3). The observed range in q_S between 50 and 62 mW m^{-2} could easily be explained by variation in the composition (heat production) of the upper crust, accompanied by more systematic spatial changes in its thickness. Trends of slightly decreasing and increasing q_S from the E–W and N–S, determined in this study, are in line with changes in the crustal structure. From the east to the west the crust show a general thinning with a thickening of the sediments at the expense of upper crystalline crust. From the north to the south it is the other way round. This part of the lithosphere is certainly not homogeneous over the entire study area as treated in the modeling. On a small scale, in areas of a relatively thinner upper crystalline crust containing a larger proportion of less-radiogenic material, q_S may be eventually as low as 45 mW m^{-2}. Conversely, in regions of thick crystalline crust, a comparatively larger amount of more-radiogenic material would cause the q_S to exceed 60 mW m^{-2}. However, a general low q_S (~45 mW m^{-2}) in the area stated by several authors (Eckstein and Simmons, 1978; Ben-Avraham et al., 1978; Aldersons et al., 2003; Shalev et al., 2012) is contradictory to the results of this study. Such a low q_S would require either an abnormal upper crustal composition of only intermediate or mafic rocks or a mantle heat flow of as low as 18 mW m^{-2}. Both are contrarily of the geophysical and geological observations.

Based on the field-determinations, a thermal model was adjusted (section 4.6.1). The most reliable model owing to the best fitting between modeled and measured q_S has a LAB temperature (1300°C) as lower boundary located in 150 km depth (cf. Figure 4.7c). Different scenarios concerning the composition of the crust were tested and considering the uncertainties in q_S a 10% more and 10% less radiogenic upper crust (cf. Table 4.2) would also match the measured q_S data. The lithosphere was therewith most likely about 150 km thick before thermal erosion, caused by subrecent processes like the DST activation, initiated by mantle plume upwelling, started. This would implement a thermal erosion of the lithosphere of 70–90 km, considering present day thickness of 60–80 km, (Mohsen et al., 2006) in a very short time (~15 Ma), which can be explained with a thermochemical plume (Sobolev et al., 2011).

The temperature predictions of the thermal model are in accordance to recent estimates on the earthquake focal depths in the area of the DSB (cf. section 4.7.1). For mantle peridotite, the transition from seismic to aseismic behavior occurs at ~600°C (McKenzie et al., 2005; Boettcher et al., 2007), which is lower than the minimum Moho-temperature of 635°C determined in this study (cf. Figure 4.7c) and in line with the absence of mantle-induced earthquakes on the territory of Israel (Aldersons et al., 2003; Shamir, 2006) (cf. section 4.7.1).

In order to understand the formation of the pull-apart DSB several authors performed modeling, with q_S values of the study area as an important input parameter. Al-Zoubi and ten Brink (2002) considered q_S values of 45–53 mW m^{-2} to explain basin subsidence and insignificant Moho uprise beneath the DSB by a strike-parallel ductile flow in the lower crust. How higher heat-flow values would affect the lower crustal viscosity was unfortunatly not examined. To explain the formation of the pull-apart DSB Petrunin and Sobolev (2006) conducted thermomechanical modeling and reached the best results with q_S values as high as 60 mW m^{-2}. Later on, Petrunin and Sobolev (2008) performed a number of numerical thermomechanical experiments including models with initial q_S values of 40−70 mW m^{-2} to understand how rheology of the lithosphere influences basin evolution. Results are shown for three particular cases with initial q_S values between 50 and 60 mW m^{-2}. These values are in line with the results from this study and corroborate the measured q_S east of the DST, in Jordan (Förster et al., 2010). Petrunin et al. (2012) performed 3-D thermomechanical modeling to understand the formation of the DSB confirming that q_S values less than 50–60 mW m^{-2} are inconsistent with the tectonic settings specific for an active continental plate boundary and with the crustal structure of the DSB.

This study contributes an important step in understanding the thermal regime of the area and the LAB depth of pre-Oligocene times. It also improves the knowledge about the heat-flow pattern of the AS. The crustal thickness of the AS commonly range between 32 and 39 km. Heat flow determined in this study in crustal segments of the same thickness is in the order of ~55 mW m^{-2} and consistent with the q_S patterns established in provinces of Neoproterozoic age (Nyblade and Pollack, 1993; Rudnick et al., 1998). Furthermore, the bulk heat flow of the crust, determined from its thickness and the total RHP (cf. Table 4.2, Figure 4.6b), displays values between 22 and 32 mW m^{-2}, thereby being in the range estimated for bulk continental crust (Rudnick et al., 1998).

This is in accordance to values determined by Förster et al. (2007) in Jordan. Hence q_S values of ~55 mW m^{-2} may be representative for the northern AS. Open questions remain if this range typifies the entire AS and if the q_S of the APl is in fact significantly lower ≤ 45 mW m^{-2}, like recently performed studies (Lucazeau et al., 2008; Rolandone et al., 2013) determined (section 4.7.2).

6 References

Aldersons, F., Ben-Avraham, Z., Hofstetter, A., Kissling, E. and T. Al-Yazjeen (2003), Lower-crustal strength under the Dead Sea basin from local earthquake data and rheological modeling, Earth Planet. Sci. Lett., 214, 129–142.

Al-Zoubi, A., and U. ten Brink (2002), Lower crustal flow and the role of shear in basin subsidence: an example from the Dead Sea basin, Earth Planet. Sci. Lett., 199, 67–79.

Bartov, Y., Steinitz, G., Eyal, M., and Y. Eyal (1980), Sinistral movement along the Gulf of Aqaba – its age and relation to the opening of the Red Sea, Nature, 285, 220–221.

Beck, A.E. (1957), A steady state method for the rapid measurement of the thermal conductivity of rocks, J. Sci. Instr., 34 , 186–189.

Ben-Avraham, Z., Hänel, R. and H., Villinger (1978), Heat flow through the Dead Sea Rift, Mar. Geol., 28, 253–269.

Beyth, M., Stern, R., Altherr, R., and A. Kröner (1994), The Late Precambrian Timna igneous complex, Southern Israel: Evidence for comagmatic-type sanukitoid monzodiorite and alkali granite magma, Lithos, 31, 103–124.

Birch, F. (1950), Flow of heat in the Front Range, Colorado, Bull. Geol. Soc. Am., 61, 567–630.

Boettcher, M. S., Hirth, G., and B. Evans (2007), Olivine friction at the base of oceanic seismogenic zones, J. Geophys. Res., 112, B01205, doi:10.1029/2006JB004301.

Bogoch, R., Avigad, D., and T. Weissbrod (2002), Geochemistry of the quartz diorite-granite association, Roded area, southern Israel, J. Afr. Eart. Sci., 35, 51–60.

Bohannon, R. G., Naeser, C. W., Schmidt, D. L., and R. A. Zimmermann (1989), The timing of uplift, volcanism, and rifting peripheral to the Red Sea: a case for passive rifting? J. Geophys. Res., 94, B2, 1683–1701.

Eckstein, Y., and G. Simmons (1978), Measurement and interpretation of terrestrial heat flow in Israel, Geothermics, 6, 117–142.

Eyal, M., Litvinovsky, B., Jahn, B. M., Zanvilevich, A., and Y. Katzir (2010), Origin and evolution of post-collisional magmatism: Coeval Neoproterozoic calc-alkaline and alkaline suites of the Sinai Peninsula, Chemical Geology, 269, 153–179.

Förster, A., and H.-J. Förster (2000), Crustal composition and mantle heat flow: Implications from surface heat flow and radiogenic heat production in the Variscan Erzgebirge (Germany), J. Geophys. Res., 105, B12, 27,917–27,938.

Förster, A., Förster, H.-J., Masarweh, R., Masri, A. and K. Tarawneh (2007), The surface heat flow of the Arabian Shield in Jordan, J. Asian Earth Sci., 30, 271–284.

Förster, H.-J., Förster, A., Oberhänsli, R., and D. Stromeyer (2010), Lithospheric composition and

thermal structure of the Arabian Shield in Jordan, Tectonophysics, 481, 29–37.

Fowler, C. M. R. (1990), The Solid Earth. An Introduction to Global Geophysics, Cambridge University Press, Cambridge, 418 pp.

Freund, R., Garfunkel, Z., Zak, I., Goldberg, M., Weissbrod, T., and B. Derin (1970), The shear along the Dead Sea rift, Philosophical Transaction of the Royal Society of London, Series A267, 107–130.

Gardosh, M. A., and Y. Druckman (2006), Seismic stratigraphic and tectonic evolution of the Levantine Basin, offshore Israel, in The tectonic evolution of the Eastern Mediterranean region, edited by Robertson A.H.F and D. Mountrakis, pp. 201–227, Geological Society, London, Special Publications, 260.

Garfunkel, Z., and B. Derin (1984), Permian-early Mesozoic tectonism and continental margin formation in Israel and its implications for the history of the Eastern Mediterranean, Geological Society, London, Special Publications, 17, 187–201.

Garfunkel, Z. (1988), The pre-Quaternary geology of Israel, in The zoogeography of Israel, edited by Yom-Tov, Y., and Tchernov, E., pp. 7–33, Dr. W. Junk Publishers, Dordrecht, Netherlands.

Garfunkel, Z. (1998), Constrains on the origin and history of the Eastern Mediterranean basin, Tectonophysics, 298, 5–35.

Gazit, O. (2005), Mafic Granulite Xenoliths from Qarnei Hittin and the the Evolution of the Lower Crust Beneath Northern Israel, Report GSI/11/05, Geological Survey of Israel, Jerusalem.

Gill, D. (1992), Israel's Petroleum Discovery Curve, Nonrenewable Resources, 1, 3, pp 231-238.

Ginzburg, A., and J. Makris (1979), Gravity and density distribution in the Dead Sea rift and adjoining areas, Tectonophysics, 54, 17–25.

Gvirtzman, Z. (2004), Chronostratigraphic table and subsidence curves of southern Israel, Isr. J. Earth Sci., 53, 47–61.

Hansen, S. E., Rodgers, A. J., Schwartz, S. Y., and A.M.S. Al-Amri (2007), Imaging ruptured lithosphere beneath the Red Sea and Arabian Peninsula, Earth Planet. Sci. Lett., 259, 256–265.

Hasterok, D., and D. S. Chapman (2011), Heat production and geotherms for the continental lithosphere, Earth Planet. Sci. Lett., 307, 1−2, 59−70.

Heimann, A., Steinitz, G., Mor, D., and G. Shaliv (1996), The Cover Basalt Formation, its age and its regional and tectonic setting: Implications from K–Ar and $^{40}Ar/^{39}Ar$, Isr. J. Earth Sci., 45, 55–71.

Hofstetter, A., Feldman, L., and Y. Rotstein (1991), Crustal structure of Israel: constraints from teleseismic and gravity data, Geophys. J. Int., 104, 371–379.

Johnson, P. R., Andresen, A., Collins, A. S., Fowler, A. R., Fritz, H., Ghebreab, W. Kusky, T., and R. J. Stern (2011), Late Cryogenian–Ediacaran history of the Arabian–Nubian Shield: A review of depositional, plutonic, structural, and tectonic events in the closing stages of the northern East African Orogen, J. Afr. Earth. Sci., 61, 167–232.

Kröner, A., Eyal, M., and Y. Eyal (1990), Early Pan-African evolution of the basement around Elat, Israel, and the Sinai Peninsula revealed by single-zircon evaporation dating, and implications for crustal accretion rates, Geology, 18, 545–548.

Lemmon, E. W., McLinden, M. O., and D. G. Friend (2005), Thermophysical properties of fluid systems, in NIST Chemistry WebBook, NIST Standard Reference Database, edited by Linstrom, P. J., Mallard, W. G., Number 69. National Institute of Standards and Technology, Gaithersburg MD, pp. 20899, http://webbook.nist.gov.

Lucazeau, F., Leroy, S., Bonneville, A., Goutorbe, B., Rolandone, F., D'Acremont, E., Watremez, L., Düsünur, D., Tuchais, P., Huchon, P., Bellahsen, N., and K. Al-Toubi (2008), Persistent thermal activity at the Eastern Gulf of Aden after continental break-up, Nature Geoscience, 1, 854–858.

Mahmoud, S., Reilinger, R., McClusky, S., Vernant, P., and A. Tealeb (2005), GPS evidence for northward motion of the Sinai Block: Implications for E. Mediterranean tectonics, Earth Planet. Sci. Lett., 238, 217–224.

Mareschal, J. C., and C. Jaupart (2004), Variations of surface heat flow and lithospheric thermal structure beneath the North American craton, Earth Planet. Sci. Lett., 233, 65−77.

McKenzie, D., Jackson, J., and K. Priestley (2005), Thermal structure of oceanic and continental lithosphere, Earth Planet. Sci. Lett., 233, 337– 349.

Mechie, J., Abu-Ayyash, K., Ben-Avraham, Z., El-Kelani, R., Qabbani, I., Weber, M., and DESIRE Group (2009), Crustal structure of the southern Dead Sea basin derived from project DESIRE wide-angle seismic data, Geophys. J. Int., 178, 1, 457–478.

Mechie, J., Ben-Avraham, Z., Weber, M.H., Götze, H.-J., Koulakov, I., Mohsen, A., and M. Stiller (2013), The distribution of Moho depths beneath the Arabian plate and margins, Tectonophysics, http://dx.doi.org/10.1016/j.tecto.2012.11.015.

Mohsen, A., Kind, R., Sobolev, S. V., Weber, M., and DESERT Group (2006), Thickness of the lithosphere east of the Dead Sea Transform, Geophys. J. Int., 167, 845–852.

Mushkin, A., Navon, O., Halicz, L., Hartmann, G., and M. Stein (2003), The Petrogenesis of A-type Magmas from the Amram Massif, Southern Israel, J. Petrol, 44, 815–832.M

Navon, O., Gazit, O., Halicz, L., Don, A., Garfunkel, Z., and M. Stein (2007), The composition and evolution of the crust beneath: Inferences from xenoliths and granites, Final report, ES-46–2006, Geological Survey of Israel, Jerusalem.

Nyblade, A. A., and H. N. Pollack (1993), A Global Analysis of Heat Flow From Precambrian Terrains: Implications for the Thermal Structure of Archean and Proterozoic Lithosphere, J. Geophys. Res., 98, B7, 12,207–12,218.

Perry, H. K. C., Jaupart, C., Mareschal, J.-C., and G. Bienfait (2006), Crustal heat production in the Superior Province, Canadian Shield, and in North America inferred from heat flow data, J. Geophys. Res., 111, B04401.

Petrunin, A., and S. Sobolev (2006), What controls thickness of sediments and lithospheric deformation at a pull-apart basin? Geology, 34, 389–392.

Petrunin, A., and S. Sobolev (2008), Three-dimensional numerical models of the evolution of pull-apart basins, Phys. Earth Planet. Inter., 171, 387–399.

Petrunin, A., Rioseco, E. M., Sobolev, S., and M. Weber (2012), Thermomechanical model reconciles contradictory geophysical observations at the Dead Sea Basin, Geochem. Geophys. Geosyst., 13, 4, doi:10.1029/2011GC003929, in press.

Pollack, H. N., and D. S. Chapman (1977), Mantle heat flow, Earth Planet. Sci. Lett., 34, 174−184.

Rolandone, F., Lucazeau, F., Leroy, S., Mareschal, J.-C., Jorand, R., Goutorbe, B., and H. Bouquerel (2013), New heat flow measurements in Oman and the thermal state of the Arabian shield and platform, Tectonophysics, 589, 77–89.

Rudnick, L. R., McDonough, F. W., and R. J. O'Connell (1998), Thermal structure, thickness and composition of continental lithosphere, Chem. Geol., 145, 395–411.

Rybakov, M., and A. Segev (2004), Top of the crystalline basement in the Levant, Geochem. Geophys. Geosyst., 5, 1–8.

Salamon, A, Hofstetter, A., Garfunkel, Z., and H. Ron (2003), Seismotectonics of the Sinai subplate – the eastern Mediterranean region, Geophys. J. Int., 155, 149–173.

Schütz, F., Norden, B., Förster, A., and DESIRE Group (2012), Thermal properties of sediments in southern Israel: a comprehensive data set for heat flow and geothermal energy studies, Basin Research, 24, 357–376.

Segev, A. (2000), Synchronous magmatic cycles during the fragmentation of Gondwana: radiometric ages from the Levant and other provinces, Tectonophysics, 325 (3–4), 257–277.

Shalev, E., Lyakhovsky, V., Weinstein, Y., and Z. Ben-Avraham (2012), The thermal structure of Israel and the Dead Sea Fault, Tectonophysics, 602, 69–77.

Sobolev, S. V., Petrunin, A., Garfunkel, Z., Babeyko, A. Y., and DESERT Group (2005), Thermo mechanical model of the Dead Sea Transform, Earth Planet. Sci. Lett., 238, 78–95.

Stern, R. J., and A. Kröner (1993), Geochronologic and isotopic constraints on Late Precambrian crustal evolution in NE Sudan, J. Geol., 101, 555–574.

Stern, R. J., and M. G. Abdelsalam (1998), Formation of juvenile continental crust in the Arabian-

Nubian Shield: Evidence from granitic rocks of the Nakasib Suture, NE Sudan, Int. J. Earth Sci., 87, 150–160.

Stern, R. J., and P. Johnson (2010), Continental lithosphere of the Arabian Plate: A geologic, petrologic, and geophysical synthesis, Earth Sci. Rev., 101, 29–67.

Vila, M., Fernández, M. and, I. Jiménez-Munt (2010), Radiogenic heat production variability of some common lithological groups and its significance to lithospheric thermal modelling, Tectonophysics, 490, 152–164.

Von Herzen, R.P., and A.E. Maxwell (1959), The measurement of thermal conductivity of deep-sea sediments by a needle probe method, J. Geophys. Res., 64 , 1557–1563.

Weber, M., et al. (2004), The crustal structure of the Dead Sea Transform, Geophysical Journal International, 156, 3, 655–681.

Wilson, M., Shimron, A. E., Rosenbaum, J. M., and J. Preston (2000), Early Cretaceous magmatism of Mount Hermon, Northern Israel, Contrib. Mineral. Petrol., 139, 54–67.

7 Appendix

A1 Modeling

The modeling described in chapter 4.6 is performed with two different depths of the lower boundary. In scenario (1) the lower boundary (LAB temperature, 1300°C) is set in 150 km depth and in scenario (2) in 120 km depth. The resulting isotherms are only shown for scenario (1) (chapter 4.6.2, Figure 4.7). The resulting isotherm-plot of scenario 2 (Figure A1.1) is shown here.

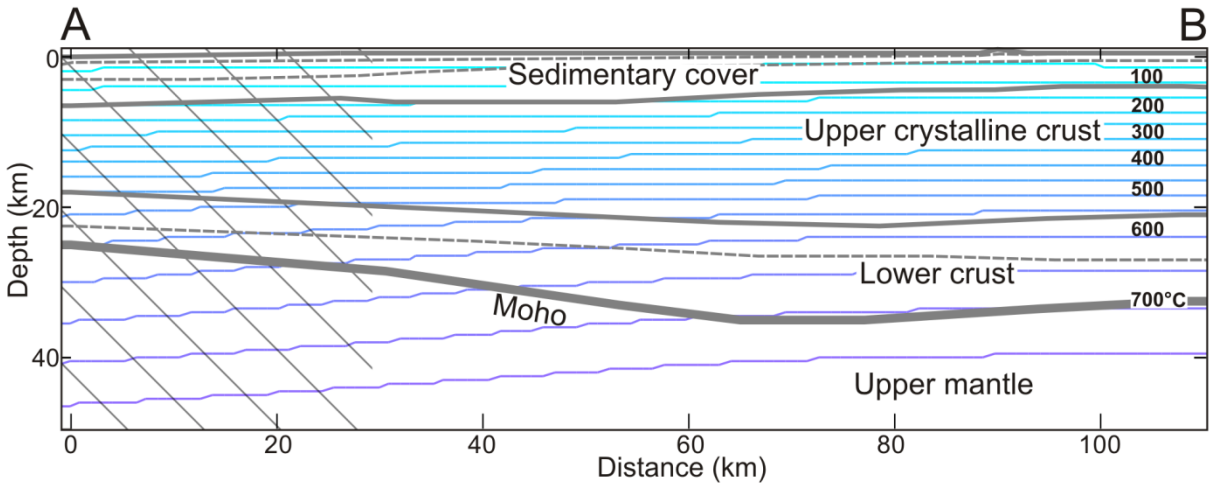

Figure A1.1: Modeled isotherms for a lower boundary (1300°C) set in 120 km depth (scenario 2) using the thermal rock properties shown in Table 4.2. Shaded is the portion of the profile with no measured surface heat flow.

A2 Modeling based on the DESERT profile

The modeling procedure is explained in detail in Chapter 4.6. Additionally to the modeling based on the DESIRE seismic profile, the DESERT seismic profile (location see Figure A2.1; Weber et al., 2004) was used as model-basis. The conceptual model is the same (see chapter 4.6.1) except for the structure. Structure and results of this second modeling approach are shown here with a short discussion.

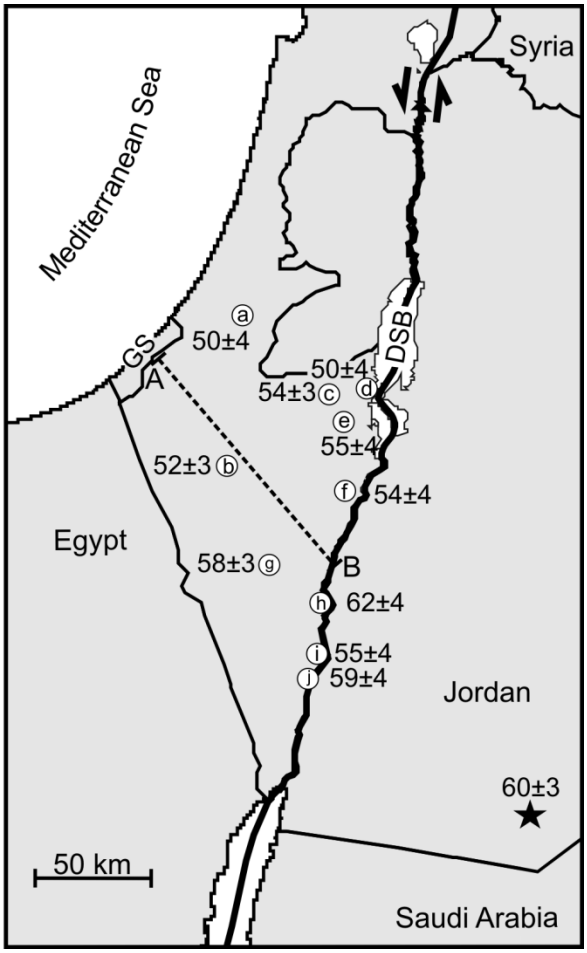

Figure A2.1: Surface heat flow (in mW m^{-2} with mean absolute error) determined in this study at 10 wells (cf. Figure 4.3). Letters in circles refer to the name of wells and the thermal data shown in Table 4.1. The dashed line marks the trace of the DESERT seismic profile (A–B) along which lithosphere thermal modeling was performed (cf. Figures A2.2–2.4). The star indicates the approximate position of the heat-flow borehole cluster studied by Förster et al. (2007).

A2.1 Structure

The DESERT seismic profile completed 2000, was the first to cross the DST and is 260 km long. The seismological model based on the DESERT profile distinguishes only four different crustal layers (Figure A2.2a) compared to seven layers in the DESIRE seismic profile. The uppermost two layers consist of sedimentary rocks (Vp 3.5−3.7 km s^{-1}, 5.1 km s^{-1}). Top of the third layer marks, after Mechie et al. (2005), the intersection to the Precambrian basement (Vp 6.2−6.4 km s^{-1}). The boundary between upper and lower crust is marked by an increase in Vp velocity to 6.7 km s^{-1}. Both seismological models (DESIRE and DESERT) indicate a Moho depth of ~35 km close to the transform in the east and a flattening of the Moho depth towards the west to ~25 km. The sedimentary veneer in the DESIRE profile thickens towards the west. This observation cannot be

made in the DESERT model. The sedimentary thickness is over the whole length of the DESERT seismic profile more than 5 km which is not coherent with well log observations. Several wells in southeastern area penetrate the basement (Gvirtzman, 2004; Rybakov and Segev, 2004) and indicate that the sediments thin towards the southeast. The well log data implement a thinning of the sediments from about 6 km to 2.5 km along the DESERT profile. Part of the misfit probably results from a false classification of basement rocks as pre-DST sediments. For the thermal modeling the DESERT seismic model hence will not be used in the original form but with an offset of the basement depth (compare Figure A2.2a and A2.2b).

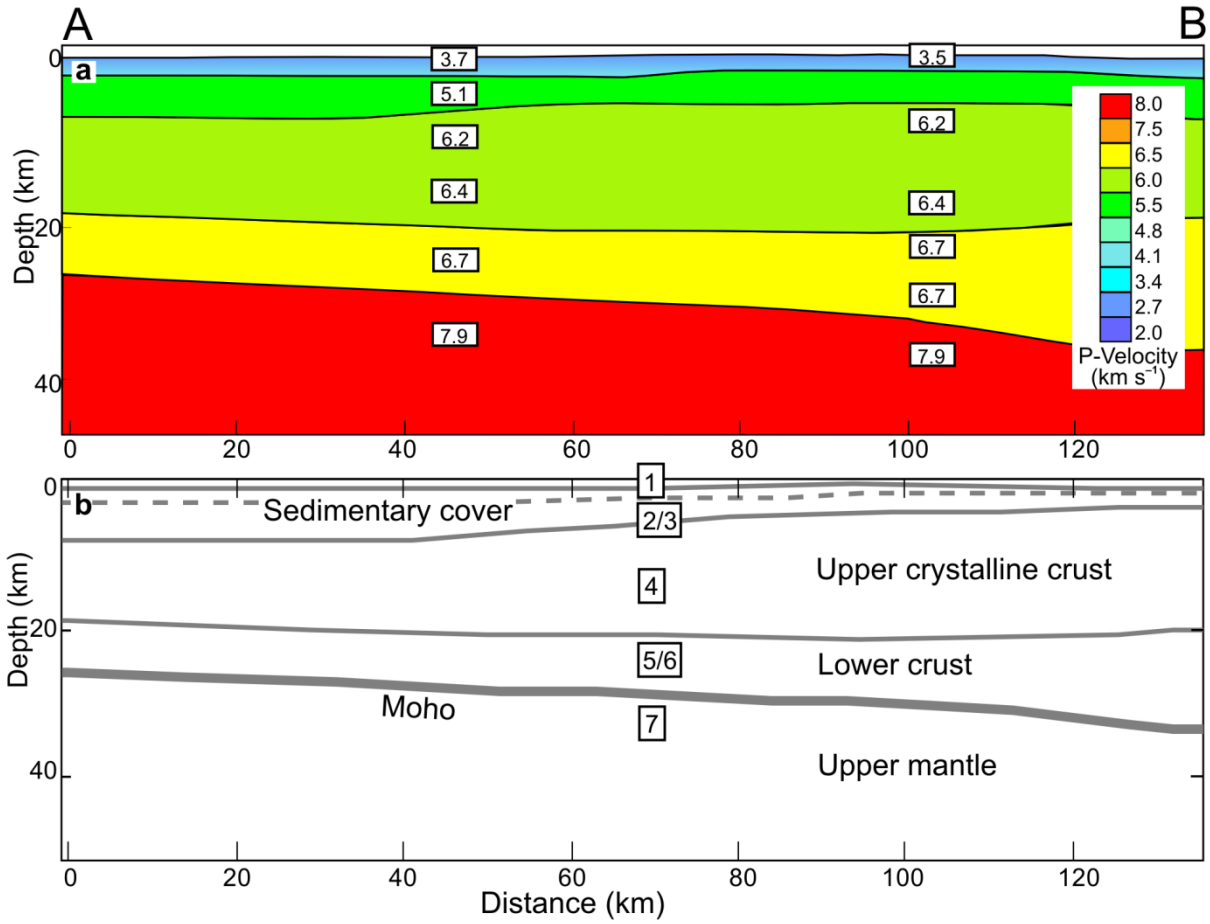

Figure A2.2: (a) Lithosphere structure and Vp along DESERT seismic profile (Weber et al., 2004) (cf. Figure A2.1). (b) Geological interpretation. The numbering of the lithosphere units refers to the conceptual model for thermal modeling explained in detail in section 4.5.1 (cf. Table 4.2).

The crustal thinning in the DESERT model is mainly on the expense of the lower crust and only to a minor part of the upper crust. After readjusting the basement depth, the thickness of the upper crust, without the sedimentary cover, is 17.5 km in the southeastern part of Israel close to the transform.

A2.2 Results

The thermal parameters applied for the modeling are listed in Table 4.2. Where two layers are subsumed to one layer (Figure A2.2b) a mean value of both is applied.

Scenario 1 (LAB = 150 km): The modeled q_S reproduces the measured q_S in a satisfying way. However, the misfit between the q_S values based on the modeling and based on the measurements is higher in this example (max. deviation 4 mW m^{-2}, RMSE 6.4) compared to the modeled q_S based on the structure derived from the DESIRE-profile. Nevertheless the increase of q_S towards the south is observable in the measured and the modeled values. Given the uncertainties in q_S, the measured data would also be matched, if the upper crust would be either about 10% more or less radiogenic than reported in Table 4.2.

The slightly higher q_S fits very well with the somewhat different crustal setup. The smaller amount of sediments leads to a higher amount of basement rocks with higher RHP values. Towards the coast the crustal setup equals with the crustal setup based on the DESIRE profile and therewith also the q_S based on the DESERT and the DESIRE seismic profiles is consistent.

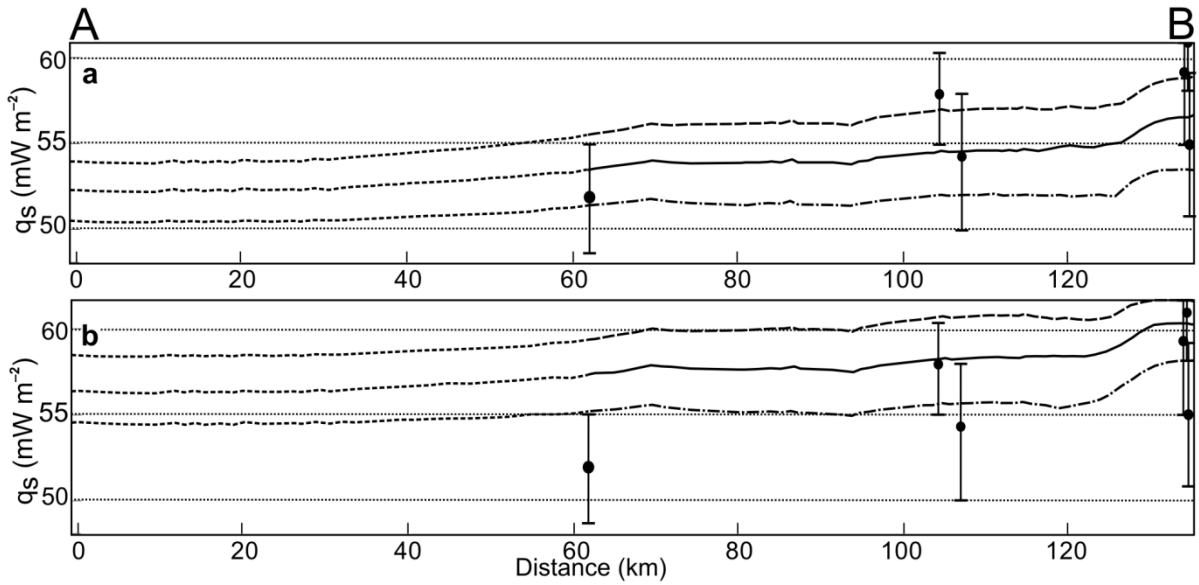

Figure A2.3: Modeled surface heat-flow (q_S) patterns along the DESERT seismic profile shown in Figure A2.1. The dots with the mean absolute error bars refer to the q_S values determined for the six sites closest to the profile (cf. Figure A2.1) Modeling was conducted for pre-Oligocene LAB depths of 150 km (a) and 120 km (b). Full lines represent the modeled q_S patterns obtained with the thermal parameters listed in Table 4.2. Dashed and dashed-dotted lines mark the patterns modeled for an upper crystalline crust 10% richer resp. poorer in RHP (A) relative to the A data in Table 4.2. Dotted portions of lines indicate the section of the profile, for which there is no q_S control (km 0–60).

Scenario 2 (LAB = 120 km): The modeled q_S (58−62 mW m^{-2}) overestimate the measured q_S (50−62 mW m^{-2}). Especially towards the Mediterranean Sea the modeled values highly

overestimate the measured values. Only if the upper crystalline crust would have a lower RHP by 10% or more, which would reflect a more mafic upper crust, than the original input parameters (Table 4.2) imply, the fit would be reasonable. However, the misfit between measured and modeled q_S towards the south-west would still be significant.

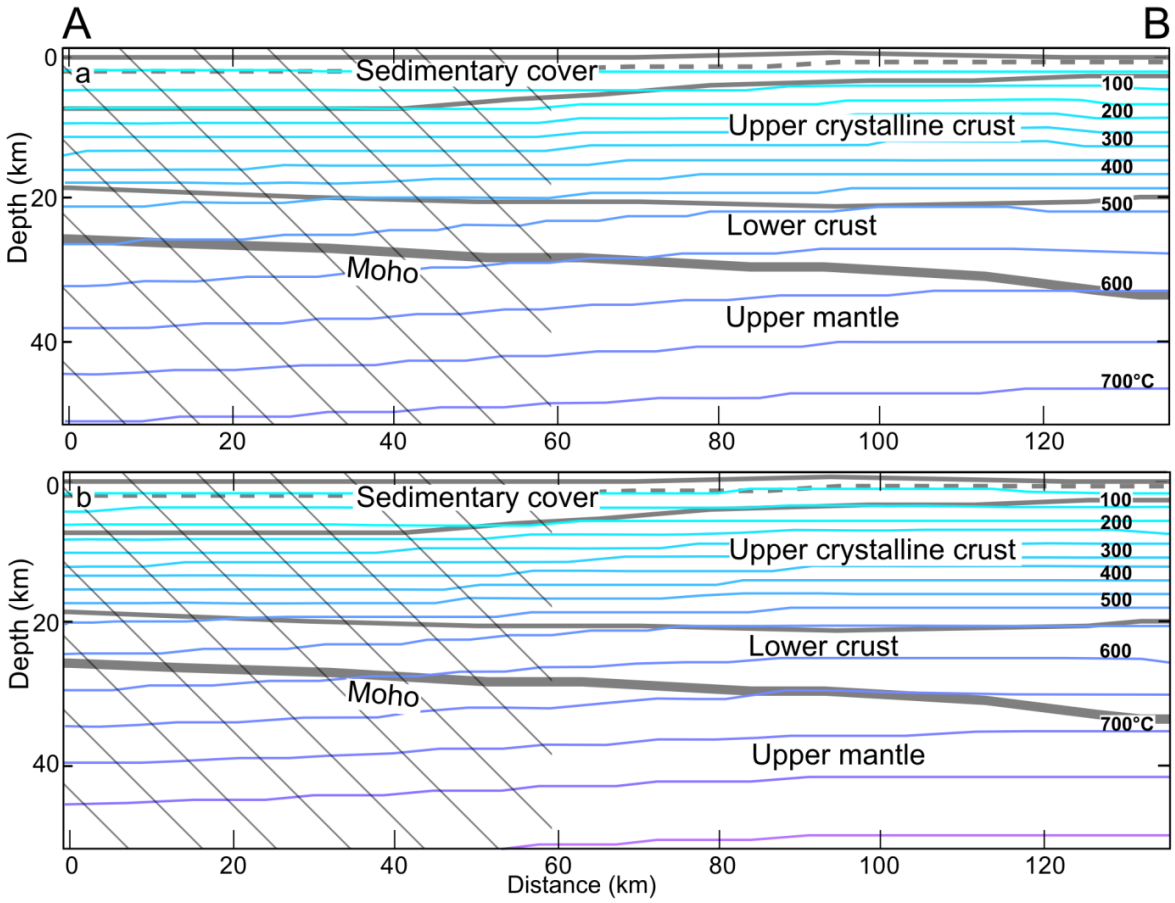

Figure A2.4: Modeled isotherms for a LAB depth of 150 km (a) and 120 km (b) using the thermal rock properties shown in Table 4.2. Shaded is the portion of the profile with no measured surface heat flow.

A3 Lower crustal and upper mantle xenoliths

Modeling requires information about the thermal properties of the lower crust and the upper mantle. Xenoliths provide a good opportunity to study composition and thermal properties of deep parts of the lithosphere. Xenolith samples from Israel are restricted to the northern part, however, deep geophysical studies of p-wave velocities and density show changes in the structure, thickening of the sediments and deepening of the Moho, but no significant changes in crustal composition from the south to the north (Ginzburg and Makris, 1979; Hofstetter et al., 1991). Eight xenoliths from northern Israel were considered as representative also for central and southern Israel and analyzed in terms of their thermal conductivity (TC) to then use the results in the model parameterization. As this investigation and the results were not examined in one of the manuscripts it will be enlightened here.

A3.1 Introduction

In terms of this study eight lower crustal and upper mantle xenoliths were analyzed concerning TC and porosity. The lower crustal xenoliths were interpreted as mafic granulites with a basaltic cumulate as educt (Navon et al., 2007). The upper mantle xenolith is a harzburgite. Volcanism in the Levantine Basin (LB) extended from Early Mesozoic to recent times. The xenoliths analyzed in this study originate from the Pliocene basaltic volcanism (4.3 ± 0.1 to 4.1 ± 0.2 Ma, Heimann et al., 1996) of the Qarnei Hittin area in northern Israel. The volcanism is linked to the DST development and belongs to a larger Cenozoic volcanic field extending from the eastern Galilee through western and southern Syria and Jordan to Saudi Arabia.

Measurements of the bulk thermal conductivity (BTC) of the dry and water-saturated xenolith samples resulted in unexpected low values. Thus the BTC was calculated based on modal mineralogy and porosity, applying mineral TCs and the TC of water as pore content. The calculated BTC values are overall considerably higher than the measured BTC values. The geometric mean model, discussed in detail in chapter 3, constitute the base of the calculation. The appliance of mineral TCs is restricted to literature values. These literature values report TC values only for a limited number of minerals and often a large range is indicated, basically related to high anisotropies of the minerals (Horai, 1971; Clauser and Huenges, 1995). Orientation of the minerals is unknown therefore mean values were applied. For the comparability of the values and to exclude affects related to porosity the matrix thermal conductivity (MTC), based on the measured and the calculated BTC was calculated. The misfit, however, remains in the same order. This poses the

question if the low measured BTC values are affected by overprinting and destabilization of primary minerals or textural changes. Studying them under the microscope and the electron microprobe should help understanding the discrepancy between measured and calculated TC.

A3.2 Xenolith analysis

The TC and the porosity of seven xenoliths from the lower crust and one sample from the upper mantle were determined (Table A3.1). Bulk chemistry was studied by Gazit (2005) and Navon et al. (2007), (Table A3.2). TC was measured at the GFZ-Potsdam, under dry and also water-saturated conditions using a TC Scanning (TCS) apparatus (Lippmann and Rauen, GbR). In preparation of the measurements the xenoliths were cut to produce one plane surface, and two scanning lines were painted on the plane surfaces, considering foliation, if present. The porosity of the rock samples was analyzed using the Archimedes method (cf. section 2.5). The samples are between 8 and 20 cm in diameter. They exhibit metamorphic fabric, partly gneissic texture (Figure A3.1) and partly granular texture.

The measured water-saturated BTC (TC mean) of the xenoliths ranges between 1.8 and 2.4 W m^{-1} K^{-1} (Table A3.1). The calculated water-saturated BTC (TCsat cal) is considerably higher, ranging between 2.5 and 3.4 W m^{-1} K^{-1} (Table A3.3). The MTC (TCm mea, TCm cal) was calculated based on both TCsat mea and TCsat cal.

The following mineral TCs were applied: plagioclase 2.3 W m^{-1} K^{-1} (Clauser and Huenges, 2003), amphibole 2.9 W m^{-1} K^{-1}, garnet 3.3 W m^{-1} K^{-1}, pyroxene 4.5 W m^{-1} K^{-1} (Horai, 1971) and water 0.6 W m^{-1} K^{-1} (Lemmon et al., 2005).

Figure A3.1: Sample Hl-14 with gneissic texture macroscopically comprising of plagioclase (bright) and pyroxene (dark).

Table A3.1: TC measurements of dry and water-saturated xenolith samples. The mean, min and max TC values of each scanning line are indicated. TC mean values average over the *sat mean* values of the different scanning lines. Direction of measurement is either p-perpendicular or f-parallel to foliation, if present. Porosity (ϕ in %) was determined with the Archimedes method.

Xenolith	*TC ($Wm^{-1}K^{-1}$)*							TC mean	ϕ
Sample	*dry mean*	*dry min*	*dry max*	*sat mean*	*sat min*	*sat max*	direction	($Wm^{-1}K^{-1}$)	*%*
Hl-05	1.48	1.21	1.66	1.85	1.64	2.09	p	1.75	6.03
	1.50	1.44	1.56	1.80	1.60	2.08	p		
	1.52	1.45	1.59	1.71	1.51	2.08	p		
	1.54	1.42	1.66	1.71	1.49	1.98	f		
	1.51	1.40	1.67	1.72	1.57	2.02	f		
	1.50	1.42	1.57	1.71	1.59	2.03	f		
	1.55	1.45	1.63	1.76	1.60	1.94	f		
	1.57	1.47	1.64	1.77	1.68	1.93	f		
	1.45	1.31	1.64	-	-	-	p		
	1.46	1.32	1.65	-	-	-	p		
Hl-06	1.85	1.70	2.08	2.13	1.75	2.48	-	2.13	4.59
	1.86	1.69	2.04	2.11	1.83	2.41	-		
	1.82	1.63	1.98	2.12	1.74	2.41	-		
	1.84	1.69	1.99	2.14	1.78	2.50	-		
	1.71	1.55	1.82	2.12	1.89	2.32	-		
	1.70	1.57	1.89	2.14	1.92	2.37	-		
Hl-07	1.75	1.53	2.10	1.99	1.66	2.38	-	1.99	7.83
	1.69	1.52	1.87	2.13	1.87	2.60	-		
	1.70	1.52	1.91	1.86	1.61	2.09	-		
	1.69	1.53	1.87	1.97	1.76	2.12	-		
	1.69	1.53	1.89	-	-	-	-		
	1.70	1.54	1.95	-	-	-	-		
	1.71	1.64	1.77	-	-	-	-		
	1.82	1.78	1.87	-	-	-	-		
Hl-10	1.89	1.68	2.08	2.04	1.87	2.21	p	2.11	3.28
	1.87	1.73	2.08	2.00	1.89	2.16	p		
	1.90	1.73	2.06	2.19	1.89	2.50	p		
	1.96	1.90	2.01	2.19	1.93	2.57	f		
	1.94	1.90	2.00	-	-	-	f		
	1.93	1.87	1.97	-	-	-	f		
Hl-11	1.71	1.57	1.86	2.07	1.78	2.37	-	2.10	3.78
	1.70	1.59	1.84	2.04	1.69	2.31	-		
	1.69	1.58	1.79	2.14	1.97	2.37	-		
	1.70	1.59	1.88	2.14	1.91	2.41	-		
Hl-14	1.58	1.40	1.81	1.89	1.61	2.36	-	1.88	4.90
	1.59	1.38	1.87	1.91	1.60	2.19	-		
	1.55	1.44	1.66	1.88	1.70	2.11	-		
	1.55	1.45	1.73	1.86	1.65	2.09	-		
Hl-18	1.84	1.72	1.95	2.09	1.87	2.31	p	2.22	4.01
	1.86	1.78	1.96	2.00	1.81	2.15	p		
	2.02	1.77	2.49	2.41	1.84	3.09	f		
	2.08	1.78	2.52	2.38	1.91	3.38	f		
	2.06	1.75	2.42	-	-	-	f		
Mantel	1.81	1.70	1.92	2.38	2.07	2.70	-	2.40	11.06
	1.83	1.70	1.92	2.44	2.18	2.77	-		
	1.85	1.69	1.96	2.37	2.18	2.58	-		
	1.85	1.68	2.04	2.39	2.27	2.65	-		

Mineralogy

The xenoliths are composed of plagioclase, clinopyroxene, orthopyroxene, partly with garnet and amphibole. Distinguishing trends is problematic: plagioclase-rich samples (≥ 50%) are Hl-11 and Hl-14, pyroxene-rich samples (≥ 50%) are Hl-07 and Hl-06 others are either rich in both or contain high amounts of amphibole or garnet (see Table A3.3).

Additionally to the mineral assemblage identified macroscopically, some samples contain spinel and apatite as accessory minerals visible under the microscope.

To better evaluate the overprinting of the samples four xenolith samples were scanned by electron microprobe without analyzing mineral chemistry. The samples were studied with the Jeol JXA 8500F field-emission electron microprobe at the GFZ-Potsdam.

The sample H1-10 shows significant amounts of garnet. Also the H1-06 sample contains garnet but less frequent. The samples H1-07 and H1-11 contain no garnet; however, small amounts of amphibole were detected.

The garnets in the xenoliths (Hl-06; Hl-10) are totally replaced by fine-grained symplectite (Figure A3.2; A3.3). The breakdown products consist of ferrosilite+anorthite+herzynite±olivine. Two pyroxenes can be distinguished in the sample Hl-06, diopside and hypersthene. The hypersthene is enriched in Fe towards the rim and occasionally shows kelyphitic rims of olivine+apatite+Cr-spinel. The plagioclase minerals also show rims but less striking. The sample Hl-10 contains only diopside as pyroxene. Both samples contain spinel.

The samples Hl-07 and Hl-11 are garnet-free. The sample Hl-11 consists mainly of plagioclase and diopside, and minor amphibole, basically hornblende. Composition of the Hl-07 is the same with more diopside. The diopside grains are rimmed by amphibole. Plagioclase grains also show rims in both samples but less developed compared to the samples Hl-06 and Hl-10. Alteration overall is less striking, only the reaction rims of pyroxene and partly plagioclase are noticeable.

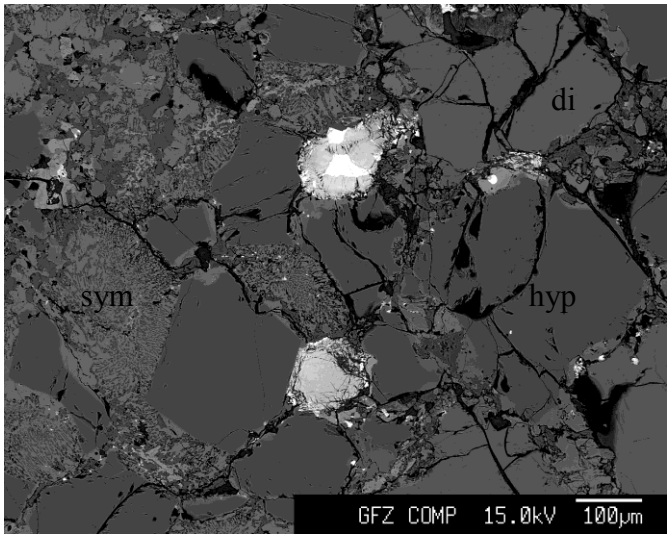

Figure A3.2: Overview of sample Hl-06 originally containing garnet+orthopyroxene+plagioclase+spinel (BSE-image). All garnets are replaced by symplectite (sym-symplectite; hyp-hypersthene; di-diopside).

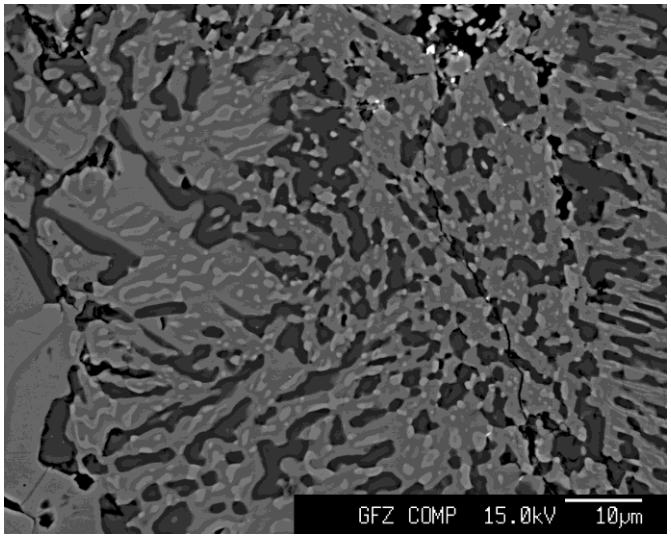

Figure A3.3: Detailed view of the garnet breakdown products ferrosilite+anorthite+herzynite (BSE-image).

Table A3.2: Major element concentration (wt. %) of xenolith samples from the lower crust and the upper mantle (Gazit, 2005).

Sample	Hl-05	Hl-06	Hl-07	Hl-10	Hl-11	Hl-14	Hl-18	Hl-19
SiO2	50.9	49.6	50.6	49.1	52.5	51.0	47.9	49.5
TiO2	0.3	0.3	0.4	0.4	0.3	0.3	0.1	0.3
Al2O3	22.5	18.0	16.9	18.1	18.2	22.3	18.2	19.9
Fe2O3	4.5	7.6	6.7	10.4	5.9	3.5	9.2	6.7
MnO	0.1	0.1	0.1	0.2	0.1	0.0	0.1	0.1
MgO	4.8	9.9	8.6	8.3	9.5	4.0	14.0	7.4
CaO	12.7	13.2	15.1	12.5	12.6	13.7	8.9	12.2
Na2O	3.1	2.1	2.4	2.6	2.4	3.3	1.4	2.5
P2O5	0.0	0.1		0.0	0.0	0.0	0.0	0.1
SO3	0.1	0.2	0.2	0.2	0.1	0.1	0.1	0.1
LOI	0.5	0.3	0.5	-0.1	0.1	0.6	0.0	0.9
total	99.4	101.3	101.4	101.6	101.7	98.9	99.9	99.7

LOI-loss on ignition, giving the concentration of all volatile components

Table A3.3: Modal mineralogy (vol. %) of xenolith samples from the lower crust and the upper mantle (Gazit, 2005). Water-saturated BTCs (in $Wm^{-1}K^{-1}$) measured (TCsat mea) and calculated (TCsat cal). Geo mean model was applied for the calculation using modal mineralogy and porosity (ϕ in %). MTCs were calculated based on both measured and calculated BTC (TCm mea; TCm cal).

sample	Pl	Grt	Opx/ Cpx	Amp	Spl	ϕ	TCsat mea	TCsat cal	TCm mea	TCm cal
Hl-05	35.0		35.0	30.0		6.03	1.75	2.85	1.80	2.94
Hl-06	40.0	10.0	50.0			4.59	2.13	3.07	2.18	3.14
Hl-07	30.0		60.0	10.0		7.83	1.99	3.30	2.06	3.42
Hl-10	20.0	35.0	45.0			3.28	2.11	3.37	2.14	3.43
Hl-11	50.0		45.0	5.0		3.78	2.10	2.98	2.14	3.04
Hl-14	60.0		30.0	8.0	2.0	4.90	1.88	2.63	1.93	2.69
Hl-18	35.0	30.0	30.0		5.0	4.01	2.22	2.84	2.26	2.90
Hl-19	40.0		45.0	5.0	10.0	11.06	2.40	2.48	2.52	2.61

Pl-plagioclase; Grt-garnet; Opx, Cpx- Ortho- and Clinopyroxene; Amp-amphibole; Spl-spinel

Micro cracks

Intragranular cracks (Figure A3.4; A3.5) occur in all samples running basically through all the plagioclase and pyroxene grains, disrupting the original crystal shape. Less frequent are grain-boundary cracks. Furthermore, intergranular cracks running from one grain to another are observed. The cracks are basically open. Healed cracks are usually filled with iron oxide. The open cracks constitute a fraction of the effective porosity of the samples, ranging from 3.3−11.0 % (Table A3.3).

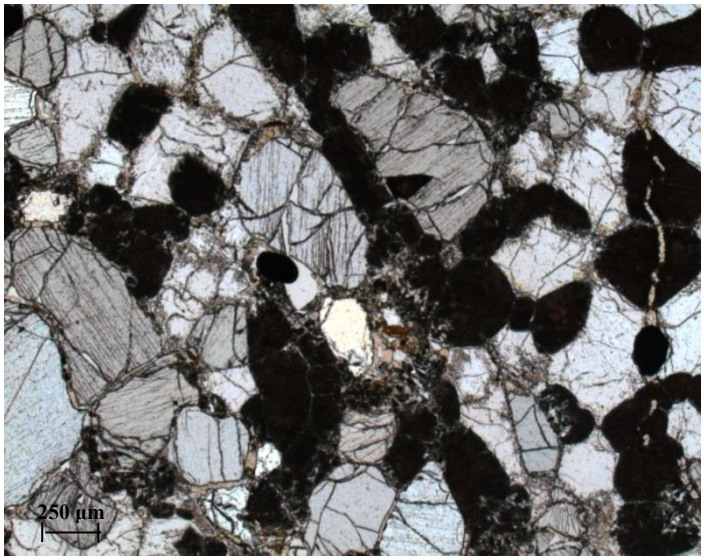

Figure A3.4: Overview of sample Hl-10 with micro cracks running through all the plagioclase and pyroxene grains. The dark, round-shaped crystals represent garnet (transmitted light).

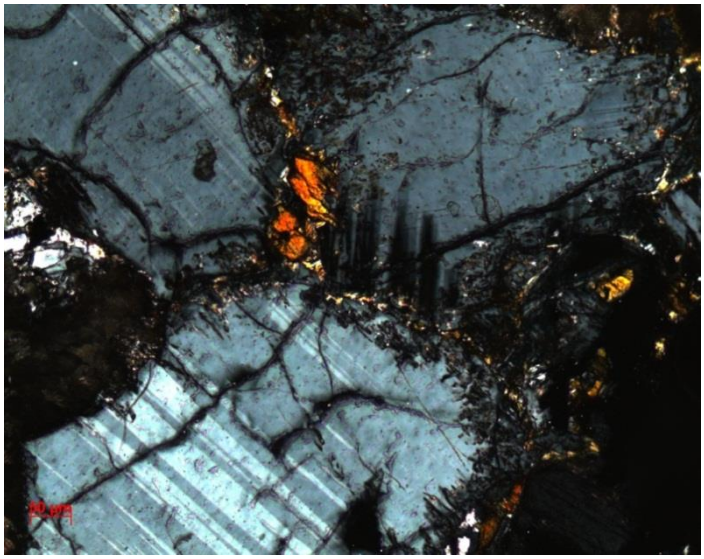

Figure A3.5: Intragranular micro cracks in plagioclase grains of the Hl-10 sample. Note that the plagioclase displays a reaction rim (transmitted light with crossed nicols).

A3.3 Discussion

Alteration of primary minerals through overprinting is evident in all samples particularly the destabilization of alteration-prone garnet minerals is striking. They are totally replaced by symplectites but also pyroxene and plagioclase minerals often show a reaction rim. The alteration of the minerals gave rise to new mineral assemblages and new texture as the garnet break-down is connected with a reduction in grain size. Consequently, new thermal rock properties developed and the measurements of TC on lower crustal and upper mantle xenoliths do not reflect in-situ TC values. The different degrees of alteration of the xenolith samples are not reflected in the misfit between measured and calculated BTC. Although garnet-free xenolith samples show a less significant alteration of primary minerals, the difference between measured and calculated TC is on the same order as for the originally garnet-bearing samples. Hence another parameter affected the TC, with micro cracks being the most plausible explanation as they are omnipresent in all samples. They constitute a strong thermal barrier, especially because the cracks are basically open and not filled with fine-grained minerals.

Therefore the measurements of TC on lower crustal and upper mantle xenoliths do not reflect in-situ TC values for two reasons: the samples are cracked and primary mineralogy is altered. In order to best determine in-situ TC the original composition of the rock and the porosity as a multi-component system has to be reconstructed as basis for BTC calculations. For this calculation mineral TC has to be applied, which is affected by high uncertainties resulting from the restricted

values available in the literature and the anisotropy of the mineral TC. Nevertheless for this study the calculation from modal mineralogy was considered as best approximation if corrected for temperature and pressure. As the micro cracks, constituting basically the porosity, are most likely the results of decompression and not present under in-situ pressure conditions, porosity is assumed to be zero. Hence for the modeling of the thermal conditions of the lithosphere the following values were applied for the lower crustal model layers (cf. section 4.6): plagioclase-rich granulite of 3.5 W m^{-1} K^{-1} and pyroxene-rich granulite of 3.1 W m^{-1} K^{-1} (cf. Table 4.3).

Nevertheless, to better understand the parameters influencing the TC and the porosity of lower crustal and upper mantle xenolith samples a more detailed study is needed which goes beyond the scope of this study.

A4 Example of well information available in the database of the Geological Survey of Israel

HEIMAR 01

Well Number:	188		Company:	NAPHTHA				
East	181546		North	1049741				
Spudding date:	21/05/196		Completion date:	20.10.1966		TD (m)	2437	
Well type and status: O-DH			KB (m)	-256	GL (m)	-259.6	RT (m)	WD (m)

Age at TD PALEOZOIC

ENGINEERING DATA

CASING/LINER			ABANDONMENT PLUG		PERFORATED ZONE	
Diameter (inch)	Depth (m)	Retrieved from (m)	No.	Interval (m)	No.	Interval (m)
18-5/8	31		1	2035-2050		
13-3/8	589		2	2035-1530		
9-5/8	1371		3	2035-1310		

CORE DATA

Type	No.	Interval (m)			Recovery (%)	Analysis
CORE	1	513	-	516.5	100	No
CORE	2	643	-	653	0	No
S.W.C	1	712	-			No
S.W.C	2	793	-			No
S.W.C	3	860	-			No
S.W.C	4	908	-			No
CORE	3	983	-	991	100	No
S.W.C	5	1200	-			No
S.W.C	6	1225	-			No
S.W.C	7	1250	-			No
S.W.C	8	1425.5	-			No
S.W.C	9	1462.5	-			No
CORE	4	1466	-	1471.5	100	Yes
S.W.C	10	1560	-			No
S.W.C	11	1654	-			No
CORE	5	1659	-	1665.5	100	Yes
S.W.C	12	1716	-			No
S.W.C	13	1851	-			No
S.W.C	14	2024.5	-			No
CORE	6	2028	-	2033.5	100	Yes
S.W.C	15	2092.5	-			No
S.W.C	16	2145	-			No
S.W.C	17	2146.5	-			No
S.W.C	18	2175	-			No
S.W.C	19	2184	-			No
S.W.C	20	2194	-			No
CORE	7	2294	-	2,295.00	100	No
CORE	8	2403	-	2,406.50	100	Yes

Lithostratigraphy

Top	Bottom	Strat.	Rock1	Rock2	Rock3	Rock4
0	10		MARL			
10	30	DSU	SANDSTONE			
30	32		CONGLOMERATE			
32	39		MARL	SANDY (10-20%)		
39	55		SANDSTONE			
55	67		CLAY	PYRITE (PYRITIC)		
67	71		SANDSTONE			
71	82		MARL	PYRITE (PYRITIC)		
82	87		CONGLOMERATE	DOLOMITIC (10-20%)		
87	93		MARL	PYRITE (PYRITIC)		
93	115	DSU1	CONGLOMERATE	MARL	CHERT	DOLOMITIC (20-40%)
115	127		SHALE	SANDY (10-20%)	CONGLOMERATE	
127	140	SC2	CONGLOMERATE	SHALE	CALCAREOUS (10-20%)	
140	170		PHOSPHATE (-ATIC)	LIMESTONE	SILICEOUS(CHERTY)	
170	173	SC3	CHERT	LIMESTONE		
173	198		CHALK	CHERT		
198	202	SC4	CHALK	SANDY (10-20%)	SILICEOUS(CHERTY)	
202	208		LIMESTONE	CHALKY		
208	210		MARL			
210	217		LIMESTONE			
217	252	JU2	DOLOMITE			
252	513	JU3	TOTAL LOSS OF CIRC			
513	516.5	JU4	LIMESTONE	ARGILLACEOUS	DOLOMITIC (10-20%)	
516.5	600	JU5	TOTAL LOSS OF CIRC			
600	621		LIMESTONE	ARGILLACEOUS		
621	626	JU6	LIMESTONE	GLAUCONITE (-ITIC)	SANDY (20-40%)	
626	640		SANDSTONE	CALCAREOUS (20-40%)	PYRITE (PYRITIC)	
640	686		SANDSTONE	LIGNITE (LIGNITIC)	ARGILLACEOUS	
686	688		LIMESTONE			
688	713	KU1	SANDSTONE	CALCAREOUS (10-20%)	PYRITE (PYRITIC)	
713	719		LIMESTONE	SANDY (20-40%)	ARGILLACEOUS	PYRITE (PYRITIC)
719	723		SANDSTONE	CALCAREOUS (10-20%)	PYRITE (PYRITIC)	
723	724		LIMESTONE			
724	733		SANDSTONE	CALCAREOUS (10-20%)	PYRITE (PYRITIC)	
733	734		LIMESTONE			
734	755		SANDSTONE	CALCAREOUS (10-20%)	PYRITE (PYRITIC)	
755	759		LIMESTONE	ARGILLACEOUS	SANDY (10-20%)	
759	769		SANDSTONE	CALCAREOUS (10-20%)	PYRITE (PYRITIC)	ARGILLACEOUS
769	772		LIMESTONE	ARGILLACEOUS		
772	788		SANDSTONE	ARGILLACEOUS	CALCAREOUS (10-20%)	
788	789	KU2	LIMESTONE	ARGILLACEOUS		
789	812		SANDSTONE	ARGILLACEOUS	PYRITE (PYRITIC)	
812	814		MARL			
814	840	KU3	SANDSTONE	PYRITE (PYRITIC)	CALCAREOUS (10-20%)	
840	841		MARL			
841	844		SHALE	CALCAREOUS (10-20%)		
844	848		MARL	PYRITE (PYRITIC)		
848	850		SANDSTONE	CALCAREOUS (10-20%)		
850	855		MARL	PYRITE (PYRITIC)		
855	863		SANDSTONE	CALCAREOUS (10-20%)		

863	865		LIMESTONE	ARGILLACEOUS	
865	873	KU4	SANDSTONE	CALCAREOUS (10-20%)	
873	875		LIMESTONE		
875	881		SANDSTONE	CALCAREOUS (10-20%)	
881	884		CLAY		
884	889		SANDSTONE		
889	892		MARL	SANDY (10-20%)	
892	894		SANDSTONE	CALCAREOUS (10-20%)	
894	901		MARL	SANDY (10-20%)	
901	917		SANDSTONE	CALCAREOUS (10-20%)	PYRITE (PYRITIC)
917	919		LIMESTONE		
919	928		SANDSTONE	CALCAREOUS (10-20%)	PYRITE (PYRITIC)
928	930		SHALE		
930	934		SANDSTONE	CALCAREOUS (10-20%)	
934	936		SHALE		
936	940		SANDSTONE	CALCAREOUS (10-20%)	PYRITE (PYRITIC)
940	943		MARL		
943	949		SANDSTONE	CALCAREOUS (10-20%)	PYRITE (PYRITIC)
949	953		LIMESTONE	ARGILLACEOUS	
953	969		SANDSTONE	CALCAREOUS (10-20%)	
969	974		LIMESTONE	ARGILLACEOUS	
974	980		DOLOMITE		
980	983		LIMESTONE		
983	987		LIMESTONE	SANDY (20-40%)	ARGILLACEOUS
987	990		SANDSTONE	CALCAREOUS (10-20%)	
990	1001		SHALE	MARL	CALCAREOUS (10-20%)
1001	1015		LIMESTONE	SANDY (10-20%)	ARGILLACEOUS
1015	1017		MARL		
1017	1025		LIMESTONE	SANDY (10-20%)	
1025	1028		SANDSTONE	CALCAREOUS (10-20%)	
1028	1035		LIMESTONE	ARGILLACEOUS	SANDY (10-20%)
1035	1038		SANDSTONE	CALCAREOUS (10-20%)	
1038	1040		LIMESTONE	SANDY (10-20%)	ARGILLACEOUS
1040	1042		SANDSTONE	CALCAREOUS (10-20%)	
1042	1046	AR5	LIMESTONE	ARGILLACEOUS	SANDY (10-20%)
1046	1048		SANDSTONE	CALCAREOUS (10-20%)	
1048	1053		LIMESTONE	SANDY (10-20%)	ARGILLACEOUS
1053	1056		SANDSTONE	CALCAREOUS (10-20%)	
1056	1068		LIMESTONE	ARGILLACEOUS	SANDY (10-20%)
1068	1071		SANDSTONE	CALCAREOUS (10-20%)	
1071	1089		LIMESTONE		
1089	1101		SANDSTONE	LIGNITE (LIGNITIC)	
1101	1112		SILTSTONE	ARGILLACEOUS	CALCAREOUS (10-20%)
1112	1125		SANDSTONE	ARGILLACEOUS	CALCAREOUS (10-20%)
1125	1144		SANDSTONE		
1144	1151		LIMESTONE	ARGILLACEOUS	
1151	1153		MARL		
1153	1158		LIMESTONE	SANDY (10-20%)	ARGILLACEOUS
1158	1166		SILTSTONE	ARGILLACEOUS	
1166	1175		LIMESTONE	ARGILLACEOUS	LIGNITE (LIGNITIC)
1175	1177		SHALE		
1177	1188		DOLOMITE	PYRITE (PYRITIC)	
1188	1190		SANDSTONE		
1190	1200		LIMESTONE	DOLOMITIC (10-20%)	

1200	1212		LIMESTONE			
1212	1216		SHALE			
1216	1219		MARL			
1219	1223		LIMESTONE			
1223	1231		DOLOMITE			
1231	1234		SANDSTONE			
1234	1238		LIMESTONE	SANDY (10-20%)		
1238	1241		LIMESTONE	ARGILLACEOUS		
1241	1242		SANDSTONE			
1242	1244		SHALE	SANDY (10-20%)		
1244	1251		SANDSTONE			
1251	1257		DOLOMITE	SANDY (20-40%)		
1257	1265		SANDSTONE	CALCAREOUS (10-20%)	PYRITE (PYRITIC)	
1265	1267		EXTRUSIVE			
1267	1269		SANDSTONE			
1269	1271		DOLOMITE	SANDY (10-20%)		
1271	1277		LIMESTONE			
1277	1279		SHALE			
1279	1283		SANDSTONE			
1283	1285		DOLOMITE			
1285	1292	AR6	SANDSTONE	CALCAREOUS (10-20%)	PYRITE (PYRITIC)	
1292	1304	AR8	DOLOMITE			
1304	1310	AR10	SHALE	SANDY (10-20%)		
1310	1372	RA1	DOLOMITE	CHALKY		
1372	1386		DOLOMITE	GYPSUM		
1386	1389		SHALE			
1389	1398		LIMESTONE	GYPSUM	SANDY (10-20%)	
1398	1400		SANDSTONE			
1400	1416		LIMESTONE	ARGILLACEOUS		
1416	1417		SHALE			
1417	1423		LIMESTONE	SANDY (10-20%)	ARGILLACEOUS	
1423	1428		LIMESTONE	ARGILLACEOUS		
1428	1430		SHALE	CALCAREOUS (10-20%)	GYPSUM	
1430	1438		LIMESTONE	ARGILLACEOUS	GYPSUM	
1438	1440		SHALE	CALCAREOUS (10-20%)		
1440	1442		LIMESTONE	ARGILLACEOUS		
1442	1443		SHALE	CALCAREOUS (10-20%)	GYPSUM	
1443	1448		LIMESTONE	DOLOMITIC (10-20%)		
1448	1450		SHALE	CALCAREOUS (10-20%)	GYPSUM	
1450	1458		LIMESTONE	GYPSUM	ARGILLACEOUS	
1458	1466		LIMESTONE	SANDY (40-50%)	GYPSUM	
1466	1468		SANDSTONE			
1468	1472		LIMESTONE	ARGILLACEOUS		
1472	1476		SHALE			
1476	1524		DOLOMITE	GYPSUM	ARGILLACEOUS	FOSSILIFEROUS
1524	1528		SANDSTONE	CALCAREOUS (10-20%)		
1528	1533		SILTSTONE	ARGILLACEOUS		
1533	1537		LIMESTONE	DOLOMITIC (20-40%)	SANDY (20-40%)	
1537	1546	RA2	SHALE	SANDY (20-40%)		
1546	1553		SHALE			
1553	1555		SANDSTONE			
1555	1557		SHALE			
1557	1559		LIMESTONE			
1559	1567		SANDSTONE	COAL	ARGILLACEOUS	PYRITE (PYRITIC)

1567	1574		LIMESTONE	ARGILLACEOUS		
1574	1576		SANDSTONE			
1576	1582		LIMESTONE	GYPSUM		
1582	1588		SHALE			
1588	1592		LIMESTONE	GYPSUM	ARGILLACEOUS	
1592	1594		SHALE			
1594	1602		LIMESTONE	GYPSUM	ARGILLACEOUS	
1602	1604		SHALE			
1604	1607		DOLOMITE	GYPSUM		
1607	1611		SHALE			
1611	1613		LIMESTONE	GYPSUM		
1613	1615		MARL			
1615	1617		LIMESTONE			
1617	1622		SHALE			
1622	1624		MARL			
1624	1630		DOLOMITE	GYPSUM		
1630	1651		SHALE	MARL	GYPSUM	
1651	1655		LIMESTONE	SANDY (40-50%)		
1655	1678		SANDSTONE	CALCAREOUS (20-40%)	ARGILLACEOUS	
1678	1682		SHALE			
1682	1685		SANDSTONE			
1685	1687		LIMESTONE			
1687	1689		SHALE			
1689	1691		LIMESTONE			
1691	1695		LIMESTONE	SANDY (20-40%)		
1695	1709		SHALE	SANDY (20-40%)		
1709	1719		LIMESTONE	DOLOMITIC (40-50%)		
1719	1722		IGNEOUS			
1722	1729	RA3	SHALE	SANDY (20-40%)		
1729	1760		DOLOMITE			
1760	1780		LIMESTONE	DOLOMITIC (10-20%)		
1780	1786		LIMESTONE	DOLOMITE		
1786	1792		LIMESTONE	SANDY (10-20%)		
1792	1798		LIMESTONE			
1798	1813	RA4	LIMESTONE	SANDY (20-40%)	CHALKY	
1813	1832		SHALE	LIMESTONE	SANDY (10-20%)	CHALKY
1832	1844		LIMESTONE	SANDY (20-40%)	CHALKY	
1844	1848		SHALE	CALCAREOUS (10-20%)		
1848	1850		LIMESTONE	SANDY (20-40%)		
1850	1856		SANDSTONE	GLAUCONITE (-ITIC)		
1856	1878		LIMESTONE	SANDY (10-20%)		
1878	1884		SANDSTONE	CALCAREOUS (20-40%)		
1884	1898		LIMESTONE	DOLOMITIC (10-20%)		
1898	1903		DOLOMITE			
1903	1910		SHALE	CALCAREOUS (10-20%)		
1910	1914		LIMESTONE			
1914	1944		SHALE	GYPSUM	CALCAREOUS (10-20%)	GLAUCONITE (-ITIC)
1944	1948		LIMESTONE			
1948	1960		DOLOMITE			
1960	1969		SHALE	GYPSUM		
1969	1977		INTRUSIVE			
1977	2007		SHALE	SANDY (40-50%)		
2007	2035		INTRUSIVE			
2035	2042		LIMESTONE			

2042	2045		SHALE	SANDY (20-40%)	
2045	2049		LIMESTONE		
2049	2060		LIMESTONE	SANDY (10-20%)	
2060	2077		LIMESTONE	DOLOMITIC (20-40%)	GLAUCONITE (-ITIC)
2077	2083		SANDSTONE	CALCAREOUS (10-20%)	
2083	2088		LIMESTONE	ARGILLACEOUS	SANDY (10-20%)
2088	2092		SANDSTONE	CALCAREOUS (10-20%)	
2092	2096		LIMESTONE	ARGILLACEOUS	SANDY (10-20%)
2096	2105		SANDSTONE	CALCAREOUS (10-20%)	
2105	2108		LIMESTONE		
2108	2116		SHALE	CALCAREOUS (10-20%)	
2116	2123		LIMESTONE	SANDY (20-40%)	
2123	2125		SHALE		
2125	2129		IGNEOUS		
2129	2150		SANDSTONE	CALCAREOUS (10-20%)	
2150	2171		SHALE	SANDY (10-20%)	
2171	2202	NE1	SANDSTONE	CALCAREOUS (10-20%)	
2202	2209		SHALE	GYPSUM	
2209	2228		DOLOMITE	GYPSUM	ARGILLACEOUS
2228	2232		SHALE	CALCAREOUS (10-20%)	
2232	2234		SANDSTONE		
2234	2237		SHALE	CALCAREOUS (10-20%)	
2237	2303		INTRUSIVE		
2303	2312		CLAY	IGNEOUS	
2312	2383	NE2	SANDSTONE	CALCAREOUS (10-20%)	GLAUCONITE (-ITIC)
2383	2396		INTRUSIVE		
2396	2423		SANDSTONE	GYPSUM	ARGILLACEOUS
2423	2437	NE3	INTRUSIVE		

Stratigraphy: DSU-Upper Dead Sea Gr., Lisan Fm.; DSU-Upper Dead Sea Gr., Samra Fm.; SC2-Mt.Scopus Gr., Ghareb Fm.; SC3- Mt.Scopus Gr., Mishash Fm.; SC4- Mt.Scopus Gr., Menuha Fm.; JU2-Judea Gr., Tamar Fm.; JU3-Judea Gr., Avnon Fm.; JU4-Judea Gr., Zafit Fm.; JU5-Judea Gr., En Yorqeam Fm.; JU6-Judea Gr., Hevyon Fm.; KU1-Kurnub Gr., Uza Fm.; KU2-Kurnub Gr., Malhata Fm.; KU3-Kurnub Gr., Dragot Fm.; KU4-Kurnub Gr., Zeweira Fm.; AR5-Arad Gr., Sherif Fm.; AR6-Arad Gr., Daya Fm.; AR8-Arad Gr., Ardon Fm.; AR10-Arad Gr., Mishhor Fm.; RA1-Ramon Gr., Mohilla Fm.; RA2-Ramon Gr., Sahronim Fm.; RA3-Ramon Gr., Gevanim Fm.; RA4-Ramon Gr., Raaf Fm.; NE1-Negev Gr., Zafir Fm.; NE2-Negev Gr., Yamin Fm.; NE3-Negev Gr., Arqov Fm.

A5 Printed well report

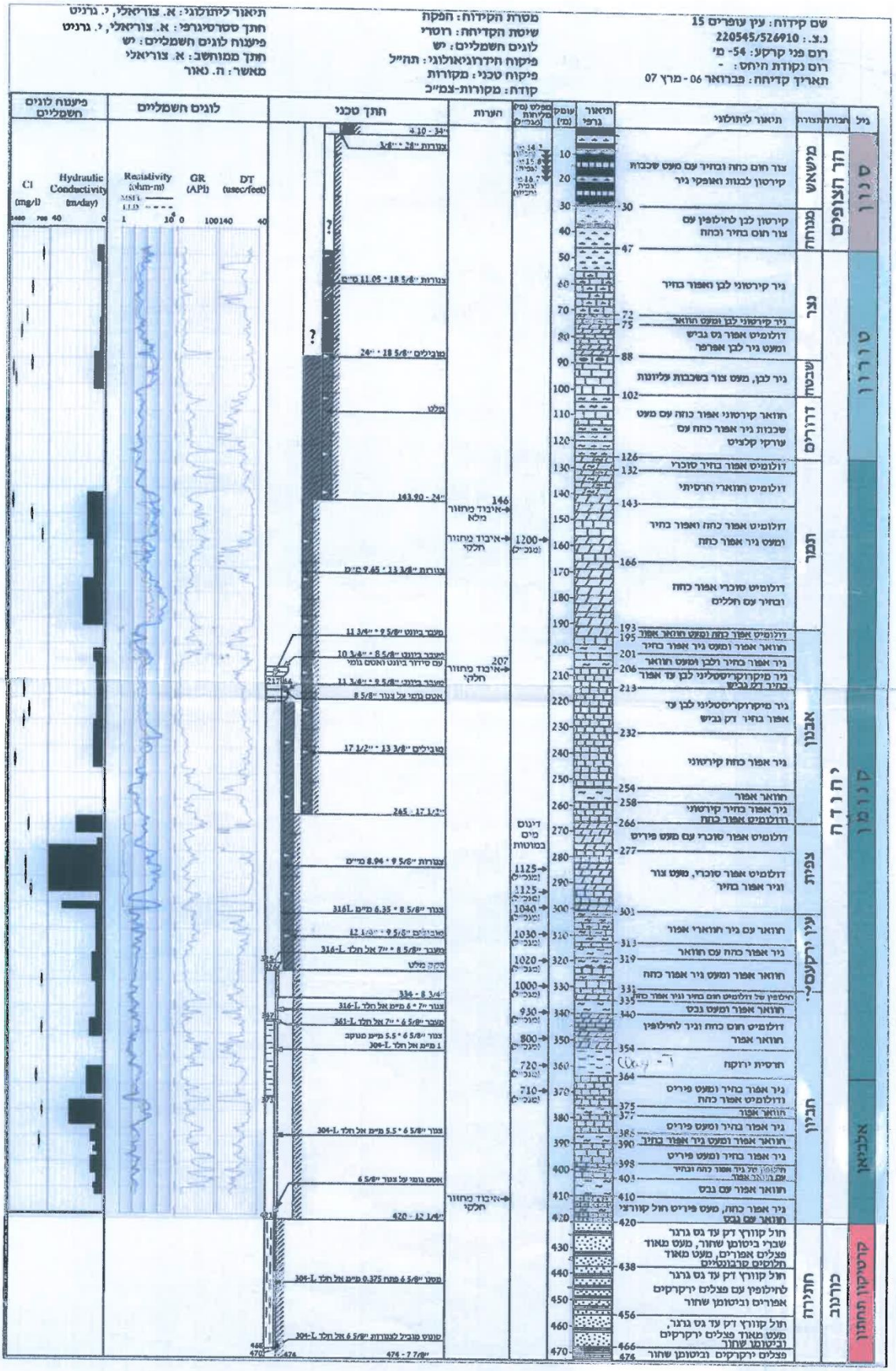

A6 Thermal conductivity data

Table A6.1: TC measurements of dry and water-saturated drill core samples. Measurements were performed on the core top/bottom (⊥) and the core mantle (‖) surface. The *min, max* and *mean TC* value of each scanning line is indicated. TC mean value averages over the *sat mean* values of the different scanning lines. TC mean values shaded in grey were calculated based on the *dry mean* value and the porosity appling the geometric mean model. Porosity (ϕ) was determined with the Archimedes method, when no water-saturation was possible samples were saturated with isooctane instead (cf. section 2.4).

Drillcore	Well -			Stratigraphy			*TC ($Wm^{-1}K^{-1}$)*							TC mean	ϕ
Sample	Nr.	Depth	Age	Gr.	Fm.	Litho.	*dry mean*	*dry min*	*dry max*	*sat mean*	*sat min*	*sat max*	Surface	($Wm^{-1}K^{-1}$)	%
Avdat-1_01	1	1365.6	Aptian	Arad	Zohar	Ss	2.37	2.24	2.48	4.63	4.24	5.35	‖	4.77	22.75
							2.36	2.24	2.47	4.84	4.19	5.52	‖		
							2.40	2.22	2.54	4.84	4.35	5.66	⊥		
							2.44	2.31	2.57	4.78	4.23	5.37	⊥		
							2.49	2.33	2.69	-	-	-	‖		
							2.49	2.34	2.69	-	-	-	‖		
							2.94	2.71	3.31	-	-	-	⊥		
							2.93	2.66	3.19	-	-	-	⊥		
Avdat-1_02	1	1425.9	Callovian	Arad	Zohar	Ls	2.10	2.00	2.17	2.32	2.18	2.50	‖	2.34	3.55
							2.10	2.01	2.17	2.36	2.22	2.51	‖		
							2.11	2.03	2.18	2.30	2.16	2.48	⊥		
							2.11	2.02	2.17	2.35	2.24	2.48	⊥		
Avdat-1_03	1	1438.2	Callovian	Arad	Zohar	Cl	1.84	1.72	1.96	-	-	-	‖	2.14	6.29
							1.82	1.70	1.96	-	-	-	‖		
							1.68	1.61	1.76	-	-	-	⊥		
							1.68	1.61	1.75	-	-	-	⊥		
Avdat-1_04	1	1702.2	Bath./Baj.	Arad	Daya	Ss	3.04	2.25	3.77	3.59	2.91	4.42	‖	3.67	5.47
							3.03	2.21	3.68	3.73	3.15	4.41	‖		
							-	-	-	3.79	3.16	4.40	‖		
							2.80	2.39	3.28	3.57	3.16	4.29	⊥		
							2.78	2.41	3.32	3.65	3.18	4.04	⊥		
Avdat-1_05	1	2583.5	Scythian	Ramon	Zafir	Cl	1.81	1.69	1.93	-	-	-	⊥	2.10	10.00
							1.78	1.66	1.90	-	-	-	⊥		
Avdat-1_07	1	2989.9	Late-Early P.	Negev	Arqov	Si	2.61	2.41	2.82	3.53	2.91	4.22	‖	3.36	10.00

Table A6.1: continued

							2.63	2.43	2.83	3.54	2.93	4.13	‖		
							2.42	2.25	2.60	3.20	2.95	3.20	⊥		
							2.43	2.26	2.59	3.18	2.96	3.19	⊥		
Avdat-1_09	1	3145.2	Early Permian	Negev	Saad	Ss	4.30	4.02	5.14	6.51	6.04	6.92	‖	6.44	5.37
							4.26	4.03	4.73	6.59	6.19	6.85	‖		
							4.03	3.53	4.39	6.29	5.69	6.79	⊥		
							4.07	3.66	4.46	6.38	5.71	6.99	⊥		
							4.59	4.15	5.11	-	-	-	‖		
							4.43	3.99	4.86	-	-	-	‖		
							3.95	3.47	4.53	-	-	-	⊥		
							3.95	3.51	4.63	-	-	-	⊥		
BShev-1_01	2	1199.8	Albian	Kurnub	Zeweira	Cl	1.94	1.80	2.05	-	-	-	‖	2.06	9.00
							1.96	1.86	2.17	-	-	-	‖		
							1.31	1.00	1.54	-	-	-	⊥		
							1.29	0.99	1.49	-	-	-	⊥		
							1.26	0.94	1.58	-	-	-	⊥		
BShev-1_02	2	1459.2	Kimmeridge	Arad	Haluza	Si	2.44	2.28	2.74	2.85	2.54	3.32	‖	2.77	5.08
							2.52	2.24	2.86	2.88	2.69	3.29	‖		
							2.22	2.06	2.36	2.65	2.49	2.88	⊥		
							2.22	2.08	2.35	2.72	2.47	2.95	⊥		
BShev-1_03	2	2451.8	Bajocian	Arad	Daya	Ss	3.38	3.14	3.65	3.90	3.44	4.45	‖	3.89	2.38
							3.36	3.12	3.60	3.88	3.44	4.40	‖		
							3.19	3.02	3.37	3.93	3.36	4.38	⊥		
							3.13	2.94	3.31	3.84	3.56	4.26	⊥		
BShev-1_04	2	2634.0	Aalenian	Arad	Inmar U.	Ss	3.87	3.68	4.10	5.67	4.93	6.41	‖	5.56	12.09
							3.84	3.64	3.98	5.83	5.01	7.41	‖		
							3.65	3.46	3.88	5.10	4.38	5.97	⊥		
							3.67	3.47	3.81	5.62	4.89	6.35	⊥		
							3.73	3.42	4.12	-	-	-	‖		
							3.61	3.34	3.92	-	-	-	‖		
							3.48	3.23	3.69	-	-	-	⊥		

Table A5.1: continued

							3.52	3.14	3.89	-	-	-	⊥		
BShev-1_05	2	2704.4	Aalenian	Arad	Inmar U.	Ss	3.83	3.30	4.36	3.84	3.02	4.55	‖	4.32	3.78
							3.87	3.37	4.27	3.93	3.05	4.46	‖		
							4.18	3.61	4.81	4.77	4.07	5.64	⊥		
							4.26	3.73	4.82	4.75	3.80	6.01	⊥		
Daya-1_01	3	829.7	L.Oxfordian	Arad	Beersh.	Ls	2.24	2.10	2.37	2.73	2.56	2.89	‖	2.73	5.93
							2.25	2.13	2.36	2.78	2.59	2.97	‖		
							2.33	2.20	2.48	2.69	2.53	2.84	⊥		
							2.31	2.11	2.54	2.74	2.58	2.90	⊥		
Daya-1_02	3	839.5	L.Oxfordian	Arad	Beersh.	Ls	2.19	2.09	2.29	2.62	2.56	2.68	‖	2.61	0.17
							2.15	2.09	2.22	2.62	2.54	2.70	‖		
							2.19	2.09	2.29	2.61	2.53	2.68	⊥		
							2.15	2.02	2.29	2.58	2.47	2.69	⊥		
Daya-1_03	3	1018.1	Callovian	Arad	Zohar	Ign	2.02	1.83	2.15	2.01	1.60	2.38	‖	1.95	0.00
							2.02	1.90	2.13	2.03	1.80	2.22	‖		
							1.90	1.72	2.02	1.89	1.74	1.98	⊥		
							1.93	1.83	2.08	1.89	1.76	2.05	⊥		
Daya-1_04	3	1088.6	Callovian	Arad	Zohar	Ls	2.12	2.02	2.27	2.34	2.19	2.48	‖	2.42	2.96
							2.13	2.03	2.27	2.39	2.21	2.52	‖		
							2.31	2.14	2.44	2.47	2.34	2.63	⊥		
							2.25	2.13	2.41	2.49	2.21	2.69	⊥		
Daya-1_05	3	1121.6	Callovian	Arad	Zohar	Ls	1.99	1.91	2.08	2.29	2.19	2.39	‖	2.37	8.11
							2.00	1.87	2.12	2.38	2.26	2.55	‖		
							2.05	1.97	2.16	2.37	2.23	2.53	⊥		
							2.04	1.91	2.14	2.42	2.24	2.58	⊥		
Daya-1_06	3	1121.6	Callovian	Arad	Zohar	Cl	1.77	1.61	1.93	-	-	-	⊥	2.20	7.00
							1.75	1.59	1.90	-	-	-	⊥		
Daya-1_07	3	1124.8	Callovian	Arad	Zohar	Cl	1.62	1.53	1.71	-	-	-	⊥	1.90	6.00
							1.63	1.54	1.72	-	-	-	⊥		
Daya-1_08	3	1261.5	Bathonian	Arad	Sherif	Si	1.84	1.75	1.94	-	-	-	‖	2.44	10.00
							1.83	1.76	1.91	-	-	-	‖		

Table A5.1: continued

Daya-1_09	3	1267.4	Bathonian	Arad	Sherif	Si	2.16	1.92	2.67	-	-	-	‖	2.65	12.50
							2.07	1.19	2.58	-	-	-	‖		
							1.74	1.40	2.05	-	-	-	⊥		
							1.77	1.41	2.04	-	-	-	⊥		
Daya-1_10	3	1305.2	Bathonian	Arad	Sherif	Dol Ls	2.33	2.10	2.62	3.10	2.71	3.46	‖	3.15	10.37
							2.34	2.09	2.61	3.20	2.84	3.66	‖		
							2.34	2.15	2.66	3.09	2.76	3.44	⊥		
							2.38	2.07	2.82	3.22	2.75	3.63	⊥		
Daya-1_11	3	1304.3	Bathonian	Arad	Sherif	Dol	2.89	2.66	3.03	3.98	3.41	4.86	‖	4.04	4.62
							2.92	2.75	3.11	4.07	3.50	4.93	‖		
							-	-	-	3.88	3.22	4.30	⊥		
							-	-	-	4.21	3.68	4.84	⊥		
							2.99	2.75	3.37	-	-	-	‖		
							3.03	2.72	3.41	-	-	-	‖		
							3.28	2.95	3.62	-	-	-	⊥		
							3.34	2.67	3.84	-	-	-	⊥		
Daya-1_12	3	1312.3	Bathonian	Arad	Sherif	Ls	2.15	1.92	2.39	2.40	2.20	2.67	‖	2.32	3.98
							2.13	1.93	2.39	2.41	2.22	2.60	‖		
							1.94	1.73	2.14	2.20	1.89	2.62	⊥		
							1.94	1.75	2.13	2.27	2.02	2.81	⊥		
Daya-1_13	3	1443.3	Bathonian	Arad	Sherif	Si	2.06	1.87	2.23	-	-	-	‖	2.51	7.00
							2.08	1.96	2.32	-	-	-	‖		
Daya-1_14	3	1457.9	Bathonian	Arad	Sherif	Dol	2.64	2.46	2.88	3.64	2.97	4.81	‖	3.74	9.82
							2.71	2.47	2.95	3.93	3.17	5.23	‖		
							2.81	2.61	3.07	3.60	3.23	4.15	⊥		
							2.83	2.61	3.13	3.80	3.36	4.29	⊥		
Daya-1_15	3	1490.8	Bathonian	Arad	Sherif	Si	2.21	2.03	2.44	-	-	-	‖	2.60	11.00
							2.23	2.05	2.50	-	-	-	‖		
							1.68	1.60	1.82	-	-	-	⊥		
							1.70	1.58	1.86	-	-	-	⊥		
Daya-1_16	3	1579.5	Bajocian	Arad	Daya	Si	2.00	1.91	2.16	2.42	2.17	2.70	‖	2.42	7.00

Table A6.1: continued

							2.00	1.91	2.16	2.43	2.25	2.64	‖		
Daya-1_17	3	1584.8	Bajocian	Arad	Daya	Ls	2.61	2.51	2.70	2.62	2.40	2.84	‖	2.60	0.42
							2.61	2.53	2.72	2.69	2.50	2.86	‖		
							2.44	2.26	2.59	2.50	2.24	2.72	⊥		
							2.45	2.25	2.62	2.60	2.38	2.85	⊥		
Daya-1_18	3	1589.5	Bajocian	Arad	Daya	Ls	2.56	2.43	2.73	2.65	2.45	2.89	‖	2.70	1.14
							2.60	2.45	2.74	2.69	2.52	2.93	‖		
							2.60	2.40	2.76	2.75	2.48	2.99	⊥		
							2.58	2.40	2.83	2.70	2.57	2.96	⊥		
Daya-1_19	3	1623.3	Bajocian	Arad	Daya	Coal	0.35	0.33	0.36	0.62	0.61	0.61	⊥	0.60	
Daya-1_20	3	1639.8	Bajocian	Arad	Inmar U.	Ss	5.11	4.32	5.73	6.61	6.27	7.05	‖	6.60	3.68
							5.09	4.12	5.76	6.61	6.09	7.11	‖		
							5.16	4.64	5.67	6.59	6.24	6.99	⊥		
							5.22	4.49	5.75	6.61	6.18	6.97	⊥		
Daya-1_21	3	1631.1	Bajocian	Arad	Daya	Cl	1.57	1.12	1.88	-	-	-	⊥	1.92	6.00
							1.61	1.16	1.88	-	-	-	⊥		
Daya-1_23	3	1736.5	Bajocian	Arad	Inmar U.	Ss	2.34	2.09	2.68	4.63	4.10	5.20	‖	4.96	17.47
							2.32	2.18	2.59	4.86	4.06	5.77	‖		
							2.48	2.37	2.65	4.82	4.31	5.41	⊥		
							2.49	2.35	2.65	5.52	5.27	6.15	⊥		
							2.45	2.22	2.63	-	-	-	‖		
							2.50	2.26	2.81	-	-	-	‖		
							2.53	2.43	2.68	-	-	-	⊥		
							2.56	2.25	2.77	-	-	-	⊥		
Daya-1_24	3	1840.1	Aalenian	Arad	Inmar L.	Ss	2.94	2.69	3.19	3.13	2.91	3.41	‖	3.14	1.53
							3.01	2.78	3.30	3.18	2.91	3.52	‖		
							2.88	2.75	3.02	3.09	2.86	3.41	⊥		
							2.88	2.73	3.06	3.14	2.95	3.43	⊥		
Daya-1_25	3	1847.7	Aalenian	Arad	Inmar L.	Ss	4.49	3.46	5.26	5.03	3.82	7.17	‖	5.05	3.75
							4.14	3.34	5.21	5.54	4.01	9.71	‖		
							4.45	3.64	5.04	4.82	3.95	6.12	⊥		

Table A6.1: continued

							4.38	3.58	5.30	4.82	3.94	6.04	⊥		
Daya-1_26	3	1852.1	Aalenian	Arad	Inmar L.	Cl,Ss	2.75	2.65	2.85	2.92	2.67	3.18	‖	3.26	1.57
							2.79	2.67	2.90	2.96	2.75	3.36	‖		
							2.50	2.42	2.61	2.77	2.60	2.95	⊥		
							2.45	2.38	2.52	2.84	2.64	3.13	⊥		
Daya-1_27	3	1876.3	Aalenian	Arad	Inmar L.	Ss	3.46	3.29	3.67	4.83	3.97	5.56	‖	4.92	17.45
							3.44	3.20	3.67	5.14	4.44	6.06	‖		
							3.17	3.02	3.30	4.74	3.98	5.54	⊥		
							3.17	3.05	3.42	4.98	4.34	5.79	⊥		
							3.34	2.87	3.89	-	-	-	‖		
							3.34	2.67	3.92	-	-	-	‖		
							3.16	2.91	3.49	-	-	-	⊥		
							3.18	2.98	3.48	-	-	-	⊥		
Daya-1_28	3	1905.6	Aalenian	Arad	Inmar L.	Ss	3.10	2.78	3.55	4.60	3.98	5.34	‖	4.55	14.49
							3.16	2.83	3.49	4.74	4.33	5.28	‖		
							3.05	2.82	3.38	4.38	3.67	5.11	⊥		
							3.06	2.82	3.50	4.46	3.75	5.30	⊥		
Daya-1_29	3	1917.9	Sinemurian	Arad	Ardon	Ls	2.66	2.53	2.89	2.64	2.37	2.80	‖	2.64	0.20
							2.66	2.53	2.73	2.71	2.39	2.95	‖		
							2.68	2.52	2.91	2.59	2.28	2.84	⊥		
							2.72	2.58	2.94	2.63	2.31	2.90	⊥		
Daya-1_30	3	1927.6	Sinemurian	Arad	Ardon	Cl	1.72	1.64	1.80	-	-	-	‖	1.90	3.00
							1.74	1.59	1.90	-	-	-	‖		
Dshet-1_01	4	907.6	Cenomian	Kurnub	Helez	Cl	1.59	1.51	1.65	-	-	-	‖	1.93	6.00
							1.60	1.52	1.65	-	-	-	‖		
							1.60	1.54	1.66	-	-	-	⊥		
							1.61	1.54	1.69	-	-	-	⊥		
Dshet-1_02	4	1413.9	Callovian	Arad	Zohar	Ls	2.36	2.22	2.51	2.48	2.28	2.64	‖	2.49	2.20
							2.35	2.21	2.50	2.45	2.30	2.64	‖		
							2.40	2.34	2.49	2.52	2.36	2.76	⊥		
							2.41	2.33	2.52	2.50	2.31	2.74	⊥		

Table A6.1: continued

Dshet-1_03	4	1470.3	Callovian	Arad	Zohar	Ls	2.39	2.20	2.66	2.57	2.41	2.75	‖	2.63	3.24
							2.41	2.25	2.57	2.67	2.50	2.83	‖		
							2.47	2.29	2.73	2.60	2.44	2.85	⊥		
							2.46	2.21	2.59	2.70	2.47	2.88	⊥		
Dshet-1_04	4	1475.7	Callovian	Arad	Zohar	Ls	2.34	2.26	2.43	2.42	2.05	2.79	‖	2.28	4.13
							2.37	2.30	2.43	2.40	2.16	2.66	‖		
							2.27	2.07	2.50	2.14	1.34	2.76	⊥		
							2.28	2.06	2.48	2.15	1.43	2.61	⊥		
Dshet-1_05	4	1622.6	Bathonian	Arad	Sherif	Ls	2.46	2.33	2.60	2.57	2.42	2.83	‖	2.60	0.00
							2.48	2.31	2.65	2.62	2.43	2.82	‖		
							2.38	2.10	2.86	-	-	-	⊥		
							2.37	2.16	2.63	-	-	-	⊥		
Dshet-1_06	4	1969.3	Bathonian	Arad	Daya	Ls	2.81	2.48	3.26	3.13	2.75	3.61	⊥	3.16	1.15
							2.74	2.42	3.12	3.26	2.78	3.63	⊥		
							-	-	-	3.10	2.69	3.60	⊥		
Dshet-1_07	4	1988.2	Bajocian	Arad	Daya	Ls	2.17	2.04	2.31	2.34	2.13	2.60	‖	2.27	1.13
							2.21	2.08	2.33	2.36	2.21	2.56	‖		
							2.07	1.94	2.19	2.21	2.09	2.34	⊥		
							2.11	2.03	2.22	2.15	1.97	2.26	⊥		
Dshet-1_08	4	2046.2	Bajocian	Arad	Daya	Si	2.52	1.63	3.41	-	-	-	⊥	3.10	10.00
							2.41	1.61	3.21	-	-	-	⊥		
Gurim-3_01	5	1108.7	Callovian	Arad	Zohar	Ls	1.71	1.65	1.78	-	-	-	‖	2.20	9.00
							1.71	1.66	1.79	-	-	-	‖		
							1.61	1.59	1.64	-	-	-	⊥		
							1.60	1.57	1.64	-	-	-	⊥		
Gurim-3_02	5	1119.6	Callovian	Arad	Zohar	Cl	1.79	1.72	1.85	-	-	-	‖	2.12	6.00
							1.79	1.73	1.85	-	-	-	‖		
							1.74	1.69	1.78	-	-	-	⊥		
							1.72	1.66	1.75	-	-	-	⊥		
Gurim-3_03	5	1130.7	Callovian	Arad	Zohar	Ls	2.40	2.34	2.55	2.61	2.47	2.74	‖	2.59	2.55
							2.37	2.29	2.44	2.64	2.48	2.80	‖		

Table A6.1: continued

							2.35	2.23	2.45	2.56	2.41	2.74	⊥		
							2.35	2.21	2.43	2.56	2.40	2.78	⊥		
Gurim-3_04	5	1318.9	Bathonian	Arad	Sherif	Ls	2.69	2.48	2.89	-	-	-	‖	2.93	4.50
							2.69	2.49	2.92	-	-	-	‖		
							2.49	2.05	2.96	-	-	-	⊥		
							2.46	2.00	2.97	-	-	-	⊥		
Gurim-3_05	5	1368.9	Bathonian	Arad	Sherif	SS	3.94	3.10	4.54	4.13	1.90	6.45	‖	4.56	7.59
							3.97	3.26	4.63	4.18	1.92	6.21	‖		
							3.84	3.46	4.18	4.99	4.31	5.71	⊥		
							3.88	3.56	4.19	4.96	4.24	5.80	⊥		
Gurim-3_06	5	1365.2	Bathonian	Arad	Sherif	SS	3.47	3.16	3.69	4.37	3.79	4.99	‖	4.44	6.86
							3.46	3.24	3.72	4.68	3.97	5.28	‖		
							-	-	-	4.59	4.17	5.16	‖		
							3.31	3.10	3.47	4.27	3.71	4.72	⊥		
							3.35	3.22	3.48	4.28	3.89	4.93	⊥		
Gurim-3_07	5	1564.3	Bath./Baj.	Arad	Daya	SS	4.79	4.46	5.10	6.17	5.15	7.29	‖	6.17	2.63
							4.81	4.41	5.10	6.32	5.14	7.63	‖		
							4.67	3.96	5.05	5.88	5.01	6.79	⊥		
							4.75	4.06	5.04	6.30	5.42	8.00	⊥		
Gurim-3_08	5	1509.3	Bath./Baj.	Arad	Daya	Ls	2.35	2.21	2.45	2.53	2.38	2.76	‖	2.54	1.03
							2.32	2.21	2.44	2.50	2.20	2.72	‖		
							2.47	2.39	2.55	2.54	2.26	2.78	⊥		
							2.48	2.42	2.55	2.58	2.39	2.77	⊥		
Gurim-3_09	5	1566.9	Bath./Baj.	Arad	Daya	Si	2.52	2.41	2.63	2.65	2.36	2.99	‖	2.75	3.50
							2.53	2.41	2.63	2.67	2.35	3.08	‖		
							2.59	2.47	2.69	2.87	2.69	3.15	⊥		
							2.62	2.52	2.77	2.75	2.54	3.04	⊥		
							-	-	-	2.82	2.55	3.15	⊥		
Hltza-2_01	6	787.0	Albian	Judea	Yagur	M	2.35	2.15	2.49	2.68	2.42	2.95	‖	2.77	6.96
							2.38	2.20	2.55	2.81	2.57	3.22	‖		
							2.38	2.14	2.59	2.71	2.41	3.10	‖		

Table A6.1: continued

							-	-	-	2.86	2.56	3.21			
Hltza-2_02	6	788.0	Albian	Judea	Yagur	Ls	2.13	1.90	2.45	-	-	-	‖	2.51	8.00
							2.16	1.93	2.56	-	-	-	‖		
							1.93	1.81	2.06	-	-	-	⊥		
							1.94	1.80	2.08	-	-	-	⊥		
							1.92	1.77	2.06	-	-	-	⊥		
Hltza-2_03	6	1431.2	Aptian	Kurnub	Zeweira	SS	3.07	2.69	3.45	5.22	4.67	6.06	‖	5.09	10.10
							3.08	2.82	3.34	5.59	4.94	6.31	‖		
							2.46	2.21	2.64	4.65	4.15	5.67	⊥		
							2.45	2.28	2.70	4.91	4.39	5.74	⊥		
							3.05	2.80	3.31	-	-	-	‖		
							3.17	2.92	3.43	-	-	-	‖		
							2.42	2.27	2.60	-	-	-	⊥		
							2.50	2.37	2.65	-	-	-	⊥		
Hltza-2_04	6	1986.2	Callovian	Arad	Zohar	Ls	2.18	2.07	2.33	-	-	-	‖	2.50	4.00
							2.20	2.14	2.31	-	-	-	‖		
							2.19	2.10	2.26	-	-	-	⊥		
							2.26	2.19	2.34	-	-	-	⊥		
Hltza-2_05	6	2223.6	Bathonian	Arad	Sherif	Ls	2.00	1.92	2.09	-	-	-	‖	2.30	4.00
							2.02	1.93	2.11	-	-	-	‖		
							2.05	2.01	2.09	-	-	-	⊥		
							2.03	1.97	2.11	-	-	-	⊥		
Hlz-2_01	7	396.0	Albian	Judea	Yagur	Ls	2.76	2.64	2.93	3.09	2.65	3.36	‖	3.12	7.00
							2.79	2.63	2.96	3.11	2.80	3.40	‖		
							2.75	2.64	2.89	3.09	2.59	3.45	⊥		
							2.75	2.63	2.88	3.19	2.82	3.76	⊥		
Hlz-2_02	7	475.0	Albian	Judea	Yagur	Dol	3.03	2.84	3.27	4.33	3.49	4.97	‖	4.45	1.93
							3.02	2.88	3.22	4.42	3.42	5.10	‖		
							4.16	2.98	5.33	4.54	3.77	5.27	⊥		
							4.12	2.99	5.25	4.53	3.53	5.25	⊥		
							2.97	2.84	3.10	3.10	2.76	3.75	‖		

Table A6.1: continued

							2.99	2.90	3.07	3.00	2.71	3.28	‖		
							4.79	4.11	5.37	-	-	-	⊥		
							5.02	4.52	5.42	-	-	-	⊥		
							5.04	4.46	5.53	-	-	-	⊥		
Hlz-2_03	7	545.3	Albian	Judea	Yagur	Ls	2.63	2.53	2.75	2.73	2.53	2.96	‖	2.74	2.07
							2.63	2.53	2.75	2.85	2.58	3.14	‖		
							2.52	2.46	2.63	2.67	2.49	2.86	⊥		
							2.55	2.46	2.63	2.73	2.53	2.92	⊥		
Hlz-2_04	7	563.5	Albian	Judea	Yagur	Ls	2.26	1.57	2.61	2.83	2.38	3.07	‖	2.65	9.00
							2.28	1.61	2.64	2.85	2.26	3.23	‖		
							1.82	1.38	2.21	2.42	2.11	2.73	⊥		
							1.82	1.33	2.21	2.62	2.33	2.92	⊥		
							-	-	-	2.54	2.13	2.88	⊥		
Hlz-2_05	7	564.1	Albian	Judea	Yagur	Ls	2.36	2.12	2.65	2.68	2.33	3.02	‖	2.67	7.00
							2.37	2.11	2.69	2.69	2.36	3.03	‖		
							2.10	1.65	2.44	2.65	2.19	2.82	⊥		
							2.11	1.63	2.43	2.66	2.25	2.91	⊥		
Hlz-2_06	7	610.1	Albian	Judea	Yagur	Dol	3.94	3.76	4.17	4.35	3.76	5.05	‖	4.32	7.58
							3.94	3.79	4.12	4.39	3.79	4.92	‖		
							3.93	3.54	4.21	4.12	3.82	4.60	⊥		
							3.92	3.61	4.19	4.44	4.06	4.83	⊥		
Hlz-2_07	7	661.6	Albian	Judea	Yagur	Ls	2.79	2.68	2.85	2.91	2.65	3.12	‖	2.88	0.96
							2.82	2.71	2.93	2.90	2.66	3.17	‖		
							2.75	2.64	2.87	2.84	2.62	3.08	⊥		
							2.84	2.68	3.01	2.87	2.56	3.11	⊥		
Hlz-2_08	7	731.2	Albian	Judea	Yagur	Ls	2.10	1.83	2.35	-	-	-	‖	2.60	8.00
							2.12	1.77	2.35	-	-	-	‖		
							2.13	1.99	2.27	-	-	-	⊥		
							2.15	2.04	2.31	-	-	-	⊥		
Hlz-2_09	7	783.2	Alb./Apt.	Kurnub	Yakhini	Dol Ls	2.21	2.08	2.36	2.48	2.33	2.73	‖	2.48	3.36
							2.20	2.07	2.35	2.53	2.33	2.75	‖		

Table A6.1: continued

							2.10	1.87	2.30	2.43	2.25	2.66	⊥		
							2.17	1.92	2.37	2.46	2.31	2.68	⊥		
Hlz-2_10	7	807.7	Alb./Apt.	Kurnub	Yakhini	Cl	2.70	2.56	2.83	-	-	-	⊥	2.80	2.00
							2.69	2.57	2.82	-	-	-	⊥		
Hlz-2_11	7	1078.0	Alb./Apt.	Kurnub	Yakhini	Dol Ls	2.57	2.48	2.68	2.57	2.49	2.65	∥	2.53	3.97
							2.59	2.46	2.70	2.57	2.48	2.67	∥		
							2.03	1.67	2.31	2.44	2.37	2.51	⊥		
Hlz-2_11a	7	1078.0	Alb./Apt.	Kurnub	Yakhini	Dol Ls	2.60	2.49	2.70	2.79	2.54	3.03	∥	2.79	
							2.60	2.48	2.71	2.83	2.59	3.04	∥		
							2.20	2.02	2.59	2.76	2.34	4.17	⊥		
							2.20	2.00	2.58	2.78	2.43	3.23	⊥		
Hlz-2_12	7	1126.2	Albian/Aptian	Kurnub	Yakhini	Ls	1.49	1.41	1.56	2.07	1.91	2.23	∥	2.08	9.00
							1.49	1.42	1.57	2.09	2.02	2.17	∥		
							1.39	1.29	1.43	2.11	1.99	2.23	⊥		
							1.38	1.28	1.42	2.05	1.88	2.22	⊥		
Hlz-2_13	7	1130.2	Alb./Apt.	Kurnub	Yakhini	Ls	1.97	1.85	2.06	2.20	1.95	2.46	∥	2.22	4.00
							1.97	1.85	2.07	2.36	2.25	2.47	∥		
							1.78	1.65	1.97	2.16	1.95	2.37	⊥		
							1.81	1.67	2.00	2.16	1.97	2.36	⊥		
Hlz-2_14	7	1167.7	Haut./Val.	Kurnub	Helez	Ls	2.33	2.25	2.40	2.55	2.49	2.63	∥	2.60	3.41
							2.36	2.22	2.42	2.59	2.51	2.65	∥		
							2.34	2.21	2.46	2.58	2.48	2.66	⊥		
							2.37	2.23	2.46	2.63	2.54	2.73	⊥		
							-	-	-	2.62	2.53	2.70	⊥		
Hlz-2_15	7	1351.0	Haut./Val.	Kurnub	Helez	Dol	3.17	2.89	3.54	3.61	3.00	4.54	∥	3.72	4.72
							3.20	2.90	3.67	3.68	3.06	4.34	∥		
							3.47	3.15	3.66	3.73	3.10	4.45	⊥		
							3.48	3.11	3.70	3.85	3.41	4.47	⊥		
Hlz-2_16	7	1504.6	Haut./Val.	Kurnub	Helez	Cl	1.37	1.27	1.42	-	-	-	∥	1.60	8.00
							1.37	1.29	1.42	-	-	-	∥		
							1.11	0.64	1.40	-	-	-	⊥		

Table A6.1: continued

							1.12	0.64	1.40	-	-	-	⊥		
Hlz-2_17	7	1510.8	Haut./Val.	Kurnub	Helez	Ls	2.23	1.96	2.41	2.58	2.33	2.72	‖	2.57	4.89
							2.20	1.91	2.33	2.58	2.40	2.71	‖		
							2.09	1.87	2.31	2.55	2.25	2.75	⊥		
							2.13	1.94	2.33	2.56	2.29	2.80	⊥		
							-	-	-	2.57	2.33	2.76	⊥		
Hlz-2_18	7	1974.4	Haut./Val.	Kurnub	Gvaram	Ls	2.22	2.13	2.29	2.45	2.41	2.51	‖	2.48	4.34
							2.20	2.10	2.27	2.50	2.40	2.58	‖		
							2.13	1.89	2.37	2.41	2.24	2.60	⊥		
							2.13	1.84	2.37	2.50	2.30	2.66	⊥		
							-	-	-	2.52	2.40	2.68	⊥		
Hlz-37_01	8	1524.7	Haut./Val.	Kurnub	Helez	SS	3.98	3.74	4.17	4.19	3.58	4.91	‖	4.32	0.82
							3.98	3.72	4.26	4.28	3.81	5.09	‖		
							4.01	3.15	4.59	4.39	3.93	4.89	⊥		
							4.01	3.25	4.54	4.41	3.90	5.12	⊥		
Hlz-37_02	8	1527.9	Haut./Val.	Kurnub	Helez	SS	4.61	4.06	4.94	4.89	4.27	5.59	‖	4.84	1.45
							4.56	4.03	4.96	4.90	4.19	5.58	‖		
							4.26	3.47	4.91	4.81	4.04	5.69	⊥		
							4.35	3.58	5.08	4.77	4.00	5.86	⊥		
Hlz-37_03	8	1528.4	Haut./Val.	Kurnub	Helez	Cl	1.29	1.20	1.45	-	-	-	‖	1.64	8.00
							1.29	1.19	1.44	-	-	-	‖		
							1.25	1.18	1.35	-	-	-	⊥		
							1.26	1.20	1.34	-	-	-	⊥		
Hlz-37_04	8	1546.0	Haut./Val.	Kurnub	Helez	Ls	1.61	1.49	1.83	2.12	1.90	2.42	‖	2.11	11.97
							1.61	1.50	1.81	2.14	1.96	2.40	‖		
							1.59	1.46	1.73	2.08	1.82	2.33	⊥		
							1.61	1.48	1.76	2.11	1.91	2.41	⊥		
Hlz-37_05	8	1557.8	Haut./Val.	Kurnub	Helez	Ls	1.93	1.66	2.22	2.25	1.99	2.55	‖	2.27	7.66
							1.92	1.63	2.25	2.30	2.01	2.72	‖		
							1.93	1.64	2.27	2.25	2.06	2.49	⊥		
							1.95	1.64	2.31	2.28	2.03	2.51	⊥		

Table A6.1: continued

Hm-1_01	9	513.3	Cenomanian	Judea	Hevyon	Ls, ar.	1.89	1.75	2.08	-	-	-	‖	1.97	1.37
							1.91	1.74	2.12	-	-	-	‖		
							1.88	1.73	2.05	-	-	-	⊥		
							1.85	1.70	2.00	-	-	-	⊥		
Hm-1_02	9	985.2	Bathonian	Arad	Sherif	SS	3.56	3.22	4.01	4.69	4.18	5.67	‖	4.47	6.79
							3.56	3.18	4.03	4.76	4.16	5.41	‖		
							3.32	2.99	3.75	4.14	3.52	4.91	⊥		
							3.39	2.89	3.78	4.30	3.73	5.00	⊥		
Hm-1_03	9	2028.0	Scythian	Ramon	Yamin	Ign	2.22	2.06	2.39	2.32	2.03	2.52	‖	2.33	4.04
							2.20	2.04	2.38	2.33	2.11	2.58	‖		
							2.17	2.08	2.29	2.27	2.12	2.44	⊥		
							2.19	2.09	2.31	2.40	2.25	2.55	⊥		
Hm-1_04	9	2030.7	Scythian	Ramon	Yamin	Ign	1.97	1.86	2.13	2.05	1.94	2.23	‖	2.09	1.94
							1.99	1.88	2.13	2.11	1.95	2.23	‖		
							2.03	1.90	2.21	2.09	1.99	2.21	⊥		
							2.01	1.88	2.11	2.10	1.95	2.27	⊥		
Hm-1_05	9	2031.6	Scythian	Ramon	Yamin	Ign	2.22	2.13	2.40	2.28	2.14	2.40	‖	2.32	1.50
							2.20	2.10	2.26	2.31	2.20	2.45	‖		
							2.21	2.10	2.31	2.38	2.17	2.54	⊥		
							2.25	2.09	2.33	2.32	2.15	2.47	⊥		
Hm-1_06	9	2294.0	L. Permian	Negev	Arqov	Ign	2.20	2.09	2.39	2.20	2.07	2.37	‖	2.20	0.36
							2.21	2.09	2.32	2.19	2.08	2.30	‖		
							2.20	2.09	2.30	2.20	2.06	2.33	⊥		
							2.21	2.10	2.38	2.20	2.10	2.35	⊥		
HmCH-1_01	9	314.5	Cenomanian	Judea	Zafit	Dol	4.85	4.18	5.97	4.66	3.43	5.56	⊥	4.91	5.00
							4.75	4.33	5.36	5.12	3.22	8.69	⊥		
							-	-	-	4.96	4.49	6.15	⊥		
HmCH-1_02	9	306.6	Cenomanian	Judea	Zafit	Dol	4.49	3.97	5.05	5.10	4.66	5.80	‖	5.21	8.83
							4.60	4.17	5.44	5.55	4.71	7.68	‖		
							-	-	-	5.62	4.74	6.78	‖		
							4.21	3.65	4.68	4.84	3.88	5.75	⊥		

Table A6.1: continued

							4.33	3.81	4.99	5.17	4.20	5.91	⊥		
HmCH-1_03	9	241.8	Cenomanian	Judea	Tamar	Ls	2.86	2.65	3.06	3.07	2.85	3.36	‖	3.08	2.43
							2.78	2.61	3.00	3.09	2.81	3.45	‖		
							2.92	2.76	3.07	3.02	2.82	3.30	⊥		
							2.96	2.84	3.12	3.14	2.90	3.35	⊥		
HmCH-1_04	9	232.7	Cenomanian	Judea	Tamar	Ls	2.80	2.49	3.07	3.16	2.89	3.41	‖	3.17	2.07
							2.83	2.43	3.13	3.12	2.85	3.39	‖		
							2.83	2.53	3.08	3.18	2.99	3.38	⊥		
							2.85	2.61	3.19	3.21	3.05	3.42	⊥		
HmCH-1_05	9	202.3	Cenomanian	Judea	Tamar	Ls	1.86	1.71	2.04	2.54	2.36	2.86	‖	2.60	14.40
							1.89	1.69	1.99	2.61	2.32	2.88	‖		
							1.96	1.77	2.07	2.62	2.28	2.89	⊥		
							1.98	1.82	2.12	2.63	2.46	2.79	⊥		
HmCH-1_06	9	200.9	Cenomanian	Judea	Tamar	Ls, ar.	2.43	2.21	2.69	-	-	-	‖	2.63	4.50
							2.44	2.24	2.56	-	-	-	‖		
							2.22	1.66	2.50	-	-	-	⊥		
							2.19	1.61	2.46	-	-	-	⊥		
HmCH-1_07	9	149.1	Campanian	Mt. Sc.	Mishash	Dol	4.24	3.64	4.72	4.73	4.12	5.74	‖	4.86	3.23
							4.28	3.79	4.98	5.10	4.22	6.42	‖		
							4.31	3.65	5.00	4.67	3.72	5.83	⊥		
							4.30	3.58	5.04	4.92	3.79	6.15	⊥		
HmCH-1_08	9	310.6	Cenomanian	Judea	Zafit	Dol	3.82	3.55	4.08	4.07	3.88	4.25	⊥	4.06	4.00
							4.05	3.81	4.29	4.06	4.00	4.11	⊥		
HmCH-1_09	9	312.6	Cenomanian	Judea	Zafit	Cl	1.55	1.52	1.58	-	-	-	⊥	2.00	8.00
							1.55	1.51	1.59	-	-	-	⊥		
Hzm-1_01	10	2735.8	Bajocian	Arad	Inmar U.	SS	3.73	3.33	4.19	5.49	4.78	6.52	‖	5.44	13.21
							3.89	3.22	4.33	5.74	4.94	6.57	‖		
							3.83	3.55	4.19	5.07	4.37	5.91	⊥		
							3.98	3.41	4.44	5.48	4.97	6.16	⊥		
							3.88	3.51	4.45	-	-	-	⊥		
							3.66	3.37	4.18	-	-	-	‖		

Table A6.1: continued

							3.71	3.37	4.08	-	-	-	‖		
							3.75	3.39	4.07	-	-	-	⊥		
							3.76	3.32	4.18	-	-	-	⊥		
Hzm-1_02	10	3063.5	Aalenian	Arad	Qeren	SS	4.76	3.21	6.95	4.55	3.57	6.10	‖	5.14	5.14
							4.71	3.04	6.76	4.91	3.68	6.52	‖		
							4.14	3.10	4.84	5.10	4.09	6.17	⊥		
							4.11	3.22	4.92	5.53	4.75	6.27	⊥		
							-	-	-	6.03	4.98	7.51	⊥		
Hzm-1_03	10	3581.2	Sinemur	Arad	Ardon	Ls	2.79	2.60	2.98	2.80	2.50	2.96	‖	2.78	1.71
							2.79	2.53	2.99	2.75	2.41	2.93	‖		
							-	-	-	2.78	2.29	3.02	‖		
Hzm-1_04	10	3581.2	Sinemur	Arad	Ardon	Ls, ar.	2.37	2.14	2.60	-	-	-	‖	2.60	2.38
							2.39	2.09	2.70	-	-	-	‖		
Hzrm-1_05	10	1905.8	Callovian	Arad	Zohar	Ls	2.20	2.04	2.34	2.58	2.30	2.88	‖	2.60	8.87
							2.19	2.07	2.29	2.66	2.40	2.95	‖		
							-	-	-	2.50	2.34	2.72	⊥		
							2.12	1.95	2.22	2.62	2.41	2.85	⊥		
							2.12	1.96	2.23	2.58	2.36	2.80	⊥		
MaKa-36A	11	2838.0	Precambrian			Ign	2.61	2.46	2.87	2.59	2.38	2.94	‖	2.59	
							2.62	2.44	2.82	2.59	2.37	2.91	‖		
							2.37	2.09	2.83	-	-	-	‖		
MaKa-36B	11	2838.0	Precambrian			Ign	2.18	1.89	2.77	2.31	2.06	2.79	⊥	2.33	0.47
							2.17	1.86	2.71	2.34	2.03	2.89	⊥		
Negba-1_03	12	180.8	Cenomanian	Judea	Negba	Ls	1.96	1.82	2.07	2.60	2.52	2.67	‖	2.58	8.00
							1.98	1.80	2.35	2.62	2.60	2.65	‖		
							2.01	1.93	2.10	2.52	2.43	2.60	⊥		
							2.03	1.94	2.15	2.59	2.54	2.65	⊥		
Negba-1_04	12	448.3	Cenomanian	Judea	Negba	Ls	1.69	1.67	1.71	2.29	2.27	2.31	⊥	2.30	8.00
							1.70	1.67	1.73	2.30	2.27	2.33	⊥		
Negba-1_05	12	449.1	Albian	Judea	Yagur	Ls	1.75	1.54	1.98	-	-	-	‖	2.50	13.00

Table A6.1: continued

							1.73	1.56	1.92	-	-	-	‖		
							1.73	1.51	2.07	-	-	-	⊥		
							1.81	1.53	2.15	-	-	-	⊥		
Negba-1_06	12	535.5	Albian	Judea	Yagur	Dol	3.65	2.93	3.99	3.89	3.51	4.60	‖	3.79	1.43
							3.69	3.21	4.36	3.89	3.51	4.41	‖		
							-	-	-	3.54	3.26	3.79	⊥		
							3.66	3.19	4.13	3.67	3.30	4.00	⊥		
							3.70	3.38	4.41	3.83	3.45	4.16	⊥		
Negba-1_07	12	541.6	Albian	Judea	Yagur	Dol Ls	2.96	2.81	3.15	3.09	2.94	3.23	‖	3.10	0.32
							2.99	2.85	3.19	3.18	2.93	3.42	‖		
							2.98	2.86	3.09	3.04	2.98	3.10	⊥		
							2.98	2.91	3.06	3.08	2.97	3.18	⊥		
Negba-1_08	12	887.0	Albian	Judea	Yagur	Dol Ls	2.89	2.74	3.15	2.96	2.77	3.17	‖	2.95	1.56
							2.83	2.60	3.08	2.94	2.74	3.23	‖		
							2.81	2.60	2.96	2.94	2.72	3.16	⊥		
							2.87	2.61	3.13	2.96	2.69	3.22	⊥		
Negba1_09	12	977.1	Albian	Kurnub	Yakhini	Ls	2.45	2.34	2.54	2.83	1.94	3.64	‖	2.88	9.12
							2.44	2.35	2.57	2.89	2.12	3.58	‖		
							2.28	1.95	2.65	2.83	2.53	3.14	⊥		
							2.30	1.98	2.71	2.95	2.69	3.23	⊥		
							-	-	-	2.98	2.65	3.43	⊥		
Negba-1_10	12	1025.7	Albian	Kurnub	Yakhini	Ls	2.14	2.03	2.30	2.32	1.99	2.57	‖	2.35	5.71
							2.18	2.07	2.35	2.38	2.09	2.66	‖		
Negba-1_11	12	1190.4	Albian	Kurnub	Yakhini	M	2.11	1.96	2.27	-	-	-	‖	2.62	9.00
							2.11	1.93	2.29	-	-	-	‖		
							2.07	1.87	2.27	-	-	-	⊥		
							2.06	1.88	2.25	-	-	-	⊥		
Negba-1_12	12	1346.7	Barremian	Kurnub	Telamin	Ls	2.39	2.32	2.46	-	-	-	‖	2.60	2.44
							2.43	2.35	2.50	2.66	2.48	2.91	‖		
							2.44	2.33	2.53	2.59	2.37	2.85	‖		
							2.32	2.21	2.45	2.55	2.40	2.75	⊥		

Table A6.1: continued

							2.29	2.18	2.44	2.58	2.40	2.76	⊥		
Negba-1_13	12	1430.0	Aptian	Kurnub	Telamin	Ls	2.49	2.38	2.60	2.92	2.65	3.19	‖	2.79	5.67
							2.48	2.38	2.61	2.99	2.70	3.25	‖		
							2.22	2.11	2.38	2.58	2.43	2.82	⊥		
							2.23	2.14	2.39	2.66	2.50	2.83	⊥		
Negba-1_14	12	1428.3	Aptian	Kurnub	Helez	Ls	2.65	2.53	2.78	3.08	2.67	3.44	‖	3.08	4.33
							2.70	2.54	2.95	3.08	2.74	3.44	‖		
Negba-1_15	12	1542.8	Barremian	Kurnub	Helez	Ls	1.93	1.84	2.07	-	-	-	‖	2.29	7.40
							1.93	1.84	2.02	-	-	-	‖		
							1.68	1.55	1.90	-	-	-	⊥		
							1.71	1.57	1.97	-	-	-	⊥		
Negba-1_16	12	1721.8	Barremian	Kurnub	Helez	Ls	2.42	2.31	2.58	3.10	2.84	3.31	‖	3.18	8.13
							2.40	2.27	2.59	3.03	2.79	3.36	‖		
							-	-	-	3.14	2.82	3.57	‖		
							2.51	2.30	2.74	3.19	2.88	3.52	⊥		
							2.56	2.34	2.81	3.28	2.97	3.65	⊥		
							-	-	-	3.33	3.04	3.69	⊥		
Negba-1_17	12	1855.1	Oxfordian	Arad	Kidod	M	2.01	1.92	2.11	-	-	-	‖	2.29	4.00
							2.03	1.95	2.18	-	-	-	‖		
Negba-1_18	12	1884.2	Oxfordian	Arad	Kidod	Cl	1.58	1.51	1.68	-	-	-	⊥	2.12	9.00
							1.60	1.52	1.71	-	-	-	⊥		
Ramon-1_01	13	619.6	Scythian	Ramon	Zafir	Si	2.34	2.26	2.40	-	-	-	‖	2.76	6.00
							2.35	2.31	2.43	-	-	-	‖		
							2.23	2.17	2.29	-	-	-	⊥		
							2.22	2.15	2.30	-	-	-	⊥		
Ramon-1_02	13	624.3	Scythian	Ramon	Zafir	M	1.86	1.71	2.06	1.94	1.85	2.17	⊥	1.94	0.90
							1.83	1.71	2.03	1.94	1.84	2.20	⊥		
Ramon-1_04	13	977.6	Scythian	Ramon	Yamin	SS	3.94	3.71	4.17	5.76	5.42	6.17	‖	5.88	10.55
							3.90	3.68	4.07	5.95	5.72	6.31	‖		
							3.88	3.69	4.10	5.81	5.32	6.20	⊥		
							4.01	3.81	4.16	6.00	5.56	6.42	⊥		

Table A6.1: continued

							3.92	3.69	4.15	-	-	-	⊥		
Ramon-1_05	13	1196.1	Scythian	Ramon	Arqov	SS	3.01	2.86	3.21	4.73	4.45	5.04	‖	4.95	13.18
							3.05	2.83	3.30	4.74	4.56	5.00	‖		
							3.41	3.23	3.60	5.13	4.86	5.36	⊥		
							3.46	3.25	3.64	5.19	4.92	5.48	⊥		
Ramon-1_06	13	1264.7	Early Permian	Negev	Saad	SS	4.63	4.32	5.04	6.32	5.62	6.81	‖	6.30	9.06
							4.70	4.43	5.08	6.25	5.31	6.87	‖		
							4.66	4.22	5.05	6.30	5.85	6.67	⊥		
							4.71	4.13	5.06	6.33	5.99	6.54	⊥		
Ramon-1_07	13	1345.0	Early Permian	Negev	Saad	SS	4.81	4.52	5.16	6.06	5.74	6.38	⊥	6.11	2.22
							4.97	4.56	5.35	6.14	5.84	6.43	⊥		
							4.67	4.41	4.88	5.99	5.66	6.36	‖		
							4.66	4.35	4.98	6.24	5.95	7.51	‖		
							4.52	4.22	4.82	-	-	-	‖		
Ramon-1_08	13	1350.0	Early Permian	Negev	Saad	SS	4.21	4.03	4.48	-	-	-	‖	5.09	11.24
							4.21	3.97	4.44	-	-	-	‖		
							-	-	-	4.83	4.24	5.52	⊥		
							-	-	-	5.35	4.66	6.86	⊥		
							3.77	3.53	4.16	7.40	6.01	9.65	⊥		
							3.86	3.65	4.14	7.37	5.85	9.66	⊥		
							-	-	-	3.96	3.29	4.57	⊥		
							-	-	-	3.87	3.32	4.51	⊥		
							-	-	-	4.21	3.56	4.69	‖		
							-	-	-	4.14	3.59	4.83	‖		
Ramon-1_09	13	1473.4	Precambrian	Sinaf	Zenifim	SS	2.20	2.12	2.28	2.24	2.07	2.52	⊥	2.26	4.27
							2.19	2.11	2.30	2.28	2.03	2.44	⊥		
Ramon-1_10	13	1476.2	Precambrian	Sinaf	Zenifim	Ark	2.53	2.42	2.59	2.77	2.61	3.02	‖	2.78	2.41
							2.53	2.44	2.60	2.87	2.72	3.07	‖		
							-	-	-	2.86	2.66	3.05	‖		
							2.40	2.33	2.48	2.71	2.52	3.06	⊥		
							2.42	2.33	2.51	2.73	2.57	2.91	⊥		

Table A6.1: continued

							2.42	2.36	2.49	-	-	-	⊥		
Ramon-1_11	13	1480.2	Precambrian	Sinaf	Zenifim	Ark	3.04	2.93	3.17	3.40	3.18	3.66	‖	3.29	2.62
							3.10	2.99	3.17	3.55	3.10	3.94	‖		
							2.86	2.57	3.06	3.01	2.62	3.56	⊥		
							2.92	2.68	3.10	3.21	2.65	3.61	⊥		
Ramon-1_12	13	1480.5	Precambrian	Sinaf	Zenifim	Ark	2.36	2.29	2.45	2.50	2.35	2.67	‖	2.47	3.40
							2.39	2.31	2.46	2.60	2.33	2.87	‖		
							2.25	2.20	2.29	2.37	2.24	2.51	⊥		
							2.27	2.22	2.30	2.42	2.27	2.61	⊥		
							2.26	2.22	2.35	-	-	-	⊥		
Ramon-1_13	13	2973.0	Precambrian	Sinaf	Zenifim	Ark	2.37	2.29	2.50	2.57	2.42	2.72	‖	2.60	6.00
							2.39	2.26	2.53	2.65	2.44	2.81	‖		
							2.40	2.26	2.52	2.57	2.35	2.76	⊥		
Ramon-1_14	13	2973.0	Precambrian	Sinaf	Zenifim	Ark	2.40	2.30	2.51	2.62	2.34	2.96	⊥	2.83	3.22
							-	-	-	2.86	2.67	3.05	‖		
							2.69	2.56	2.80	2.98	2.77	3.26	‖		
							2.72	2.64	2.82	2.94	2.71	3.27	‖		
							2.56	2.47	2.72	2.68	2.52	3.03	⊥		
							2.58	2.45	2.73	2.71	2.53	2.89	⊥		
Ramon-1_15	13	3178.6	Precambrian	Sinaf	Zenifim	Ark	3.28	2.96	3.59	3.42	3.15	3.78	‖	3.31	1.08
							3.28	2.99	3.56	3.43	3.01	3.87	‖		
							3.17	2.98	3.46	3.10	2.85	3.29	⊥		
							3.18	3.00	3.48	3.31	3.08	3.73	⊥		
Ramon-1_16	13	3440.0	Precambrian	Sinaf	Zenifim	Ark	3.19	2.93	3.47	3.18	2.98	3.37	‖	3.15	0.48
							3.32	3.02	3.98	3.27	3.07	3.47	‖		
							2.98	2.73	3.38	3.06	2.80	3.32	⊥		
							2.98	2.65	3.24	3.11	2.85	3.30	⊥		
Sinaf-1_01	14	324.6	Cenomanian	Judea	Zafit	M	2.42	1.99	2.70	2.74	2.59	2.90	‖	2.79	18.02
							2.45	2.09	2.57	2.63	2.49	2.77	‖		
							2.13	1.82	2.25	2.89	2.82	2.95	⊥		
							2.15	1.85	2.23	2.92	2.85	2.99	⊥		

Table A6.1: continued

Sinaf-1_02	14	326.1	Cenomanian	Judea	Zafit	M	1.51	1.45	1.56	2.28	2.10	2.47	‖	2.32	8.00
							1.55	1.43	1.66	2.32	2.09	2.58	‖		
							1.63	1.52	1.73	2.30	2.12	2.46	‖		
							1.63	1.47	1.78	2.32	2.13	2.53	⊥		
							1.64	1.46	1.82	2.36	2.20	2.53	⊥		
Sinaf-1_03	14	370.0	Cambrian	Judea	Hevyon	Dol	3.19	2.96	3.44	3.86	3.39	4.28	‖	3.75	10.75
							3.25	3.06	3.56	3.81	3.31	4.13	‖		
							3.03	2.78	3.28	3.61	3.36	3.92	⊥		
							3.01	2.73	3.25	3.70	3.43	4.26	⊥		
Sinaf-1_04	14	447.7	Cambrian	Kurnub	Hatira	Si	2.62	2.42	2.82	3.44	3.14	3.83	‖	3.40	7.00
							2.65	2.46	2.86	3.43	3.13	3.72	‖		
							2.54	2.34	2.76	3.32	3.07	3.68	⊥		
							2.58	2.37	2.76	3.42	2.99	4.03	⊥		
Sinaf-1_05	14	449.3	Cambrian	Kurnub	Hatira	Cl	1.24	1.03	1.46	-	-	-	‖	1.64	10.00
							1.25	1.06	1.44	-	-	-	‖		
							1.13	1.07	1.18	-	-	-	‖		
							1.16	1.11	1.26	-	-	-	‖		
Sinaf-1_06	14	449.7	Cambrian	Kurnub	Hatira	Cl	1.27	1.10	1.36	-	-	-	‖	1.68	10.00
							1.23	1.08	1.33	-	-	-	‖		
Sinaf-1_07	14	494.6	Cambrian	Kurnub	Hatira	SS	3.87	3.57	4.53	4.41	3.88	5.05	‖	4.21	6.52
							4.03	3.72	4.67	4.70	4.16	5.66	‖		
							3.54	3.17	3.92	3.75	3.23	4.69	⊥		
							3.55	3.27	3.81	3.99	3.36	4.52	⊥		
Sinaf-1_08	14	533.5	Cambrian	Kurnub	Hatira	Dol	3.08	2.77	3.63	3.48	3.07	3.96	‖	3.56	6.79
							3.06	2.82	3.38	3.66	3.08	4.21	‖		
							-	-	-	3.34	3.01	3.69	‖		
							3.10	2.76	3.51	3.60	3.35	3.91	⊥		
							3.14	2.78	3.73	3.72	3.33	4.04	⊥		
							-	-	-	3.55	3.24	3.98	⊥		
Sinaf-1_10	14	563.2	Cambrian	Kurnub	Hatira	Si	2.63	2.37	2.91	-	-	-	‖	3.15	7.00
							2.64	2.37	2.89	-	-	-	‖		

Table A6.1: continued

							2.59	2.30	2.98	-	-	-	⊥		
							2.83	2.27	2.90	-	-	-	⊥		
Sinaf-1_11	14	1198.2	Precambrian	Sinaf	Zenifim	Ark	2.84	2.55	3.11	2.87	2.73	3.05	‖	2.91	1.44
							2.87	2.62	3.15	2.96	2.80	3.18	‖		
							2.64	2.46	2.84	-	-	-	⊥		
							2.67	2.45	2.95	-	-	-	⊥		
Sinaf-1_12	14	1284.0	Precambrian	Sinaf	Zenifim	Ark	2.75	2.59	2.97	2.84	2.66	3.03	‖	2.88	1.15
							2.76	2.52	3.05	2.95	2.76	3.15	‖		
							2.78	2.58	3.06	2.83	2.66	3.06	⊥		
							2.82	2.63	3.15	2.91	2.67	3.09	⊥		
Sinaf-1_13	14	1307.1	Precambrian	Sinaf	Zenifim	Ark	2.92	2.72	3.05	3.13	2.86	3.43	‖	3.30	5.38
							2.84	2.71	3.07	3.49	3.20	3.85	‖		
							2.66	2.47	2.91	3.26	2.99	3.50	⊥		
							2.71	2.60	2.84	3.32	3.09	3.55	⊥		
Sinaf-1_14	14	1377.9	Precambrian	Sinaf	Zenifim	Ark	3.02	2.81	3.24	3.23	3.07	3.48	‖	3.20	1.80
							3.09	2.86	3.29	3.30	3.04	3.69	‖		
							2.89	2.57	3.28	3.11	2.94	3.28	⊥		
							2.86	2.68	3.13	3.14	2.96	3.41	⊥		
ZhrD-8_01	15	3317.7	Precambrian	Sinaf	Zenifim	Ext	2.20	1.97	2.62	2.50	2.19	2.98	‖	2.36	2.15
							2.21	2.01	2.64	2.42	1.82	3.07	‖		
							1.92	1.26	2.28	2.25	2.08	2.42	⊥		
							1.89	1.26	2.29	2.30	2.06	2.64	⊥		
							-	-	-	2.43	2.16	2.88	‖		
ZhrD-8_02	15	3281.4	Precambrian	Sinaf	Zenifim	Ext	2.40	2.06	2.72	-	-	-	‖	2.75	2.36
							2.44	2.10	2.77	-	-	-	‖		
							2.41	2.25	2.63	2.72	2.49	3.04	⊥		
							2.40	2.17	2.58	2.78	2.51	3.33	⊥		
ZhrD-8_03	15	3220.2	Precambrian	Sinaf	Zenifim	Ext	2.58	2.30	2.98	-	-	-	‖	3.19	2.77
							2.60	2.36	3.07	-	-	-	‖		
							2.78	2.31	3.10	3.20	2.71	3.70	⊥		
							2.74	2.27	3.07	3.19	2.61	3.63	⊥		

Table A6.1: continued

ZhrD-8_04	15	3189.0	Early Permian	Negev	Saad	SS	5.35	5.04	5.61	6.55	6.09	6.88	‖	6.57	6.29
							5.27	5.01	5.73	6.57	6.18	6.90	‖		
							5.14	4.75	5.53	6.50	6.29	6.81	⊥		
							5.20	4.88	5.61	6.64	6.31	6.91	⊥		
ZhrD-8_06	15	3167.1	Early Permian	Negev	Saad	SS	5.31	5.04	5.68	6.49	5.99	7.10	‖	6.52	3.36
							5.38	4.97	5.74	6.62	6.25	7.10	‖		
							-	-	-	6.57	6.21	6.88	‖		
							5.24	4.95	5.50	6.37	6.15	6.63	⊥		
							5.20	4.88	5.54	6.58	6.38	6.84	⊥		
ZhrD-8_07	15	3136.1	Early Permian	Negev	Saad	SS	4.55	4.16	4.87	4.73	4.38	4.98	‖	4.59	0.52
							4.58	4.23	4.94	4.86	4.57	5.07	‖		
							4.31	3.98	4.70	4.38	4.14	4.61	⊥		
							4.30	4.02	4.57	4.40	4.12	4.58	⊥		
ZhrD-8_10	15	2286.8	Anisian	Ramon	Gevanim	Ls	2.60	2.38	2.83	2.74	2.41	3.07	‖	2.74	0.56
							2.63	2.44	2.82	2.75	2.46	3.04	‖		
Zohar-1_01	16	606.8	Cenomian	Kurnub	Uza	Dol	-	-	-	4.01	3.73	4.41	‖	4.04	5.05
							3.47	3.18	3.89	4.11	3.78	4.39	‖		
							3.42	3.08	3.82	4.07	3.77	4.36	‖		
							3.37	3.01	3.82	3.98	3.60	4.38	⊥		
							3.40	2.98	3.78	4.06	3.70	4.48	⊥		
Zohar-1_02	16	668.3	Cenomian	Kurnub	Uza	Ls	2.40	2.23	2.56	2.57	2.39	2.77	‖	2.66	2.58
							2.41	2.26	2.55	2.58	2.39	2.73	‖		
							2.63	2.49	2.76	2.73	2.58	2.92	⊥		
							2.66	2.53	2.79	2.78	2.56	3.01	⊥		
Zohar-1_03	16	711.3	Cenomian	Kurnub	Malhata	Cl	1.32	1.23	1.44	-	-	-	⊥	1.76	9.00
							1.33	1.21	1.46	-	-	-	⊥		
Zohar-1_04	16	786.8	Albian	Kurnub	Dragot	Cl	1.62	1.52	1.72	-	-	-	‖	2.12	9.26
							1.63	1.52	1.72	-	-	-	‖		
							1.51	1.42	1.59	-	-	-	⊥		
							1.57	1.47	1.65	-	-	-	⊥		
Zohar-1_05	16	954.7	Aptian	Kurnub	Zeweira	SS	4.37	3.75	5.12	5.46	4.47	6.68	‖	5.71	3.00

Table A6.1: continued

							4.38	3.86	4.78	5.96	4.78	7.50	‖		
							4.32	3.72	4.94	5.62	4.69	7.12	⊥		
							4.31	3.85	4.81	5.80	4.80	7.09	⊥		
							4.17	3.91	4.55	-	-	-	‖		
							4.16	3.81	4.51	-	-	-	‖		
							4.06	3.80	4.36	-	-	-	⊥		
							4.16	3.88	4.74	-	-	-	⊥		
Zohar-1_06	16	1007.2	Aptian	Kurnub	Zeweira	Si	2.06	1.96	2.15	-	-	-	‖	2.41	4.00
							2.08	1.98	2.16	-	-	-	‖		
							2.24	2.08	2.41	-	-	-	⊥		
Zohar-1_07	16	1450.3	Bathonian	Arad	Sherif	Dol	3.20	3.01	3.34	3.09	2.74	3.50	‖	3.93	4.75
							3.15	3.06	3.28	3.15	2.93	3.50	‖		
							3.02	2.79	3.24	2.87	2.59	3.10	⊥		
							3.09	2.87	3.29	2.92	2.71	3.18	⊥		
							-	-	-	-	-	-	⊥		
Zohar-1_08	16	1615.2	Bajocian	Arad	Daya	SS	4.28	3.86	4.61	5.01	4.20	6.15	‖	5.23	5.03
							4.24	3.83	4.69	5.52	4.64	6.56	‖		
							-	-	-	5.43	4.64	6.81	‖		
							4.04	3.73	4.50	4.99	4.30	5.91	⊥		
							4.18	3.72	4.70	5.28	4.71	5.96	⊥		
Zohar-1_09	16	1680.2	Bajocian	Arad	Daya	Ls	2.26	2.18	2.33	2.78	2.58	3.03	‖	2.84	12.21
							2.28	2.19	2.37	2.89	2.63	3.11	‖		
							2.32	2.26	2.39	2.99	2.80	3.23	⊥		
							2.29	2.21	2.34	2.93	2.69	3.19	⊥		
							-	-	-	2.62	2.40	2.80	⊥		
Zohar-1_10	16	1689.4	Bajocian	Arad	Daya	Si	2.35	2.18	2.48	-	-	-	‖	2.60	7.00
							2.32	2.16	2.45	-	-	-	‖		
							2.02	1.79	2.19	-	-	-	⊥		
							2.00	1.76	2.17	-	-	-	⊥		
							2.00	1.77	2.20	-	-	-	⊥		
Zohar-1_11	16	1713.0	Bajocian	Arad	Daya	SS	5.24	4.35	6.39	5.14	4.44	5.80	‖	5.51	3.47

Table A6.1: continued

							5.04	4.46	5.95	5.64	4.91	6.48	‖		
							-	-	-	5.54	4.86	6.58	‖		
							4.92	4.40	5.40	5.46	4.88	6.22	⊥		
							4.98	4.22	5.50	5.80	4.73	7.72	⊥		
							-	-	-	5.46	4.84	6.59	⊥		
Zohar-1_12	16	1784.8	Sinemurian	Arad	Ardon	Si,SS	3.07	2.89	3.18	-	-	-	‖	3.24	3.00
							3.05	2.90	3.22	-	-	-	‖		
							2.84	2.56	3.09	-	-	-	⊥		
							2.83	2.50	3.11	-	-	-	⊥		
Zohar-1_13	16	1988.1	Carnian	Ramon	Mohilla	Si	3.39	3.09	3.84	3.43	2.99	3.79	‖	3.44	1.93
							3.30	3.08	3.58	3.44	3.15	3.81	‖		
Zohar-1_14	16	1988.1	Carnian	Ramon	Sahr.	Si	2.70	2.52	2.96	2.60	2.45	2.88	‖	2.64	0.49
							2.71	2.51	2.88	2.69	2.47	2.86	‖		

Table A6.2: TC measurements of dry and water-saturated outcrop samples. Measurements were performed on the core top/bottom (⊥) and the core mantle (∥) surface. The *min, max* and *mean TC* value of each scanning line is indicated. TC mean value averages over the *sat mean* values of the different scanning lines. TC mean values shaded in grey were calculated based on the *dry mean* value and the porosity appling the geometric mean model. Porosity (ϕ) was determined with the Archimedes method, when no water-saturation was possible samples were saturated with isooctane instead (cf. section 2.4).

Outcrop			Stratigraphy			*TC ($Wm^{-1}K^{-1}$)*							TC mean	ϕ
Sample	Loc.	Age	Gr.	Fm.	Litho.	*dry mean*	*dry min*	*dry max*	*sat mean*	*sat min*	*sat max*	Surface	($Wm^{-1}K^{-1}$)	%
Avnon-1	1	Cenom.	Judea	Avnon	Ls	2.39	2.21	2.70	3.03	2.85	3.36	⊥	3.07	10.0
						2.39	2.18	2.71	3.03	2.75	3.32	⊥		
						2.51	2.30	2.86	3.11	2.80	3.41	∥		
						2.50	2.32	2.81	3.13	2.88	3.38	∥		
Avnon-2	1	Cenom.	Judea	Avnon	M	2.13	2.07	2.21	2.33	2.21	2.47	⊥	2.34	8.0
						2.07	2.01	2.13	2.36	2.20	2.49	⊥		
						2.14	2.08	2.20	2.33	2.17	2.46	⊥		
						2.09	1.93	2.25	2.34	2.19	2.44	⊥		
						2.11	1.97	2.26	-	-	-	⊥		
Avnon-3	1	Cenom.	Judea	Avnon	Ls	2.81	2.73	2.89	2.96	2.76	3.10	∥	3.03	6.3
						2.78	2.69	2.93	2.99	2.83	3.20	∥		
						2.71	2.49	2.95	3.10	2.95	3.30	⊥		
						2.70	2.51	2.98	3.07	2.91	3.23	⊥		
Avnon-4	1	Cenom.	Judea	Avnon	Dol Ls	2.86	2.83	2.89	2.99	2.86	3.12	⊥	3.05	5.5
						2.88	2.85	2.92	3.11	2.93	3.30	⊥		
Avnon-5	1	Cenom.	Judea	Avnon	Dol Ls	2.81	2.69	2.92	3.07	2.95	3.20	⊥	3.05	6.5
						2.72	2.51	2.92	3.02	2.91	3.13	⊥		
Mishash-1	1	Campanian	Mt. Sc.	Mishash	Chert	4.56	3.77	5.39	4.81	4.44	5.38	⊥	4.93	3.3
						4.67	4.17	5.68	5.01	4.58	5.54	⊥		
						4.83	4.12	5.85	4.95	4.48	5.63	⊥		
						4.61	3.89	5.85	4.95	4.51	5.42	⊥		
Mishash-2	1	Campanian	Mt. Sc.	Mishash	Chert	-	-	-	4.70	4.02	5.42	⊥	5.03	2.8
						4.24	3.74	4.92	4.74	4.12	5.20	⊥		
						4.27	3.78	5.15	5.09	4.71	5.40	∥		
						4.52	4.22	4.77	5.19	4.76	5.49	∥		

Table A6.2: continued

						4.49	4.35	4.61	5.10	4.81	5.43	‖		
						4.80	4.40	5.20	5.21	4.85	5.64	‖		
						4.75	4.60	5.05	5.20	4.83	5.49	‖		
Mishash-3	1	Campanian	Mt. Sc.	Mishash	Chert	4.76	4.07	5.77	5.11	4.16	6.55	⊥	5.21	1.0
						4.91	4.05	5.95	5.28	4.38	7.14	‖		
						4.94	4.12	6.06	5.25	4.20	6.65	‖		
Nezer-1	1	Turonian	Judea	Nezer	Ls	2.62	2.48	2.77	2.71	2.53	2.89	⊥	2.74	3.1
						2.59	2.46	2.81	2.71	2.56	2.84	⊥		
						2.65	2.57	2.77	2.72	2.57	2.90	⊥		
						2.67	2.60	2.75	2.78	2.64	2.89	⊥		
						2.66	2.56	2.74	2.77	2.67	2.87	⊥		
Nezer-2	1	Turonian	Judea	Nezer	Ls	2.00	1.85	2.21	2.42	2.23	2.54	⊥	2.55	13.0
						1.98	1.83	2.16	2.41	2.23	2.56	⊥		
						2.36	2.26	2.51	2.67	2.45	2.84	‖		
						2.44	2.36	2.59	2.71	2.50	2.92	‖		
						2.41	2.33	2.53	-	-	-	‖		
Nezer-3	1	Turonian	Judea	Nezer	Ls	-	-	-	2.64	2.50	2.75	⊥	2.72	7.1
						2.46	2.28	2.65	2.72	2.64	2.81	⊥		
						2.46	2.28	2.66	2.74	2.60	2.87	⊥		
						2.29	2.13	2.46	2.74	2.66	2.87	⊥		
						2.32	2.15	2.47	2.75	2.64	2.85	⊥		
Shivta-1	1	Turonian	Judea	Shivta	Ls	2.74	2.54	3.00	2.74	2.64	2.88	⊥	2.78	0.9
						2.72	2.43	3.01	2.74	2.63	2.90	⊥		
						2.74	2.55	3.09	2.81	2.67	2.92	⊥		
						2.76	2.53	2.98	2.83	2.72	2.98	⊥		
Shivta-2	1	Turonian	Judea	Shivta	Ls	2.79	2.68	2.88	3.13	2.95	3.29	‖	3.08	4.1
						2.81	2.72	2.92	3.13	3.01	3.27	‖		
						2.86	2.75	2.96	3.03	2.93	3.18	⊥		
						2.87	2.75	2.96	3.05	2.92	3.17	⊥		
Shivta-3	1	Turonian	Judea	Shivta	Ls	2.96	2.85	3.08	2.94	2.77	3.14	⊥	2.97	3.9
						2.79	2.62	2.97	2.97	2.86	3.13	⊥		

Table A6.2: continued

						2.75	2.55	2.91	2.97	2.80	3.16	⊥		
						2.86	2.64	3.09	3.01	2.83	3.21	⊥		
						2.81	2.56	3.08	-	-	-	⊥		
Shivta-4	1	Turonian	Judea	Shivta	Dol Ls	2.77	2.51	3.02	2.76	2.66	2.86	⊥	2.84	2.0
						2.71	2.40	3.01	2.81	2.66	2.97	⊥		
						2.86	2.54	3.19	2.96	2.90	3.02	⊥		
						2.75	2.53	2.97	2.81	2.72	2.90	⊥		
Shivta-5	1	Turonian	Judea	Shivta	Dol Ls	2.83	2.67	2.98	3.11	2.94	3.28	⊥	3.11	3.4
						2.81	2.72	2.91	3.19	3.12	3.27	⊥		
						2.85	2.77	2.94	3.06	2.94	3.18	⊥		
						2.83	2.74	2.92	3.06	2.97	3.15	⊥		
Shivta-6	1	Turonian	Judea	Shivta	Dol Ls	2.93	2.84	3.03	2.96	2.77	3.15	⊥	3.00	3.0
						2.74	2.60	2.87	2.99	2.86	3.12	⊥		
						2.66	2.51	2.81	3.00	2.84	3.16	⊥		
						2.82	2.63	3.00	3.03	2.83	3.23	⊥		
						2.81	2.54	3.08	-	-	-	⊥		
Menuha-1	2	Santonian	Mt. Sc.	Menuha	Cha	1.29	1.22	1.44	1.85	1.83	1.88	⊥	1.84	25.0
						1.29	1.20	1.44	1.78	1.75	1.82	⊥		
						1.30	1.17	1.48	1.94	1.93	1.94	⊥		
						1.32	1.18	1.46	1.80	1.75	1.86	⊥		
Menuha-2	2	Santonian	Mt. Sc.	Menuha	Cha	1.51	1.46	1.55	1.91	1.83	1.98	⊥	1.96	27.7
						1.49	1.41	1.59	1.95	1.85	2.02	⊥		
						1.50	1.38	1.67	1.97	1.93	2.00	⊥		
						1.51	1.41	1.73	2.00	1.95	2.06	⊥		
Tamar-1	3	Cenom.	Judea	Tamar	Cha	1.44	1.39	1.48	2.04	1.99	2.13	⊥	2.06	18.4
						1.40	1.35	1.45	2.06	2.00	2.15	⊥		
						1.40	1.35	1.48	2.04	1.95	2.12	⊥		
						1.48	1.43	1.58	2.09	2.00	2.19	⊥		
						1.51	1.44	1.61	-	-	-	⊥		
Tamar-2	3	Cenom.	Judea	Tamar	Ls	2.42	2.27	2.55	2.56	2.44	2.67	⊥	2.62	3.9
						2.41	2.27	2.57	2.58	2.47	2.69	⊥		

Table A6.2: continued

						2.54	2.47	2.61	2.64	2.55	2.77	⊥		
						2.49	2.34	2.64	2.68	2.54	2.84	⊥		
						2.55	2.44	2.71	-	-	-	⊥		
Tamar-3	3	Cenom.	Judea	Tamar	M	2.33	2.21	2.48	2.57	2.44	2.66	⊥	2.51	4.9
						2.36	2.28	2.43	2.55	2.42	2.65	⊥		
						2.33	2.25	2.40	2.44	2.35	2.52	⊥		
						2.32	2.23	2.39	2.49	2.40	2.59	⊥		
Tamar-4	3	Cenom.	Judea	Tamar	Ls	2.04	1.81	2.28	2.14	2.04	2.23	⊥	2.14	
						2.06	1.88	2.23	2.15	2.09	2.21	⊥		
Tamar-5	3	Cenom.	Judea	Tamar	M	1.79	1.61	1.98	2.07	2.04	2.09	⊥	2.00	
						1.81	1.78	1.83	1.93	1.92	1.95	⊥		
Tamar-6	3	Cenom.	Judea	Tamar	M	2.32	2.24	2.41	2.64	2.55	2.72	⊥	2.64	
						2.31	2.22	2.39	2.63	2.48	2.79	⊥		
EnYorq-1	4	Cenom.	Judea	EnYor.	M	2.11	1.99	2.30	2.32	2.22	2.46	⊥	2.37	7.3
						2.09	1.98	2.29	2.34	2.25	2.50	⊥		
						2.21	2.11	2.33	2.42	2.36	2.52	‖		
						2.20	2.08	2.31	2.41	2.34	2.55	‖		
EnYorq-2	4	Cenom.	Judea	EnYor.	M	2.03	1.90	2.14	2.29	2.22	2.34	⊥	2.28	10.9
						2.07	1.95	2.14	2.26	2.16	2.32	⊥		
						2.17	2.08	2.30	2.27	2.17	2.39	‖		
						2.14	2.02	2.29	2.32	2.17	2.44	‖		
EnYorq-3	4	Cenom.	Judea	EnYor.	Sh	1.67	1.42	1.88	2.03	1.98	2.09	⊥	2.05	12.6
						1.67	1.42	1.86	2.06	2.01	2.13	⊥		
EnYorq-4	4	Cenom.	Judea	EnYor.	Cl	1.74	1.60	1.85	2.04	1.98	2.10	⊥	2.05	
						1.74	1.62	1.84	2.06	2.01	2.12	⊥		
Hevyon-1	4	Albian	Judea	Hevyon	Ls	2.58	2.50	2.69	2.73	2.49	2.87	⊥	2.76	8.1
						2.62	2.51	2.76	2.75	2.54	2.90	⊥		
						2.59	2.52	2.68	2.75	2.65	2.86	⊥		
						2.57	2.49	2.70	2.82	2.69	2.94	⊥		
						2.56	2.46	2.68	2.76	2.68	2.87	⊥		
Hevyon-2	4	Albian	Judea	Hevyon	Ls	2.95	2.87	3.05	3.21	3.04	3.38	⊥	3.18	19.9

Table A6.2: continued

						2.86	2.62	3.12	3.23	3.03	3.47	⊥		
						2.83	2.67	3.04	3.14	2.91	3.37	⊥		
						2.73	2.65	2.81	3.13	2.97	3.31	⊥		
						2.64	2.48	2.76	-	-	-	⊥		
						2.70	2.58	2.82	-	-	-	⊥		
Hevyon-3	4	Albian	Judea	Hevyon	Dol Ls	2.41	2.27	2.54	3.14	2.99	3.30	⊥	3.19	13.0
						2.38	2.25	2.51	3.24	3.17	3.31	⊥		
Hevyon-4	4	Albian	Judea	Hevyon	Dol Ls	2.37	2.28	2.46	2.82	2.75	2.89	⊥	2.78	14.0
						2.35	2.25	2.46	2.75	2.62	2.87	⊥		
Ghareb-1	5	Maastr.	Mt. Sc.	Ghareb	Cha	0.62	0.60	0.63	1.19	1.17	1.21	⊥	1.25	15.0
						0.61	0.59	0.64	1.23	1.20	1.26	⊥		
						0.63	0.62	0.66	1.27	1.25	1.28	⊥		
						0.63	0.59	0.65	1.32	1.29	1.35	⊥		
Ghareb-2	5	Maastr.	Mt. Sc.	Ghareb	M	1.73	1.62	1.84	2.13	2.01	2.22	⊥	2.13	17.7
						1.73	1.64	1.83	2.14	2.05	2.23	⊥		
						1.75	1.67	1.81	2.12	2.06	2.18	⊥		
						1.71	1.66	1.77	2.12	2.04	2.18	⊥		
Ghareb-3	5	Maastr.	Mt. Sc.	Ghareb	M	1.66	1.57	1.73	2.18	2.10	2.24	⊥	2.17	14.5
						1.66	1.58	1.73	2.17	2.08	2.30	⊥		
						1.69	1.58	1.86	-	-	-	⊥		
						1.71	1.60	1.88	-	-	-	⊥		
Ghareb-4	5	Maastr.	Mt. Sc.	Ghareb	Cha	0.69	0.67	0.70	1.18	1.17	1.20	⊥	1.16	15.0
						0.71	0.65	0.76	1.16	1.15	1.16	⊥		
						0.67	0.66	0.68	1.17	1.16	1.18	⊥		
						0.74	0.72	0.75	1.14	1.12	1.15	⊥		
						0.74	0.72	0.75	1.13	1.12	1.15	⊥		
Taqiye-1	6	Paleocene	Mt. Sc.	Taqiye	Cl	1.07	1.02	1.12	-	-	-	⊥	1.90	18.0
						1.09	1.06	1.11	-	-	-	⊥		
						1.11	1.10	1.12	-	-	-	⊥		
						1.11	1.11	1.12	-	-	-	⊥		
Taqiye-2	6	Paleocene	Mt. Sc.	Taqiye	Cl	0.88	0.84	0.93	-	-	-	⊥	1.70	22.0

Table A6.2: continued

						0.85	0.82	0.88	-	-	-	⊥		
Taqiye-3	6	Paleocene	Mt. Sc.	Taqiye	Cl	1.07	1.02	1.12	-	-	-	⊥	1.90	19.0
						1.06	1.02	1.11	-	-	-	⊥		
						1.12	1.05	1.19	-	-	-	⊥		
						1.11	1.05	1.17	-	-	-	⊥		
Taqiye-4	6	Paleocene	Mt. Sc.	Taqiye	Cl	1.05	0.95	1.15	-	-	-	⊥	1.90	19.0
						1.07	1.04	1.11	-	-	-	⊥		
Taqiye-5	6	Paleocene	Mt. Sc.	Taqiye	Cl	0.92	0.82	1.01	-	-	-	⊥	1.80	20.0
						0.97	0.83	1.11	-	-	-	⊥		
						1.01	0.88	1.13	-	-	-	⊥		
						1.00	0.88	1.12	-	-	-	⊥		
Taqiye-6	6	Paleocene	Mt. Sc.	Taqiye	Sh	1.32	1.22	1.42	-	-	-	‖	2.20	18.0
						1.26	1.16	1.36	-	-	-	‖		
						1.20	1.16	1.25	-	-	-	⊥		
						1.19	1.16	1.22	-	-	-	⊥		
Taqiye-7	6	Paleocene	Mt. Sc.	Taqiye	Sh	1.03	0.94	1.13	-	-	-	‖	2.00	19.0
						1.06	1.02	1.11	-	-	-	‖		
						1.05	1.01	1.10	-	-	-	⊥		
						1.05	1.02	1.09	-	-	-	⊥		
Taqiye-8	6	Paleocene	Mt. Sc.	Taqiye	Sh	1.03	1.02	1.05	-	-	-	‖	1.80	20.0
						1.04	1.02	1.06	-	-	-	‖		
						0.93	0.85	1.01	-	-	-	⊥		
						0.92	0.81	1.03	-	-	-	⊥		
Taqiye-9	6	Paleocene	Mt. Sc.	Taqiye	Sh	1.05	1.02	1.08	-	-	-	⊥	1.70	16.0
						1.07	1.03	1.11	-	-	-	⊥		
Taqiye-10	6	Paleocene	Mt. Sc.	Taqiye	Sh	1.16	1.08	1.23	-	-	-	⊥	2.10	17.0
						1.15	1.08	1.22	-	-	-	⊥		
Evrona-1	7	Albian	Kurnub	Hatira	Ss	4.14	3.77	4.51	5.11	4.98	5.25	‖	5.07	6.0
						4.15	3.77	4.52	5.02	4.88	5.16	‖		
Evrona-2	7	Albian	Kurnub	Hatira	Ss	4.17	3.82	4.53	5.06	4.78	5.35	⊥	5.08	6.0
						4.19	3.84	4.55	5.10	4.89	5.31	⊥		

Table A6.2: continued

Gerofit-1	7	Turonian	Judea	Gerofit	Ls	1.98	1.87	2.16	2.57	2.46	2.68	⊥	2.53	14.0
						2.01	1.84	2.13	2.50	2.41	2.60	⊥		
						2.00	1.92	2.11	2.52	2.36	2.64	⊥		
Gerofit-2	7	Turonian	Judea	Gerofit	M	1.57	1.49	1.67	2.25	2.10	2.38	⊥	2.31	19.0
						1.59	1.48	1.70	2.23	2.08	2.39	⊥		
						1.78	1.62	2.01	2.38	2.31	2.47	‖		
						1.82	1.63	2.07	2.39	2.31	2.49	‖		
						1.81	1.59	2.06	-	-	-	‖		
Ora-1	7	Turonian	Judea	Orash.	Sh	1.59	1.48	1.70	-	-	-	‖	1.80	5.0
						1.57	1.48	1.65	-	-	-	‖		
						1.46	1.39	1.52	-	-	-	⊥		
						1.47	1.41	1.54	-	-	-	⊥		
						1.45	1.41	1.49	-	-	-	⊥		
						1.44	1.42	1.45	-	-	-	⊥		
Ora-2	7	Turonian	Judea	Orash.	Gyp	0.94	0.84	1.15	-	-	-	⊥	1.30	11.5
						0.93	0.82	1.13	-	-	-	⊥		
						1.07	0.98	1.16	-	-	-	⊥		
						1.03	0.97	1.10	-	-	-	⊥		
						1.02	0.94	1.09	-	-	-	⊥		
						0.81	0.78	0.82	-	-	-	⊥		
						0.77	0.73	0.79	-	-	-	⊥		
						0.69	0.67	0.73	-	-	-	⊥		
						0.72	0.71	0.74	-	-	-	⊥		
Ora-3	7	Turonian	Judea	Orash.	Sh	1.67	1.65	1.69	-	-	-	‖	1.58	6.0
						1.62	1.60	1.64	-	-	-	‖		
						1.17	1.08	1.27	-	-	-	⊥		
						1.12	1.01	1.24	-	-	-	⊥		
						1.11	1.01	1.20	-	-	-	⊥		
						1.14	1.08	1.24	-	-	-	⊥		
Ora-4	7	Turonian	Judea	Orash.	Sh	1.47	1.45	1.49	-	-	-	⊥	1.70	5.0
						1.42	1.40	1.44	-	-	-	⊥		

Table A6.2: continued

Ora-5	7	Turonian	Judea	Orash.	Sh	1.48	1.47	1.50	-	-	-	⊥	1.70	5.0
						1.46	1.46	1.47	-	-	-	⊥		
OraLime	7	Turonian	Judea	Orash.	Ls	2.49	2.41	2.59	2.58	2.45	2.74	⊥	2.38	4.7
						2.50	2.42	2.58	2.63	2.50	2.78	⊥		
						2.60	2.54	2.69	2.17	2.05	2.26	⊥		
						2.58	2.49	2.72	2.14	2.05	2.24	⊥		
Samar	7	Cenom.	Kurnub	Samar	Ss	-	-	-	5.16	4.76	5.72	⊥	5.04	14.9
						2.33	2.03	2.67	5.19	4.76	5.57	⊥		
						2.39	2.14	2.73	4.96	4.46	5.65	⊥		
						2.39	2.12	2.70	4.81	4.46	5.86	⊥		
						2.37	1.99	2.74	5.06	4.49	5.75	‖		
						2.35	1.94	2.82	5.06	4.59	5.61	‖		
Zihor-1	7	Coniacian	Mt. Sc.	Zihor	Ls	2.26	1.93	2.47	2.62	2.49	2.74	⊥	2.68	9.3
						2.28	2.00	2.49	2.67	2.47	2.82	⊥		
						2.24	1.94	2.47	2.67	2.46	2.83	⊥		
						2.40	2.28	2.52	2.72	2.60	2.82	⊥		
						2.39	2.29	2.48	2.75	2.66	2.86	⊥		
Zihor-2	7	Coniacian	Mt. Sc.	Zihor	Ls	2.12	2.01	2.31	2.52	2.38	2.69	⊥	2.59	12.2
						2.13	2.03	2.27	2.54	2.40	2.73	⊥		
						2.24	2.05	2.38	2.64	2.51	2.78	‖		
						2.25	2.05	2.41	2.66	2.51	2.83	‖		
Zihor-3	7	Coniacian	Mt. Sc.	Zihor	Ls	-	-	-	2.68	2.54	2.81	⊥	2.72	5.5
						2.51	2.34	2.70	2.74	2.60	2.88	⊥		
						2.47	2.27	2.73	2.71	2.56	2.87	⊥		
						2.49	2.32	2.73	2.68	2.48	2.86	⊥		
						2.30	2.00	2.63	2.74	2.48	2.91	⊥		
						2.35	2.02	2.69	2.76	2.53	2.94	⊥		
						2.34	1.97	2.70	2.74	2.47	2.90	⊥		
Zihor-4	7	Coniacian	Mt. Sc.	Zihor	Ls	2.68	2.55	2.77	2.72	2.60	2.86	⊥	2.73	0.4
						2.73	2.63	2.93	2.72	2.63	2.84	⊥		
						2.71	2.61	2.88	2.72	2.63	2.84	⊥		

Table A6.2: continued

						2.75	2.61	2.87	2.74	2.63	2.84	⊥		
						2.72	2.58	2.84	-	-	-	⊥		
Zihor-5	7	Coniacian	Mt. Sc.	Zihor	Ls	2.73	2.63	2.79	2.76	2.66	2.87	⊥	2.70	0.5
						2.73	2.67	2.80	2.73	2.65	2.87	⊥		
						2.64	2.49	2.78	2.70	2.57	2.84	⊥		
						2.70	2.55	2.87	2.74	2.62	2.88	⊥		
						2.65	2.52	2.80	2.64	2.54	2.71	⊥		
						2.58	2.50	2.64	2.64	2.53	2.75	⊥		
						2.62	2.48	2.70	-	-	-	⊥		
						2.59	2.51	2.67	-	-	-	⊥		
TamarDol-1	8	Cenom.	Judea	Tamar	Dol	4.53	4.32	4.76	4.55	4.29	4.78	⊥	4.56	1.3
						4.65	4.47	4.90	4.56	4.19	4.90	⊥		
						4.57	4.25	4.91	-	-	-	⊥		
TamarDol-2	8	Cenom.	Judea	Tamar	Dol Ls	2.91	2.80	3.02	2.93	2.77	3.12	⊥	2.91	0.7
						2.91	2.84	3.02	2.89	2.70	3.05	⊥		